

## ABSTRACT

KELLY, MICHAEL JASON. Reactions of High-k Gate Dielectrics: Studies in Hafnium, Zirconium, Yttrium, and Lanthanum-based Dielectrics and *in-situ* Infrared Results for Hafnium Dioxide Atomic Layer Deposition. (Under the direction of Dr. Gregory N. Parsons.)

According to the International Technology Roadmap for Semiconductors (2004) integrating a high dielectric constant (high-k) material into the gate stack will be necessary within the next two years (i.e., by 2007) to maintain the rate of scaling that has come to characterize the microelectronics industry. This work presents results for Y-, Zr-, Hf-, and La-based high-k gate dielectrics prepared by *ex-situ* oxidation of sputtered thin metal films and for HfO<sub>2</sub> prepared by atomic layer deposition (ALD).

The kinetics of substrate consumption during formation of yttrium silicate thin films were studied. We find results consistent with high-k dielectric formation by a two-step process in which yttrium metal reacts with the silicon substrate to form a metal silicide which is then oxidized to form the yttrium silicate dielectric. In other experiments, we show flatband voltage shifts of -0.2 and -0.95V in devices containing Zr-based dielectrics formed by oxidation of 8Å of Zr metal on Si at 600°C in N<sub>2</sub>O for 15 and 300s, respectively. Silicon oxidized in the same environment does not show this shift. The fixed charge scales with EOT for these films and is consistent with charge generation due to disruption of the SiO<sub>2</sub> network by metal ions. Zr-based dielectrics exhibit this effect more strongly than Hf-based dielectrics. We show that La-based dielectrics absorb atmospheric H<sub>2</sub>O and CO<sub>2</sub>, and that reactions between these materials and deposited silicon electrodes are accelerated when H<sub>2</sub>O or other OH species are present at the interface. We show that the electrical properties of gate stacks having Ru and RuO<sub>2</sub> electrodes in contact with PVD Y-silicate are more stable during thermal anneal than similar gate stacks having PVD ZrO<sub>2</sub> or CVD Al<sub>2</sub>O<sub>3</sub> dielectrics.

For this work, we configured a Fourier transform infrared spectrometer for *in-situ* attenuated total reflection measurements and investigated ALD deposition of HfO<sub>2</sub>. We report the direct reaction of tetrakis(diethylamino) hafnium (TDEAHf) with SiH groups on HF-last Si. Island growth of HfO<sub>2</sub> occurs, and SiH features are still present and shrinking after 200 cycles. To the best of our knowledge, these are the first *in-situ* FTIR results presented for atomic layer deposition using TDEAHf/H<sub>2</sub>O chemistry.

**REACTIONS OF HIGH-K GATE DIELECTRICS:**  
*Studies in Hafnium, Zirconium, Yttrium, and Lanthanum-based Dielectrics  
and in-situ Infrared Results for Hafnium Dioxide Atomic Layer Deposition*

by

**MICHAEL JASON KELLY**

A dissertation submitted to the Graduate Faculty of  
North Carolina State University  
in partial fulfillment of the  
requirements for the Degree of  
Doctor of Philosophy

**CHEMICAL ENGINEERING**

Raleigh

2005

**APPROVED BY:**

---

Dr. David F. Ollis

---

Dr. Veena Misra

---

Dr. H. Henry Lamb

---

Dr. Gregory N. Parsons  
Chair of Advisory Committee

For my grandfather, Franklin C. Kelly (1921–1996),  
who showed me the wonder in the world;

my mentor, Maurice M. Mitchell, Jr. (1929–2003),  
who shared his love of chemistry;

and my friend, Philip W. Morrison, Jr. (1960–2002),  
who was a great example of how not to take it all too seriously.

## BIOGRAPHY

MICHAEL JASON KELLY, son of Michael and Peggy Kelly, was born on September 6<sup>th</sup>, 1975. Jason grew up in a rural area of southern Ohio where he attended Coal Grove schools, had a South Point address, and had a Chesapeake phone number. He is still not sure which town to claim. He had the pleasure of being older brother to Adam, Matthew, Daniel, and Jonathan, and he hopes they recover from the experience sometime soon. He has gathered eggs, chased chickens, brought in rabbits for Sunday dinner, and been stepped on by a cow. Farming was not an occupation; it was just something his family did off and on for the satisfaction of doing it and to cut costs. His first paid job was pitching hay for his uncle. His home was located in a valley between two ridges, and he spent his spare time exploring the hills around his home and usually had a paperback somewhere on or about his person.

His mom taught him to read at an early age, but, more importantly, she taught him to like reading. He worked his way through the Hardy Boys Mysteries by the end of the 3<sup>rd</sup> grade. When his grandparents' gave him the 1<sup>st</sup> volume of a science encyclopedia written for children, he read it over and over. His grandfather, a mechanical engineer, was amused to hear him reciting random facts about abrasives and atomic energy. That gift opened his eyes to the idea that things work as they do because of what they are and sparked a lifelong love for science. Sometime toward the end of the 5<sup>th</sup> grade, he finished the school library, and his Mom introduced him to the public library where he wandered into the Science Fiction Section. It seemed natural to read them alphabetically, but he started being more selective somewhere on the second bookcase (near Ray Bradbury) when he realized there were more books than he would ever finish in his lifetime. He is still a voracious reader but usually only

allows himself pleasure reading on holidays and trips since he has to get work done sometime.

In the 6<sup>th</sup> grade, he joined the band so he could spend time with a brunette he favored. Things never quite worked out with the girl, but he learned to play the drums. He had to take a temporary break from the band in the 9<sup>th</sup> grade because it wasn't possible to march at half-time wearing his football uniform. He rejoined the band a couple of years later when he managed to win the coveted spot of drummer in the school jazz band. He enjoyed being able to perform at basketball games and pep rallies and still had a fabulous time playing football. He attended a rural high school and his high grades had more to do with the ease of the material than any skill on his part. He read more novels in school than he had any right to read.

In the 10<sup>th</sup> grade, he heard about a new program that had just been introduced in Ohio that allowed high school students to attend college at no cost. The government monies that were usually given to the high school for educating the student were reallocated to the college to pay for tuition and books. All credits earned at the college would count for both high school and college credits. This program represented an awesome opportunity, and at the age of 16 he started attending a local community college. The experience was wonderful. He enjoyed the classes and the people at college, and he was still able to be on the football team and in the jazz band at high school. The only downside was that the college used a 4.0 GPA scale (4.0=A) while his high school used a 12.0 scale (12.0=A+). An "A" at college was only worth 11 points in at high school, and he gave up the top spot at his high school to Shawna Belcher and eventually graduated Salutatorian. He was fortunate that the local community college was also a branch campus of a major university (Ohio University) and the

quality of instruction was quite good. During his first year attending the Ohio University Southern Campus, he had the pleasure of taking a chemistry class taught by Maurice Mitchell – a brilliant physical chemist who had just retired from being Vice-President of Research and Development at Ashland Oil. Jason worked hard and was the top student in this class. Maurice's enthusiasm for chemistry was contagious, and for the first time in his life Jason felt the possibility that there might be more to life than just jumping through enough hoops to get a good job. Dr. Mitchell asked Jason to be his Teaching/Lab Assistant the next year and was completely shocked to learn that he was a high school student. Luckily for Jason, Maurice kept his offer open and the fall quarter did not begin until September 7<sup>th</sup>. Jason started his second paid job the first day he was legally allowed to work – the day after his 18<sup>th</sup> birthday. Maurice kept Jason busy making stock reagents, teaching lab sections, and grading lab reports while telling what seemed like a thousand stories from his career. By the end of the year, Jason had decided he wanted a career in research and set his sights on a PhD.

In order to maximize his scholarship possibilities, Jason sent essays committing himself to studying chemistry to science organizations and chemical engineering to engineering organizations. Thus, he walked onto the campus of Case Western Reserve University registered in two majors. Because he was also classified a 2<sup>nd</sup> semester sophomore, he was able to finish this course of study along with a minor in music in four years. A scheduling conflict in his last semester prevented him from taking the last course in his English series, and he graduated Magna Cum Laude in 1998, one course short of a double minor. Once enrolled, he could have kept his scholarships without finishing both majors, and he could have graduated early. His Irish American heritage compelled him to stay and get a good value for his money.

While at Case, Jason rowed on the freshman crew team, was active in AIChE, and did undergraduate research in Phil Morrison's lab. He was inducted into the Phi Beta Kappa and Tau Beta Pi honor societies. He worked for two summers in a research lab at BFGoodrich Specialty Chemicals under the direction of a talented organic chemist, John Lai, and was able to synthesize 24 or so new compounds using reactions developed by Dr. Lai. (See US Patents 5098944, 5089614, & 5071981 for similar reactions and compounds.) He joined the Department of Chemical Engineering at North Carolina State University in 1998, and he has enjoyed his time here. He loves North Carolina and intends to stay for the foreseeable future.

## ACKNOWLEDGEMENTS

I would like to express my deepest gratitude to my parents, my brothers, and my godmother, Carla, for always believing in me. I was blessed with wonderful grandparents, and I appreciate their encouragement. I want to thank Jane Hudson, my girlfriend for almost as long as I've been in graduate school now, for her constant support and interesting perspectives. Thanks especially for telling me to "Pop up, Peanut" when I've been down.

I am grateful to my advisor Dr. Parsons for allowing me the opportunity to do research at NC State. He has taught me a lot about the research process and myself. Because of his influence I have grown in ways I never anticipated, and I am glad I joined the group.

I greatly appreciate Dr. Jim Chambers who helped me get started in Dr. Parsons' group. He was genuinely interested in my ideas and always ready to give an opinion. He trusted me with his equipment and let me make mistakes, and he didn't yell when I tripped an interlock and crashed his system. He was brutally honest in his criticisms and fair with his praise. I always knew where I stood with Jim, and that meant (and means) a great deal to me.

I want to thank Kit Yeung for his technical help. My equipment runs more smoothly and more often because of him, but he has far exceeded his professional obligations in helping me. He has come to work after hours, and he has come to my home to help me keep my furnace and my car running. He has been an ever present source of good advice, unusual opinions, and entertaining anecdotes. He is one of a kind.

I am also grateful to all the members, past and present, of Dr. Parsons' research group including Dr. Ashfaul Chowdhury, Dr. Tonya Klein, Dr. Laura Smith, Dr. Jim Chambers, Dr. Atul Gupta, Dr. Theodosia Gougousi, Mike Mantini, Dr. Kevin Bray, Dr. Dong Niu, Dr. Elisa Rosa, Dr. Changwoong Chu, Dr. Kie Jin Park, David Terry, Tom Abatermarco, Powan

Mehan, Dipak Barua, Jeong-Suk Na, Qing Peng, Kai Wang, Justin Bennett, Bill Ketchie, Rob Ashcraft, Scott Burnside, Tammi Schmidt, Leonard Nelson, Franklin Goldsmith, Jason Doub, Joe Spagnola, Bryce Sturtevant, and Katherine Schadel. I have learned something from each of you. Special thanks go to Justin, Scott, Tammi, Jason, and Joe, undergraduate researchers, who all made excellent contributions to reactor construction and research in some way.

I want to give special recognition to Dr. Theodosia Gougousi. Working with her was a pleasure. I was able to turn over film deposition to her for a time to make progress in other areas, and the collaboration that came of that was wonderful and instructive. Her views on politics and women's rights were always enriching. I hope she is enjoying Maryland and that her current proximity to President Bush is not giving her high blood pressure.

Thanks go out to all the good friends I have made here at State. You have added a splash of color to what could have been a drab experience. Two people merit special thanks. Dr. Kie Jin Park has been a constant sounding board for research ideas and equipment frustrations, and he has never hesitated to offer help when it was needed. Dr. Esther Wilcox sat behind me in Riddick 10B and was one of the first – and best – friends I made here. She has a knack for appearing at exactly the right time to say exactly the right thing.

I want to acknowledge Dr. Genzer's group for sharing their knowledge and equipment. Dr. Kirill Efimenko, Dr. Rajendra Bhatt, and Dr. Michael Tomlinson have all given me specific help during my time here.

Special thanks are due my graduate committee members, Dr. Lamb, Dr. Ollis, and Dr. Misra for their excellent mentoring. I am especially grateful to Dr. Lamb for his advice on infrared spectroscopy and letting me poke around his lab and equipment.

*-MJR*

# TABLE OF CONTENTS

<b>LIST OF TABLES .....</b>	<b>xii</b>
<b>LIST OF FIGURES .....</b>	<b>xiii</b>
<b>1 INTRODUCTION.....</b>	<b>1</b>
1.1 High-k Gate Dielectrics .....	1
1.2 Gate Electrodes .....	5
1.3 ATR-FTIR Spectroscopy .....	6
1.4 Overview of Dissertation .....	9
1.5 References.....	11
<b>2 EQUIPMENT AND METHODS.....</b>	<b>20</b>
2.1 Deposition Equipment .....	20
2.2 FTIR Equipment .....	22
2.3 Overview of ATR-FTIR .....	24
2.4 Practical Design and Measurement Considerations.....	25
2.5 Experimental Procedure.....	30
2.6 Future Work.....	34
2.7 References.....	36
<b>3 ELEMENTARY REACTION SCHEMES FOR PHYSICAL AND CHEMICAL VAPOR DEPOSITION OF TRANSITION METAL OXIDES ON SILICON FOR HIGH-K GATE DIELECTRIC APPLICATIONS .....</b>	<b>43</b>
Abstract.....	43
Specific Contribution .....	44
3.1 Introduction.....	45
3.2 Material Preparation and Analysis.....	46
3.3 Results.....	47
3.3.1 PVD yttrium silicate .....	47
3.3.2 CVD aluminum oxide.....	52
3.3.3 CVD of $Y_2O_3$ .....	54
3.3.4 Proposed elementary reaction schemes .....	55
3.3.5 Summary.....	60
3.4 Acknowledgements.....	60
3.5 References.....	61
<b>4 KINETICS OF CHARGE GENERATION DURING FORMATION OF Hf AND Zr SILICATE DIELECTRICS.....</b>	<b>70</b>
Abstract.....	70
Specific Contribution .....	71
4.1 Introduction.....	72
4.2 Experimental.....	72
4.3 Results and Discussion .....	73

4.4	Acknowledgements.....	78
4.5	References.....	78
<b>5</b>	<b>PROPERTIES OF La-SILICATE HIGH-K DIELECTRIC FILMS FORMED BY OXIDATION OF La ON SILICON.....</b>	<b>87</b>
	Abstract.....	87
	Specific Contribution.....	88
5.1	Introduction.....	89
5.2	Experimental.....	90
5.3	Results and Discussion.....	92
5.3.1	Composition of La containing dielectrics formed on clean H terminated Si(100).....	92
5.3.2	Effect of substrate on the film composition.....	94
5.3.3	Thermal stability of La-silicate films.....	97
5.3.4	Atmospheric H <sub>2</sub> O absorption of La-silicate films.....	98
5.3.5	Electrical measurements on La-silicate films.....	100
5.4	Conclusions.....	101
5.5	Acknowledgements.....	102
5.6	References:.....	102
<b>6</b>	<b>PROMISING GATE STACKS WITH Ru &amp; RuO<sub>2</sub> GATE ELECTRODES AND Y-SILICATE DIELECTRICS.....</b>	<b>112</b>
	Abstract.....	113
	Specific Contribution.....	113
6.1	Introduction.....	115
6.2	Experimental Details.....	115
6.3	Results.....	116
6.4	Discussion and Conclusion.....	119
6.5	References.....	122
<b>7</b>	<b>THE ROLE OF THE OH SPECIES IN HIGH-K/POLYCRYSTALLINE SILICON GATE ELECTRODE INTERFACE REACTIONS.....</b>	<b>128</b>
	Abstract.....	128
	Specific Contribution.....	129
	The Role of the OH Species in High-k/Polycrystalline Silicon Gate Electrode Interface Reactions.....	130
	References.....	134
<b>8</b>	<b>IN-SITU INFRARED SPECTROSCOPY AND DENSITY FUNCTIONAL THEORY MODELING OF HAFNIUM ALKYLAMINE ADSORPTION ON Si-OH AND Si-H SURFACES.....</b>	<b>138</b>
	Abstract.....	139
8.1	Introduction.....	140
8.2	Experimental Methods.....	142
8.3	Theoretical Methods.....	144
8.4	Experimental Results.....	145

8.4.1	Analysis of starting surfaces .....	145
8.4.2	TDEAHf exposure on SiO <sub>2</sub> .....	146
8.4.3	TDEAHf exposure on hydrogen-terminated silicon.....	148
8.5	Theoretical Results.....	151
8.6	Discussion and Conclusions .....	156
8.7	References.....	160
<b>9</b>	<b>APPENDIX 1: TECHNICAL DETAILS (ATR-FTIR APPARATUS).....</b>	<b>174</b>
9.1	Measurement Parameters Chosen Based on the SNR.....	174
9.2	Alignment Procedure .....	177
9.2.1	Overall system alignment .....	178
9.2.2	Sample to sample alignment – External Reflection.....	181
9.2.3	Sample to sample alignment – Internal Reflection.....	182
9.3	Pressure Dependence of Measurement.....	184
9.4	Magna 750 Optical Specifications .....	186
9.4.1	Infrared source .....	187
9.4.2	White light source.....	187
9.4.3	Source ellipse mirror.....	187
9.4.4	Source collimation mirror.....	187
9.4.5	Sample compartment mirror.....	188
9.4.6	Detector mirror.....	188
9.4.7	Iris .....	188
9.4.8	Beam divergence.....	188
9.4.9	Interferometer .....	189
9.5	ATR-FTIR Optical System – Percent Throughput.....	189
9.5.1	Factors that affect throughput.....	189
9.5.2	Beam travel losses.....	190
9.5.3	Reflection losses .....	190
9.5.4	Beam losses at IRE (quality of focus).....	191
9.5.5	Improving overall throughput.....	193
9.6	Recommendations for Future Improvements.....	194
9.6.1	Bench positioning .....	194
9.6.2	Lens specifications and fabrication.....	194
9.6.3	Temperature control.....	195
9.6.4	Infrared polarizer .....	196
9.6.5	Microscope detector.....	196
9.6.6	Modifications for transmission and reflectance measurements.....	197
9.6.7	IRE characteristics and fabrication.....	198
9.7	References.....	199
<b>10</b>	<b>APPENDIX 2: QUOTABLE (AND UNQUOTABLE) QUOTES .....</b>	<b>217</b>
10.1	Notable quotes from friends and acquaintances .....	217
10.2	Interesting quotes from famous thinkers.....	218

## LIST OF TABLES

<b>Chapter 9</b>	<b>Appendix 1: Technical Details (ATR-FTIR Apparatus)</b>	
<b>Table 9.1</b>	Spectra collected to determine the magnitude of statistically significant changes in the signal to noise ratio .....	206
<b>Table 9.2</b>	Measurements showing the effect of scanning mirror velocity .....	207
<b>Table 9.3</b>	Measurements showing the effect of varying the source aperture.....	208
<b>Table 9.4</b>	Image sizes produced at the bench detector at different aperture settings.....	209
<b>Table 9.5</b>	List of various parts that comprise the ATR-FTIR apparatus.....	210
<b>Table 9.6</b>	Infrared beam throughput losses due to beam divergence.....	211
<b>Table 9.7</b>	Infrared beam throughput losses due to imperfect reflection at mirrors and imperfect transmission at lenses and windows .....	212
<b>Table 9.8</b>	Fraction of infrared beam available for interaction with the IRE after accounting for reflection and beam transport losses.....	213
<b>Table 9.9</b>	Variation of the image diameter produced at the focal point and at the IRE bevel by this optical configuration with different aperture settings .....	214
<b>Table 9.10</b>	Fraction of infrared beam remaining at the detector after accounting for all relevant beam losses with current optical configuration.....	215
<b>Table 9.11</b>	Fraction of infrared beam remaining at the detector after accounting for all relevant beam losses with lenses having a 7 1/8 inch focal length.....	216

# LIST OF FIGURES

## Chapter 1 Introduction

**Figure 1.1** Interface layers that increase equivalent oxide thickness in a gate stack containing a high- $\kappa$  dielectric .....18

**Figure 1.2** Ideal overview of atomic layer deposition.....19

## Chapter 2 Equipment and Methods

**Figure 2.1** System configuration for plasma-assisted, DC sputtering of metal films .....37

**Figure 2.2** Leak rate of the system (configured for metal sputtering) was measured as  $4 \times 10^{-7}$  torr/s.....38

**Figure 2.3** Configuration of the main process chamber of the system in Figure 2.1 when *in-situ* FTIR spectroscopic measurements were performed.....39

**Figure 2.4** Schematic of differentially pumped flange for mounting KBr discs as windows .....40

**Figure 2.5** Leak rate of the system (configured for *in-situ* FTIR experiments) was measured as  $4 \times 10^{-9}$  torr/s. ....41

**Figure 2.6** Drawing of Internal Reflection Element (IRE) showing crystal geometry and the evanescent wave of infrared light that extends out into the vacuum above the trapezoidal IREs.....42

## Chapter 3 Elementary Reaction Schemes for Physical and Chemical Vapor Deposition of Transition Metal Oxides on Silicon for High- $\kappa$ Gate Dielectric Applications

**Figure 3.1** XPS Si 2p spectra for yttrium layers on Si(100) after various processes. ....62

**Figure 3.2** TEM for four yttrium silicate films formed from  $\sim 8 \text{ \AA}$  initial yttrium on silicon, followed by oxidation at  $900^\circ\text{C}$  .....63

<b>Figure 3.3</b>	XPS results for yttrium silicide films oxidized to form $Y_2O_3/SiO_2$ films.....	64
<b>Figure 3.4</b>	Si-O/Si integrated area ratio determined from the Si 2p XPS data in Figure 3.3 and the MEIS-determined Si fraction plotted versus $1/T$ .....	65
<b>Figure 3.5</b>	Narrow Resonant Nuclear Reaction Profiles for two $Al_2O_3$ films deposited on Si(100).....	66
<b>Figure 3.6</b>	XPS results for $Al_2O_3$ films on Si(100) after anneal.....	67
<b>Figure 3.7</b>	XPS results for “ $Y_2O_3$ ” films deposited by CVD. ....	68
<b>Figure 3.8</b>	Capacitance - Voltage results for films on clean and nitrided surfaces.....	69
<b>Chapter 4</b>	<b>Kinetics Of Charge Generation During Formation of Hf And Zr Silicate Dielectrics</b>	
<b>Figure 4.1a</b>	Capacitance - Voltage curves for $8\text{\AA}$ Zr-metal films oxidized in $N_2O$ with Al gates as a function of oxidation time .....	80
<b>Figure 4.1b</b>	Flatband voltage ( $V_{FB}$ ) for $8\text{\AA}$ Zr-metal films oxidized in $N_2O$ with Al gates as a function of oxidation time.....	80
<b>Figure 4.1c</b>	Equivalent oxide thickness for $8\text{\AA}$ Zr-metal films oxidized in $N_2O$ with Al gates as a function of oxidation time .....	80
<b>Figure 4.2</b>	XP spectra for $8\text{\AA}$ Zr metal films on Si oxidized at $600^\circ C$ in $N_2O$ .....	81
<b>Figure 4.3a</b>	Capacitance - Voltage curves for $8\text{\AA}$ Hf-metal films oxidized in $N_2O$ with aluminum gates .....	82
<b>Figure 4.3b</b>	Capacitance - Voltage curves for $8\text{\AA}$ Hf-metal films oxidized in $N_2$ gas containing trace oxygen with aluminum gates.....	82
<b>Figure 4.4</b>	Equivalent Oxide Thickness and flatband voltage for $8\text{\AA}$ Hf-metal films oxidized in $N_2$ and $N_2O$ , and for H-terminated Si oxidized in $N_2O$ .....	83

<b>Figure 4.5</b>	XP spectra for 8Å Hf-metal films oxidized in N <sub>2</sub> O for 30s, 90s, and 300s, and in N <sub>2</sub> for 300s.....	84
<b>Figure 4.6</b>	Effect of Forming Gas Anneal on the C-V curves of Hf films oxidized in N <sub>2</sub> O and N <sub>2</sub> .....	85
<b>Figure 4.7</b>	Si 2p XP spectra for 450Å Hf-metal films oxidized in N <sub>2</sub> O and N <sub>2</sub> .....	86
<b>Chapter 5</b>	<b>Properties of La-silicate high-k dielectric films formed by oxidation of La on Silicon</b>	
<b>Figure 5.1</b>	Si 2p/La 4d, O 1s, and La 3d XP spectra for a series of La metal films with thickness ranging from 15 to 330Å, oxidized at 900°C in N <sub>2</sub> O .....	105
<b>Figure 5.2</b>	O 1s and La 3d XP spectra for three identical films (170Å La metal, 5min, 900°C, N <sub>2</sub> O oxidation) deposited on i) H-terminated Si(100), ii) plasma nitrided Si(100), and iii) 1000Å of thermal SiO <sub>2</sub> .....	106
<b>Figure 5.3</b>	O 1s and La 3d XP spectra for 170Å (iii) and 1000Å (iv) La metal deposited on 1000Å of thermal SiO <sub>2</sub> and oxidized at 900°C in N <sub>2</sub> O for 5min.....	107
<b>Figure 5.4</b>	O 1s XP spectra for a 150Å metal film oxidized for 5 min at 900 or 600°C in dry air as prepared and after anneal in argon for 10 or 30s .....	108
<b>Figure 5.5a</b>	FTIR spectra for La-based dielectric films after preparation and after 10 days of air exposure. Films were formed by oxidizing 330Å La-metal films in N <sub>2</sub> O for 10 minutes at 900°C .....	109
<b>Figure 5.5b</b>	FTIR spectra for La-based dielectric films after preparation and after 10 days of air exposure. Films were formed by oxidizing 330Å La-metal films in N <sub>2</sub> O for 10 minutes at 600°C .....	109
<b>Figure 5.6</b>	Representative C-V data for a dielectric film prepared by oxidizing 10Å La metal in a 900°C, N <sub>2</sub> O atmosphere for 5s.....	110
<b>Figure 5.7</b>	Hysteresis curves for the capacitor in Figure 5.6.....	111

**Chapter 6 Promising Gate Stacks with Ru & RuO<sub>2</sub> Gate Electrodes and Y-silicate Dielectrics**

<b>Figure 6.1a</b>	XRD of RuO <sub>2</sub> on SiO <sub>2</sub> after 800°C anneal in N <sub>2</sub> .....	123
<b>Figure 6.1b</b>	XRD of Ru on SiO <sub>2</sub> after 800°C anneal in N <sub>2</sub> .....	123
<b>Figure 6.2</b>	XPS of Ru and RuO <sub>2</sub> films on ZrO <sub>2</sub> after the surfaces of Ru and RuO <sub>2</sub> films were sputtered.....	124
<b>Figure 6.3</b>	Atomic force microscopy images of Ru and RuO <sub>2</sub> films before and after rapid thermal anneal in N <sub>2</sub> .....	125
<b>Figure 6.4a</b>	C-V curves of RuO <sub>2</sub> gate electrodes on Y-Silicate after anneal in N <sub>2</sub> .....	126
<b>Figure 6.4b</b>	C-V curves of Ru gate electrodes on Y-Silicate after anneal in N <sub>2</sub> .....	126
<b>Figure 6.5a</b>	EOT as a function of annealing temperature of Ru and RuO <sub>2</sub> gate electrodes on SiO <sub>2</sub> , Al <sub>2</sub> O <sub>3</sub> and ZrO <sub>2</sub> after anneal in N <sub>2</sub> and forming gas.....	127
<b>Figure 6.5b</b>	V <sub>FB</sub> as a function of annealing temperature of Ru and RuO <sub>2</sub> gate electrodes on SiO <sub>2</sub> , Al <sub>2</sub> O <sub>3</sub> and ZrO <sub>2</sub> after anneal in N <sub>2</sub> and forming gas.....	127
<b>Chapter 7</b>	<b>The role of the OH species in high-k/polycrystalline silicon gate electrode interface reactions</b>	
<b>Figure 7.1</b>	IR absorbance spectra for the “wet” and “dry” samples.....	135
<b>Figure 7.2</b>	Si 2p and La 4d XP spectra for the “dry” and “wet” samples as prepared and after argon anneal.....	136
<b>Figure 7.3</b>	La 3d XP spectra for the “dry” and “wet” samples as prepared and after argon anneal.....	137

<b>Chapter 8</b>	<b>In-Situ Infrared Spectroscopy and Density Functional Theory Modeling of Hafnium Alkylamine Adsorption on Si-OH and Si-H Surfaces</b>	
<b>Figure 8.1</b>	Schematic of the attenuated total internal reflection FTIR system and reactor geometry used for <i>in-situ</i> spectroscopy. ....	163
<b>Figure 8.2a</b>	Attenuated total internal reflectance (ATR) infrared absorbance spectrum for a reference octadecyl trichlorosilane monolayer on thin thermal SiO <sub>2</sub> .....	164
<b>Figure 8.2b</b>	Single beam ATR-FTIR spectra showing the effect of temperature on infrared transmission through the silicon substrate. ....	164
<b>Figure 8.3a</b>	Infrared spectra for a chemical oxide surface as prepared and after vacuum anneal .....	165
<b>Figure 8.3b</b>	Infrared spectra for an HF-last Si(100) surface as prepared and after vacuum exposure .....	165
<b>Figure 8.4</b>	ATR-FTIR absorbance after various exposures of the SiO <sub>2</sub> surface to TDEAHf at room temperature .....	166
<b>Figure 8.5</b>	ATR-FTIR absorbance after exposing the hydrogen-terminated surface to various doses of TDEAHf at room temperature .....	167
<b>Figure 8.6</b>	ATR-FTIR spectra after sequential exposure of the Si-H surface to TDEAHf and water over many cycles at a substrate temperature of 250 °C .....	168
<b>Figure 8.7</b>	X-ray photoelectron spectra of Si-H and SiO <sub>2</sub> surfaces after exposure to 10 cycles of TDEAHf and H <sub>2</sub> O at 250°C .....	169
<b>Figure 8.8</b>	Si-H IR vibrational modes for the initial surface and after various precursor exposure doses at 25 and 250 °C .....	170
<b>Figure 8.9</b>	Potential energy surface for TDMAHf reacting with the silicon hydride surface adjacent to a Si-OH surface bond site .....	171
<b>Figure 8.10</b>	Calculated vibrational spectra for the species present in the H transfer process from the surface OH group .....	172

<b>Figure 8.11</b>	Calculated vibrational spectra for surface species in the Si-H abstraction process.....	173
<b>Chapter 9</b>	<b>Appendix 1: Technical Details (ATR-FTIR Apparatus)</b>	
<b>Figure 9.1</b>	Single beam spectra of a self-assembled OTS monolayer film .....	202
<b>Figure 9.2</b>	Representative FTIR single-beam spectra for our instrument when aligned for single-bounce external reflection and attenuated total internal reflection .....	203
<b>Figure 9.3</b>	A suggested process flow for preparing Si IREs chemically.....	204
<b>Figure 9.4</b>	Possible dark field mask used with positive photoresist for preparing Si(100) IREs chemically .....	205

# 1 Introduction

Size reductions in Metal Oxide Semiconductor (MOS) devices have required a simultaneous reduction in lateral dimensions and device thickness to maintain constant field scaling within the Field Effect Transistor (FET). This scaling has allowed a doubling of the transistor density with predictable frequency since the transistor was commercialized in the 1960s.<sup>1,2</sup> The dielectric of choice has been SiO<sub>2</sub> since 1959 when the transistor was invented.<sup>3,4</sup> However, the drive for ever thinner gate stacks has brought about new challenges as device sizes push physical and electrical limits.

## 1.1 High-*k* Gate Dielectrics

Electron tunneling through the dielectric becomes an important leakage mechanism for very thin dielectric layers, and expected leakage currents for SiO<sub>2</sub> layers less than ~15Å thick are on the order of 1A/cm<sup>2</sup> at an oxide bias of 1V.<sup>5</sup> For logic devices, the International Technology Roadmap for Semiconductors (ITRS) calls for gate stacks having a capacitance equivalent to an SiO<sub>2</sub> thickness of only 9Å by the year 2007 (70nm device node) and only 8Å in 2009 (50nm device node).<sup>5</sup> These Equivalent Oxide Thickness (EOT) values are especially daunting since many factors may give rise to an increase in electrical thickness besides the physical thickness of the layer.

The capacitance,  $C$ , of an insulating layer can be calculated as shown in Equation 1.1 where  $k$  is the dielectric constant or the relative permittivity of the film ( $\epsilon/\epsilon_0$ ),  $A$  is the area, and  $d$  is the thickness.

$$C = kA/d \tag{1.1}$$

The dielectric constant of SiO<sub>2</sub> is 3.9, and one would expect that replacing the SiO<sub>2</sub> gate dielectric with a material having a higher dielectric constant would allow the use of physically thicker gate dielectrics as shown in Equation 1.2. The benefit of using a high-k dielectric is that the device may be scaled laterally while benefiting from the low leakage currents associated with thick insulating layers. For example, performance equivalent to a 10Å thick SiO<sub>2</sub> film could be obtained with a 30Å thick high-k film with a dielectric constant ~12 (i.e., 3\*3.9).

$$t_{high-k} = \frac{k_{high-k}}{k_{SiO_2}} t_{SiO_2} \quad (1.2)$$

Many materials have been investigated, and many challenges to this approach have been identified.<sup>6-9</sup> Both amorphous and epitaxial dielectrics have been studied.<sup>10</sup> Although epitaxial oxides tend to have higher dielectric constants than amorphous materials, they do not block diffusion as well. In addition, if a silicide layer is needed for epitaxy it leaves 10<sup>12</sup> cm<sup>-2</sup> interface charges (based on threshold shift in CV data) that will impair device performance.<sup>11</sup> Amorphous dielectrics currently receive more attention in the literature than epitaxial. Silicon nitride and oxynitrides have been investigated,<sup>12-15</sup> and silicon oxynitrides currently find use in many devices produced by industry.<sup>5</sup>

Many candidate high-k materials have been studied in recent years. Interface layer (SiO<sub>2</sub> or a mixed metal-silicon-oxygen layer) reactions or low crystallization temperatures have been observed in many studies of metal oxides. For example, TiO<sub>2</sub> and Ta<sub>2</sub>O<sub>5</sub> react with the silicon substrate.<sup>16-19</sup> Interface layers often form during deposition or subsequent heating despite the calculated thermodynamic stability<sup>20</sup> of Y, La, Hf, Zr, and Al oxides on silicon. These oxides and binary alloys of the oxides with SiO<sub>2</sub> have been studied.<sup>21-25</sup> The interface layers tend to be SiO<sub>2</sub> or a silicate-like material like the one typically reported<sup>26</sup>

during MOCVD deposition of  $\text{Al}_2\text{O}_3$ . The oxide of aluminum is one of the few metal oxides that has been deposited on silicon without an interface layer. An abrupt interface has been demonstrated<sup>27</sup> using atomic layer deposition techniques.

The “silicates” of Hf, Zr, and Y (e.g.,  $(\text{ZrO}_2)_x (\text{SiO}_2)_y$ ,  $(\text{Y}_2\text{O}_3)_x (\text{SiO}_2)_y$ , etc.) are also very attractive. Typically, these are not stoichiometric silicates. Strictly speaking, a silicate is a crystalline compound with fixed composition and crystal structure. In this work, a more general definition of the term is applied, and a “silicate” material is any binary alloy of a transition metal oxide and  $\text{SiO}_2$  that contains metal-oxygen-silicon bonds.  $\text{SiO}_2$  which is lightly “doped” with hafnium or zirconium oxide has demonstrated good thermal stability and electrical characteristics. Silicate films containing sufficiently low (<~8%) concentrations of hafnium or zirconium are thermally stable in direct contact with Si after a 20s, 1050°C anneal.<sup>28</sup> The excellent electrical characteristics exhibited by these Hf- and Zr-doped  $\text{SiO}_2$  films shows that much of the character of the  $\text{SiO}_2/\text{Si}$  interface is conserved.<sup>28-30</sup>

Our research group has studied many high-k dielectrics including  $\text{Al}_2\text{O}_3$ ,  $\text{HfO}_2$ ,  $\text{ZrO}_2$ ,  $\text{Y}_2\text{O}_3$ , and  $\text{La}_2\text{O}_3$  and the silicates of those.<sup>26, 31-45</sup> Some of the results presented in this work build directly on another student’s yttrium-based dielectrics.<sup>24, 31</sup> Chambers’ plasma-assisted DC sputtering tool has been adapted for deposition of Hf-, Zr-, Al-, and La-based dielectrics. In this technique, ultrathin dielectric layers were formed physically by *ex-situ* thermal oxidation of sputtered metal at 600 – 900°C. The yttrium-based materials formed with these techniques that gave the best electrical performance were amorphous as formed with a dielectric constant of ~14. Capacitance-voltage (C-V) analysis of aluminum-gated, MOS capacitors (~40Å thick physically) showed an equivalent oxide thickness (EOT) of ~12Å. Capacitors on p- and n-type substrates had leakage current densities of 5.0 and 0.5 A/cm<sup>2</sup> in

accumulation, respectively. Negative flatband shifts of 0.6 to 0.8 volts were observed on n- and p-type substrates, respectively indicating positive fixed charge in these devices.<sup>46</sup>

One of the main challenges in incorporating high-k dielectrics into the gate stack is that undesired reactions may occur at the substrate/high-k interface during deposition or during subsequent thermal treatment. These undesired reactions form interface layers that tend to be either SiO<sub>2</sub> or mixtures of the high-k dielectric and SiO<sub>2</sub> and have lower permittivity values than the high-k dielectric. The overall capacitance of capacitors in series is dominated by the layer with the lowest capacitance as shown in Equation 1.3, so material interfaces must be tightly controlled in order to control gate stack capacitance.

$$C_{eq,series} = \frac{1}{\left( \frac{1}{C_1} + \frac{1}{C_2} + \frac{1}{C_3} \dots \right)} \quad (1.3)$$

Polycrystalline silicon (polysilicon) gate electrodes also add to the overall EOT. At high bias, a thin region of the polysilicon layer may be depleted of majority carriers, and this low-k region increases the electrical thickness. Higher dopant concentrations in the polysilicon layer decrease this effect, but boron penetration through the thin SiO<sub>2</sub> gate oxide into the channel region also degrades device performance. Low-k regions that limit performance are shown schematically in Figure 1.1 on an enlargement of the gate stack structure. The red and light blue regions represent undesired low-κ regions that lower the overall capacitance of the gate stack. The red regions represent interface layers containing elements from the high-κ dielectric layer and the substrate or electrode layers. They are formed by undesired interface reactions. These mixing regions tend to have a lower

dielectric constant than the high- $\kappa$  layer. The light blue region represents the low- $\kappa$  region formed by the polydepletion effect.

## 1.2 Gate Electrodes

As mentioned above there are many challenges associated with the continued use of polysilicon gate electrodes. The carrier-depleted layer that forms under high bias, the “depletion layer,” is insulating with the dielectric constant of undoped silicon. This additional capacitor lowers the overall capacitance of the gate stack in accordance with Equation 1.3. The thickness of the depletion layer,  $L_d$ , varies inversely with the root of the carrier density as shown in Equation 1.4.

$$L_d \propto 1/(N_{carriers})^{1/2} \quad (1.4)$$

As shown in Equation 1.4, depletion width decreases with increasing dopant concentrations. This relationship is the driving force for very high doping of the polycrystalline silicon (poly-Si) gate electrode. Dopant levels cannot be increased indefinitely. Since metals have intrinsic carrier concentrations much higher than even the most highly doped poly-Si, metal electrodes are a potential replacement for poly-Si. The solid solubility limit of many dopants in Si is about 1 atomic percent. Assuming a metal with about the same atomic density as silicon, Equation 1.3 shows that depletion layer widths could be reduced by a factor of 10 (at the same bias) by replacing poly-Si with a metal ( $\sim 1$ carrier/atom). Some metal oxides (e.g.,  $\text{RuO}_2$  and  $\text{IrO}_2$ ) display exceptionally high carrier concentrations and low resistivities. The metallic electrical properties of these conducting oxides make them attractive gate electrode candidates as well. The ITRS calls for a gate stack EOT of only 8Å by 2009, and depletion layer widths of only a few angstroms could easily limit the overall EOT of the gate stack at that time. The optimum work function for metal electrodes is believed to be  $\sim 4\text{eV}$  for

NMOS device gates and  $\sim 5.1$  eV for PMOS device gates. These values match the conduction and valance band energies of the Si substrate.

These work function requirements and the needs for high carrier density and thermal stability limit the list of potential gate materials somewhat, but gate stacks including various gate electrodes (e.g., Hf, Zr, Sc, Ti, Ta, Pt, TaN, Ru, Ru-Ta alloys, Ta-Mo alloys, and RuO<sub>2</sub>) have been studied.<sup>47-57</sup> For example, ruthenium and RuO<sub>2</sub> materials have shown promise as PMOS gate electrodes and have demonstrated high thermal stability, high carrier concentration, and a work function near 5eV. In one study, a gate stack containing RuO<sub>2</sub> on SiO<sub>2</sub> was stable during anneal to 600°C, and the film resistivity decreased due to grain growth in the crystalline electrode material.<sup>48</sup> The carrier concentrations in these films were  $\sim 10^{22}$  cm<sup>-3</sup>, two to three orders of magnitude higher than in heavily doped poly-Si.

### **1.3 ATR-FTIR Spectroscopy**

For the work in Chapter 8, the system was configured for *in-situ* attenuated total reflection-Fourier transform infrared spectroscopy (ATR-FTIR). This technique is a surface sensitive technique useful for characterizing surface bonding groups – OH (3500 – 3900 cm<sup>-1</sup> range), NH (3400 – 3500 cm<sup>-1</sup>), SiH (stretching modes 2000 – 2200 cm<sup>-1</sup>), and CH (2800 – 3100 cm<sup>-1</sup>) – in thin films deposited on top of the ATR crystals. The crystals are high resistivity, Si(100) terminated, trapezoidal crystals measuring 40mm long, 12mm wide, and 0.5mm thick with 45° beveled edges. The infrared light is directed out of a Magna 750 FTIR instrument and focused on the IRE beveled edge. The light enters the crystal at such an angle that it undergoes total internal reflection and interacts with the top and bottom of the crystal 40 times each. Adsorbed molecules or thin films on top of the crystal interact with the propagating light and absorb the infrared energy. The light is refocused at a narrow band gap

MCT-A detector. The optics and all parts of the beam path are enclosed and continuously flushed with purge gas (dry air with reduced CO<sub>2</sub> levels) to protect hygroscopic KBr optics and prevent bands for ambient H<sub>2</sub>O and CO<sub>2</sub> in the final spectra.

We used the ATR-FTIR apparatus to study atomic layer deposition of HfO<sub>2</sub> from tetrakis(diethylamino)hafnium (TDEAHf, Hf(N(CH<sub>2</sub>CH<sub>3</sub>)<sub>2</sub>)<sub>4</sub>) and H<sub>2</sub>O half reactions.<sup>58</sup> In atomic layer deposition chemistry, the overall reaction (i.e., TDEAHf + H<sub>2</sub>O → HfO<sub>2</sub> + DEA) is divided into two, half-reactions as shown below where \* indicates a surface species:



Each reactant is introduced into the chamber separately, and the reactions are carried out sequentially. An idealized representation of an atomic layer deposition process is shown in Figure 1.2. This chemical route is one of the most well-established ALD HfO<sub>2</sub> deposition methods.<sup>59</sup> Similar hafnium alkylamine precursors including, tetrakis(ethylmethylamino) hafnium (TEMAHf)<sup>60, 61</sup> and tetrakis(dimethylamino)hafnium (TDMAHf),<sup>62</sup> have been the focus of other studies. Most recently, ALD films deposited from TDMAHf and O<sub>3</sub> were demonstrated that contained a lower carbon concentration and exhibited a lower leakage current density than films deposited from TDMAHf and H<sub>2</sub>O. The leakage current measured was only 1.6 x 10<sup>-7</sup> A/cm<sup>2</sup> at a capacitance equivalent thickness of 14.9Å.<sup>62</sup> However, an investigation into the ALD chemistry of TEMAHf/O<sub>3</sub> half reactions showed that films deposited above 320°C were similar in composition to those prepared with TEMAHf/H<sub>2</sub>O while those prepared at lower temperatures contained higher levels of both carbon and hydrogen.<sup>63</sup> A better understanding of the reactions occurring in these deposition processes is needed to identify the factors that influence physical properties and device performance.

Chabal has reported results for depositing Al<sub>2</sub>O<sub>3</sub> from trimethylaluminum (TMA) and H<sub>2</sub>O half reactions measured by single-pass transmission infrared spectroscopy.<sup>64</sup> In another work, he reports using heavy water, D<sub>2</sub>O, to probe reactions on H-terminated silicon for both Al<sub>2</sub>O<sub>3</sub> and HfO<sub>2</sub> grown from TMA/H<sub>2</sub>O and HfCl<sub>4</sub>/H<sub>2</sub>O reactants, respectively.<sup>65</sup> He reports that TMA but not HfCl<sub>4</sub> reacts with surface SiH groups and that nearly linear growth rates can be produced if the SiH surface is saturated with a long dose of TMA before shorter dosing begins. This report points out that differences exist between related reactions, and that an understanding of chemical differences can be useful for controlling ALD reactions. In another report, Frank and Chabal report ALD of HfO<sub>2</sub> from tetrakis-tert-butoxyhafnium, Hf(OC(CH<sub>3</sub>)<sub>3</sub>)<sub>4</sub>, without an additional oxygen source.<sup>66</sup>

A recent letter from Ho (with Chabal) reports that TEMAHf reacts even more strongly with H-terminated silicon than TMA does.<sup>67</sup> He shows a linear growth rate without a significant growth barrier (i.e., no induction period). This result is in distinct contrast to our findings.<sup>68</sup> We observe that TDEAHf reacts directly with the hydrogen-terminated silicon surface, but theoretical calculations (DFT, based on TDMAHf for computational efficiency) suggest that H is abstracted by an amine ligand and that the presence of a surface OH group adjacent to the abstracted H makes the process proceed more easily. In Chapter 8, we show that the saturation surface coverage of adsorbed metal-alkylamine species (as measured by the CH intensity) on H-terminated silicon is only ~10% of the value obtained for TDEAHf on SiO<sub>2</sub> surfaces, and we attribute this to adsorption primarily at partially oxidized defect sites, SiO and SiOH, on the HF-last silicon surface.

Ho *et al.* present data showing that HfO<sub>2</sub> initially grows in islands leaving large regions of unreacted SiH. They also note that about half of the original SiH on the silicon

surface remains even after 30 cycles. These conclusions are consistent with our observation that SiH continues to be removed from the surface even after 200 TDEAHf/H<sub>2</sub>O ALD cycles on H-terminated silicon. It is not clear at this time whether the disagreements between our results and those of Ho *et al.* arise from differences between the precursors used in our studies (or modeled theoretically) or some other factor.

Their equipment allows them to observe the Hf-O, Hf-O-Si, and SiO<sub>2</sub> stretching modes. They are able to demonstrate that interfacial SiO<sub>2</sub> does not form during film deposition, but during post-deposition annealing due to reaction of the substrate with excess oxygen in the HfO<sub>2</sub> film. As far as the author knows, our report is the only *in-situ* study of HfO<sub>2</sub> deposited from tetrakis(diethylamino)hafnium in the literature. The differences between our results and those presented by Chabal's group for tetrakis(ethylmethylamino)hafnium are intriguing and merit further investigation.

## **1.4 Overview of Dissertation**

Candidate high-k metal oxides and silicates may be deposited in many ways. This dissertation focuses on two of these methods. In Chapters 3-7, metal films are deposited by a plasma-assisted DC sputter process and oxidized *ex-situ* in a tube furnace with either N<sub>2</sub>O or air. These efforts were similar in some ways to earlier work by other group members. For example, the composition and electrical performance of yttrium-based dielectrics prepared by this physical vapor deposition (PVD) process has been studied in detail.<sup>46</sup> However, the author used the earlier developed methods to study different materials (i.e., La-, Zr-, and Hf-based dielectrics) and reactions of those materials at interfaces. In Chapter 8, HfO<sub>2</sub> films were deposited by Atomic Layer Deposition and the reactions were observed *in-situ* using attenuated total reflection-Fourier transform infrared spectroscopy. This work describes the

first results obtained using a new tool constructed for this purpose and represents the first *in-situ* infrared work performed in the group.

In CHAPTER TWO, we describe the deposition equipment used for the work. We also introduce background information on the equipment used to perform and the technique of ATR-FTIR spectroscopy.

In CHAPTER THREE, details relating to the reactions that occur during oxidation of metallic yttrium films are discussed. In particular, we present evidence that high-k dielectric formation occurs via a two-step process in which yttrium metal reacts with the silicon substrate to form a metal silicide which is then oxidized to form the yttrium silicate dielectric.

In CHAPTER FOUR, we present electrical results on the generation of fixed charge in Hf- and Zr-based high-k dielectrics. We present an unexpected scaling of fixed charge with EOT for these films. The results are consistent with charge generation due to disruption of the SiO<sub>2</sub> network by metal ions, and Zr-based dielectrics exhibit this effect more strongly than those that are Hf-based.

CHAPTER FIVE discusses both electrical and physical properties of La-based dielectrics. These materials absorb atmospheric H<sub>2</sub>O and CO<sub>2</sub> to form Lanthanum hydroxides and hydrocarbonates. Their susceptibility to reaction with ambient gases is related to their processing history.

CHAPTER SIX shows a comparison of the thermal stability of devices with Ru and RuO<sub>2</sub> electrodes in contact with PVD Y-silicate, PVD ZrO<sub>2</sub>, and CVD Al<sub>2</sub>O<sub>3</sub> dielectrics.

In CHAPTER SEVEN, we present a study of reactions between deposited silicon gate electrodes on a La-based high-k dielectric and find that the presence of H<sub>2</sub>O and/or hydroxyl species in the dielectric lead to a degradation in the thermal stability of the gate stack.

In CHAPTER EIGHT, *in-situ* infrared spectroscopy is used to investigate reactions during high-k deposition. Insight is gained into the growth mechanism of HfO<sub>2</sub> deposited from tetrakis(diethylamino)hafnium and H<sub>2</sub>O via atomic layer deposition chemistry on HF-last silicon and SiO<sub>2</sub>.

CHAPTER NINE is comprised of an appendix that contains technical information relating to the ATR-FTIR apparatus that is more specific than would be of interest to the general reader. It is included primarily for students building on this work.

In CHAPTER TEN, the final appendix, we pass on some quotable (and unquotable) quotes that seem worth sharing. We hope you enjoy them.

## **1.5 References**

- 1 Moore, G. E. Cramming more components onto integrated circuits. *Electronics* April 19, 1965, pp 114 - 117.
- 2 Moore, G. E. In *Lithography and the Future of Moore's Law*, Lithographies for Manufacturing V, Santa Clara, CA, USA, February 19 - 24, 1995; Warlaumont, J. M., Ed. SPIE - The International Society for Optical Engineering: Bellingham, Washington, USA, 1995.
- 3 Kilby, J. S. Miniaturized Electronic Circuits. U.S. Patent 3,138,743, June 23, 1964.
- 4 Noyce, R. N. Semiconductor Device-and-Lead Structure. U.S. Patent 2,981,877, April 25, 1961.

- 5 *International Technology Roadmap for Semiconductors*; SIA, Semiconductor  
Industry Association, San Jose, CA: 2004.
- 6 de Almeida, R. M. C.; Baumvol, I. J. R. *Surface Science Reports* **2003**, *49*, 1-114.
- 7 Treichel, H.; Eckstein, E.; Kern, W. *Ceramics International* **1996**, *22*, 435-442.
- 8 Wallace, R. M.; Wilk, G. D. *Critical Reviews in Solid State and Materials Sciences*  
**2003**, *28*, 231-285.
- 9 Wilk, G. D.; Wallace, R. M.; Anthony, J. M. *Journal of Applied Physics* **2001**, *89*,  
5243-5275.
- 10 Kwo, J.; Hong, M.; Kortan, A. R.; Queeney, K. L.; Chabal, Y. J.; Opila, R. L.;  
Muller, D. A.; Chu, S. N. G.; Sapjeta, B. J.; Lay, T. S.; Mannaerts, J. P.; Boone, T.;  
Krautter, H. W.; Krajewski, J. J.; Sergnt, A. M.; Rosamilia, J. M. *Journal of Applied*  
*Physics* **2001**, *89*, 3920-3927.
- 11 McKee, R. A.; Walker, F. J.; Chisholm, M. F. *Physical Review Letters* **1998**, *81*,  
3014-3017.
- 12 Huff, H. R.; Brown, G. A.; Larson, L. A. In *The gate stack/shallow junction*  
*challenge for sub-100nm technology generations (preprint)*, ECS Meeting,  
Washington, DC, March 25-30, 2001, 2001; 2001.
- 13 Keister, J. W.; Rowe, J. E.; Kolodziej, J. J.; Niimi, H.; Madey, T. E.; Lucovsky, G.  
*Journal of Vacuum Science and Technology B* **1999**, *17*, 1831-1835.
- 14 Lucovsky, G.; Jing, Z.; Lee, D. R. *Journal of Vacuum Science and Technology B*  
**1996**, *14*, 2832-2839.
- 15 Yao, Z.-Q.; Harrison, H. B.; Dimitrijevic, S.; Sweatman, D.; Yeow, Y. T. *Applied*  
*Physics Letters* **1994**, *64*, 3584-3586.

- 16 Alers, G. B.; Werder, D. J.; Chabal, Y.; Lu, H. C.; Gusev, E. P.; Garfunkel, E.; Gustafsson, T. *Applied Physics Letters* **1998**, *73*, 1517-1519.
- 17 Campbell, S. A.; Kim, H.-S.; Gilmer, D. C.; He, B.; Ma, T.; Gladfelter, W. L. *IBM Journal of Research and Development* **1999**, *43*, 383-392.
- 18 Kim, H. S.; Campbell, S. A.; Gilmer, D. C.; Kaushik, V.; Conner, J.; Prabhu, L.; Anderson, A. *Journal of Applied Physics* **1999**, *85*, 3278-3281.
- 19 Mao, A. Y.; Son, K. A.; White, J. M.; Kwong, D. L.; Roberts, D. A.; Vrtis, R. N. *Journal of Vacuum Science and Technology A* **1999**, *17*, 954-960.
- 20 Hubbard, K. J.; Schlom, D. G. *Journal of Materials Research* **1996**, *11*, 2757-2776.
- 21 Lee, B. H.; Kang, L.; Nieh, R.; Qi, W.-J.; Lee, J. C. *Applied Physics Letters* **2000**, *76*, 1926-1928.
- 22 Lee, B. H.; Kang, L.; Qi, W.-J.; Nieh, R.; Jeon, Y.; Onishi, K.; Lee, J. C. *Tech. Dig. Int. Electron Devices Meet* **1999**, 133-136.
- 23 Qi, W.-J.; Nieh, R.; Dharmarajan, E.; Lee, B. H.; Jeon, Y.; Kang, L.; Onishi, K.; Lee, J. C. *Applied Physics Letters* **2000**, *77*, 1704-1706.
- 24 Chambers, J. J.; Parsons, G. N. *Applied Physics Letters* **2000**, *77*, 1-3.
- 25 Guha, S.; Cartier, E.; Gribelyuk, M. A.; Bojarczuk, N. A.; Copel, M. C. *Applied Physics Letters* **2000**, *77*, 2710-2712.
- 26 Klein, T. M.; Niu, D.; Epling, W. S.; Li, W.; Maher, D. M.; Hobbs, C. C.; Hegde, R. I.; Baumvol, I. J. R.; Parsons, G. N. *Applied Physics Letters* **1999**, *75*, 4001-4003.
- 27 Ott, A. W.; Klaus, J. W.; Johnson, J. M.; George, S. M. *Thin Solid Films* **1997**, *292*, 135-144.

- 28 Wilk, G. D.; Wallace, R. M.; Anthony, J. M. *Journal of Applied Physics* **2000**, *87*, 484-492.
- 29 Wilk, G. D.; Wallace, R. M. *Applied Physics Letters* **1999**, *74*, 2854-2856.
- 30 Wilk, G. D.; Wallace, R. M. *Applied Physics Letters* **2000**, *76*, 112-114.
- 31 Chambers, J. J.; Parsons, G. N. *Journal of Applied Physics* **2000**.
- 32 Niu, D.; Ashcraft, R. W.; Hinkle, C.; Parsons, G. N. *Journal of Vacuum Science & Technology A* **2004**, *22*, 445-451.
- 33 Gougousi, T.; Parsons, G. N. *Journal of Applied Physics* **2004**, *95*, 1391-1396.
- 34 Gougousi, T.; Niu, D.; Ashcraft, R. W.; Parsons, G. N. *Applied Physics Letters* **2003**, *83*, 3543-3545.
- 35 Ulrich, M. D.; Rowe, J. E.; Niu, D.; Parsons, G. N. *Journal of Vacuum Science & Technology B* **2003**, *21*, 1792-1797.
- 36 Niu, D.; Ashcraft, R. W.; Chen, Z.; Stemmer, S.; Parsons, G. N. *Journal of the Electrochemical Society* **2003**, *150*, F102-F109.
- 37 Gougousi, T.; Kelly, M. J.; Terry, D. B.; Parsons, G. N. *Journal of Applied Physics* **2003**, *93*, 1691-1696.
- 38 Niu, D.; Ashcraft, R. W.; Chen, Z.; Stemmer, S.; Parsons, G. N. *Applied Physics Letters* **2002**, *81*, 676-678.
- 39 Stemmer, S.; Klenov, D. O.; Chen, Z. Q.; Niu, D.; Ashcraft, R. W.; Parsons, G. N. *Applied Physics Letters* **2002**, *81*, 712-714.
- 40 Gougousi, T.; Kelly, M. J.; Parsons, G. N. *Applied Physics Letters* **2002**, *80*, 4419-4421.

- 41 Niu, D.; Ashcraft, R. W.; Parsons, G. N. *Applied Physics Letters* **2002**, *80*, 3575-3577.
- 42 Niu, D.; Ashcraft, R. W.; Kelly, M. J.; Chambers, J. J.; Klein, T. M.; Parsons, G. N. *Journal of Applied Physics* **2002**, *91*, 6173-6180.
- 43 Chambers, J. J.; Busch, B. W.; Schulte, W. H.; Gustafsson, T.; Garfunkel, E.; Wang, S.; Maher, D. M.; Klein, T. M.; Parsons, G. N. *Applied Surface Science* **2001**, *181*, 78-93.
- 44 Chambers, J. J.; Parsons, G. N. *Journal of Applied Physics* **2001**, *90*, 918-933.
- 45 Parsons, G. N.; Klein, T. M.; Niu, D. *Abstracts of Papers of the American Chemical Society* **1999**, *218*, U463-U464.
- 46 Chambers, J. J. Reactions for Yttrium Silicate High-k Dielectrics. Doctoral Dissertation, North Carolina State University, Raleigh, 2000.
- 47 Chen, Z. Q.; Misra, V.; Haggerty, R. P.; Stemmer, S. *Physica Status Solidi B-Basic Research* **2004**, *241*, 2253-2267.
- 48 Zhong, H.; Heuss, G.; Misra, V. *IEEE Electron Device Letters* **2000**, *21*, 593-595.
- 49 Zhong, H.; Heuss, G.; Misra, V.; Luan, H.; Lee, C.-H.; Kwong, D.-L. *Applied Physics Letters* **2001**, *78*, accepted.
- 50 Lee, C. K.; Kim, J. Y.; Hong, S. N.; Zhong, H. C.; Chen, B.; Misra, V. *Journal of Materials Science* **2005**, *40*, 2693-2695.
- 51 Chen, B.; Suh, Y.; Lee, J.; Gurganus, J.; Misra, V.; Cabral, C. *Applied Physics Letters* **2005**, *86*.
- 52 Suh, Y. S.; Heuss, G. P.; Lee, J. H.; Misra, V. *Ieee Electron Device Letters* **2003**, *24*, 439-441.

- 53 Misra, V.; Heuss, G. P.; Zhong, H. *Applied Physics Letters* **2001**, *78*, 4166-4168.
- 54 Zhong, H. C.; Heuss, G.; Misra, V.; Luan, H. F.; Lee, C. H.; Kwong, D. L. *Applied Physics Letters* **2001**, *78*, 1134-1136.
- 55 Park, K. J.; Doub, J. M.; Gougousi, T.; Parsons, G. N. *Applied Physics Letters* **2005**, *86*.
- 56 Yang, H.; Park, H.; Lee, D.; Choi, S.; Hwang, H. *Japanese Journal of Applied Physics Part 2-Letters & Express Letters* **2005**, *44*, L1275-L1277.
- 57 Yang, H. D.; Son, Y.; Baek, S.; Hwang, H.; Lim, H.; Jung, H. S. *Applied Physics Letters* **2005**, *86*.
- 58 Deshpande, A.; Inman, R.; Jursich, G.; Takoudis, C. *Journal of Vacuum Science & Technology A* **2004**, *22*, 2035-2040.
- 59 Hausmann, D.; Kim, E.; Becker, J.; Gordon, R. G. *Chemistry of Materials* **2002**, *14*, 4350-4358.
- 60 Kukli, K.; Ritala, M.; Lu, J.; Harsta, A.; Leskela, M. *Journal of the Electrochemical Society* **2004**, *151*, F189-F193.
- 61 Kukli, K.; Ritala, M.; Sajavaara, T.; Keinonen, J.; Leskela, M. *Chemical Vapor Deposition* **2002**, *8*, 199-204.
- 62 Cho, M. J.; Jeong, D. S.; Park, J.; Park, H. B.; Lee, S. W.; Park, T. J.; Hwang, C. S.; Jang, G. H.; Jeong, J. *Applied Physics Letters* **2004**, *85*, 5953-5955.
- 63 Liu, X. Y.; Ramanathan, S.; Longdergan, A.; Srivastava, A.; Lee, E.; Seidel, T. E.; Barton, J. T.; Pang, D.; Gordon, R. G. *Journal of the Electrochemical Society* **2005**, *152*, G213-G219.

- 64 Frank, M. M.; Chabal, Y. J.; Wilk, G. D. *Materials Research Society Symposium Proceedings* **2003**, 745, N2.4.1 - N2.4.6.
- 65 Frank, M. M.; Chabal, Y. J.; Green, M. L.; Delabie, A.; Brijs, B.; Wilk, G. D.; Ho, M. Y.; da Rosa, E. B. O.; Baumvol, I. J. R.; Stedile, F. C. *Applied Physics Letters* **2003**, 83, 740-742.
- 66 Frank, M. A.; Sayan, S.; Dormann, S.; Emge, T. J.; Wielunski, L. S.; Garfunkel, E.; Chabal, Y. J. *Materials Science and Engineering B-Solid State Materials for Advanced Technology* **2004**, 109, 6-10.
- 67 Ho, M. T.; Wang, Y.; Brewer, R. T.; Wielunski, L. S.; Chabal, Y. J.; Moumen, N.; Boleslawski, M. *Applied Physics Letters* **2005**, 87.
- 68 Kelly, M. J.; Han, J. H.; Musgrave, C. B.; Parsons, G. N. *Chem. Mater.* **2005**, 17, 5305-5314.

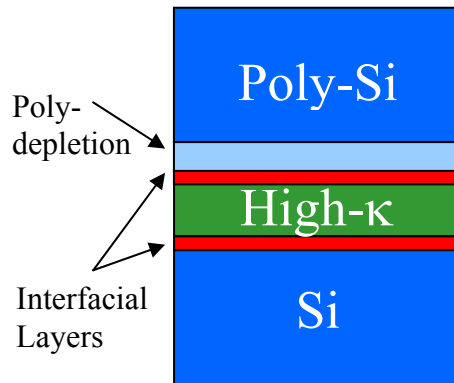
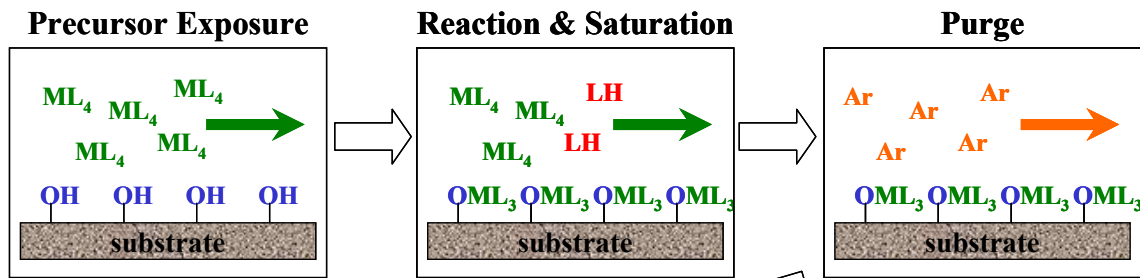


**Figure 1.1** This figure shows the interface layers that increase equivalent oxide thickness in a gate stack containing a high- $\kappa$  dielectric. These interfaces are shown as red layers in the gate stack schematic. The light blue region is a carrier depleted region that is present during the polydepletion effect.

### Half-Reaction 1:



### Half-Reaction 2:

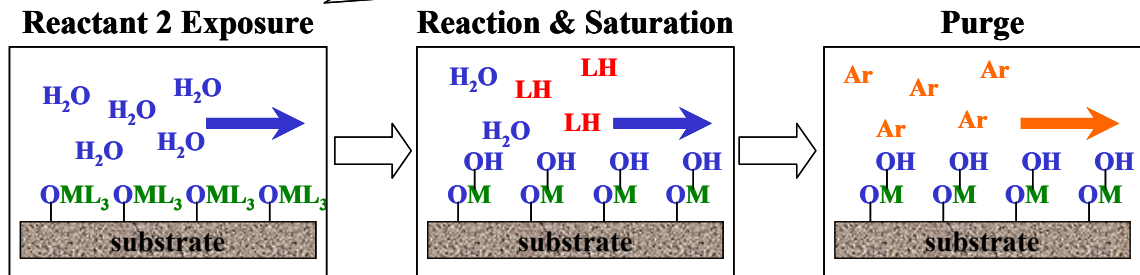


**Figure 1.2** An ideal overview of atomic layer deposition. A hydroxyl terminated surface is exposed to Reactant 1 until all the OH groups have reacted and the surface is terminated with a new species that is produced in the reaction between Reactant 1 and surface OH groups. Excess traces of Reactant 1 are removed by purging the system with argon or pumping. The surface is then exposed to Reactant 2 ( $H_2O$ , in the schematic) which oxidizes the surface bound  $OML_3$  species to produce a metal oxide and regenerate the initial hydroxyl terminated surface. Excess traces of Reactant 2 are removed by purging the system with argon or pumping. This process can be repeated until the desired film thickness is reached.

## 2 Equipment and Methods

### 2.1 Deposition Equipment

The papers presented in this work fall into two categories. Chapters 3-7 feature work in which sputtered metal films were oxidized to form high-k oxides or silicate-like materials. In Chapter 8, atomic layer deposition (ALD) chemistry is studied using *in-situ* spectroscopy. For the second work, the sputtering chamber (originally constructed by Chambers<sup>1</sup>) underwent extensive modifications. The configurations used for metal film sputtering and *in-situ* monitoring of ALD reactions are described below.

Figure 2.1 shows the system as configured for sputter deposition of metal films. It is a two-chamber system, and samples are transferred under vacuum from the load lock to the main chamber. The load-lock is pumped via a turbo pump (50l/s) backed with a dry diaphragm pump. The deposition chamber is pumped via a hybrid-turbo molecular drag (250l/s) and dry scroll pump combination. The load lock and processing chambers have base pressures of  $1 \times 10^{-7}$  and  $2 \times 10^{-7}$  torr, respectively. As shown in Figure 2.2, the processing chamber leak rate is  $4 \times 10^{-7}$  torr/s. The chamber manipulator has full X, Y, Z and  $\theta$  motion with travels of 1inch, 1inch, 2inches, and  $360^\circ$ , respectively. The system is outfitted with a plasma source that can be configured to run in either a remote or direct plasma mode. It was used in direct mode while sputtering metal films for high-k deposition and in remote mode when performing predeposition surface pretreatments (i.e., plasma oxidation or nitridation). The cylindrical plasma source is powered by a 500W, 13.56MHz radio frequency (rf) power supply with an autotuned matching network. The plasma tube is quartz and measures 5 X 15.25cm (diameter X length). The air-cooled excitation coil is 0.95cm nominal diameter

copper tubing with 2 turns of 12.7 cm diameter spanning 5 cm. It is grounded at one end and enclosed in a stainless steel electrostatic shield. The process gases (Ar, N<sub>2</sub>, N<sub>2</sub>O) are supplied to the chamber through the plasma tube and regulated from 1-100sccm (N<sub>2</sub>) via mass flow controllers. The retractable source target (Y, Zr, or La) is mounted on a linear translator and can be isolated from the system by a gate valve. During deposition the sputter target is biased at -1000V using a 200W DC power supply running in constant voltage mode. Radiant sample heating with feedback control allows sample temperatures to be maintained between room temperature and 650°C. Sputtered metallic films were oxidized *ex-situ* from the processing chamber in a standard 10cm diameter tube furnace at temperatures from 500-900°C in 1atm N<sub>2</sub>O (flowing, 10 sccm) or air (stagnant).

Figure 2.3 shows the main chamber of the system as configured for *in-situ* spectroscopy experiments. The load lock was not used. Samples were loaded directly through the front viewport of the main chamber which was o-ring sealed. The chamber walls were maintained at 90°C to limit the adsorption of contaminating species. The infrared windows were KBr crystals that were mounted in specially designed flanges as shown in Figure 2.4. These flanges include o-rings to make vacuum seals on both sides of the window with differential pumping as described by Yates.<sup>2</sup> A turbo pump (50l/s) was used to continuously pump the area between the o-rings, and the windows were heated constantly to 45°C to limit adsorption of atmospheric H<sub>2</sub>O on them. With differential pumping, there is no increase in the system leak rate or base pressure when using KBr windows. The KBr discs measure 38mm in diameter and 6mm thick. Although pressure burst calculations suggest that a disc twice as thick be used, these windows have served without incident in our lab and

others.<sup>3</sup> The discs are inspected by eye before installation. Discs having any visible defects whatsoever (small facets, chipping at the edges, etc.) are discarded.

The plasma tube is isolated from the main chamber via a UHV gate valve. Process gases and organometallic compounds are introduced directly into the chamber. The flow of these species is regulated with hand-controlled needle or leak valves. Organometallics and oxidizing species (H<sub>2</sub>O, air) were introduced through separate lines and separate ports on the chamber. Each set of lines was attached to the differential pumping manifold used to pump the windows, so the lines could be evacuated before experiments to remove any contaminants. The lines between the organometallic source and leak valve were equipped with additional valves and argon gas that allowed the line to be isolated, backfilled with argon, and pumped out. For delivery of organometallic compounds, this flushing and pumping procedure was primarily to limit exposure to decomposition products from residual chemicals that remained in the delivery lines after experiments. The oxidizing species, H<sub>2</sub>O and air, share a common delivery line, and the shared portion of the line was pumped constantly except during experiments to eliminate cross-contamination between the oxidants and to limit any leaking of these species into the chamber. When configured for *in-situ* spectroscopy the base pressure of the system is  $2 \times 10^{-7}$  torr, and the leak rate is  $4 \times 10^{-9}$  torr/s as shown in Figure 2.5. A pumping bypass line allows the system to be pumped only by the scroll pump when processing condensable species, and this pumping line is equipped with a liquid N<sub>2</sub> cooled trap to capture volatile organometallic compounds.

## **2.2 FTIR Equipment**

The optical apparatus we built works with our preexisting Fourier Transform Infrared (FTIR) spectrometer, a Thermo-Nicolet Magna 750 with a DSP-driven, Vectra interferometer

capable of better than  $0.1\text{ cm}^{-1}$  resolution. The apparatus can be used to perform internal or external reflection measurements depending on the alignment and the choice of substrate. It is equipped with a high  $D^*$  MCT-A detector (Thermo-Nicolet, P/N 840-130000) with a useful range of  $11,700$  to  $600\text{ cm}^{-1}$ . The Magna 750 is mounted on a common frame with the deposition chamber to force mechanical noise to vibrate in the deposition system and optical train at the same frequency and eliminate pathlength variations in the infrared beam. The infrared beam is directed out of the Magna 750's right-hand-side external beam port using a 3inch aluminum reflector (Thermo-Nicolet Passport Mirror, P/N 470-146900). The Passport Mirror is attached to a worm drive that is software controlled to direct the IR beam either out the external beam port for ATR-FTIR measurements or into the main sample compartment of the Magna 750 Bench for Transmission-FTIR measurements on bulk samples.

Potassium bromide single crystal lenses (focal length = 5.25inches) are mounted on the incoming and outgoing IR Ports of the chamber to focus the beam on the bevel of the single crystal, Si(100) internal reflection elements (IREs) and to recollimate the beam after it leaves the IRE. The IR Ports are vacuum sealed via KBr windows. The windows are mounted with o-rings on both faces, and the space between the o-rings is differentially pumped via a 50l/s turbo pump. Collimated light exiting the chamber is focused onto the detection element of the MCT-A detector using a 3inch diameter, 3inch focal length, gold-plated,  $90^\circ$  off-axis parabolic reflector.

Upon leaving the interferometer/beam splitter, the infrared beam interacts with the passport mirror before leaving the bench. From there it is directed straight into the IR Port. It interacts with optical elements in the following order. 1) KBr lens, 2) KBr window, 3)

Silicon (100) internal reflection element, 4) KBr window, 5) KBr lens, 6) Parabolic reflector, and 7) MCT-A detector.

### 2.3 Overview of ATR-FTIR

We used Attenuated Total Reflection FTIR (ATR-FTIR) spectroscopy to perform *in-situ* measurements during thin film deposition processes. In this technique an infrared beam is made to undergo total internal reflection and transmit through the body of a crystal as shown in Figure 2.6. The phenomenon of total internal reflection occurs when light traveling through a denser medium (i.e., a medium having index of refraction  $n_1$  where  $n_1 > n_2$ ) approaches a rarer medium and strikes the interface between the two at an angle greater than a critical angle,  $\theta_c$ . In Equation 2.1 (Snell's Law),  $n_2$  and  $n_1$  are the indices of refraction of the rarer and denser medium, respectively.

$$\theta_c = \arcsin\left(\frac{n_2}{n_1}\right) \quad (2.1)$$

Internal Reflection Elements (IREs) have geometry such that the beam undergoes total internal reflection multiple times at both the top and bottom of the optical crystal. The IREs used in this work are trapezoidal. For such a crystal, the number of reflections can be calculated using Equation 2.2 where  $l$  is the length of the crystal,  $t$  is the thickness, and  $\theta$  is the incidence angle. Our crystals are 40mm long and 0.5mm thick with an incidence angle of  $\sim 45^\circ$  corresponding to 80 total reflections and 40 front-side reflections.

$$N = \left(\frac{l}{t} \cot \theta\right) \quad (2.2)$$

A portion of the electric field extends beyond the interface into the rarer medium as shown in Figure 2.6. The intensity of this evanescent wave decays exponentially into the

rarer medium and couples with the rarer material. If the rarer material is absorbing then the intensity is attenuated, and Attenuated Total Reflection occurs. The distance over which the evanescent wave extends into the rarer medium is referred to as the penetration depth. The penetration depth varies between about 1800 and 4800Å at 4000 and 1500cm<sup>-1</sup>, respectively for our substrates and geometry, and measurements of bulk films would exhibit exaggerated peak intensity for vibrational modes at lower wavenumbers (i.e., longer wavelengths). In our experiments, the films were deposited directly on top of the crystal and were always thin enough that the evanescent wave penetrated completely through the film. This measurement characteristic is referred to as the thin film limit, and the spectra closely resemble transmission spectra. Since the measurements sample the entire film and the mathematical manipulations applied to the spectra are equivalent to those applied to transmission data, it is appropriate to present the data in terms of absorbance units.

ATR-FTIR spectroscopy is sensitive to in-plane and out-of-plane molecular vibrations. The polarization of the incident, infrared radiation is sometimes controlled in order to identify specific vibrational modes. In this work, unpolarized infrared radiation was used for all experiments, so both in- and out-of-plane vibrations are detected in all spectra. Typically, properly designed equipment can detect 0.1 monolayer coverage or lower. No specific experiments were performed to determine the detection limit of our apparatus.

## ***2.4 Practical Design and Measurement Considerations***

A few simple ideas were considered while designing the optical apparatus. The important figure of merit for any optical technique is the signal to noise ratio (SNR) obtained in the actual measurements, and there are two main parameters that must be controlled to

obtain a high SNR. The first parameter is the optical “throughput” of the design defined for our purposes as the fraction of the radiation that reaches the detector relative to its initial intensity. The second is “noise” which is a random variation in the detected signal at a given frequency.

The throughput was maximized in two key ways. First, we minimized the overall distance over which the radiation was transmitted from the optical bench to the deposition chamber (i.e., its “travel”). This is important because the beam diverges as it travels, and only the central portion of the beam passes through the apertures formed by the various optical elements in the beam path. For example, the KBr window on the deposition chamber (i.e., the IR Port) forms an aperture 1.37inches in diameter. Regardless of the beam size, all but the center 1.37 inches of the beam will be attenuated as it passes through the window.

Second, we used lenses of the shortest practical focal length to focus the beam into the chamber and onto the bevel of the Internal Reflection Element. As described below, the size of the beam at the focal point depends on the focal length of the optic used to produce it, and shorter focal length optics produce a more tightly focused beam at the IRE bevel. Any portion of the focused beam that extends beyond the edges of the bevel is lost. Focusing the beam is synonymous with imaging the source of the infrared light. The minimum achievable image size is defined by the initial image size ( $I_1$ ), the focal length of the optic used to collect and collimate the light coming from the image ( $f_1$ ), and the focal length ( $f_2$ ) of the optic used to refocus it as shown in Equation 2.3.

$$\frac{I_2}{I_1} = \frac{f_2}{f_1} \quad (2.3)$$

In our system,  $I_1 = 3.0\text{mm}$  (the iris diameter used in the ATR experiments in this work),  $f_1 = 6.00\text{in}$  (the focal length of the mirror that collects the light from the iris), and  $f_2 = 5.25\text{in}$

(focal length of lens that focuses light on the IRE bevel). Therefore, the smallest diameter one can expect for the image size is  $I_2 = I_1 f_2 / f_1$  or 2.625mm. This roughly circular image is focused onto a rectangular bevel measuring 12.0mm long and 0.7mm wide, and only the portion of the light striking the bevel is coupled into the IRE. Dividing the lighted area of the rectangle ( $2.625 \times 0.707 \text{ mm}^2$ ) by the overall image area ( $\pi(2.625/2)^2 \text{ mm}^2$ ) indicates that about 34% of the radiation enters the IRE bevel when it is positioned 5.25 inches from the lens. In principal, this 66% loss could be reduced by using shorter focal length optics, but the focal length of the focusing lens is constrained by the size of the vacuum chamber (Figure 2.3). In our case, the IRE is not located at the focal point of 5.25inches from the IR port but instead at 7.125inches. More details of the effects of this unfortunate mismatch and the severe loss of beam throughput it causes are described in the Appendix, Section 9.5.4. For the purposes of this section, it should be noted that lenses of the shortest practical focal length should be used in order to couple as large a percentage of the IR light into the IRE as possible.

Minimizing the path length by directing the radiation straight from the bench into the deposition chamber offers another advantage in that requires fewer optical elements than would be necessary otherwise. Using fewer optical elements increases the overall optical throughput because intensity is lost each time the beam interacts with an optical element. For example, an alternative design for our measurement apparatus included a fixed-position bench/radiation source and two additional planar mirrors to direct the beam into the chamber. Reflective losses at these two additional reflectors would have lowered the overall radiation throughput by 8 to 19% depending on the types of mirrors used.

Using lenses has an additional benefit in that it eliminates a degree of freedom from the alignment process. Another alternative design used parabolic reflectors in place of the lenses to focus light passing through the infrared beam ports. With such a design, each parabolic reflector would have to be aligned at the proper height, x and y positions in the measurement plane, and at the correct angle relative to the IR port. Such systems have been used many times in the literature and are extremely flexible. However, that flexibility is a disadvantage in that the high number of variables actually over constrains the optical system and complicates alignment. Lenses simply introduce fewer degrees of freedom into our system than parabolic reflectors would. In addition, the design allows the positions of most of the optical elements to be locked after the initial alignment. The practical effect is decreased alignment time and increased reproducibility in the measurements. The sample-to-sample alignment procedure is treated in the Appendix, Sections 9.2.2 and 9.2.3. Lenses do exhibit chromatic aberration. That is, some frequencies of light are bent more than others because the index of refraction is a function of frequency. However, the index of refraction of KBr varies only slightly at infrared frequencies, so any variations in focus at different wavelengths are very small. In addition, infrared spectroscopy is a relative measuring technique, so any effect introduced into the single-beam measurements will be eliminated in the final two-beam spectra which show relative changes from the background spectrum.

The materials chosen for the optical elements are important. Turned aluminum mirrors are typically ~90% reflective while mirrors that are coated evaporatively with gold are ~96% reflective. Our design uses a gold-plated parabolic reflector to focus the light on the detector and gain an additional 6% of the beam. In addition, there are reflective losses at each lens. Light incident on each lens is partially transmitted and partially reflected. For near normal

incidence the fraction of light reflected increases along with the index of refraction as shown in Equation 2.4 where  $R$  is the overall fraction of light reflected and  $n_1$  and  $n_2$  are the indices of refraction of medium 1 and 2, respectively.

$$R = \left[ \frac{n_1 - n_2}{n_1 + n_2} \right]^2 \quad (2.4)$$

Solving Equation 2.4 for light passing from air ( $n_1=1.00$ ) to KBr ( $n_2=1.54$ ) shows that 4.5% of the incident light reflects and is lost from the experiment. Other candidate lens materials exist which are transparent over the necessary wavelengths and offer superior handling benefits over KBr which is quite brittle and hygroscopic. However, their indices of refraction tend to be higher than KBr's. For example, ZnSe, which is stronger and less brittle than KBr and is insoluble in  $H_2O$ , has an index of refraction of 2.49 which corresponds to a loss of 18.2% for each reflection. While antireflective coatings may be applied to offset these reflective losses, the lenses become prohibitively expensive. Potassium bromide's lower index of refraction makes up for its handling difficulties since a higher fraction of light passes through the windows and lenses to participate in the measurement. Because of KBr's hygroscopic nature, the lenses were maintained at  $\sim 45^\circ C$  to limit the adsorption of atmospheric  $H_2O$ .

In addition to designing the system to maximize the overall optical throughput, it is also important to limit the amount of noise in the system to obtain a high signal to noise ratio. Physical vibration of the instrument is a source of noise, and steps were taken to limit its effect on the measurement. Vibrations perpendicular to the beam path result in an averaging of the intensity at the detector and, because of the nature of FTIR measurements, have little effect on the measurement unless they are severe enough to misalign the beam. However, the effect of vibrations parallel to the beam path can be severe. These vibrations change the

path length of the infrared beams and the interference pattern formed by the two infrared beams in the instrument. Since the spectrum derives directly from this interference pattern, it is extremely sensitive to this type of vibration. In our work, we limited the possibility of vibrations along the beam path by mounting the spectrometer and the deposition tool on a common frame. In this way, the spectrometer and the deposition tool must vibrate together at the same frequency. In control experiments, we made measurements under normal conditions and then repeated the measurement while physically shaking the frame (displacement ~1inch) for the duration of the measurement and found no difference in the SNR of the spectra produced.

A certain amount of noise is inherent in any single measurement no matter how carefully it is performed. The noise observed in a final spectrum can be reduced by co-adding multiple scans. In general, the amplitude of the noise is related to the number of measurements,  $N$ , as shown in Equation 2.5.

$$A = k\sqrt{N} \quad (2.5)$$

The prefactor,  $k$ , is inherent to the system and was treated above. This relation shows that to reduce the noise of a spectrum by half, one must quadruple the number of scans. We often collected 1024 scans which corresponds to a ~10minutes measurement. In certain situations we were able to obtain a reasonable SNR after only 32 scans. These measurements completed in 19s allowing a spectrum to be collected every 30s.

## **2.5 Experimental Procedure**

In general, experiments were performed in the following steps.

- 1) A timed plan was prepared in Microsoft Excel showing target pressures, exposure times, and when to open/shut each valve.

- 2) Any solutions necessary for surface pretreatment were prepared. These were always prepared the day of the experiment to provide the cleanest, most reproducible surfaces possible.
- 3) The MCT-A dewar was filled with liquid N<sub>2</sub>. Note that dewars should be filled slowly to avoid underfilling due to the geyser effect. The liquid nitrogen was added slowly until some started to come out of the fill port. The detector was allowed to sit for 5-10 minutes and refilled. Once filled in this way, a charge of liquid N<sub>2</sub> will last at least 8 hours (the detector signal does not decline during this period). However, during experimentation we refilled the dewar every 6 hours to absolutely ensure the integrity of the measurements.
- 4) The internal reflection elements (IRE) were reused, and steps were taken to ensure that no contamination occurred due to the previous experiment. After an experiment depositing, for example, HfO<sub>2</sub>, the IRE was cleaned as follows:
  - A. Etch in dilute HF solution (10s overetch past dewet)
  - B. Rinse in deionized H<sub>2</sub>O
  - C. Grow ~30Å thermal SiO<sub>2</sub> in a tube furnace –3min at 900°C in stagnant air (sample horizontal)
  - D. Etch the sacrificial oxide in dilute HF (10s overetch past dewet)
  - E. Prepare fresh, dilute HF solution.
  - F. Repeat steps C & D
- 5) Samples were loaded immediately after the surfaces were prepared. The IRE was affixed to the platen, and the platen was mounted on the chuck.

- 6) Access to the deposition chamber is through the front view port which is vacuum-sealed to the chamber using an o-ring. The window was typically left off for a few minutes during which rough sample alignment (as described in the Appendix, Section 9.2.3) was performed to verify that sufficient signal strength could be obtained. If necessary, the IRE was removed from the chamber and repositioned. The chamber was purged with N<sub>2</sub> gas while the window was removed.
- 7) When it was clear that reasonable signal strength could be obtained, the window was attached and the system evacuated. Pumping typically began within 10 minutes of surface preparation. The system was pumped for 30 minutes to allow the pressure to reach the 10<sup>-7</sup> torr range. Final sample alignment was performed while pumping.
- 8) After alignment and chamber evacuation were complete, the sample was heated to the desired reaction temperature. The temperature is controlled via feedback control, but the output voltage and current can be limited manually. The heater voltage was reduced in order to limit any temperature swings in the sample. The sample temperature was allowed to equilibrate for 30 minutes after reaching the set point.
- 9) A background spectrum was collected after 30 minutes of heating. Another background spectrum was collected after 10 additional minutes and compared to the first to verify thermal equilibrium. Additional spectra were collected every 10 minutes if the sample temperature was not stable. The experiment was started as soon as two of the spectra were identical. Most often the 40 and 50minute spectra were identical. Occasionally, the 30 and 40minute spectra (usually for temperatures below 150°C) or the 50 and 60minute spectra (usually for temperatures above

250°C) matched. Sometimes, we started the experiments after only 10 minutes heating if the stability of the initial surface was a concern. In these instances, baseline correction was necessary to correct curvature in the final spectra.

- 10) The experiment timer was started and all actions and measurements were recorded in Excel spreadsheets with a time stamp. The pressure was usually noted every 30s and used to calculate the exposure numerically using a trapezoidal algorithm. Once the pressure stabilized, it was recorded less often.
- 11) When exposing a surface to organometallic species, the system gate valve was closed and precursor vapor was leaked into the system via a UHV leak valve. When the desired pressure was reached, the leak valve was closed. Pressures between 0.1 to 100mtorr (0.0001 to 0.1torr) are accessible and were measured using a heated capacitance manometer gauge. Spectra were measured at intervals ranging from 30s to 10minutes during such exposures. As discussed in the Appendix, Section 9.3, spectral features due to the presence of gas phase species in the beam path may be observed at pressures as low as  $\sim 1$ mtorr.
- 12) After the desired exposure was reached, the gate valve was opened to evacuate the processing chamber. Spectra were collected.
- 13) For oxidizing species (air and H<sub>2</sub>O), the system was operated under flow conditions. The system butterfly valve was closed to limit the pumping conductance and diaphragm valves were opened to allow the flow of air and H<sub>2</sub>O vapor through the system. The experimental pressure was adjusted using needle valves on the air and H<sub>2</sub>O lines. The positions of these valves were set before the experiments were

performed. Spectra were measured at intervals ranging from 30s to 10minutes during such exposures.

- 14) After the desired exposure was reached, the butterfly valve was opened and the air or H<sub>2</sub>O valve closed. Spectra were collected.

## **2.6 Future Work**

The *in-situ* spectroscopy experiments presented here represent the first investigations performed using a new piece of equipment in our lab. The techniques employed thus far will be improved and built on by future graduate students. One obvious weakness in the current work is the lack of tools for confirming the identity of adsorbed species associated with vibrational modes. The following experiment which combines a powerful surface science technique, temperature programmed desorption, with real-time, *in-situ* FTIR was designed to fill this need but was not implemented due to funding and time constraints. Because the information produced in this experiment is fundamental in nature, we expect it would dovetail nicely with almost any new investigation in which the nature of surface bonded species is of interest.

The experiment is to perform Temperature Dependent Spectroscopy using simultaneous ATR-FTIR and Mass Spectroscopy measurements. The first step would be to condense organometallic species on an IRE crystal at cryogenic temperatures. Infrared measurements of this sample would clearly define the vibrational signature of physisorbed species not bonded to the surface. The temperature would be ramped slowly while continuously collecting gas-phase mass spectra and surface ATR-FTIR spectra. A standard Temperature Programmed Desorption measurement allows one to determine how many species bond to the surface and to estimate the binding energy of each by noting the

temperature at which the species desorbed. This measurement has the additional advantage that one could deconvolve the vibrational spectrum of each species from the time series of FTIR spectra. This information would help to identify each surface species and would prove very useful in subsequent reaction studies when identifying species participating in reactions.

We currently have a cryogenic chuck (liquid N<sub>2</sub> cooled) and a differentially pumped mass spectrometer with a range of 300 atomic mass units that can be installed in the system. The mass spectrometer can easily be equipped with a capillary tube positioned near the face of the crystal. The main challenge in implementing this plan is temperature control. We would need to purchase a controller to accurately control the ramp rate and mount the thermocouple either directly on the sample or in very close proximity to it. Temperature control issues are discussed more fully in the Appendix, Section 9.6.3, but the best method in terms of process control may be resistive heating through the sample for this experiment. The other challenge is in data input/output as the sample temperature, FTIR measurement, and Mass Spectrometer measurement must all be coordinated. The group has used LabView for similar tasks.<sup>4</sup> If Labview is used, then it is not necessary to purchase a separate temperature controller as these features can be built into the computer program. It is an investment of time, but this experiment would yield a wealth of fundamental information and will be useful if studying surface reactions with IR spectroscopy continues to be a focus in the group.

## 2.7 References

- 1 Chambers, J. J. Reactions for Yttrium Silicate High-k Dielectrics. Doctoral Dissertation, North Carolina State University, Raleigh, 2000.
- 2 Yates, J. T., Jr *Experimental Innovations in Surface Science: A Guide to Practical Laboratory Methods and Instruments*. Springer-Verlag: New York, 1998.
- 3 Morrison, P. W., Jr. Associate Professor, Chemical Engineering, CWRU, Personal Communication, July 2, 2002
- 4 *LabVIEW, Version 8.0*, National Instruments Corporation: Austin, Texas, Copyright 2005.

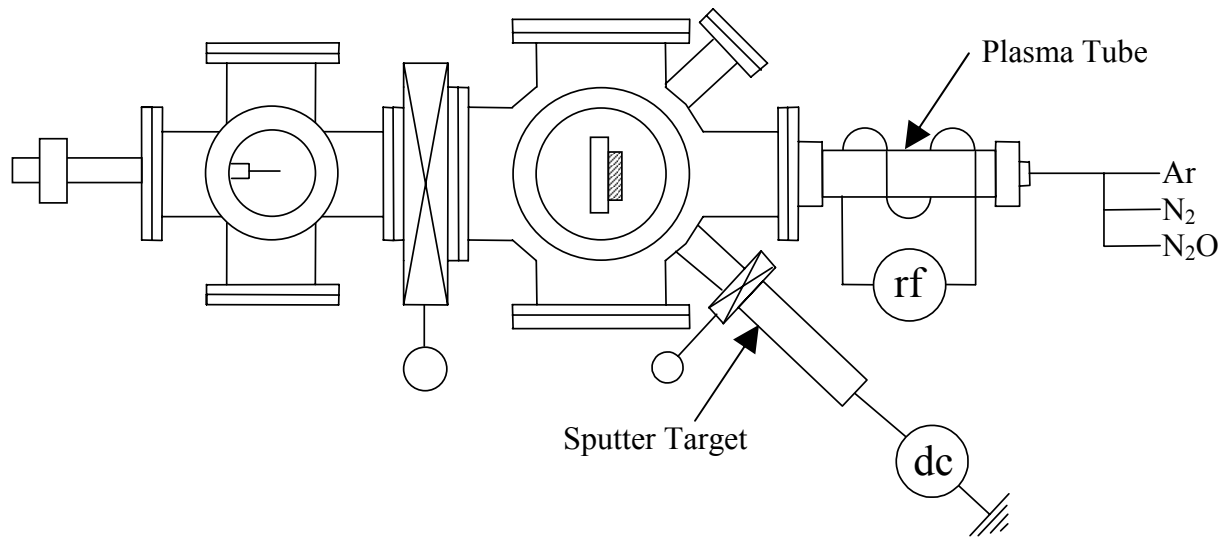


**Figure 2.1** The system when configured for plasma-assisted, DC sputtering of metal films. It is a two chamber system. The sputtering target is retractable so it can be isolated from reactive plasmas used during surface pretreatments (i.e., oxidation and nitridation) and from the ambient during system maintenance.

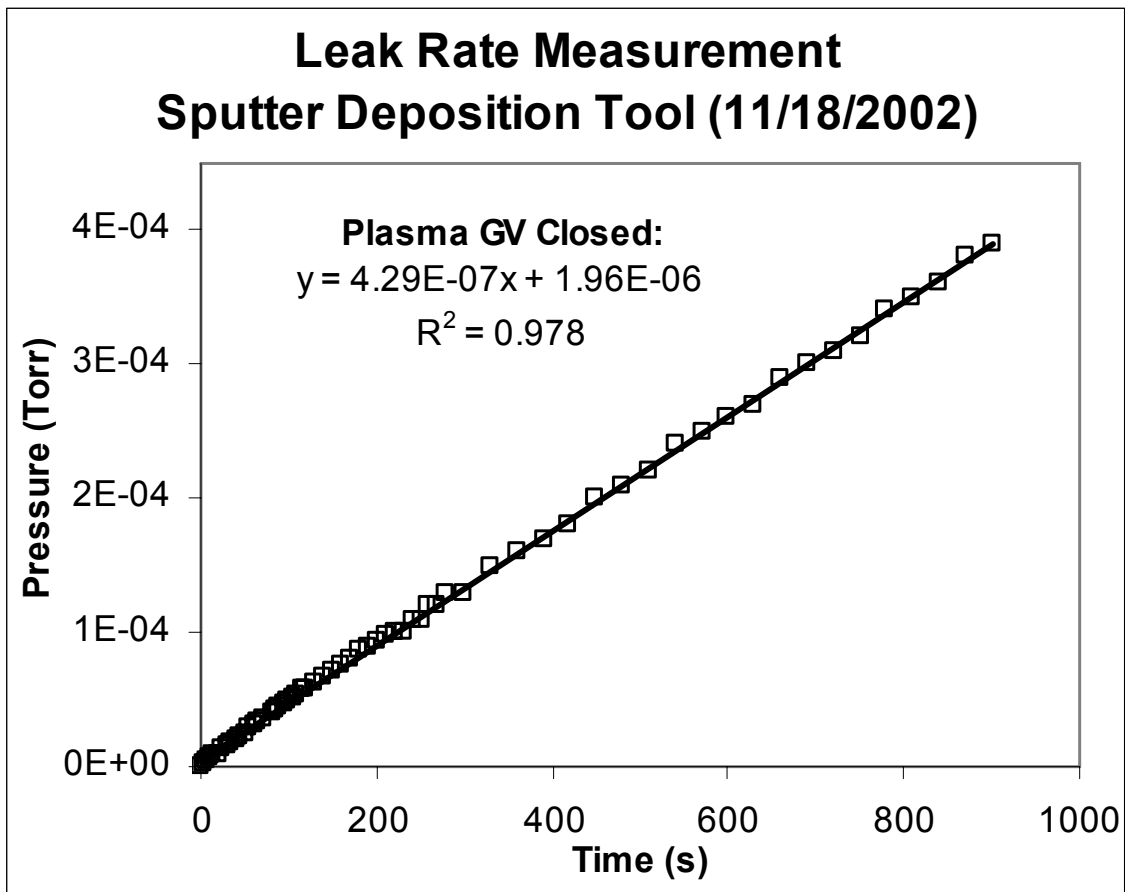


**Figure 2.2** The leak rate of the system (configured for metal sputtering) was measured via ion gauge over a period of 15 minutes. The gate valve between the deposition chamber and plasma tube was closed during this measurement, but similar leak rate values were obtained with an open gate valve. The leak rate was  $4 \times 10^{-7}$  torr/s.

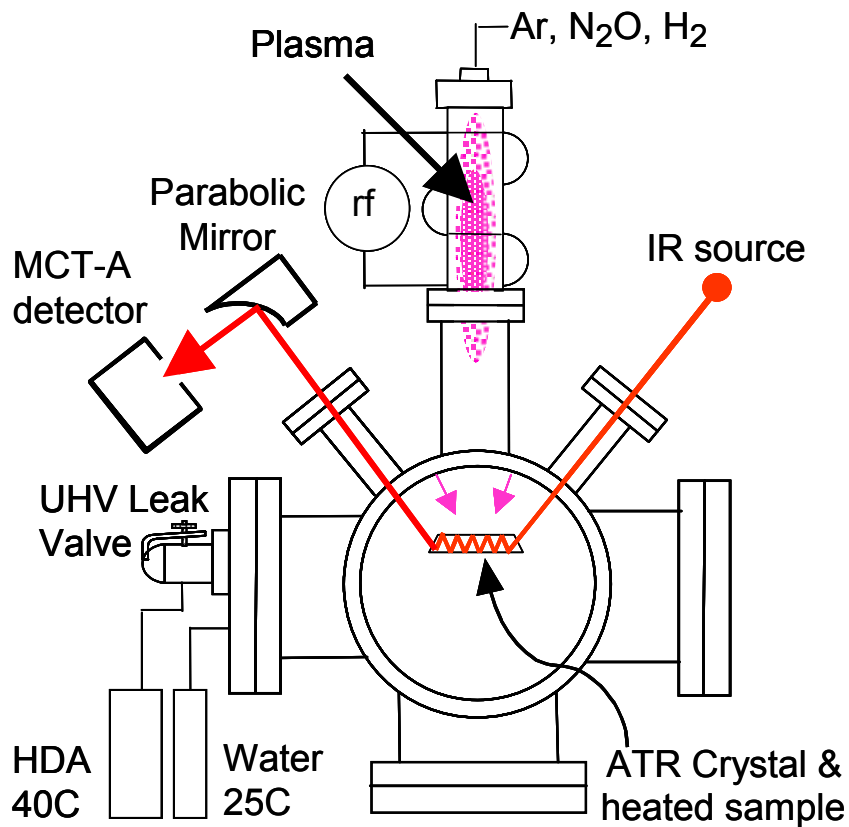


**Figure 2.3** This figure shows the configuration of the main process chamber of the system in Figure 2.1 when *in-situ* spectroscopic measurements were performed. The infrared light is focused into the system using KBr lenses and is focused on the narrow band gap, HgCdTe detector using a parabolic mirror. A purge gas generator is used to constantly purge the entire beam path with dry air with greatly reduced CO<sub>2</sub> levels. Films are deposited directly on the IREs allowing attenuated total reflectance-FTIR measurements to be performed.

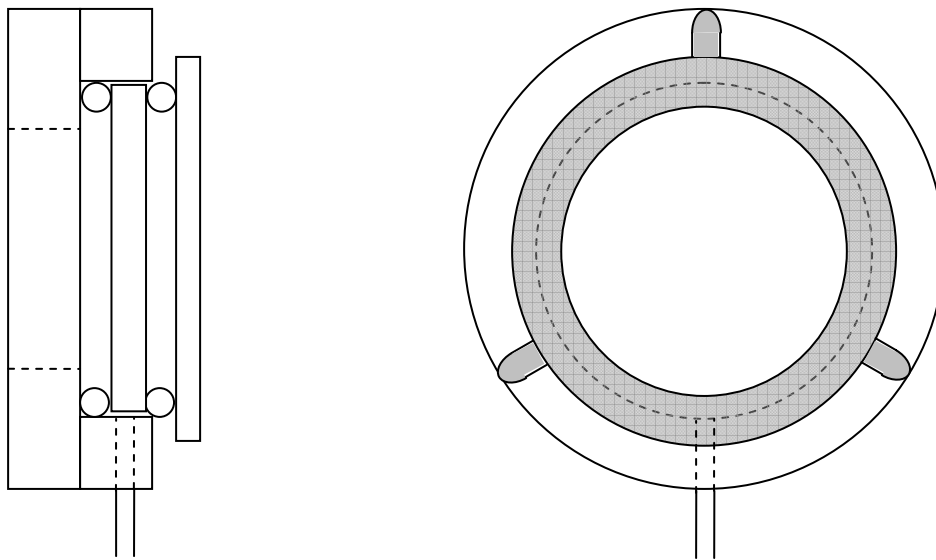


**Figure 2.4** Schematic of differentially pumped flange for mounting KBr discs as windows. The flange is a modified 2 3/4" conflat flange. The space between the o-rings sealing the window is differentially pumped via a 50L/s turbo so there is no appreciable difference in the system base pressure or leak rate upon installation of these windows. We use 38mm x 6mm (diameter x thickness) KBr discs which are easily replaced and polished as needed.

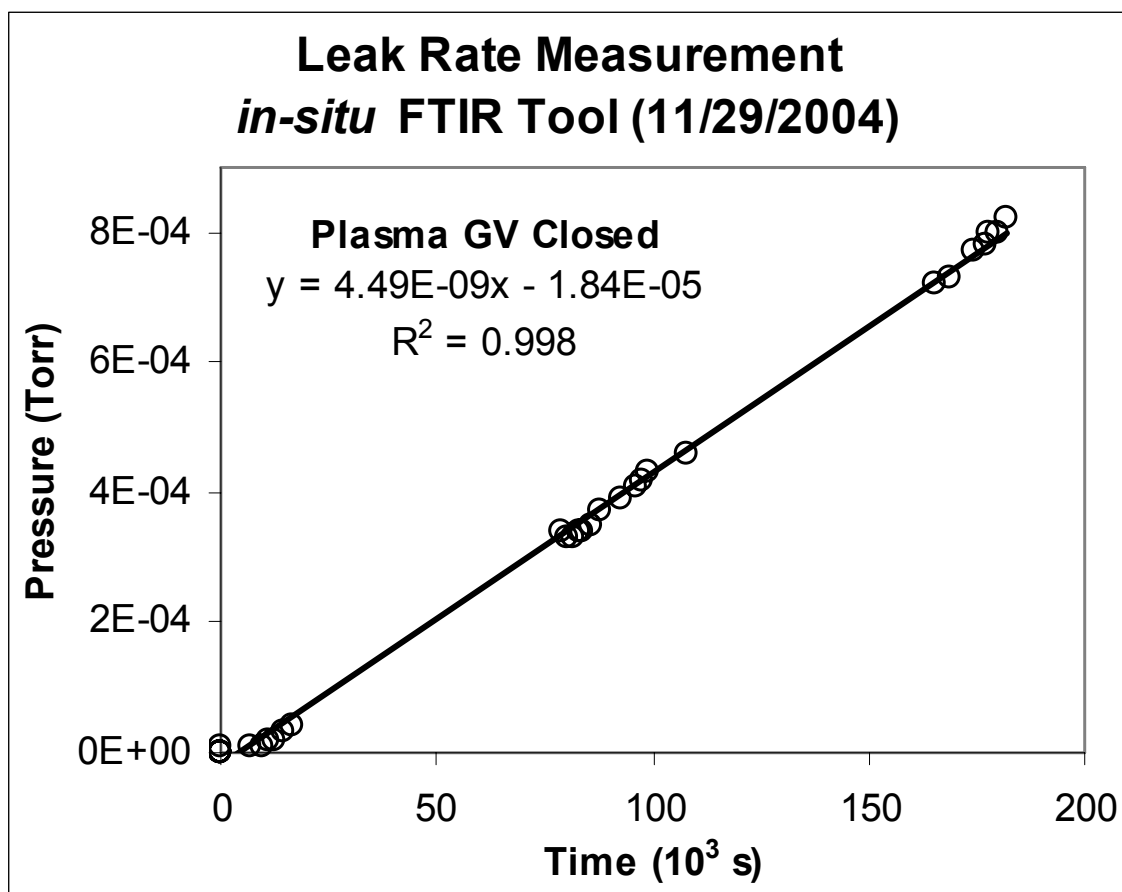


**Figure 2.5** The leak rate of the system (configured for *in-situ* FTIR experiments) was measured via capacitance manometer gauge over a period of 50 hours. The gate valve between the deposition chamber and plasma tube was closed during this measurement. The leak rate was  $4 \times 10^{-9}$  torr/s.

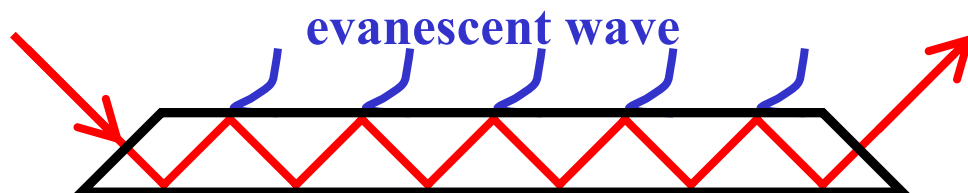


**Figure 2.6** An evanescent wave of exponentially decaying IR radiation extends out into the vacuum (and through thin films deposited onto the crystals) above the trapezoidal Internal Reflection Elements (IREs) used in these experiments. The IREs are trapezoidal, high resistivity Si with 45° bevels polished such that the top and bottom of the crystal are a Si (100) surface. The drawing is not to scale. The IREs measure 40x12x0.5mm. The IREs are 500 $\mu\text{m}$  thick, and the evanescent wave extends beyond the IRE by about 0.2 $\mu\text{m}$  at 4000 $\text{cm}^{-1}$  and 0.5 $\mu\text{m}$  at 1500 $\text{cm}^{-1}$ .

Chapter 3 is a reprint of a paper that appeared on pages 6173 – 6180 of the Journal of Applied Physics, Volume 91, Number 9 in May 2002

## **Elementary Reaction Schemes for Physical and Chemical Vapor Deposition of Transition Metal Oxides on Silicon for High-k Gate Dielectric Applications**

D. Niu, R. W. Ashcraft, M. J. Kelly, J. J. Chambers<sup>†</sup>, T. M. Klein<sup>#</sup>, G. N. Parsons

*Department of Chemical Engineering, North Carolina State University, Raleigh, NC 27695*

<sup>†</sup> *Texas Instruments, Dallas TX 75243*

<sup>#</sup> *Department of Chemical Engineering, University of Alabama Tuscaloosa, Tuscaloosa AL*

### **Abstract**

This article describes the kinetics of reactions that result in substrate consumption during formation of ultra-thin transition metal oxides on silicon. Yttrium silicate films (~40 Å) with an equivalent silicon dioxide thickness of ~11 Å are demonstrated by physical vapor deposition (PVD) routes. Interface reactions that occur during deposition and during post-deposition treatment are observed and compared for PVD and chemical vapor deposition (CVD) yttrium oxides and CVD aluminum-oxide systems. Silicon diffusion, metal-silicon bond formation, and reactions involving hydroxides are proposed as critical processes in interface layer formation. For PVD of yttrium silicate, oxidation is thermally activated with an effective barrier of 0.3 eV, consistent with the oxidation of silicide being the rate-limited step. For CVD aluminum oxide, interface oxidation is consistent with a process limited by silicon diffusion into the deposited oxide layer.

## Specific Contribution

For this article, I worked in collaboration with Jim Chambers to produce yttrium silicate films including deposition of the yttrium and oxidation of the metal to form yttrium oxide and yttrium silicate. Specifically, I sputter deposited yttrium films which were either oxidized *ex-situ* or vacuum annealed and oxidized *ex-situ* in air or N<sub>2</sub>O. I also collected X-ray Photoelectron spectra of some of the films and collaborated on the peak analysis and interpretation. This work helped to improve control over the film deposition and oxidation processes and helped to identify interface reaction processes that occur during deposition of high dielectric constant films.

### 3 Elementary Reaction Schemes for Physical and Chemical Vapor Deposition of Transition Metal Oxides on Silicon for High-k Gate Dielectric Applications

#### 3.1 Introduction

The semiconductor industry improves performance by decreasing the gate length with each metal oxide semiconductor (MOS) device generation. The silicon dioxide gate dielectric thickness scales with gate length to promote high channel transconductance. The *International Technology Roadmap for Semiconductors* predicts that a 50 nm device generation will require the equivalent of a sub-1.0 nm silicon dioxide.<sup>1</sup> A variety of metal oxides, including  $\text{Y}_2\text{O}_3$ ,  $\text{Ta}_2\text{O}_5$ ,  $\text{TiO}_2$ ,  $\text{HfO}_2$ ,  $\text{ZrO}_2$  and  $\text{Al}_2\text{O}_3$ , have been suggested as high-k ( $k > k_{\text{SiO}_2} = 3.9$ ) replacements for silicon dioxide.<sup>2-5</sup> Thermodynamic calculations have been used to evaluate the stability, with respect to no silicide or  $\text{SiO}_2$  formation, of binary metal oxides in contact with silicon.  $\text{ZrO}_2$ ,  $\text{HfO}_2$ ,  $\text{Al}_2\text{O}_3$ ,  $\text{Y}_2\text{O}_3$ ,  $\text{La}_2\text{O}_3$ , and other rare earth oxides are the most promising binary metal oxides from using this thermodynamic analysis.<sup>6</sup> However, pure metal oxides tend to crystallize at relatively low temperatures resulting in possible high conductivity pathways along grain boundaries counteracting the benefits of the high-k dielectric.

Zirconium silicate and hafnium silicate have been demonstrated as potential high-k gate dielectrics with  $k \sim 11$  and an amorphous microstructure after annealing at  $1050^\circ\text{C}$  for 20 seconds.<sup>5</sup> Yttrium silicate also possesses desirable thermodynamic, dielectric and structural properties that make it attractive as a high-k candidate. The Y-O bond is quite strong, since the free energy of formation per oxygen atom ( $-\Delta G_f$ ) (at  $25^\circ\text{C}$ ) is  $2.40 \times 10^{-22}$  kcal for  $\text{Y}_2\text{O}_3$

compared to  $1.70 \times 10^{-22}$  kcal for  $\text{SiO}_2$ .<sup>7</sup> Previous studies have demonstrated the formation of yttrium silicate by the oxidation of yttrium on silicon in dry air at 500-700°C.<sup>2</sup> Yttrium silicate films with the composition  $\text{Y}_{2.45}\text{Si}_{0.55}\text{O}_5$  approximately 26.0 nm thick were created using this process. Capacitance measurements on MOS capacitors with an  $\text{Al}/\text{Y}_{2.45}\text{Si}_{0.55}\text{O}_5/\text{Si}$  structure yielded  $k \sim 12$  for the silicate layer, which should be suitably large to obtain equivalent oxide thickness (EOT)  $< 1.0$  nm with low tunneling. These films also exhibited acceptable current-voltage and breakdown characteristics.

Scaling the gate insulator into the sub-1.0 nm regime requires a material with suitably high- $k$  that remains amorphous during typical annealing cycles, and is stable with respect to reaction with the substrate semiconductor. For many cases, the stability of the deposited material with the substrate limits performance and dielectric scaling. This paper will focus on recent results that highlight details of potential interface reaction mechanisms, and direct measurements of interface reaction product and reaction rates. This work focuses on oxides of the Group III metals (Al and Y) to better understand the viability of Group III metal oxides, and to understand fundamental properties common to Group III and Group IV oxide deposition.

### **3.2 Material Preparation and Analysis**

Yttrium silicate thin films (Y-O-Si) were formed on silicon and pretreated silicon by depositing thin layers of yttrium, then oxidizing in  $\text{N}_2\text{O}$  at 900°C. Some deposited Y films were annealed in vacuum to form Y-silicide before oxidation. Silicon surface pretreatments studied included *in-situ* oxidation and *in-situ* nitridation. Aluminum oxide films were deposited on clean silicon by plasma assisted chemical vapor deposition (CVD) using metal-organic precursors. Details of the material preparation processes are described in previous

articles.<sup>8-10</sup> Yttrium oxide was also deposited by plasma assisted CVD using yttrium diketonate precursors.

X-ray photoelectron spectroscopy (XPS), Fourier transform infrared spectroscopy (FTIR), and transmission electron microscopy (TEM) were used to identify the bulk chemical structure of the films.<sup>9</sup> TEM, XPS, angle resolved XPS, medium energy ion scattering (MEIS), and resonant nuclear reaction profiling (RNRP) were also used to characterize interface structure.<sup>8,10</sup> Current vs. voltage (I-V) and capacitance vs. voltage (C-V) testing was used to determine the electrical quality of the dielectrics. Electrical thickness is described as an EOT determined from a fit of the C-V curve that includes the quantum mechanical effect.<sup>11</sup> TEM and atomic force microscopy (AFM) were used to identify film morphology. For the physical vapor deposition (PVD) yttrium deposition process, films with EOT  $\cong$  1.1 nm are demonstrated with leakage less than 1 A/cm<sup>2</sup> at 1 V above flat band, indicating that these materials are interesting candidates for high dielectric constant insulators.

### **3.3 Results**

#### **3.3.1 PVD yttrium silicate**

Yttrium silicate films with  $\sim$ 40 Å physical thickness, were formed by oxidizing  $\sim$ 8 Å of Y on silicon for 15 seconds in N<sub>2</sub>O at 900°C. Electrical characterization of these materials showed low EOT ( $\sim$ 10 Å) with dielectric constant of  $\sim$ 14 (based on thickness determined from TEM). Using aluminum gates, the flat band voltages ( $V_{FB}$ ) were measured to be  $-0.74$  and  $-1.63$  V for n- and p-type substrates, respectively, indicating positive fixed charge in the dielectric. The current density for the 10-12 Å EOT was less than 1 A/cm<sup>2</sup> in accumulation at 1 V greater than  $V_{FB}$ .

To better understand the process involved with dielectric formation, XPS analysis in the Si 2p region of various thicknesses of yttrium layers on silicon after various process steps is shown in Figure 3.1. Spectrum (i) from a thick (1000 Å) Y film deposited on silicon and annealed for several minutes at 600°C in vacuum ( $\sim 10^{-8}$  Torr), and the Si 2p peak at 98.5 eV is consistent with a yttrium silicide bonding structure. Spectrum (ii) corresponds to a thick silicide film (same as in spectrum (i)) that has been oxidized in N<sub>2</sub>O for several minutes at 900°C. The single peak at 102.2 eV is consistent with silicon bound to oxygen in a metal “silicate” (102-103 eV).<sup>12</sup> The term “silicate” is used here to describe an amorphous material with Y-O-Si local bonding, similar to that found in a true crystalline silicate. Spectra (iii) and (iv) correspond to much thinner initial Y depositions and much thinner oxidized layers, consistent with the intensity of the substrate Si-Si bond at  $\sim 99.3$  eV. Spectrum (iii) is for a film that underwent vacuum annealing (forming a silicide) then oxidation (forming the silicate). The Si-O peak position is shifted to slightly higher binding energy compared to the thicker film in spectrum (ii), corresponding to a higher concentration of silicon in this sample. Spectrum (iv) is for a Y metal film that was subjected to only a 900°C oxidation step. This oxidation step was the same as imposed on the metal silicide sample corresponding to spectrum (iii). The Si 2p spectra (iii) and (iv) show nearly indistinguishable peak position and peak shape, and with the Y 3d and O 1s spectra (not shown), indicate the metal deposition and oxidation process results in a thin Y-O-Si “yttrium silicate” dielectric on silicon. The similarity between the vacuum annealed/oxidized film (spectrum iii) and the film that was only oxidized (spectrum iv) suggests that the silicide reaction proceeds much more quickly than the oxidation step. This will be discussed below in more detail in context with other deposition results.

To characterize the kinetics of silicide oxidation, the effect of oxidation time on dielectric thickness and structure was characterized using TEM. Figure 3.2 shows TEM images of yttrium silicate formed with  $\sim 8 \text{ \AA}$  of yttrium and oxidation at  $900^\circ\text{C}$  in air for times from 6 seconds to 20 minutes. Figure 3.2(a), (b), and (c) show films oxidized for 6, 15 and 60 seconds that were capped with  $2000 \text{ \AA}$  of Al after oxidation with no post-metallization anneal. The physical thickness of the films determined using the Si-Si bond length as a reference is 30, 42 and  $42 \text{ \AA}$  respectively. In all instances, lattice fringes are observed in the silicon substrate, but not in the Y-O-Si film indicating amorphous Y-O-Si structure. The interface for the 6 seconds oxidation appears slightly roughened, perhaps due to the presence of silicide, but the interface is smooth for oxidation at 15 and 60 seconds. The images in Figure 3.2(a), (b), and (c) all indicate the presence of one layer without any  $\text{SiO}_2$  at the Y-O-Si/Si interface. Figure 3.2(d) shows a TEM image of a film oxidized for 20 minutes. This film was not capped with Al after oxidation, and the top layer is epoxy. The thickness is  $75 \text{ \AA}$  and the contrast in the image suggests that for long oxidation times  $\text{SiO}_2$  grows beneath the Y-O-Si layer. This data is consistent with a rapid reaction between the metal and silicon followed by oxidation of the metal-silicide. The TEM results in Figure 3.2 are consistent with an under-oxidized silicide in Figure 3.2(a) and a more fully oxidized silicide (i.e. “silicate”) in 3.2(b) and (c). For extended oxidation times, the TEM results in Figure 3.2(d) are consistent with slower oxidation of the substrate silicon after formation of the silicate top layer. It is important to note that the combined silicide formation and silicide oxidation reactions are observed to proceed more rapidly than oxidation of a control silicon surface.<sup>9</sup>

The effect of yttrium oxidation temperature for a fixed oxidation time was also characterized. Figure 3.3 shows: (a) the O 1s; (b) Y 3d; and (c) Si 2p regions of the photoelectron spectrum for Y-O-Si films formed by the oxidation of thin (25 Å) yttrium films on silicon in 1 atm. N<sub>2</sub>O at temperatures between 500 and 900°C. The figure also shows the spectra for a 25 Å yttrium film on silicon exposed in ambient conditions (25°C, 1 atm. air) for ~1 day. Consistent with silicate bonding, the Y 3d peaks (Figure 3.3b) for films oxidized at 25-900°C are all shifted to higher binding energy than expected for Y 3d<sub>3/2</sub> and Y 3d<sub>5/2</sub> (158.8 and 156.8 eV, respectively) in Y<sub>2</sub>O<sub>3</sub>.<sup>12</sup> The Y 3d<sub>5/2</sub> peaks shift from 158.0 eV for oxidation at 25°C to 159.3 eV for oxidation at 900°C. The Y 3d spectrum for the film oxidized at 25°C exhibits a shoulder near ~156.0 eV consistent with yttrium metal (156.0 eV) or Y<sub>2</sub>O<sub>3</sub> (156.8 eV), but the spectrum does not indicate the presence of any yttrium silicide (155.8 eV).<sup>13</sup> The Y 3d spectra for the Y-O-Si films oxidized at 500-700°C do not exhibit evidence for Y<sub>2</sub>O<sub>3</sub>, yttrium metal or yttrium silicide. The Y 3d satellite and Si 2s photoelectrons cause the small peaks at ~153 and ~151 eV. The low binding energy peak in the Si 2p spectra (Figure 3.3c) is due to the silicon substrate and the higher binding energy peaks are assigned to metal silicate. The Si-O mode shifts from 101.8 eV for oxidation at 25°C to 103.1 eV for oxidation at 900°C. The Si-O mode also increases in intensity when the oxidation temperature is increased, and the Si-O mode for oxidation at 900°C is ~3 times the integrated area of the Si-O mode for the film oxidized at 25°C. The intensity of the silicon substrate peak is largest for oxidation at 25°C. Increasing the oxidation temperature results in an increasingly attenuated silicon substrate peak consistent with an increase in overlayer thickness. The O 1s peak positions for oxidation from 25-900°C are measured at ~532 eV. The O 1s peaks are broad peaks resulting from a combination of oxygen bonding

to yttrium and to silicon. As a result, the full-width-half-maximum (FWHM) for all the O 1s peaks is ~3.0 eV, which is considerably wider than for a binary oxide (i.e. measured FWHM for SiO<sub>2</sub> is 1.8 eV). The FWHM generally decreases when the oxidation is performed at higher temperature, and the measured FWHM is 3.0 and 2.6 eV for oxidation at 25 and 900°C, respectively. The spectrum for the Y-O-Si film oxidized at 25°C exhibits a shoulder at ~530.5 eV, which is consistent with an increase in O-Y-O bonding.

The MEIS proton energy spectra for Y-O-Si films oxidized at 600 and 900°C were also analyzed. Consistent with the XPS results of Figure 3.3, the MEIS spectra (not shown) exhibit peaks for yttrium (~94 keV), silicon (~86.5 keV) and oxygen (~79.5 keV). The MEIS detects near surface silicon (i.e. silicon in the dielectric film) as a high energy (~87 keV) shoulder on the larger silicon substrate background. For the film annealed at 600°C this shoulder is much smaller than for the film oxidized at 900°C. The composition calculated from the MEIS spectrum of the film oxidized at 600°C is (Y<sub>2</sub>O<sub>3</sub>)<sub>0.60</sub>·(SiO<sub>2</sub>)<sub>0.40</sub>, which represents a greater metal fraction than the most metal-rich yttrium silicate, Y<sub>2</sub>SiO<sub>5</sub>. The absence of phase separated Y<sub>2</sub>O<sub>3</sub> in the Y 3d XPS spectrum (Figure 3.3a) may be due to instrument sensitivity, or due dispersal of the Y<sub>2</sub>O<sub>3</sub> clusters within the silicate bulk. The composition calculated from the MEIS spectrum of the film oxidized at 900°C is (Y<sub>2</sub>O<sub>3</sub>)<sub>0.45</sub>·(SiO<sub>2</sub>)<sub>0.55</sub>, which is consistent with Y<sub>2</sub>SiO<sub>5</sub> (x = 0.50) considering the experimental error of x ± 0.04.

The results from the XPS analysis (Figure 3.3) and the MEIS data are shown in an Arrhenius plot in Figure 3.4, which shows the extent of silicon oxidation vs. the inverse of the anneal temperature. From the XPS data, the ratio of the Si 2p Si-O and Si 2p substrate integrated peak areas approximates the relative amounts of silicon in the Y-O-Si, and these

data points are plotted (as circles) in Figure 3.4. The integrated area of the Si 2p Si-O is a measure of the total amount of silicon in the Y-O-Si film, and the integrated area of the Si 2p substrate peak is a measure of total film thickness, which also takes into account the attenuation of the Si 2p Si-O mode with increasing film thickness. A more detailed analysis of the XPS data would need to confirm that the Si-O mode intensity was independent of thickness for a set of silicate films with uniform composition. However, the MEIS data can be used to confirm the trend observed in the current XPS data. The silicon content in the film is obtained from the MEIS data by multiplying the silicon fraction times the film thickness, and the points are included (as the triangles) in Figure 3.4. The slope gives an activation energy ( $E_a$ ) for the consumption of silicon during the oxidation of yttrium to be  $E_a \approx 0.3$  eV. The  $E_a = 0.3$  eV for oxidation of Y/Si is consistent with the activation energy for Gd/Si, Tb/Si and Er/Si oxidation reaction (0.37, 0.35 and 0.5 eV, respectively). Interface reaction schemes consistent with the XPS, MEIS, TEM, and electrical data are presented in the discussion section below.

### 3.3.2 CVD aluminum oxide

Interface reactions during plasma enhanced CVD of aluminum oxide were also characterized. For these experiments, thin ( $\sim 50$  Å)  $\text{Al}_2\text{O}_3$  was deposited on clean hydrogen terminated silicon from metal organic precursors using a process detailed previously.<sup>10</sup> Figure 3.5 shows results of narrow resonant nuclear reaction profiling for two different  $\text{Al}_2\text{O}_3/\text{Si}$  samples. The depth distribution of  $^{27}\text{Al}$  concentration was obtained using the narrow and isolated resonance in the cross sections of the nuclear reaction  $^{27}\text{Al}(p, \gamma)^{28}\text{Si}$  at 405 keV, and a tilted sample geometry was used to obtain a depth resolution of about 0.5 nm near the film surface.<sup>10,14</sup> Concentration profiles were obtained assuming a density of 3.8

g/cm<sup>3</sup> for the stoichiometric Al<sub>2</sub>O<sub>3</sub> film. The two films were similar physical thickness, but were grown using different reactor preparation conditions. Also, sample (a) was exposed to the ambient atmosphere for several weeks before characterization, whereas sample (b) was exposed for a shorter time. Sample (a) shows clear evidence for a mixed Al<sub>2</sub>O<sub>3</sub>/SiO<sub>2</sub> interface layer, whereas sample (b) shows an abrupt Al<sub>2</sub>O<sub>3</sub>/Si interface. It is important to note that Al<sub>2</sub>O<sub>3</sub> differs significantly from the other metal oxides currently studied for high-k applications, in part because aluminum metal, unlike Zr, Hf, La, and Y, does not readily mix with silicon to form a silicide. This means that any reaction pathway that involves silicide intermediates (such as the process for PVD Y-silicate described above) will not be active during deposition.

After deposition, the interface between an Al<sub>2</sub>O<sub>3</sub> film (~50 Å) and silicon was characterized using XPS as a function of anneal temperature for a fixed time (30 seconds). The effects of annealing on the Si 2p spectra are shown in Figure 3.6. The response of the Al<sub>2</sub>O<sub>3</sub>/Si interface to rapid thermal annealing in argon (with residual oxygen) is qualitatively similar to the yttrium silicate/silicon interface annealed in 1 atm. O<sub>2</sub> shown in Figure 3.3 above. The lower oxygen partial pressure for the aluminum oxide interface oxidation suggests that the active source of oxygen may be excess oxygen present in the Al<sub>2</sub>O<sub>3</sub> film, possibly bound as hydride. The Si-O feature at the interface in Figure 3.6 is observed to increase with anneal temperature, and the position of the Si-O is at a lower binding energy than expected for SiO<sub>2</sub>, indicating that mixing has occurred between the deposited Al and the Si substrate. As described above for the data in Figure 3.3, the extent of substrate oxidation can be estimated from the ratio of the Si-O peak area to the Si-Si peak area. The ratio values

increase with temperature, consistent with a thermally activated process, but the data is not sufficient to extract a well-defined activation energy for the process.

### 3.3.3 CVD of $Y_2O_3$

Yttrium oxide layers have recently been deposited in our lab using oxygen plasma assisted CVD with yttrium diketonate precursors. For these depositions, argon carrier gas flows through a heated tube containing solid precursor, and the precursor flows into the reactor just above the substrate, below a source of plasma excited oxygen.<sup>15</sup> Films were deposited on clean Si(100), and Si(100) surfaces pre-exposed *in-situ* to plasma excited  $O_2$  or  $N_2$  to produce oxide or nitrided-silicon interface layers. For deposition temperature of  $400^\circ C$  with typical gas flow and pressure conditions,<sup>15</sup> the deposition rate is  $\sim 15-20 \text{ \AA/minute}$ .

X-ray photoelectron spectra of three films deposited for 3, 6.5, and 30 minutes on clean Si(100) are shown in Figure 3.7. The thickest film shows features consistent with  $Y_2O_3$  structure in the Y 3d spectra, consistent with a thick  $Y_2O_3$  film. The spectra for the film deposited for 3 minutes show significant shifts in Y 3d binding energy, consistent with an oxide structure that contains significant Y-O-Si (Y-silicate) bonding. The position of the Si 2p Si-O feature is also consistent with the thinnest films consisting of significant yttrium silicate bonding structure (spectra not shown here).

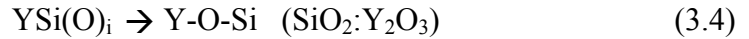
Figure 3.8 shows C-V curves for thin “yttrium oxide” films deposited on clean and pretreated Si(100). The gate metal was evaporated aluminum. The film on clean silicon was deposited under the same conditions as that shown in Figure 3.7 for the 3-minute deposition time, consistent with the films having significant yttrium silicate bonding structure. All films were annealed at  $900^\circ C$  for 1 minute and received a post-metallization anneal in  $N_2/H_2$  at  $400^\circ C$ . Fitting the C-V data for the film on clean silicon results in EOT of  $\sim 29 \text{ \AA}$ . The

flatband position of this film is shifted in the negative direction, consistent with positive fixed charge in the dielectric. Some hysteresis ( $\sim 20$  mV) in the C-V is also observed for this film. C-V curves for films deposited under the same conditions on *in-situ* pretreated silicon are also shown. For these examples, the nitridation processes do not change the net oxide thickness significantly, and the net EOT is  $\sim 30$  Å. Even for these relatively thick pretreatment layers, XPS spectra (not shown) for the films on pretreated silicon show evidence for significant silicon content in the deposited film, indicating that the pretreatment layers (oxynitride) and the silicon substrate mix with the deposited yttrium oxide, both during deposition and post-deposition annealing.

### **3.3.4 Proposed elementary reaction schemes**

The data presented above show that a clear understanding of reactions that occur at high-k dielectric interfaces, both during deposition and during post-deposition annealing, is critically important to control electronic properties of the gate stack. Various sets of elementary interface reactions can be proposed that are consistent with the results shown above. Comparing results from CVD and PVD experiments, and the effects of surface pretreatments, can further help define likely interface reaction schemes. The ultimate goal of this effort will be to understand, control, and minimize, or ideally avoid, interface reaction processes that lead to undesired gate stack capacitance, dielectric charges, interface trap states, etc. that degrade electronic device performance.

For the case of thermal oxidation of PVD yttrium on silicon, a reaction scheme of elementary reactions for formation of yttrium silicate can be written as follows:



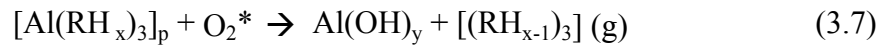
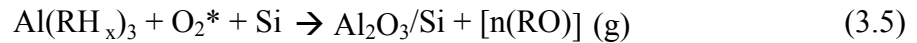
Reaction 3.1 is the formation of yttrium silicide, which occurs through diffusion of silicon from the substrate into the yttrium metal layer.<sup>16, 17</sup> The silicon diffusion happens quickly upon annealing PVD yttrium deposited on silicon, even at moderate temperatures.

Rutherford backscattering analysis of metal silicide systems has shown that silicon is the dominating diffusion species in  $YSi_x$ , and the yttrium atoms remain relatively immobile even after 1 hour anneal at 1000°C.<sup>16</sup> Step 3.2 is oxygen dissociation, and Step 3.3 is oxygen diffusion through the film bulk. The above scenario assumes that oxygen diffuses as atomic oxygen, but diffusion of molecular oxygen and water as oxidizing species, as well as silicon diffusion, must also be considered in a full detailed kinetic analysis. Step 3.4 is oxidation of the silicide, which is presumed here to occur upon insertion of O atoms into a Y-Si bond.

Repeating this reaction leads eventually to the yttrium silicate structure. Thermodynamics indicates that the favored product in the reaction between Y, Si, and  $O_2$  should be  $Y_2O_3$  and Si. However, processing conditions in thin film formation are generally far from equilibrium, and kinetic intermediates (such as the proposed yttrium silicide in this case) can form and further react (in this case forming silicate) resulting in products “unexpected” from bulk thermodynamics that can dominate the resulting film. The measured activation energy

of 0.3 eV shown in Figure 3.4 is a net reaction barrier (including for example forward and reverse reactions) so that it cannot precisely be ascribed to any elementary reaction in this process. However, since the silicide formation and oxygen diffusion can be presumed to occur relatively rapidly, the measured reaction barrier likely involves the silicide oxidation step, Reaction 3.4. This barrier is small compared to the barrier of ~3.0 eV measured for reduction of SiO<sub>2</sub> to form transition metal oxides,<sup>18</sup> which implies that this reaction could occur during CVD processes at typical deposition temperatures, providing there are metal-silicon bonds present at or near the deposition surface.

For the case of aluminum oxide CVD, a hypothetical set of reactions governing film deposition from a generic metal-organic precursor (Al(RH<sub>x</sub>)<sub>3</sub>) are written as



Reaction 3.5 corresponds to the (non-elementary) process of aluminum metal-organic reacting with oxygen to form an abrupt Al<sub>2</sub>O<sub>3</sub>/Si interface and oxidation of the organic ligand (R). This process likely involves the metal organic adsorbing on the surface in a variety of product states, including molecular physisorption, dissociative physisorption, or dissociative chemisorption. Equation 3.6 shows molecular physisorption as an example. In Equation 3.7, the physisorbed molecule is oxidized, leading to a hydroxide product on the surface. Equation 3.8 shows diffusion of silicon into the Al<sub>2</sub>O<sub>3</sub>. Then, in Equation 3.9, the hydroxide

reacts with interstitial silicon (or silicon available at the substrate interface) to form the interfacial silicate. Silicate formation from Si and  $\text{Al}_2\text{O}_3$  alone is not expected to occur, but the addition of excess oxygen (i.e. hydroxide) enables aluminum silicate formation to be favored energetically.<sup>10</sup> This reaction scheme then can be used to understand the results shown in Figures 3.5-6. The fact that the interface reaction proceeds to a greater extent in some samples than in others (i.e. sample (a) vs. sample (b) in Figure 3.5) could result from a different density of hydroxide present in the two samples. In addition to the hydroxide production route shown in Reaction 3.7, hydroxide will diffuse into the material from exposure to atmospheric water (not shown explicitly in the reaction scheme above), so that different degrees of interface oxidation may be expected from samples with different history. It is also possible that variations in chamber history or surface preparation conditions could result in enhanced interface reactivity.

The temperature dependence of the interface oxidation observed in Figure 3.6 could also result from hydroxide present in the material, and the activation barrier could then be related to the oxidation of the interstitial silicon (Reaction 3.9), or could relate to the barrier for Si diffusion (Reaction 3.8). Based on the smaller barrier observed for oxidation in the yttrium case, we can conclude that the measured barrier is more likely related to silicon diffusion into the deposited film.

For yttrium oxide CVD, the set of elementary equations for deposition are analogous to those for aluminum. However, an important distinction between the results presented above for  $\text{Al}_2\text{O}_3$  and those for  $\text{Y}_2\text{O}_3$  is that it is possible to make an abrupt  $\text{Al}_2\text{O}_3/\text{Si}$  interface by CVD methods. Atomically abrupt interfaces have not been clearly demonstrated to date in other metal oxide/silicon or metal silicate/silicon interfaces of interest for high-k

applications. Therefore, it is important to consider what other possible elementary steps could be present in the  $Y_2O_3$  system that lead to the non-abrupt interface. One such reaction that could be considered in addition to those shown above for  $Al_2O_3$  is the formation of metal-silicon bonds during diffusion of silicon into the metal oxide structure:



where the Y-Si could be on the deposition surface, i.e. with the precursor ligands still bonded to the surface as shown in Equation 3.10, or it could be at the interface or near surface region, as shown in Equation 3.11. Equation 3.11 is likely not favored for Si in contact with a true bulk oxide, but may proceed in a deposition process at the near surface where other species are present and bonded, for example, to the oxygen. The formation of metal-silicon bonds (Equations 3.10 and 3.11) could occur in the yttrium case (or for Hf, Zr, La, etc.) but is not expected in the case of aluminum because yttrium readily forms a silicide, whereas aluminum does not. This intermediate product could then oxidize to form a silicate in a process similar to that observed in Reaction 3.4 above. The route to interfacial silicate involving hydroxides [including those resulting from deposition products, Reaction 3.9, and from post-deposition atmospheric exposure] is also expected to be active. This means that there are likely multiple separate kinetic routes to interface silicate formation in these material systems. Data in Figure 3.8 indicates shows that significant interfacial silicate results during CVD of yttrium oxide on silicon. The observed limited thickness of the silicate in Figure 3.7 suggests that the reaction is limited by diffusion of silicon into the deposited layer. The reaction scheme suggests that the degree of interface reaction could be controlled by changing growth precursor (to change adsorption process and reaction-by

products) and by limiting reaction of the deposited film to ambient. The relative importance of these mechanisms in controlling substrate consumption reactions will need more studies to optimize material systems for sub-1 nm gate dielectric layers.

### **3.3.5 Summary**

Interface reactions that occur between transition metal oxides during deposition and during post-deposition processing have been examined, and elementary process steps consistent with the observed data have been presented. It is proposed that interface reactions for Al<sub>2</sub>O<sub>3</sub> deposition are significantly different than for Hf, Zr, La, and Y-based dielectrics because Al will tend to not form stable silicide structures, whereas the other metals of interest typically do form silicide bonds, which can act as kinetic intermediate to interface layer formation. Mixed metal/silicon/oxygen interface layers can result from reaction with hydroxides present in as-deposited films or introduced post-deposition from ambient exposure. Further understanding of interface elementary processes, including detailed differences between various precursors in how they adsorb and react, will be important to control interface structure for advanced gate stacks in high performance and low power MOS devices.

### **3.4 Acknowledgements**

The authors thank E. Garfunkel and B.W. Busch at Rutgers University for the MEIS results, D. Maher and S. Wang at NC State for TEM, and Israel Baumvol from Instituto de Fisica, Porto Alegre, for RNRA results. Support is from the SRC/SEMATECH Center for Front End Processes and NSF # 0072784.

### 3.5 References

- 1 S. I. Association, *The International Technology Roadmap for Semiconductors, 1999 edition* (Austin, TX, 1999).
- 2 M. Gurvitch, L. Manchanda, and J. M. Gibson, *Appl. Phys. Lett.* **51**, 919 (1987).
- 3 J. Shappir, A. Anis, and I. Pinsky, *IEEE Trans. Electron Devices* **33**, 442 (1986).
- 4 L. Manchanda, W. H. Lee, J. E. Bower, F. H. Baumann, W. L. Brown, C. J. Case, R. C. Keller, Y. O. Kim, E. J. Laskowski, M. D. Morris, R. L. Opila, P. J. Silverman, T. W. Sorsch, and G. R. Weber, *Tech. Dig. Int. Electron Devices Meet.*, 605 (1998).
- 5 G. D. Wilk, R. M. Wallace, and J. M. Anthony, *J. Appl. Phys.* **87**, 484 (2000).
- 6 K. J. Hubbard and D. G. Schlom, *J. Mater. Res.* **11**, 2757 (1996).
- 7 I. Barin, *Thermochemical Data of Pure Substances* (VCH Verlagsgesellschaft, Weinheim, Germany, 1989).
- 8 J. J. Chambers, B. W. Busch, W. H. Schulte, T. Gustafsson, E. Garfunkel, S. Wang, D. M. Maher, T. M. Klein, and G. N. Parsons, *Appl. Surf. Sci.* **181**, 78 (2001).
- 9 J. J. Chambers and G. N. Parsons, *J. Appl. Phys.* **90**, 918 (2001).
- 10 T. M. Klein, D. Niu, W. S. Epling, W. Li, D. M. Maher, C. C. Hobbs, R. I. Hegde, I. J. R. Baumvol, and G. N. Parsons, *Appl. Phys. Lett.* **75**, 4001 (1999).
- 11 N. Yang, W. K. Henson, J. R. Hauser, and J. J. Wortman, *IEEE Trans. Electron Devices* **46**, 1464 (1999).
- 12 J. F. Moulder, W. F. Stickle, P. E. Sobol, and K. D. Bomben, *Handbook of X-ray Photoelectron Spectroscopy* (Perkin-Elmer Corporation, Eden Prairie, MN, 1992).
- 13 R. Baptist, A. Pellissier, and G. Chauvet, *Solid State Commun.* **68**, 555 (1988).
- 14 G. Battistig, G. Amsel, I. Trimaille, J. J. Ganem, S. Rigo, F. C. Stedile, I. J. R. Baumvol, W. H. Schulte, and H. W. Becker, *Nucl. Instrum. Methods Phys. Res. Sect. B-Beam Interact. Mater. Atoms* **85**, 326 (1994).
- 15 D. Niu, R. W. Ashcraft, G. N. Parsons, and S. Stemmer, (to be submitted).
- 16 J. E. E. Baglin, F. M. Dheurle, and C. S. Petersson, *J. Appl. Phys.* **52**, 2841 (1981).
- 17 A. Pellissier, R. Baptist, and G. Chauvet, *Surf. Sci.* **210**, 99 (1989).
- 18 S. Q. Wang and J. W. Mayer, *J. Appl. Phys.* **64**, 4711 (1988).

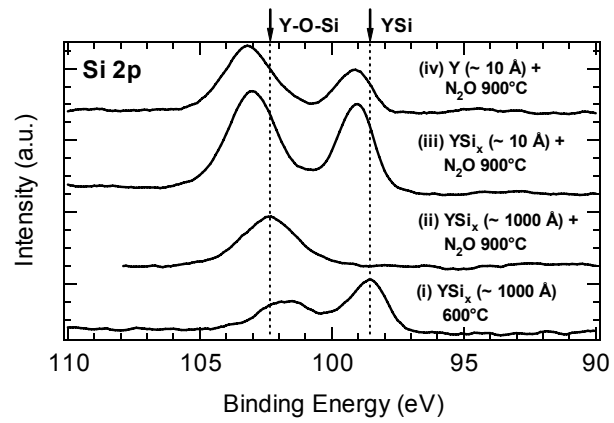


**Figure 3.1** XPS Si 2p spectra for various thicknesses of yttrium layers on Si(100) after various processes.

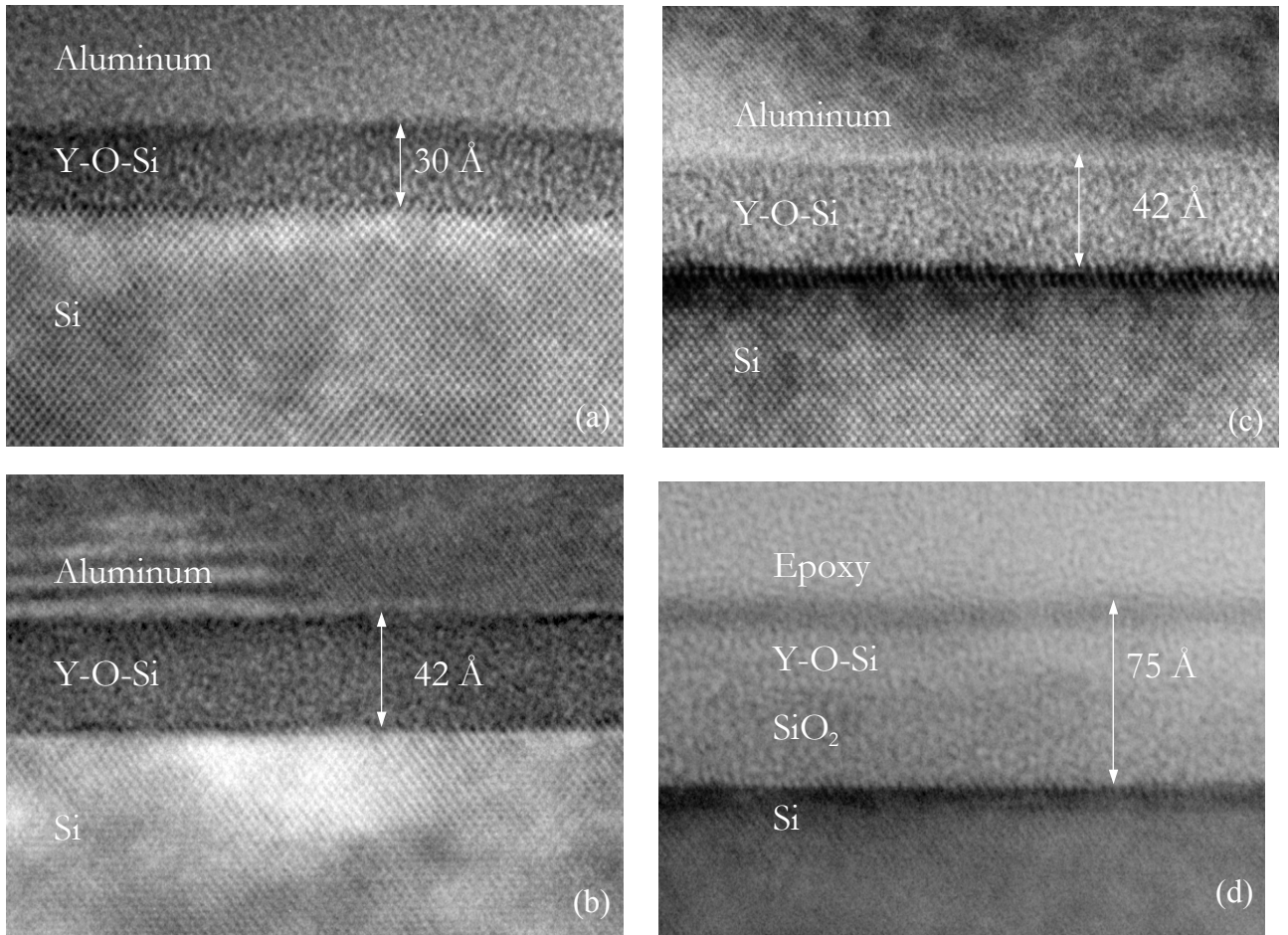


**Figure 3.2** TEM for four yttrium silicate films formed with  $\sim 8$  Å initial yttrium on silicon, followed by oxidation at 900°C for various times.

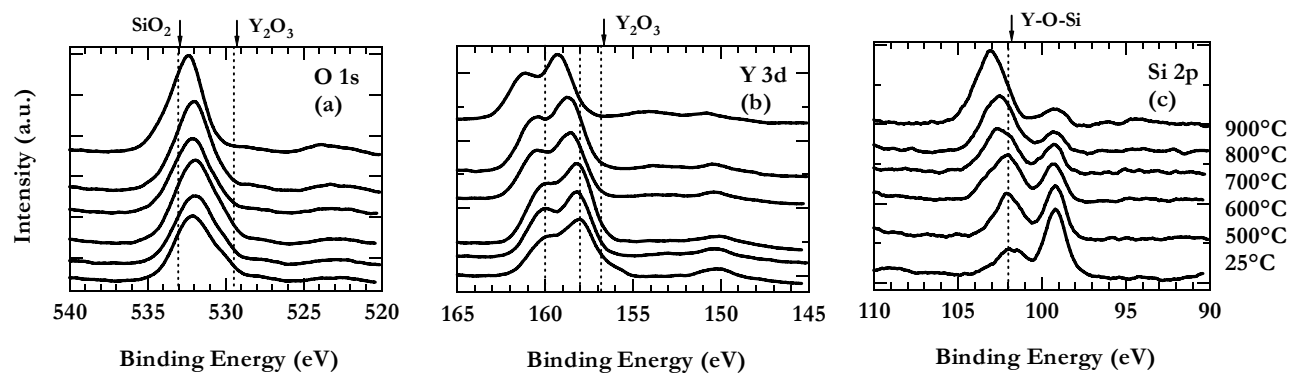


**Figure 3.3** XPS results for yttrium silicide films oxidized at various temperatures to form  $\text{Y}_2\text{O}_3/\text{SiO}_2$  films.

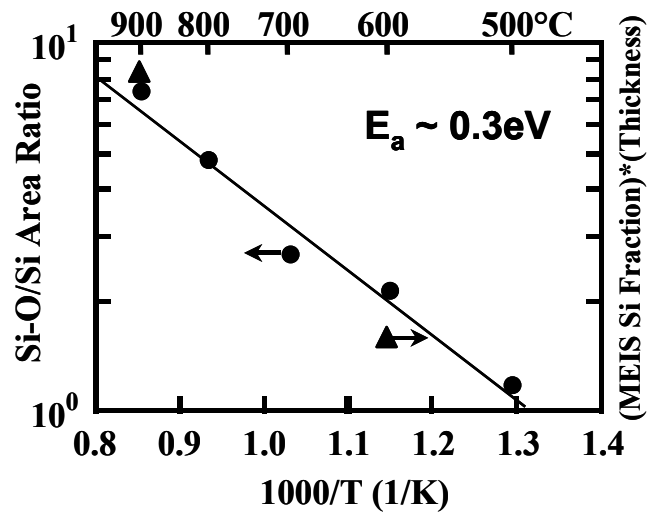


**Figure 3.4** Si-O/Si integrated area ratio determined from the Si 2p XPS data in Figure 3.3 vs. 1/T. The MEIS Si fraction is also plotted vs. inverse oxidation temperature.

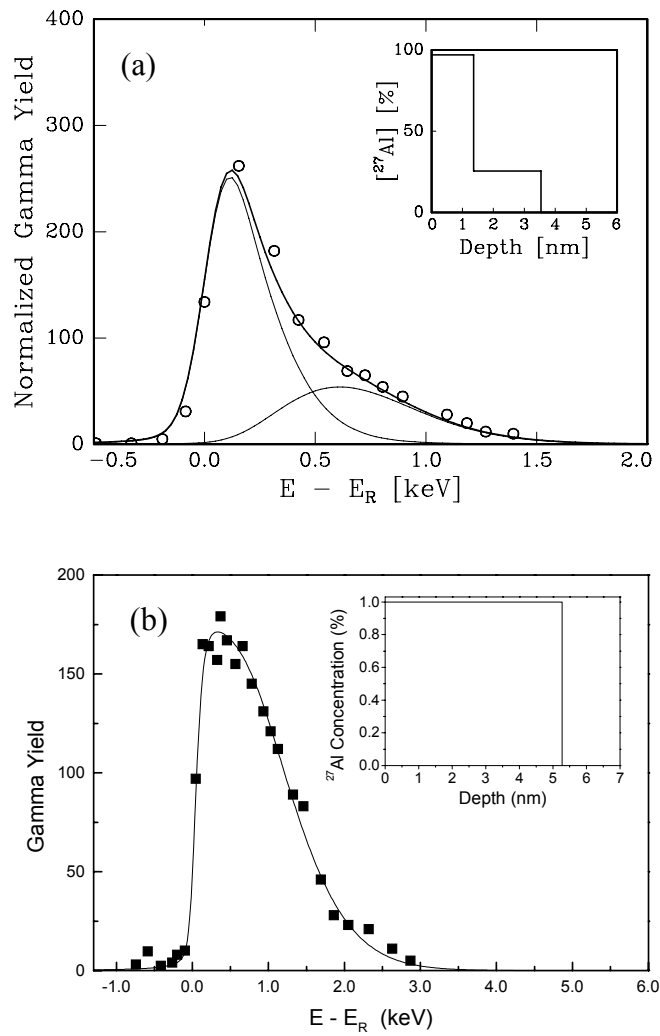


**Figure 3.5** Narrow Resonant Nuclear Reaction Profiles for two  $\text{Al}_2\text{O}_3$  films deposited on Si(100).

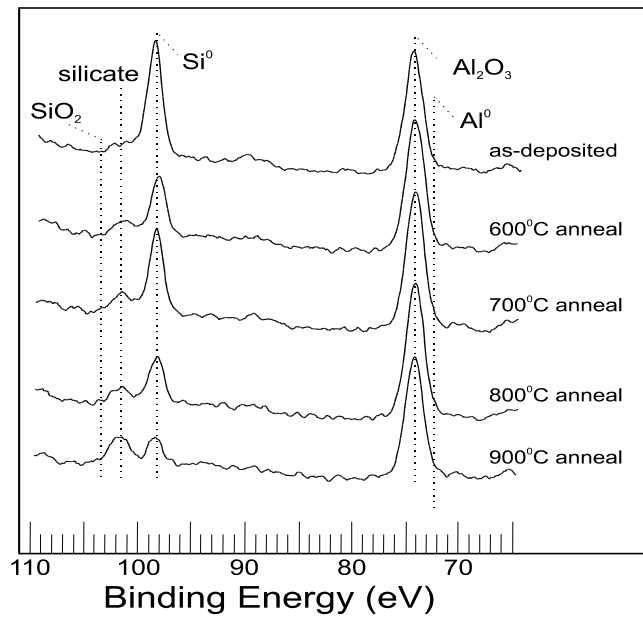


**Figure 3.6** XPS results for Al<sub>2</sub>O<sub>3</sub> films on Si(100) after anneals at various temperatures.

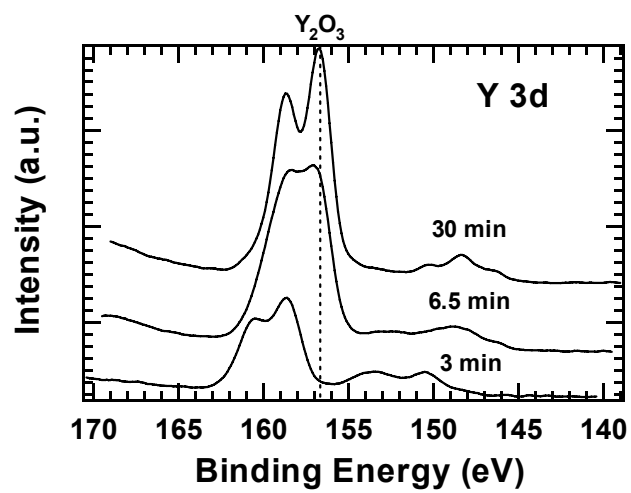


**Figure 3.7** XPS results for “ $Y_2O_3$ ” films deposited by CVD.

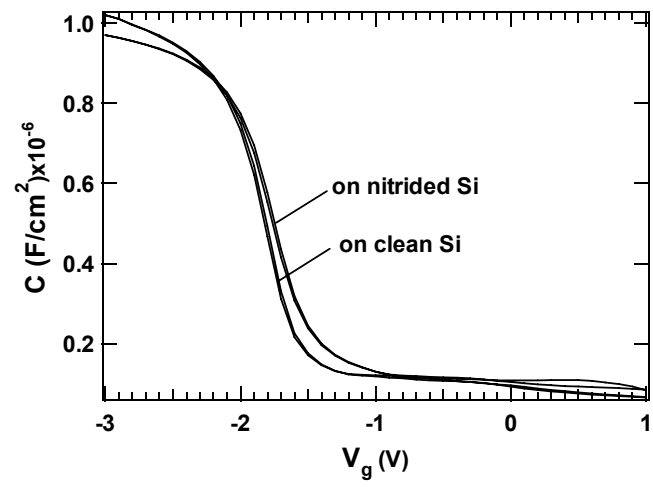


**Figure 3.8** CV results for thin films on clean and nitrated surfaces.

Chapter 4 is a reprint of a paper that appeared in Materials Research Society Symposium  
Proceedings Vol. 765, D3.4, proceedings of the MRS Spring Meeting, April 2003

## **Kinetics of Charge Generation During Formation of Hf And Zr Silicate Dielectrics**

Theodosia Gougousi, M. Jason Kelly, and Gregory N. Parsons  
Dept. of Chemical Engineering, NC State University, Raleigh, NC

### **Abstract**

Understanding charged defects in high dielectric constant insulators is a critical challenge for advanced devices. We have formed thin Zr and Hf silicates by oxidation of thin metal films sputtered on clean Si(100), and studied the effect of oxidation time (15 to 300s) and temperature (600 or 900°C) on the flatband voltage using capacitance vs. voltage measurements. We find that the thermal budget during oxidation and the type of oxidizing agent (slow vs. fast) affect the amount of fixed charge in the film significantly. Oxidation of 8Å of Zr metal on Si at 600°C in N<sub>2</sub>O for 15s results in EOT=12Å and a shift in the flatband voltage by ~-0.2V indicating generation of positive fixed charge. Oxidation of similar films for 300s result in EOT=28Å and shift of the flatband voltage by ~-0.95V. Hf films oxidized in N<sub>2</sub>O also show increased concentrations of fixed

charge for longer oxidation times. By comparison, Si oxidized in the same environment does not show this extent of flatband voltage shift. A significantly reduced charge generation rate is observed for Hf oxidation under low O<sub>2</sub> partial pressure. Extended oxidations (up to 1h) show minimal increase in EOT with a slight decrease in the charged defect state density. X-ray photoelectron spectroscopy indicates formation of Zr and Hf-silicates. However, for the Hf films the low O<sub>2</sub> oxidation process results in less silicon incorporation in the film as compared to films oxidized in N<sub>2</sub>O. Post metallization anneal (PMA) results in partial neutralization of the charge. PMA after the Al gate deposition also leads to significant decrease of the EOT (from 27 to 21Å) indicating significant reaction of the film with the gate metal. Results suggest that understanding oxidation mechanisms will be important in isolating and controlling fixed charge in high-k dielectrics.

### **Specific Contribution**

For this work, I was primarily responsible for XPS measurements and characterization. I was directly involved in planning the thickness series required for the analysis of charge generation kinetics and determining the conditions and procedures used to deposit the ultra-thin metals. I also worked closely with Theodosia to develop the proposed schemes for defect creation described in the discussion.

## **4 Kinetics of Charge Generation During Formation of Hf and Zr Silicate Dielectrics**

### **4.1 Introduction**

Approaching the tunneling limit for the SiO<sub>2</sub> gate dielectric in CMOS devices has fueled research for an alternative material with a higher dielectric constant that will permit the use of physically thicker films. Several prospective materials are currently under investigation, mainly oxides and silicates of group III and IV metals. Formation of low-k interfacial layers and significant concentration of fixed charge are two of the main misgivings of most of the materials investigated to date.<sup>1</sup> For some materials, fixed charge appears to be an intrinsic property and as such very hard to neutralize.<sup>2</sup> In other cases, though, significant concentrations of charged defects are generated as a result of processing conditions. Formation of interfacial layers and mixing of Si in the film are also shown to occur as a result of the deposition process.<sup>3</sup> In this article, we present our findings regarding the effect of the oxidation rate and thermal budget on the Si content and the amount of charge defects detected in ultra-thin Hf and Zr high-k films on Si.

### **4.2 Experimental**

We deposit 8-10Å of Hf or Zr metal films on cleaned Si(100) substrates using dc sputtering as described by Chambers.<sup>4</sup> After deposition of the metal, the films are oxidized ex-situ in a tube furnace at 600°C in the presence of N<sub>2</sub>O, which is known to cause rapid oxidation. Another set of metal films is oxidized using the impurity O<sub>2</sub> present in dry N<sub>2</sub> at atmospheric pressure, following the procedure initially described by

B. H. Lee et al.<sup>5</sup> As a control experiment, several clean silicon substrates are oxidized in N<sub>2</sub>O for 20 to 60 min which produces ~18 to 25Å of SiO<sub>2</sub>.

Metal-Insulator-Semiconductor capacitors are fabricated by resistive heating evaporation of Al through shadow masks. Capacitance vs. voltage (CV) measurements are performed with a HP4284 impedance meter at 1MHz and 100KHz. Capacitor surface areas (typically  $4 \times 10^{-4} \text{cm}^2$ ) are determined by digital photography. The NCSU program that corrects for quantum mechanical effects is used to obtain the Equivalent Oxide Thickness (EOT) and the position of the flatband voltage. For each sample the CV characteristics for several capacitors are measured and the results are averaged. Compositional analysis of the samples is performed with a Riber LAS3000 (MAC2 analyzer, Mg K $\alpha$  ( $h\nu=1253.6 \text{ eV}$ ) non-monochromatic X-ray source) at 75° take-off-angle with 0.1eV step size. We compensate for sample charge effects by setting the adventitious C 1s peak to a binding energy of 285.0eV.

### **4.3 Results and Discussion**

Figure 4.4a shows the C-V curves for 8Å Zr films oxidized in N<sub>2</sub>O at 600°C for 15 to 300s. Figures 4.1b and 4.1c present the flatband voltage ( $V_{\text{FB}}$ ) and the equivalent oxide thickness (EOT) as a function of the oxidation time respectively. The data points represent the average of measurements on several capacitors of the same sample and the error bars represent one standard deviation. If no error bar is shown, the size of the error bar is equal to (or less than) the size of the data point symbol. The expected position of  $V_{\text{FB}}$ , calculated from the work function of the Al gate and the doping of the Si substrate is ~0V. We find that an increase in the oxidation times leads to smaller capacitances and at the same time the C-V curve is shifted to more negative. The EOT more than doubles,

from  $\sim 12\text{\AA}$  for 15s oxidation to  $28\text{\AA}$  for 300s oxidation due to the formation of a thick interfacial layer. The flatband voltage shifts from  $\sim -0.25\text{V}$  for the 15s process to  $\sim -0.95\text{V}$  for the 300s process, indicating the generation of substantial amounts of positive fixed charge in the film.

Si 2p, Zr 3d and O 1s XP spectra for the Zr samples are shown in Fig. 4.2. The location and width of the Si 2p peak at  $\sim 102.5\text{eV}$ , O 1s peak at  $\sim 532\text{eV}$  suggest that the films are silicates<sup>6,7</sup> with  $\text{SiO}_2$  at the interface. The ratio of the  $\text{ZrSiO}_x/\text{SiO}_2$  to the substrate  $\text{Si}^0$  peak areas increases with oxidation indicating the formation of an interfacial layer. The  $\text{Si}^0$  peak is detected for all samples and appears at a lower binding energy than expected. Opila et al. have reported and explained the relationship between fixed charge and the position of the  $\text{Si}^0$  peak in XP spectra for Hf and Zr silicate films.<sup>8</sup> The shift in  $\text{Si}^0$  peak in our films can be explained by the existence of fixed charge in the layers that the substrate photoelectrons have to transverse.

Figure 4.3a shows the C-V curves for  $8\text{\AA}$  Hf-metal films oxidized in  $\text{N}_2\text{O}$  at  $600^\circ\text{C}$  for 30 to 300s. In general, we find that an increase in the oxidation times leads to smaller capacitances (i.e. thicker interface layers) but the shape and position of the curve remains practically unchanged for oxidation up to 120s. For the sample oxidized for 300s we observe a reduction in the capacitance and a significant shift of the curve to more negative voltage. Figure 4.4b is a plot of the C-V curves for  $8\text{\AA}$  Hf films oxidized in the  $\text{N}_2$  ambient for 45, 90 and 300s. The capacitance of the gate stack decreases with longer oxidation, but the rate of decline is significantly slower than for  $\text{N}_2\text{O}$  oxidation, and the position of the curve is not significantly affected.

Figure 4.4a presents the equivalent oxide thickness (EOT) as a function of the oxidation time for the N<sub>2</sub>, N<sub>2</sub>O process, and the control SiO<sub>2</sub> films. For oxidation in N<sub>2</sub>O (circles), the EOT increases by almost a factor of two, from ~14Å for 30s oxidation to 26Å for 300s oxidation. The N<sub>2</sub> process (squares) results in negligible increase in the EOT from 15Å to ~16Å for oxidation between 15 and 300s, and increases substantially to ~23Å for a 1h oxidation. The EOT for the control SiO<sub>2</sub> film data (triangles) oxidized in N<sub>2</sub>O varies between 16 and 22Å, comparable in thickness to the interfacial layer produced during N<sub>2</sub>O oxidation of Hf-metal films. The SiO<sub>2</sub> data exhibit significant scattering, which is probably due to the poor quality of SiO<sub>2</sub> produced with this technique. On Fig. 4.4b we present the flatband voltage (V<sub>FB</sub>) vs. duration of oxidation for N<sub>2</sub>O (circles), N<sub>2</sub> (squares) ambient, and control SiO<sub>2</sub> films (triangles). For the N<sub>2</sub> process, prolonged exposure leads to marginal reduction in the V<sub>FB</sub> from ~-0.375 to -0.3V. For the N<sub>2</sub>O process, the V<sub>FB</sub> is comparable to that for the N<sub>2</sub> process and remains almost constant at -0.35V for oxidations up to 120s. For 300s, though, V<sub>FB</sub> becomes substantially more negative. For the control SiO<sub>2</sub> films V<sub>FB</sub> decreases somewhat for longer oxidation times, tracking fairly well the trend exhibited by the N<sub>2</sub> process.

Si 2p XP spectra for some of the samples are shown in Fig. 4.5. The substrate peak Si<sup>0</sup> can be detected for all samples and the peak at ~102.5eV suggests that the films are silicates<sup>6,7</sup> with some SiO<sub>2</sub> at the interface. For the samples (a) and (b) oxidized in N<sub>2</sub>O for 30 and 90s respectively, the ratio of the HfSiO<sub>x</sub>/SiO<sub>2</sub> to the Si<sup>0</sup> peak areas is approximately the same and less than 1. However, for sample (c) oxidized in N<sub>2</sub>O for 300s we observe a substantial increase in the HfSiO<sub>x</sub>/SiO<sub>2</sub> peak area. The spectrum for the sample (d) oxidized for 300s in N<sub>2</sub> is comparable to spectrum (a) oxidized for 30

seconds in N<sub>2</sub>O. The Si<sup>0</sup> peaks appear at a lower binding energy than expected corroborating similar observations for the Zr-based films. Based on the electrical and the XPS data for both the Hf and Zr films we can conclude that the increase in the EOT results from an increase in the thickness of the SiO<sub>2</sub> interfacial layer. In general, it is believed that SiO<sub>2</sub> leads to a better quality silicon interface than metal oxide. For N<sub>2</sub>O oxidation we find that rapid oxidation of the interface is accompanied by trapping of charge in both the Hf and Zr films. The data indicate that the growth rate of the interfacial layer correlates with the amount of charge generated in the film. For the Zr-based films, there is a linear relationship between the flatband voltage and the EOT (figure not shown) indicating a relationship between the interface layer thickness and the amount of charge generated in the film. The Hf-based films appear more resistant to the generation of charged defects. For oxidation times in N<sub>2</sub>O up to 120s there is no substantial effect. However, oxidation in N<sub>2</sub>O at 600°C in for 300s results to the growth of ~13 and ~18Å of interfacial SiO<sub>2</sub> and a substantial shift of the flatband voltage. For the control samples, growth of 16-22Å of SiO<sub>2</sub> on Si in N<sub>2</sub>O in 20-60 min leads to significantly lower trapped charge. For the Hf samples oxidized in O-deficient environment growth of 7Å of interfacial SiO<sub>2</sub> at 600°C in 1h results in marginal reduction in the amount of charge in the film. It appears that the defect generation mechanism involves participation of the metal atoms. High growth rate of the interfacial layer facilitates trapping of hetero-atoms near the interface. Where the covalent SiO<sub>2</sub> network is disrupted by the introduction of ionic bonding due to the metal atom, defects are generated. This mechanism may cause the difference in the film quality observed for

fast vs. slow oxidation. It is not clear, though, why there is difference in the quality of the Hf and Zr films oxidized in  $N_2O$ .

Generation of positive fixed charge has been observed during postdeposition reoxidation of  $ZrO_2/SiO_2$  gate stacks formed by atomic layer deposition, and the fixed charge has been attributed to formation of overcoordinated O center induced by a large density of H atoms originating from the  $H_2O$  precursor.<sup>9</sup> Our process is  $H_2O$  free, and IR measurements on thick samples do not show any appreciable absorption of  $H_2O$  even after long ambient exposures.<sup>10</sup> Clearly, more detailed experiments are required to trace the origin of this type of charge.

For the Hf-based samples forming-gas-anneal (10% $H_2$  in  $N_2$  for 30min at 400°C) results in partial neutralization of the charges when performed before metallization, and almost complete removal after Al deposition. In the latter case, however, neutralization of the charge is accompanied by significant increase in the gate capacitance indicative of reaction at the dielectric-gate metal interface. FGA performed on Zr samples after the deposition of the Al gate also indicates significant reaction of the film with the gate metal. While forming gas anneal may remove part of these defects, from a reliability standpoint it is desirable to avoid introducing the charges in the first place, as further thermal treatment and stress on the device may lead to desorption of the H-atoms and regeneration of the defects, which will deteriorate carrier mobility in devices significantly.

Finally, we examined the effect of the oxidizing agent on the film composition. On Fig. 4.7 we display the Si 2p XP spectra for two similar thick ( $>500\text{\AA}$ ) Hf-metal films, one oxidized in  $N_2O$  and the other oxidized in  $N_2$ . We observe that for the film oxidized

in N<sub>2</sub>O there is a peak at ~102eV indicative of silicate bonding in the film. For the film oxidized at low O<sub>2</sub> partial pressure this spectral region is practically flat. The O 1s and Hf 4d spectra are consistent with formation of a top HfO<sub>2</sub> layer. It appears that fast oxidation of a Hf-metal film results not only in significant oxidation of the dielectric/Si interface but also promotes Si incorporation in the bulk of the film. These findings are consistent with observations reported by Rangarajan et al.<sup>11</sup> for CVD Hf-based high-k films.

#### **4.4 Acknowledgements**

Financial support from SRC and NSF 00-72784 is gratefully acknowledged.

#### **4.5 References**

- 1 G.D. Wilk, R.M. Wallace and J.M. Anthony, *J. Appl. Phys.* **89**(10), 5243 (2001) and references therein.
- 2 M. Copel, E. Cartier, and F.M. Ross, *Appl. Phys. Lett.* **78**(11), 1607 (2001)
- 3 D. Niu, R.W. Ashcraft, M.J. Kelly, J.J. Chambers, T.M. Klein, and G.N. Parsons, *J. Appl. Phys.* **91**(9) (2002)
- 4 J.J. Chambers and G.N. Parsons, *J. Appl. Phys.* **90** (2), 918 (2001)
- 5 B.H. Lee, L. Kang, R. Nieh, W.J. Qi, and J.C. Lee, *Appl. Phys. Lett.* **76** (14), 1926 (2000)
- 6 Y. Hoshino, Y. Kido, K. Yamamoto, S. Hayashi, and M. Niwa, *Appl. Phys. Lett.* **81** (14) 2659 (2002)
- 7 P.D. Kirsch, C.S. Kang, J. Lozano, J.C. Lee, and J.G. Ekerdt, *J. Appl. Phys.* **91** (7), 4353 (2002)

- 8 R.L. Opila, G.D. Wilk, M.A. Alam, R.B. van Dover, and B.W. Busch, *Appl. Phys. Lett.* **81** (10), 1788 (2002)
- 9 M. Houssa, V.V. Afanas'ev, A. Stesmans, and M.M. Heyns, *Appl. Phys. Lett.* **77** (12), 1885 (2000)
- 10 T. Gougousi, and G.N. Parsons, in preparation.
- 11 V. Rangarajan, H. Bhandari, and T.M. Klein, *Thin Sol. Films*, **419**, 1 (2002)

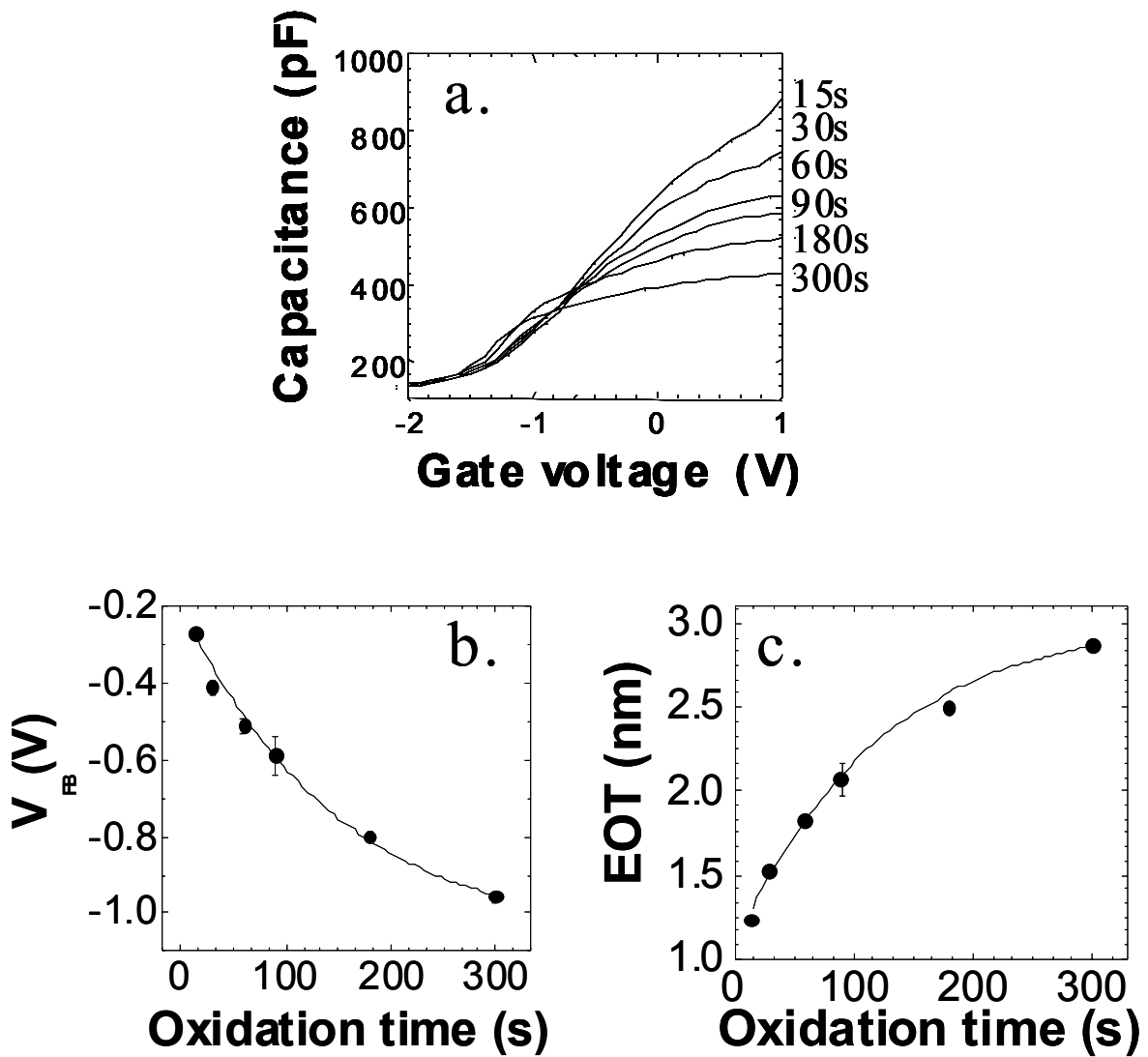


**Figure 4.1** Capacitance vs. Voltage curves (Fig. 4.1a) for 8Å Zr-metal films oxidized in N<sub>2</sub>O with Al gates as a function of oxidation time (legend). The flatband voltage ( $V_{FB}$ ) (Fig. 4.1b) and EOT (Fig. 4.1c) vs oxidation time plots show that extended oxidation results in oxidation of the interface that is accompanied by generation of positive fixed charge in the film.

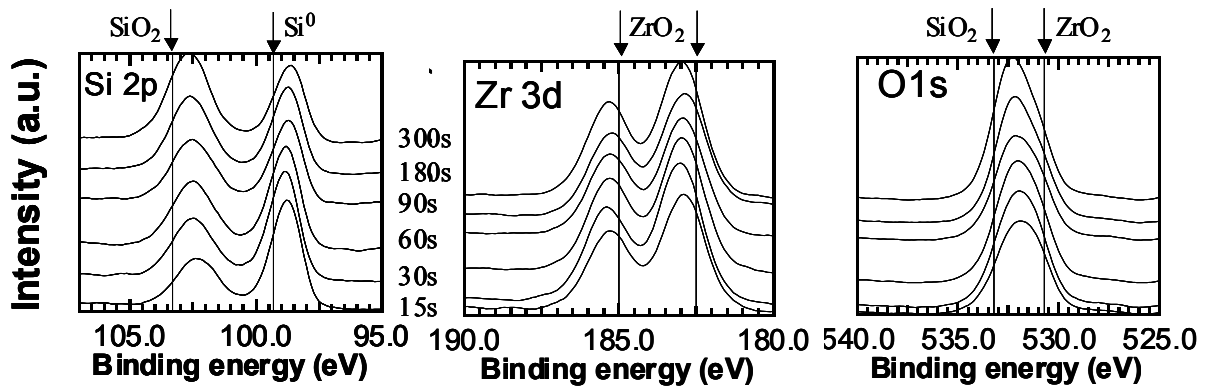


**Figure 4.2** Si 2p, Zr 3d, and O 1s XP spectra for 8Å Zr metal films on Si oxidized at 600°C in N<sub>2</sub>O. The oxidation time is given in the legend. The film is ZrSiO with a substantial SiO<sub>2</sub> interfacial layer.

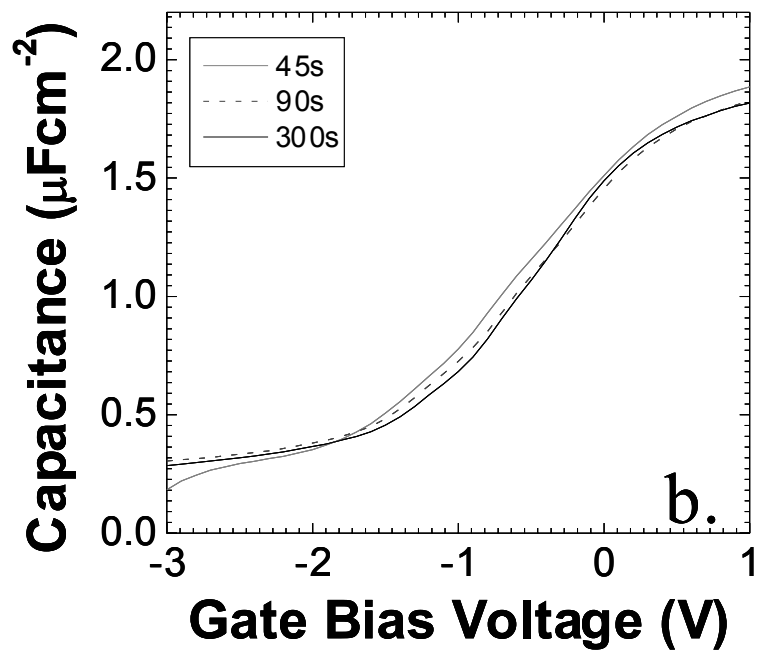
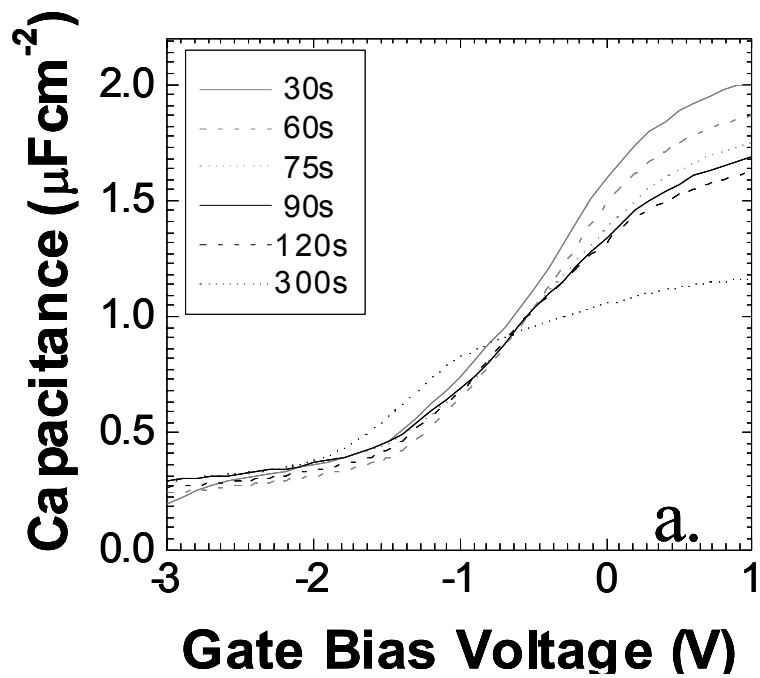


**Figure 4.3** Capacitance vs. Voltage measurements for 8Å Hf-metal films oxidized in  $\text{N}_2\text{O}$  (Fig. 4.3a) and  $\text{N}_2$  (Fig. 4.3b) with Al gates as a function of oxidation time (legend).

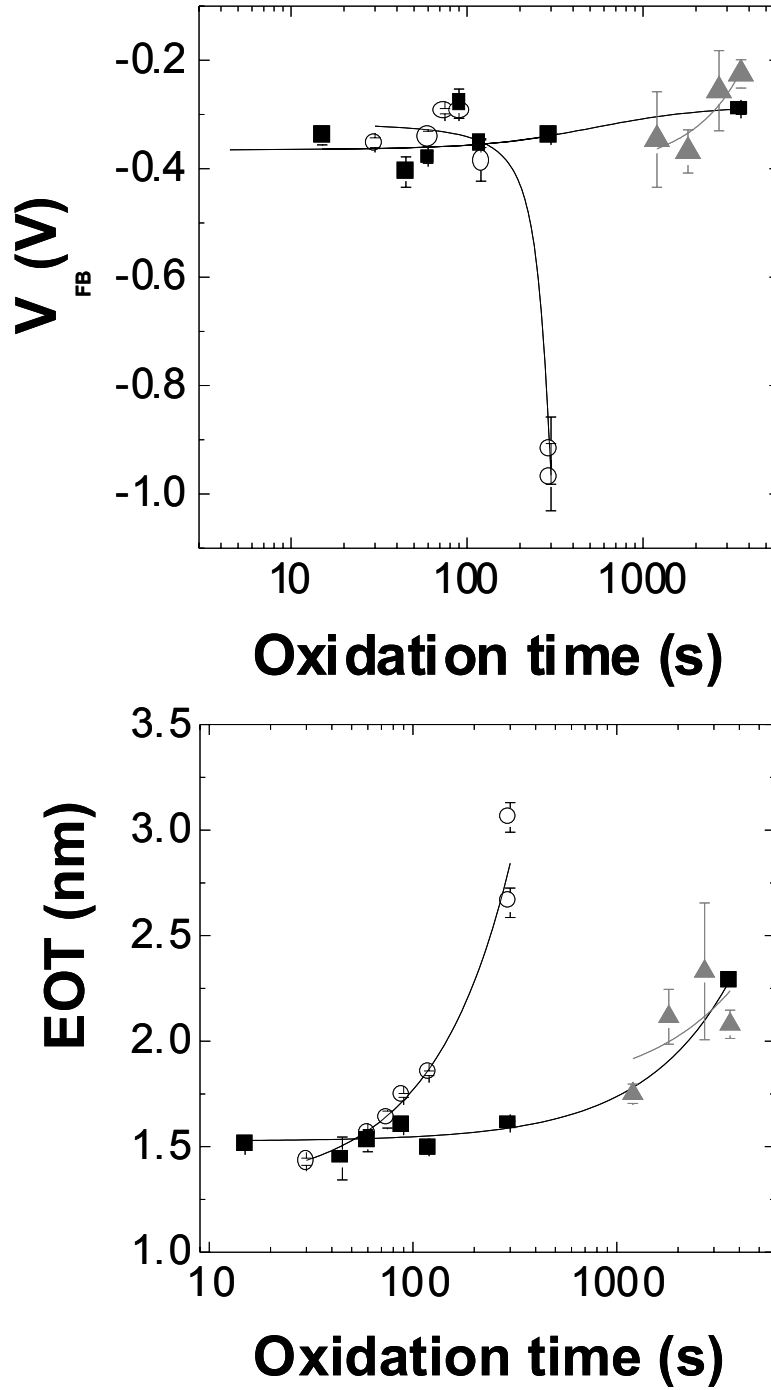


**Figure 4.4** Equivalent Oxide Thickness (EOT) and flatband voltage  $V_{FB}$  vs. oxidation time for 8Å Hf-metal films oxidized in N<sub>2</sub> (squares) and N<sub>2</sub>O (circles), and for H-terminated Si oxidized in N<sub>2</sub>O (triangles).

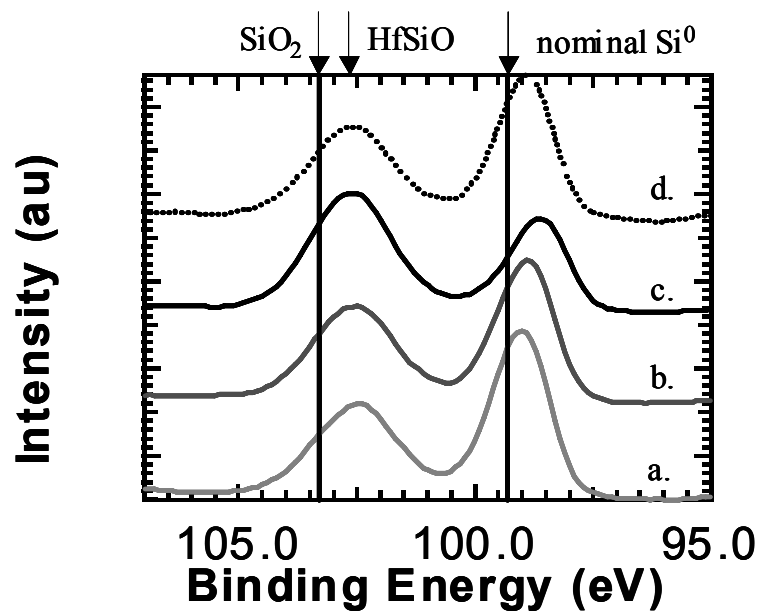


**Figure 4.5** XPS spectra for 8Å Hf-metal films oxidized in N<sub>2</sub>O for (a) 30s, (b) 90s, (c) 300s, and (d) N<sub>2</sub> for 300s. Spectra (a), (b) and (d) are practically identical and correspond to samples with comparable electrical properties. The HfSiO/SiO<sub>2</sub> peak is enhanced in spectrum (c), result of the fast interface oxidation achieved in N<sub>2</sub>O.

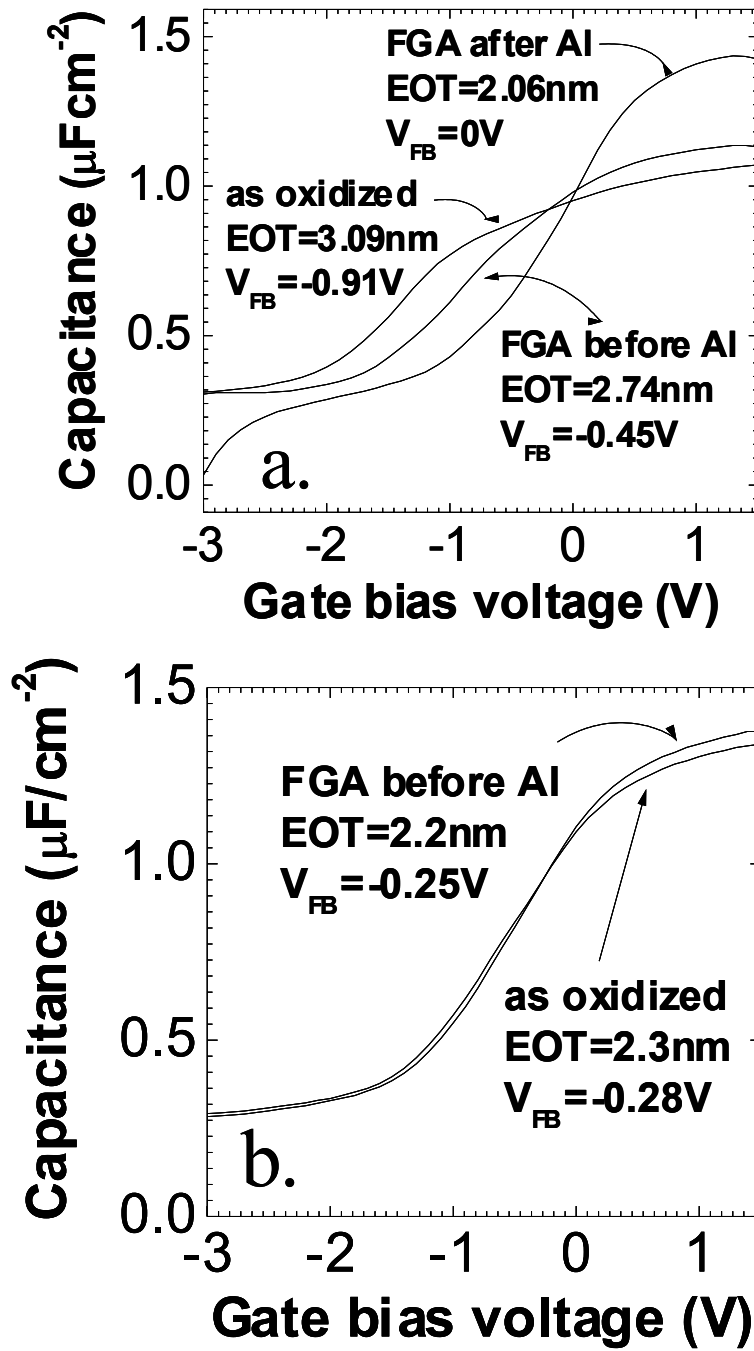


**Figure 4.6** The effect of FGA on the CV curves of Hf films oxidized in  $\text{N}_2\text{O}$  (a) and  $\text{N}_2$  (b).

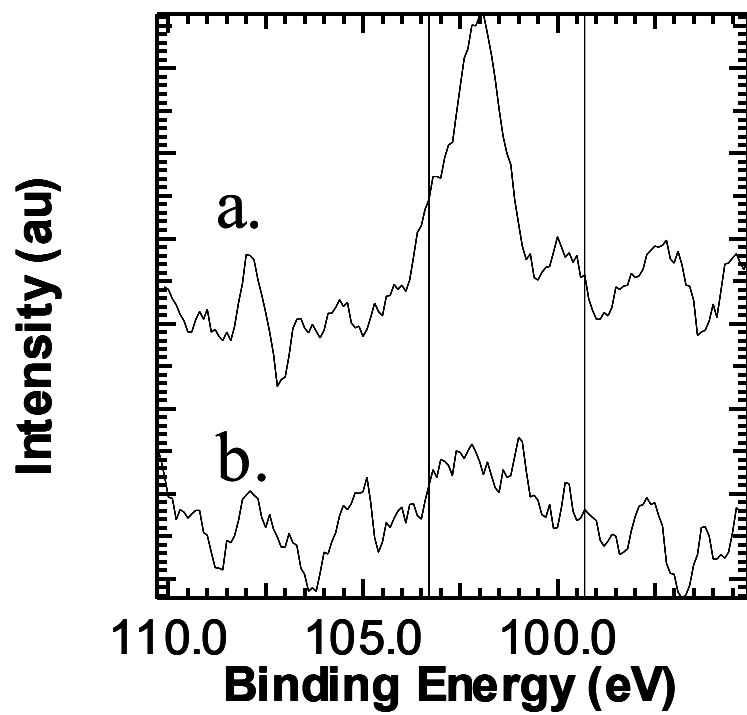


**Figure 4.7** Si 2p XP spectra for 450Å Hf-metal films oxidized in (a) N<sub>2</sub>O and (b) N<sub>2</sub>.

The film oxidized in N<sub>2</sub>O shows Si incorporation in the film.

Chapter 5 is a reprint of a paper that appeared on pages 1691 – 1696 of the  
Journal of Applied Physics, Volume 93, Issue 3, in 2003

## **Properties of La-Silicate High-k Dielectric Films Formed by Oxidation of La on Silicon**

Theodosia Gougousi, M. Jason Kelly, David B. Terry, and Gregory N. Parsons  
Department of Chemical Engineering, North Carolina State University

### **Abstract**

In this article we present data on the properties of La-based high-k dielectric films prepared by oxidation of La deposited by physical vapor deposition on silicon. Films are characterized by X-ray photoelectron spectroscopy, infrared absorption, and capacitance vs. voltage analysis. We find that when we oxidize La metal sputter deposited on Si substrates, it reacts with the silicon substrate to form La-silicate. La films as thick as 300Å will react completely with Si under moderate oxidation conditions (900°C for 10 min) suggesting a very rapid silicidation reaction between La and Si. Under some processing conditions the as-deposited films contain a small La<sub>2</sub>O<sub>3</sub> component that reduces to La-silicate upon anneal at high temperatures. La-silicate films do not phase separate into La<sub>2</sub>O<sub>3</sub> and SiO<sub>2</sub> upon annealing at 1050°C, and their resistance to H<sub>2</sub>O incorporation depends critically on the oxidation temperature. Electrical measurements show a high concentration of positive fixed charge.

## Specific Contribution

In this work, I participated in several different aspects of the investigation. Theodosia and I designed the experimental details required to map out the compositional range of  $\text{La}_2\text{O}_3$ - $\text{SiO}_2$  pseudo-binary alloys formable by oxidizing metallic La films on silicon. These deposition experiments were performed by Theodosia as I trained her on the dc sputter deposition apparatus. I evaporated aluminum to make metal-insulator-semiconductor capacitors, and I performed some of the electrical and x-ray photoelectron spectroscopy measurements. Theodosia and I discussed the interpretation of the x-ray photoelectron spectra and electrical data, and we collaborated to develop a mechanism to interpret the IR results. In particular, we found that the La-based high-k films produced for this study tended to react with atmospheric gases, resulting in OH and CO stretching modes in the infrared transmission spectra. A key contribution was my specific suggestion that  $\text{La}_2\text{O}_3$  likely incorporates  $\text{H}_2\text{O}$  into its lattice to form stable hydrates, and therefore the films are expected to be extremely hygroscopic. I also suggested that  $\text{La}_2\text{O}_3$  could react with atmospheric  $\text{CO}_2$  to explain the features just below  $1500\text{cm}^{-1}$ , and this was subsequently supported by other cited literature results.

## 5 Properties of La-Silicate High-k Dielectric Films Formed by Oxidation of La on Silicon

### 5.1 Introduction

Continuing miniaturization of the CMOS devices has resulted in the need for a new higher dielectric constant material to replace SiO<sub>2</sub> as the gate dielectric.<sup>1</sup> Several such high-k materials, mainly oxides and silicates of group III and IV metals, are currently under investigation.<sup>2,3</sup> Most of the attention has focused on materials that are reported to be stable in contact with silicon.<sup>4</sup> These thermodynamic calculations apply strictly to the metal oxide and silicon in contact at equilibrium conditions. In reality, physical and chemical deposition processes are inherently non-equilibrium and involve many potential reactions that are not taken into account by purely thermodynamic considerations. Interaction between deposition precursors, reaction intermediates, and/or the substrate can lead to the formation of interfacial layers, which may be SiO<sub>2</sub>, a silicate, or both. For dielectrics derived from Y, a group III metal, it has been found that a rapid silicidation reaction competes with the oxidation process and leads to the formation of multiple layer stacks consisting of SiO<sub>2</sub>/YSiO/Y<sub>2</sub>O<sub>3</sub> in both Physical Vapor Deposition (PVD)<sup>5</sup> and Chemical Vapor Deposition<sup>6</sup> (CVD) dielectrics. The oxide of La, another group III metal, is predicted to be stable in contact with Si. However, several recent studies report preferential formation of La-silicate materials over the oxide due to a very efficient mechanism for Si diffusion in La-metal and/or La oxide.<sup>7,8</sup> In this article we report the composition, stability, and electrical properties of La based high-k materials prepared by oxidation of thin La films sputter deposited on Si surfaces. We study the effect of

substrate pretreatment on La and Si reactivity and, additionally, we investigate the role of the oxidation temperature on the film's propensity to absorb H<sub>2</sub>O from the ambient.

## **5.2 Experimental**

We have prepared La-based high-k films by plasma assisted DC sputtering of La metal on H-terminated Si(100) substrates and ex-situ furnace oxidation in the presence of N<sub>2</sub>O as described by Chambers et al.<sup>5,9</sup> The H-terminated Si (100) substrates were prepared by J T Baker 100 Clean dip for 5 min, deionized water (DI) rinse for 5 min and Buffered Oxide Etch (BOE) dip for 1min. They were subsequently blown dry with dry nitrogen and placed in the loadlock of the deposition system. Nitrided Si substrates were prepared by in-situ exposure of the H-terminated Si to N<sub>2</sub> plasma at 300°C and 50mtorr for 20 min. This procedure results in ~10 Å of nitride.

The La metal target was purchased from ESPI metals and was 99.9% pure. The films described in Section 5.3.3 were deposited in a different PVD system equipped with magnetron sputtering and a La target from Target Materials with a purity of 99.9%; Oxidation was performed in dry air in a Rapid Thermal Annealing furnace.

Metal film thickness was calculated from a calibration curve obtained by ex situ step height measurements performed with a Tencor S profilometer. Steps were prepared by partially covering Si substrates with a glass slide during deposition. This calibration should be regarded as an upper limit to the metal film thickness since La undergoes oxidation when exposed to moisture and oxygen. Films exposed to air for over a day gained significant (at least 50%) thickness indicating that they were only partially oxidized during the initial step height measurements.

Characterization of the film composition was performed by X-ray Photoelectron Spectroscopy (XPS) and Infrared spectroscopy (IR). A Riber LAS3000 instrument equipped with a single-pass, cylindrical mirror (MAC2) analyzer and a Mg K $\alpha$  ( $h\nu=1253.6$  eV), non-monochromatic X-ray source was used at a 90° take-off angle with 0.1 eV step size to obtain the XP spectra. Charge compensation was performed by setting the adventitious C 1s peak to a binding energy of 286.0 eV. Fourier Transform Infrared (FTIR) transmission spectra were obtained using a Magna-IR System 750 from ThermoNicolet. All spectra were corrected by subtracting the FTIR spectrum of a plain Si substrate. High resistivity, double polished Si substrates were used for that part of the study.

Metal-Insulator-Semiconductor (MIS) capacitors were fabricated via shadow mask deposition of evaporated Al (2000Å). The electrical properties of the films were investigated by Capacitance vs. Voltage (C-V) measurements using an HP4284 LCR. All C-V measurements, unless otherwise stated, were performed at a frequency of 1MHz and scanned from depletion to accumulation. A Nikon Eclipse Optical Microscope equipped with a digital camera was used to photograph selected capacitors. The digital images were then processed using ImageJ<sup>10</sup> to obtain the capacitor area, which was typically  $3.5 \times 10^{-4} \text{cm}^2$ . Capacitors with small areas were selected for the measurements so as to avoid instrumental errors associated with measuring large capacitances. The C-V data were analyzed using the NCSU CV Program<sup>11</sup> to obtain the Equivalent Oxide Thickness (EOT), and flat band voltage.

## 5.3 Results and Discussion

### 5.3.1 Composition of La containing dielectrics formed on clean

#### H-terminated Si(100)

La-metal films with thicknesses from 15 to 330 Å were deposited on H terminated Si (100) substrates and oxidized ex-situ at 900°C in N<sub>2</sub>O (5slpm) at atmospheric pressure for times ranging from 30s to 10 min and equal to the duration of the deposition. X-ray Photoelectron spectroscopy was then used to analyze the surface composition (top ~50 Å) of the films, and the spectral regions containing the Si 2p/La 4d, O 1s, and La 3d peaks are displayed on Figure 5.1. The thicknesses given correspond to the original thickness of the metal deposited. The resulting dielectric film thickness is approximately twice the original metal thickness. For the thinner films, we were able to probe the Si-dielectric interface and detect the substrate Si<sup>0</sup> peak<sup>12</sup> at 99.3 V in the Si 2p spectra. The absence of silicide peaks is consistent with the selected oxidation conditions. The spectral region around the Si 2p peaks (Figure 5.1a) also contains contributions from the La 4d peaks<sup>13</sup> at 101.9eV and 105.5eV that overlap with the SiO<sub>2</sub> peak expected at 103.3eV.<sup>12</sup> No attempts were made to deconvolve the peaks.

For the O 1s spectra in Figure 5.1b we can observe a clear transition from a double to a single peak as the film thickness increases. The shoulder at ~533.0 eV is clearly visible for the thinnest (15 Å of La metal) film and indicates the presence of a SiO<sub>2</sub> interfacial layer.<sup>12</sup> As the film thickness increases and we lose the ability to probe the interface, the O 1s spectra exhibit a single peak at ~531.8eV. This peak lies between the SiO<sub>2</sub> and La<sub>2</sub>O<sub>3</sub> peaks at 533.3 and 529.9eV<sup>13</sup> respectively, consistent with the formation of La-O-Si silicate bonding units. For the thinnest film, the peak position is marginally

shifted to higher binding energy indicating the presence of a more Si-rich silicate layer close to the interface. The O 1s XPS data (not shown) from significantly thicker films (2500Å of La metal oxidized at 900°C for 2 min) showed features similar to the thickest films in Figure 5.1b and consistent with silicate bonding. The La 4d and La 3d spectra in Figures 5.1a and 5.1c are also consistent with silicate composition for all thicknesses studied. The La 3d and La 4d features shift slightly to lower binding energy as the film thickness increases suggesting a higher La fraction in the thicker films. However, this shift is very slight with the largest changes occurring between 15 and 25Å.

The O 1s and La 3d peak positions remain practically unchanged with film thickness implying that the diffusion of Si atoms into the La metal film proceeds very rapidly at the temperatures studied and the silicidation reaction may proceed at a faster rate than the oxidation. Mixing of La with Si probably occurs even during the metal film deposition at room temperature, and exposure to the oxidizing ambient at high temperature increases the La and Si mobility. These results are consistent with a mechanism in which La silicide is formed, and subsequently as oxidants diffuse through the film it oxidizes to form La-silicate, and interfacial SiO<sub>2</sub>. Such a mechanism is consistent with previous studies<sup>14,15</sup> that report fairly rapid intermixing of Si and La layers even at temperatures as low as 150°C. However, we acknowledge that our results could also be explained by rapid Si diffusion in La<sub>2</sub>O<sub>3</sub> films as observed recently both for Metalorganic Chemical Vapor Deposition<sup>7</sup> and e-beam evaporated oxide films.<sup>8</sup>

These findings share some common features with previous observations regarding Y-based films formed in similar manner. Chambers et al.<sup>5</sup> found that competition between two reactions, silicidation at the bottom of the deposited metal and oxidation at

the top, resulted in two regimes for growth. For thin, Y films, the Si/Y mixing was sufficiently fast to form a single layer having silicate composition as observed in our lanthanum studies. However, a second regime was identified for relatively thicker films ( $>80\text{\AA}$ ) in which competition between silicidation and oxidation resulted in the formation of a  $\text{SiO}_2/\text{YSiO}/\text{Y}_2\text{O}_3$  layered structure. This second regime was never identified in our work, and the difference is quite interesting since both Y and La are group III metals and may be expected to have similar chemical properties. An IR study of the interfacial reactions between rare-earth-metal oxides and Si substrates by Ono et al.<sup>16</sup> found that the fraction of silicate bonding increases with the ionic radius of the rare earth element. Larger atoms, in general, leave more free space for Si diffusion. The extent of silicate formation for PVD Y- and La- based dielectrics corroborates the conclusion that enhanced Si diffusivity in the lanthanum system is a key factor that controls whether the oxide or silicate of the metal is preferentially formed.

### **5.3.2 Effect of substrate on the film composition**

We analyzed the composition of thick films ( $170\text{\AA}$  metal) deposited on various substrates, and results are shown in Figure 5.2. Figures 5.2a and 5.2b show O 1s and La 3d XP spectra respectively for three films:  $170\text{\AA}$  of La metal oxidized at  $900^\circ\text{C}$  for 5 min in  $\text{N}_2\text{O}$  deposited on i) H-terminated Si(100); ii) in-situ plasma nitrided Si(100); and iii)  $1000\text{\AA}$  of thermal  $\text{SiO}_2$ . The O 1s spectra for samples (i) and (ii) are practically identical and are consistent with La-silicate formation. Sample (iii), formed on  $1000\text{\AA}$  thermal  $\text{SiO}_2$ , shows a primary feature at  $\sim 531.5\text{eV}$  and a significantly smaller one at  $529.9\text{eV}$ , indicating that La-O-Si with a small fraction of  $\text{La}_2\text{O}_3$  bonding are present in the film. The La 3d spectrum for sample (iii) is shifted towards the low binding energies compared

to those for samples (i) and (ii), consistent with the presence of  $\text{La}_2\text{O}_3$  in sample (iii), and with our interpretation of the O 1s spectra for this film. The peak broadening may be due to a graded composition in sample (iii).

To gain further insight into the reactions of La metal on thick  $\text{SiO}_2$ , a very thick La film (1000Å) was deposited on  $\text{SiO}_2$  for comparison with sample (iii). Figure 5.3 shows XPS data for samples formed by depositing 170Å of La on 1000Å  $\text{SiO}_2$  (sample iii), and 1000Å La on 1000Å  $\text{SiO}_2$  (sample iv). Film stacks were oxidized at 900°C for 5 min. The O 1s XP spectra (Figure 5.3a) for both films exhibit a primary peak at ~531.5eV, and a secondary peak at ~530eV consistent with the presence of some  $\text{La}_2\text{O}_3$  in a mainly silicate film. The thicker La layer results in a more pronounced and narrower  $\text{La}_2\text{O}_3$  feature. The broadening of the La 3d peaks (Figure 5.3b) for samples (iii) and (iv) towards the low binding energies compared with films (i) and (ii) is also consistent with the existence of  $\text{La}_2\text{O}_3$  in films (iii) and (iv).

We now discuss differences in reactions on plasma nitrated and thermally oxidized substrates. Comparing data from samples (i) and (ii), the presence of an ultra-thin layer of nitrated Si in sample (ii) does not impede significantly the diffusion of Si atoms into the La-metal film. This result is in contrast to that obtained from studies of Y on nitrated Si<sup>17</sup> where the presence of ~10Å of nitrated Si did impede reaction of Y and Si. The larger ionic radius of the La atom compared to that of Y may account for this difference. It is also conceivable that in both cases, metal nitride layers (La-N or Y-N) are formed at the interface. The lattice constants for La-N is expected to be ~5.33Å<sup>18</sup> which is significantly larger than the 4.88Å<sup>18</sup> expected for Y-N, thus facilitating the diffusion of the Si atoms through the La-N layer.

The XPS detection of Si near the top of films (iii) and (iv), which were deposited on 1000Å of thermal SiO<sub>2</sub>, shows the remarkable ability of La metal to reduce SiO<sub>2</sub> during thermal treatment likely by breaking Si-O bonds. It was shown above that Si atoms are highly mobile in La and La oxide and diffuse through >1000Å of deposited metal to form La-O-Si units at the sample surface. In the case of La-SiO<sub>2</sub> reactivity, the silicidation reaction requires additionally the breaking of fairly strong (4.85 eV) Si-O bonds. As a result, one expects thicker metal films would be more likely to have La<sub>2</sub>O<sub>3</sub> at the surface. The data in Figure 5.3 supports this idea. The intensity of the La<sub>2</sub>O<sub>3</sub> peak in the La 3d spectrum is significantly larger for the film prepared from the thicker (1000Å) original La metal. The O 1s peak for sample (iv) in Figure 5.3a is narrower than that of sample (iii) consistent with a more homogeneous composition for sample (iv). Neither samples spectra show evidence for a SiO<sub>2</sub> O 1s feature at 533.3eV consistent with a La-rich top layer.

The broadening of the O 1s spectra for sample (iii) towards high binding energies may be ascribed to the presence of more SiO<sub>2</sub> in the film as compared to samples (i), (ii), and (iv). This result is consistent with a large amount of SiO<sub>2</sub> initially under the deposited metal. As discussed below in Section 5.3.3, we do not see evidence for phase separation of La-silicate into La<sub>2</sub>O<sub>3</sub>/SiO<sub>2</sub> even after annealing for 30 seconds at 1050°C. Thus we believe that the presence of La<sub>2</sub>O<sub>3</sub> in films (iii) and (iv) is likely due to a slower reaction between La and SiO<sub>2</sub>, compared to the reaction between La metal and Hf-last Si or nitrated Si substrates in samples (i) and (ii).

The conclusions of this work regarding the ability of La metal to reduce thick layers of SiO<sub>2</sub> during thermal treatment corroborate previous observations by Copel et

al.<sup>8</sup> who demonstrated that reoxidation of a 23Å LaO<sub>x</sub>/20Å thermal SiO<sub>2</sub> structure at 850°C resulted in the complete reduction of the SiO<sub>2</sub> and the formation of La-O-Si. Stemmer et al.<sup>19</sup> also reports some silicate formation for La<sub>2</sub>O<sub>3</sub>/SiO<sub>2</sub>/Si structures, annealed at 800°C.

### 5.3.3 Thermal stability of La-silicate films

The propensity of the La-silicate films to phase separate into the La<sub>2</sub>O<sub>3</sub> and SiO<sub>2</sub> components was investigated by subjecting the films to extended thermal treatment at 1050°C in a Rapid Thermal Anneal (RTA) instrument in Ar atmosphere. For this purpose, La metal (150Å) was deposited via magnetron sputtering on H-terminated Si and RTA oxidized ex-situ at either 600 or 900°C in dry air for 5min. Each dielectric film was cleaved into 3 pieces and subjected to a different thermal treatment. Sample (v) received no further annealing beyond the oxidation step. Sample (vi) was annealed in Ar at 1050°C for 10s, and sample (vii) was annealed at the same temperature for 30s. Figure 5.4 shows the O 1s XP spectra for samples (v) through (vii) for films oxidized at 900 and 600°C. With longer annealing time, the O 1s peak position shifts marginally towards lower binding energies, but phase separation is not observed.

Additionally, both 900 and 600°C as-deposited films exhibit a small La<sub>2</sub>O<sub>3</sub> content as evidenced by the low binding energy shoulders in the O 1s and La 3d (not shown) peaks. This oxide is not present in the N<sub>2</sub>O oxidized films and is probably due to the different oxidation environment or the faster temperature ramp in the RTA instrument than in the conventional furnace used for samples discussed in previous sections. The oxide is reduced to silicate upon thermal anneal, and this silicate exhibits remarkable

thermal stability even upon a 30s thermal excursion at 1050°C which exceeds the thermal budget currently experienced by the CMOS gate dielectric during dopant activation.

### 5.3.4 Atmospheric H<sub>2</sub>O absorption of La-silicate films

The hygroscopic nature of the silicate films was investigated by FTIR. Thick La films (330Å metal) were deposited on high resistivity Si substrates and oxidized for 10 min at either 600 or 900°C. The IR spectrum of each sample was recorded within 10 min of the oxidation. The films were left in ambient air, and the IR spectrum between 4000 and 400cm<sup>-1</sup> was recorded periodically.

Figure 5.5 shows spectra recorded immediately (within 10 min after oxidation) and after 10 days of ambient exposure for films oxidized at 900 (Figure 5.5a) or 600°C (Figure 5.5b). The 900°C film oxidized exhibits an absorption feature at 1100cm<sup>-1</sup> corresponding to the Si-O-Si asymmetric stretch in SiO<sub>2</sub>.<sup>20</sup> The peak due to the Si-O-Si bending mode located at 810cm<sup>-1</sup> is super imposed onto a broader set of peaks located between 780-1020cm<sup>-1</sup> and indicative of La-silicate structure.<sup>16</sup> The La<sub>2</sub>O<sub>3</sub> feature<sup>21</sup> at 450cm<sup>-1</sup> could not be investigated due to instrument limitations. The IR spectrum of the film oxidized at 900°C remains practically unchanged after 10-days of air exposure.

The film oxidized at 600°C exhibits a far richer absorption spectrum. Following oxidation, interfacial SiO<sub>2</sub> formation is revealed by the Si-O-Si asymmetric stretching mode at 1100cm<sup>-1</sup>. The intensity of the silicate peaks between 780-1020cm<sup>-1</sup> is significantly reduced while several other peaks appear in the spectrum. Significant reaction with moisture is revealed by the hydroxyl group stretching mode peaks at 3440cm<sup>-1</sup> for OH in LaO(OH) and the small shoulder near 3600cm<sup>-1</sup> caused by OH in La(OH)<sub>3</sub>. The broad feature between 1500 and 1300 cm<sup>-1</sup> suggests the presence of

hydrocarbonate phases,  $\text{La}_2(\text{OH})_{6-3x}(\text{CO}_3)_x$ , possibly from reaction with atmospheric  $\text{CO}_2$ , and has been observed previously.<sup>22,23,24</sup> After 10 days of ambient exposure, the peaks become more intense, and three new peaks at  $3610$ ,  $1580$ , and  $640\text{cm}^{-1}$  appear in the spectrum. The very strong features at  $3610$  and  $640\text{cm}^{-1}$  are assigned to the O-H stretching and La-OH bending modes of  $\text{La}(\text{OH})_3$ .<sup>22,23</sup> The peak at  $1580\text{cm}^{-1}$  is probably due to the formation of another La hydrocarbonate.<sup>23,24,25</sup>

The oxidation temperature appears to affect significantly the film's reactivity with atmospheric components such as moisture and  $\text{CO}_2$ . Rare earth oxides and  $\text{La}_2\text{O}_3$  powders<sup>23</sup> are known to react with atmospheric components. Rosynek et al.<sup>22</sup> demonstrated that prolonged ( $\sim 40\text{h}$ ) annealing of La-hydrocarbonate in vacuum leads to a first stage dehydration at  $200^\circ\text{C}$  and complete dehydration at around  $400^\circ\text{C}$ . The carbonate decomposes between  $400$  and  $800^\circ\text{C}$ . XPS analysis of films oxidized at  $600$  and  $900^\circ\text{C}$  and kept in the controlled atmosphere of a desiccator reveals that both materials have similar silicate compositions. Thus, we believe that oxidation at either  $600$  or  $900^\circ\text{C}$  is sufficient to desorb all the impurities that form within the 1-2min air exposure prior to oxidation. The oxidation temperature was the only step in the preparation of these samples that was varied. It is likely that oxidation at  $900^\circ\text{C}$  results in a more densely packed film structure than oxidation at  $600^\circ\text{C}$ . A higher porosity would facilitate the diffusion of atmospheric elements in the  $600^\circ\text{C}$  silicate film and allow hydrocarbonate formation within minutes of air exposure.

Nieminen et al.<sup>26</sup> have reported IR results for  $\text{La}_2\text{O}_3$  films grown on Si. The as-deposited films exhibit  $\text{LaO}(\text{OH})$  and carbonate features that disappear following a 30 min  $\text{N}_2$  anneal at  $800^\circ\text{C}$ . However, these reappear and strong  $\text{La}(\text{OH})_3$  features develop

after subsequent exposure to air. The chemical stability exhibited by the 900°C La-silicate in this study is quite remarkable and noteworthy.

### 5.3.5 Electrical measurements on La-silicate films

The electrical properties of the La-silicate films were evaluated by C-V measurements on MIS capacitors with Al gates. No forming gas anneal was performed. Figure 5.6 shows a representative curve taken at 1MHz and 100 KHz for 10Å La metal oxidized at 900°C for 5s in N<sub>2</sub>O. The area of the capacitor was measured at 3.53x10<sup>-4</sup> cm<sup>2</sup> optically. The transition from depletion to accumulation appears to stretch over 1V. This voltage stretch-out is characteristic of interface trap charge that is uniformly distributed throughout the band gap. Analysis of the 1MHz curve with the NCSU CV Program<sup>11</sup> that corrects for quantum-mechanical effects yields an equivalent oxide thickness (EOT) of 15.3Å. The flat band voltage was -1.08V, shifted by about -1.1V from its expected position, in agreement with previous findings by Guha et al.<sup>27</sup> and Copel et al.<sup>8</sup> The direction and magnitude of the flat band voltage shift indicates the presence of positive fixed charge with a density of about 1x10<sup>13</sup>cm<sup>-2</sup>, which is unacceptably high for CMOS technology. The origin of the charge is not yet understood, and no attempt was made to distinguish oxide trapped and interface trapped charge in this work. However, Copel et al.<sup>8</sup> report that the charge appears to be an intrinsic material feature rather than due to oxygen deficiency of the film. Physically thinner films exhibited unacceptably high leakage currents. The frequency dispersion of the C-V curve is relatively small. Overall, the electrical results are reasonable and consistent with previous reports. It is not clear whether forming gas anneal would reduce the number of interface traps. Figure 5.7 presents hysteresis of the same film on the first and fifth cycle.

The insert graph shows a magnified portion of the curves around the flat band voltage. The hysteresis is about 50mV, corresponding to a mobile charge density of about  $4 \times 10^{11} \text{ cm}^{-2}$ . The flat band voltage shift for the fifth cycle appears marginally smaller than for the first cycle.

## **5.4 Conclusions**

Thin dielectric films were created by La metal PVD and ex-situ furnace oxidation in  $\text{N}_2\text{O}$ . XPS analysis revealed that regardless of the initial metal thickness the films were a La-silicate material with fairly constant composition. Oxidation at  $600^\circ\text{C}$  and  $900^\circ\text{C}$  yielded materials of fairly similar silicate composition that did not phase separate into  $\text{La}_2\text{O}_3$  and  $\text{SiO}_2$  even when subjected to inert atmosphere anneals at  $1050^\circ\text{C}$  for 30s, conditions that exceed the current gate dielectric thermal stability requirements. The oxidation temperature, however, had a severe effect on the chemical stability of the films to air exposure. La-silicate films oxidized at  $600^\circ\text{C}$  were susceptible to La-hydrocarbonate and  $\text{LaO}(\text{OH})$  formation within minutes of air exposure. Prolonged ambient exposure resulted in the formation of  $\text{La}(\text{OH})_3$ . Films oxidized at  $900^\circ\text{C}$ , on the other hand, showed no sign of reaction with moisture or  $\text{CO}_2$  that were within the detection limits of the FTIR instrument. Despite the good properties of these silicate films, large concentrations of positive fixed charge seem to be intrinsic to the material. Unless it can be neutralized or somehow reduced, this charge limits the usefulness of La-silicate as a replacement for  $\text{SiO}_2$  in CMOS technology

## 5.5 Acknowledgements

The authors would like to thank Scott Burnside, Tammi Schmit and Justin Bennett for assistance with the film deposition and characterization, Rob Ashcraft and Dong Niu for assistance with the IR and RTA. Financial support from SRC customization funding through LSI Logic Inc., and NSF (Grant# CTS-0072784) is gratefully acknowledged.

## 5.6 References:

- 1 S. I. Association, The International Technology Roadmap for Semiconductors, 1999 Edition, International SEMATECH Austin, TX, 1999
- 2 G.D. Wilk, R.M. Wallace and J.M. Anthony, *J. Appl. Phys.* **89**(10), 5243 (2001) and references therein.
- 3 J.-P. Maria, D. Wicaksana, A. I. Kingon, B. Busch, H. Schulte, E. Garfunkel, and T. Gustafsson, *J. Appl. Phys.* **90** (7), 918 (2001)
- 4 K. B. Hubbard and D. G. Schlom, *J. Mater. Res.* **11**, 2757 (1996)
- 5 J.J. Chambers and G.N. Parsons, *J. Appl. Phys.* **90** (2), 918 (2001)
- 6 D. Niu, R. W. Ashcraft, Z. Chen, S. Stemmer, and G. N. Parsons, *Appl. Phys. Lett.*, **81**(4), 676 (2002)
- 7 H. Yamada, T. Shimizu, and E. Suzuki, *Jpn. J. Appl. Phys.* **41**, L368 (2002)
- 8 M. Copel, E. Cartier, and F. M. Ross, *Appl. Phys. Lett.* **78**(11), 1607 (2001)
- 9 J. J. Chambers, B.W. Busch, W.H. Schulte, T. Gustafsson, E. Garfunkel, S. Wang, D.M. Maher, T.M. Klein, and G. N. Parsons, *Appl. Surf. Sci.* **181**, 78 (2001)
- 10 <http://rsb.info.nih.gov/ij/>

- 11 N. Yang, K. W. Henson, J. R. Hauser, and J. J. Wortman, IEEE Trans. Electron Devices **46**, 1464 (1999)
- 12 J. F. Moulder , W. F. Stickle, P.E. Sobol, and K.D. Bomben, *Handbook of X-ray Photoelectron Spectroscopy* (Perkin-Elmer Corporation, Eden Prairie, MN, 1992)
- 13 Y. Uwamino, T. Ishizuka, and H. Yamatera, J. Electr. Spectrosc. Relat. Phenom, **34**, 67 (1984)
- 14 C. C. Hsu, J. Ho, J.J. Qian, Y.T. Wang and Y. X. Wang, Vacuum **41**(4-6) 1425 (1990)
- 15 R.D. Thompson, B.Y. Tsaur, and K.N. Tu, Appl. Phys. Lett. **38**(7), 535 (1991)
- 16 H. Ono and T. Katsumata, Appl. Phys. Lett. **78**(13), 1832 (2001)
- 17 J.J. Chambers and G. N. Parsons, Appl. Phys. Lett. **77**(15), 2385 (2000)
- 18 J. C. Fitzmaurice, A. Hector, T. Rowley, and I. P. Parkin, Polyhedron, **13**(2) 235 (1994)
- 19 S. Stemmer, J.-P. Maria and A. I. Kingon, Appl. Phys. Lett. **79**(1), 102 (2001)
- 20 C.T. Kirk, Phys. Rev. B **38**(2), 1255 (1988)
- 21 F. Petru, and A.Muck, Z. Chem. **6**, 386 (1966)
- 22 M.P. Rosynek and D.T. Magnuson, J.Cat. **46**, 402 (1977)
- 23 S. Bernal, J. A. Diaz, R. Garcia, and J.M. Rodriguez-Izquierdo, J. Mat. Sci. **20**, 537 (1985)

- 24 P. Caro and M. Lamaitre Blaise, *Compt. Rend. Acad. Sci. Paris, ser. C* **269**, 687 (1969)
- P. Caro, J.C. Achard and O. Pous, *Colloque International du CNRS sur les elements des terres rares* **1**, 285 (1970)
- P.E. Caro, J. O. Sawyer, and L. Eyring, *Spectrochim. Acta* **28**, 1167 (1972)
- 25 B. Klingenberg and M. A. Vannice, *Chem. Mater.* **8**, 2755 (1996)
- 26 M. Nieminen, M. Putkonen, and L. Niinistö, *Appl. Surf. Sci.* **174**, 155 (2001)
- 27 S. Guha, E. Cartier, M. A. Gribelyuk, N.A. Bojarczuk, and M.C. Copel, *Appl. Phys. Lett.* **77**(17), 2710 (2000)

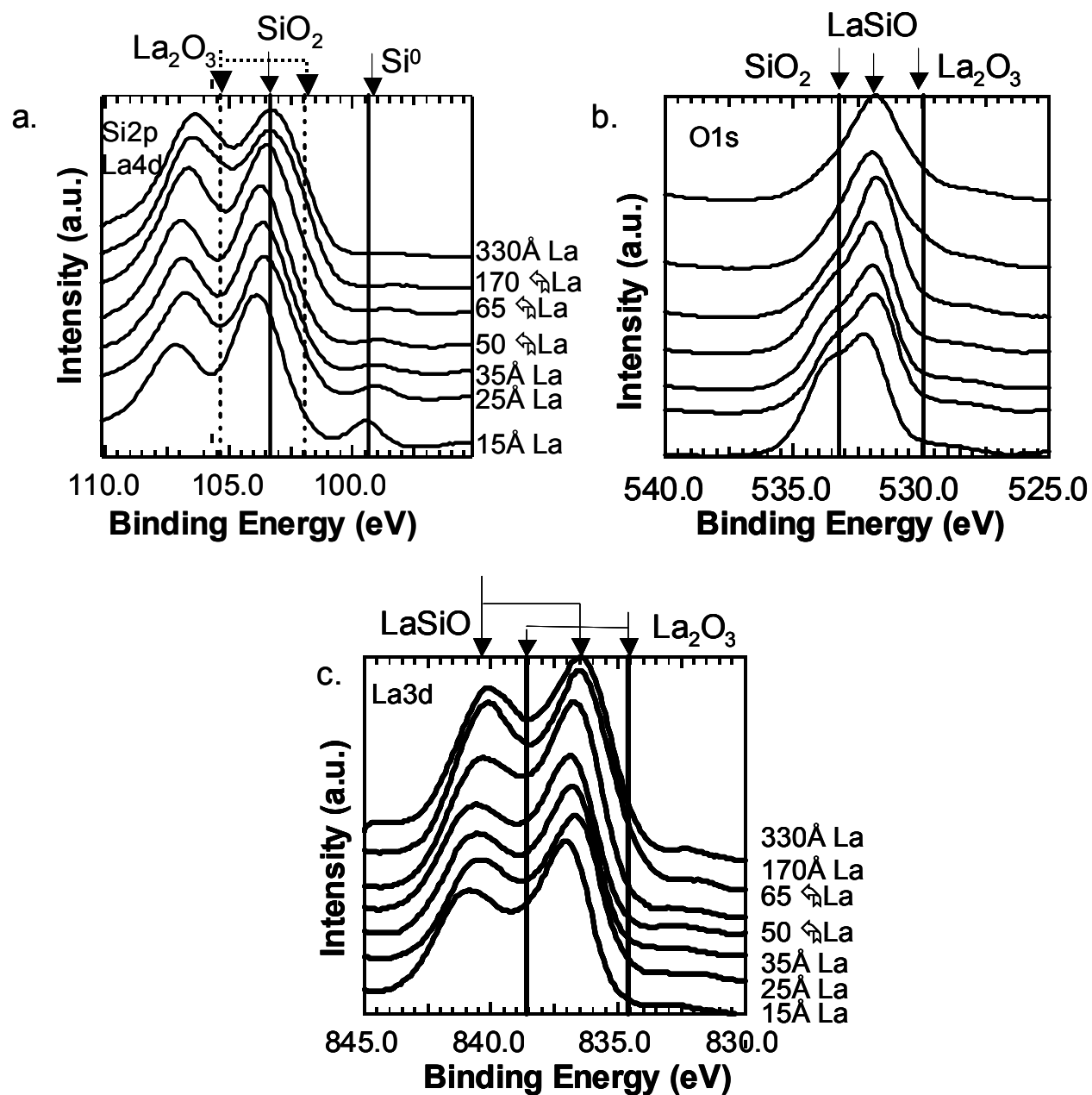


**Figure 5.1** Si 2p/La 4d, O 1s, and La 3d spectra for a series of La metal films with thickness ranging from 15 to 330 Å, oxidized at 900°C in N<sub>2</sub>O. Interfacial SiO<sub>2</sub> was detected for the thinnest films. Based on the position of the O 1s and the La 3d peaks, we conclude that the material is La-silicate for all thicknesses studied.

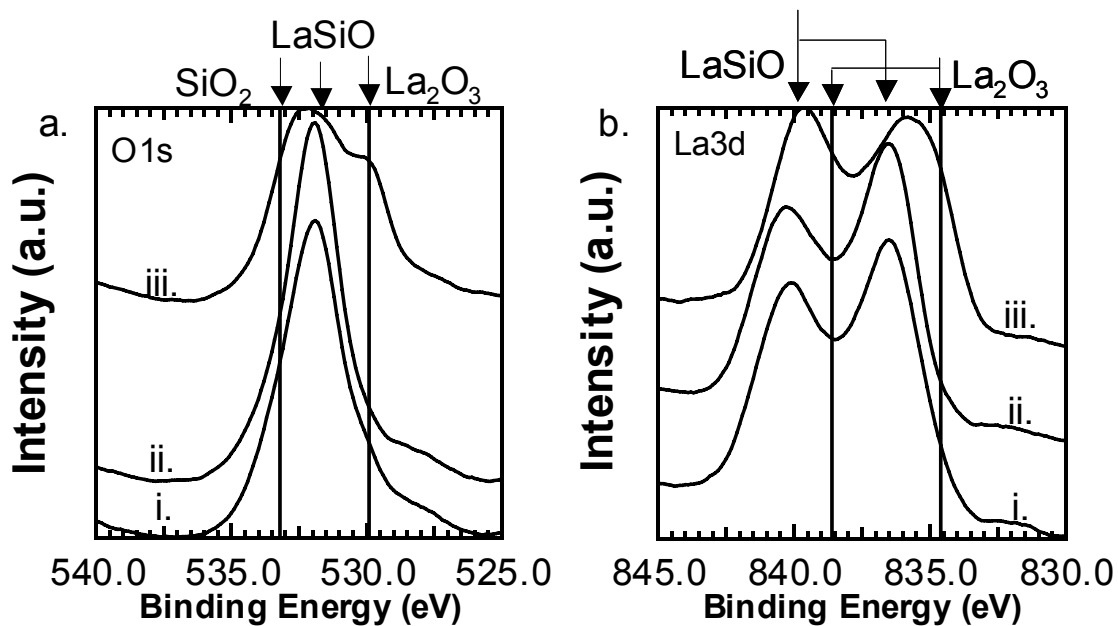


**Figure 5.2** O 1s and La 3d XP spectra for three identical films (170Å La metal, 5min, 900°C, N<sub>2</sub>O oxidation) deposited on i) H-terminated Si(100), ii) plasma nitrated Si(100), and iii) 1000Å of thermal SiO<sub>2</sub>. Films (i) and (ii) have practically identical composition as measured by XPS, while film (iii) is also a silicate but has a small La<sub>2</sub>O<sub>3</sub> content as evidenced by the shoulder of the O 1s peak at ~530eV and the shift of the La 3d peak towards lower binding energies.

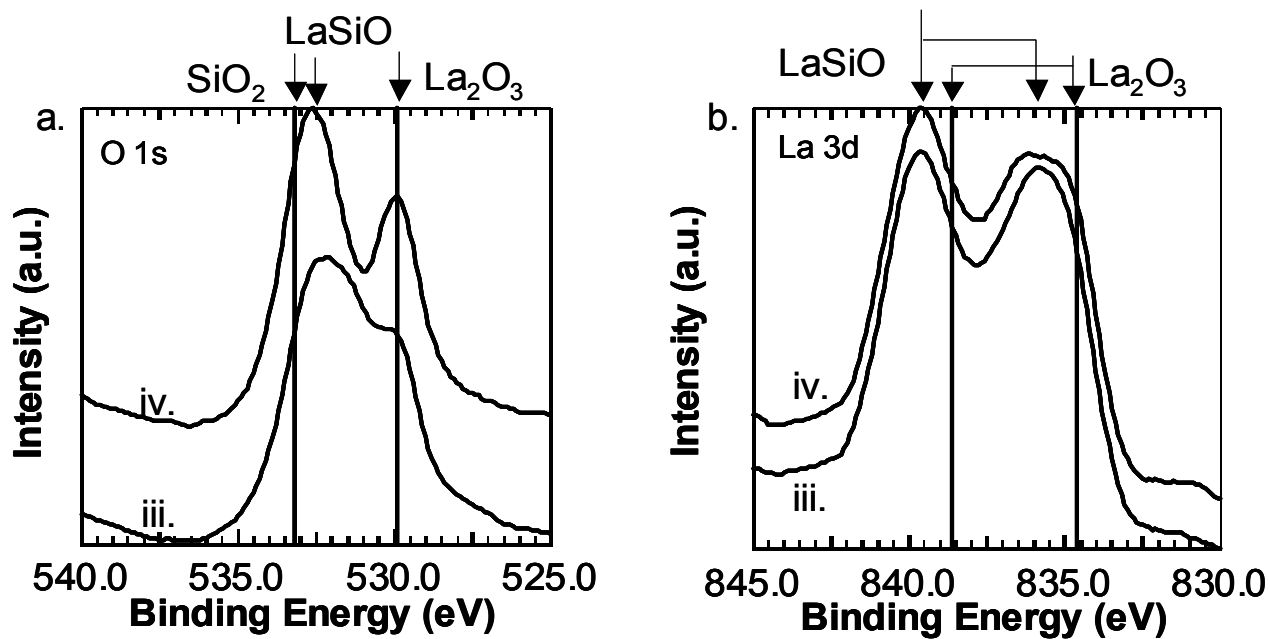


**Figure 5.3** O 1s and La 3d XP spectra for 170 Å (iii) and 1000 Å (iv) La metal deposited on 1000 Å of thermal SiO<sub>2</sub> and oxidized at 900°C in N<sub>2</sub>O for 5min. Both films have primarily silicate composition with a small fraction of La<sub>2</sub>O<sub>3</sub>. The thicker film exhibits a higher La<sub>2</sub>O<sub>3</sub> content.

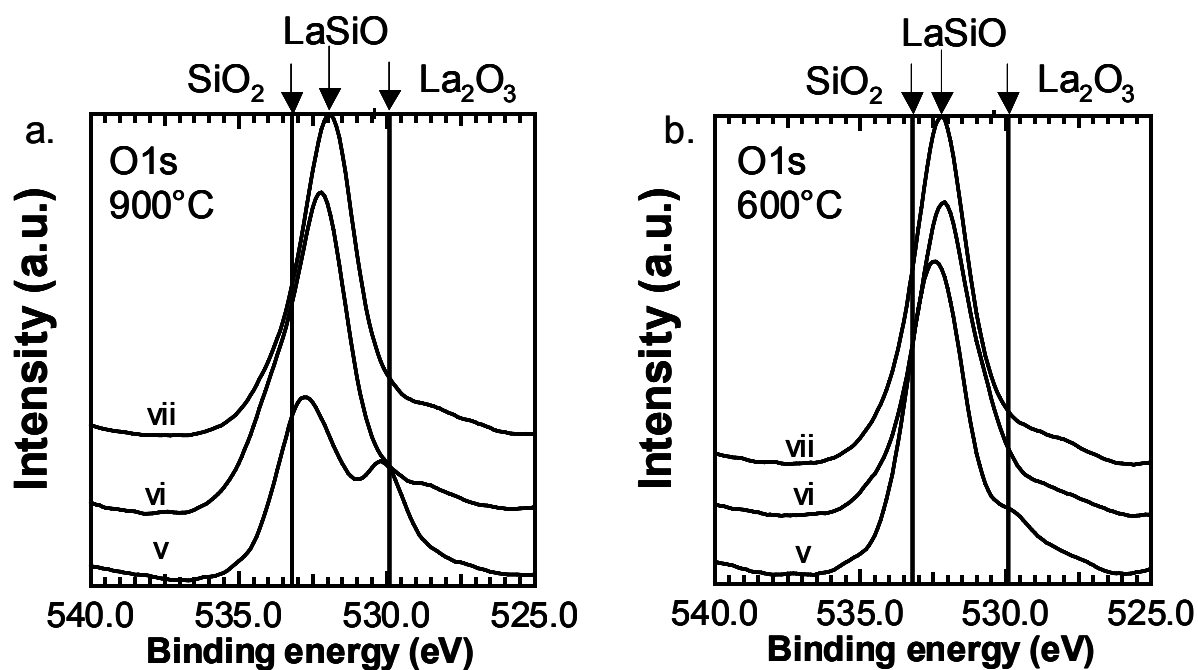


**Figure 5.4** O 1s XP spectra for a 150Å metal film oxidized for 5 min at 900 or 600°C in dry air. Sample (v) is as-deposited. Sample (vi) was annealed at 1050°C in Ar for 10s, and sample (vii) was annealed at 1050°C in Ar for 30s. The La-silicate can withstand 30s inert anneal at 1050°C without phase separation. The small amount of La<sub>2</sub>O<sub>3</sub> present in the as-deposited films is reduced to silicate upon anneal.

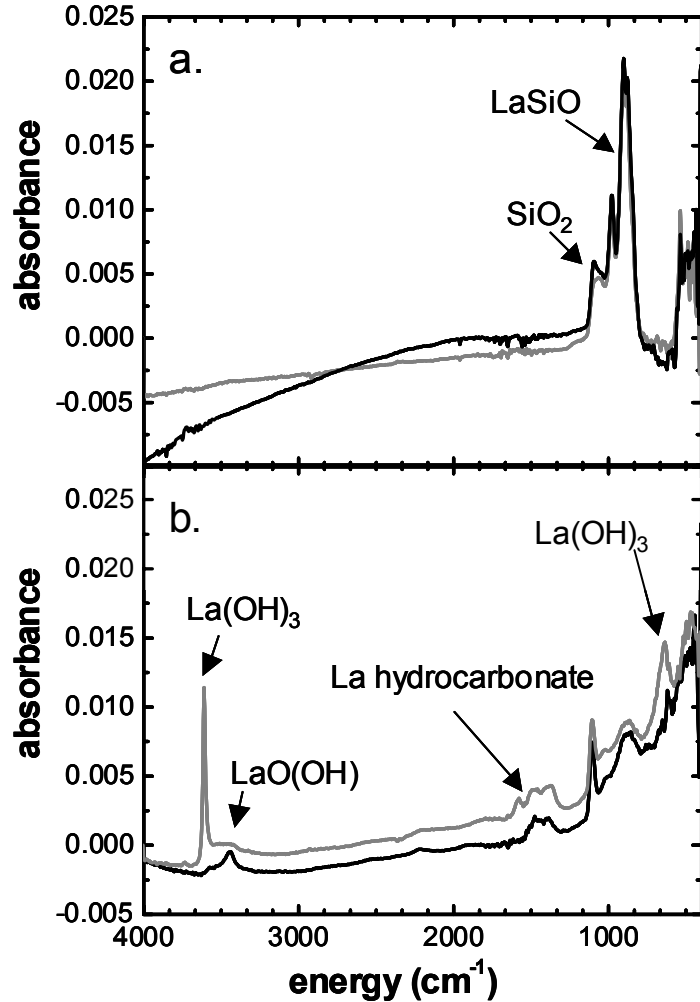


**Figure 5.5** FTIR spectra for two dielectric films taken about 10 min after oxidation (solid black line) and after 10 days of air exposure (solid gray line). The films were formed by oxidizing 330Å La-metal films at either 900°C (5a) or 600°C (5b) for 10min in N<sub>2</sub>O. The film oxidized at 900°C exhibits features consistent with the presence of SiO<sub>2</sub> and La-O-Si. No significant reaction with H<sub>2</sub>O or CO<sub>2</sub> is detected even after a 10-day exposure to ambient air. The film oxidized at 600°C is chemically unstable in contact with air, and its spectrum exhibits features consistent the formation of a La-hydrocarbonate. Air exposure intensifies those features.

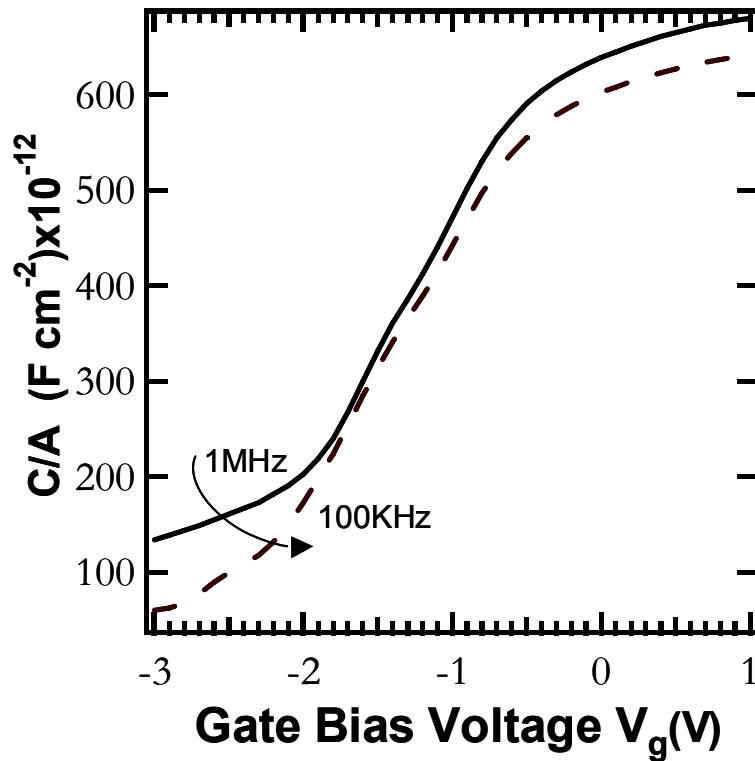


**Figure 5.6** Representative C-V data for a dielectric film prepared by oxidizing 10Å La metal in a 900°C, N<sub>2</sub>O atmosphere for 5s. The low frequency (100kHz) curve tracks quite well the high frequency (1MHz) one. The stretch-out of the curve along the V<sub>g</sub> axis is indicative of significant concentration of interface traps distributed throughout the band gap. Analysis of the 1MHz curve yields an EOT=15.3Å. The flat band voltage (-1.08eV) is shifted by approximately -1.1eV revealing the presence of positive fixed charge. No attempt was made to distinguish oxide trapped and interface trapped charge. The gate material is Al and the area of the capacitor is 3.53x10<sup>-4</sup>cm<sup>-2</sup>.

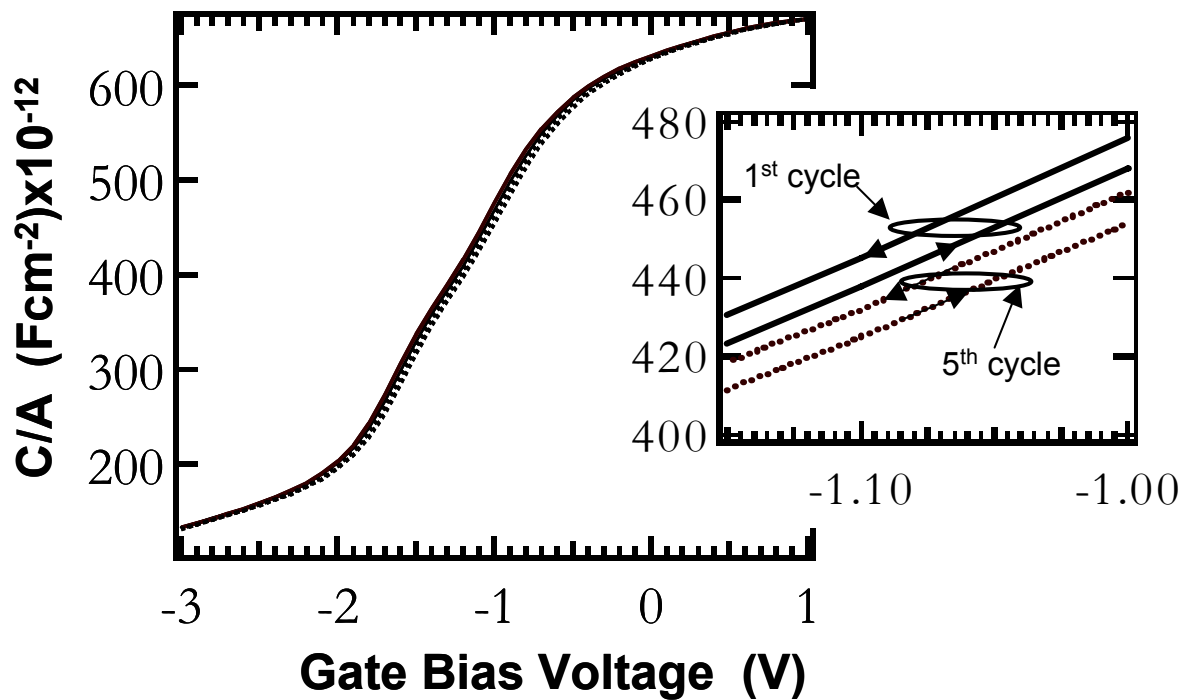


**Figure 5.7** Hysteresis curves for the capacitor in Figure 5.6. The inset shows a magnification of the flat band voltage area. The magnitude is  $\sim 50\text{mV}$  without Post Metallization Anneal.

Chapter 6 is a reprint of a paper that appeared in Materials Research  
Society Symposia Proceedings Vol. 670, K3.1, (2001)

## **Promising Gate Stacks with Ru & RuO<sub>2</sub> Gate Electrodes and Y-silicate Dielectrics**

Huicai Zhong<sup>1</sup>, Greg Heuss<sup>1</sup>, You-Seok Suh<sup>1</sup>, Shin-Nam Hong<sup>2</sup> and Veena Misra<sup>1</sup>  
Jason Kelly<sup>3</sup> and Gregory Parsons<sup>3</sup>

<sup>1</sup> Department of Electrical Engineering, North Carolina State University, Raleigh, NC

<sup>2</sup> Department of Electrical Engineering, Hankuk Aviation University, Seoul, Korea

<sup>3</sup> Department of Chemical Engineering, North Carolina State University, Raleigh, NC

## **Abstract**

In this work, we studied the electrical and thermal stability of Ru and RuO<sub>2</sub> electrode on Y-silicate dielectrics in contrast to ZrO<sub>2</sub> and Al<sub>2</sub>O<sub>3</sub> dielectrics. Very low resistivity Ru and rutile stoichiometric RuO<sub>2</sub> films, deposited via reactive sputtering, were evaluated as gate electrodes on ultrathin Y-silicate, ZrO<sub>2</sub> and Al<sub>2</sub>O<sub>3</sub> films for Si-MOS devices. Thermal and chemical stability of the electrodes was studied at annealing temperatures up to 800°C in N<sub>2</sub> and subsequently forming gas anneal. XRD and XPS were measured to study grain structure and interface reactions. The morphology of the films was tested by atomic force microscopy (AFM). Electrical properties were evaluated via MOS capacitors. The role of oxygen inside dielectrics was studied by comparing equivalent oxide thickness change as a function of annealing temperature for capacitors with Y-silicate, ZrO<sub>2</sub> and Al<sub>2</sub>O<sub>3</sub> dielectrics. Good stability of Ru and RuO<sub>2</sub> gate electrodes on all dielectrics studied was found. Flatband voltage and gate current as a function of annealing temperature was also studied. It was found that capacitors with Y-silicate after high-temperature anneal had less positive flatband voltage shift than ZrO<sub>2</sub> and Al<sub>2</sub>O<sub>3</sub>. For capacitors with Ru gate electrode, the significant flatband voltage shift after high temperature anneal could be partially removed by a forming gas anneal.

## **Specific Contribution**

For this study I provided yttrium silicate-like (Y-silicate) dielectrics and contributed to the theory of the paper during conversations with the principal author. My research focused on studying Y-silicate as a potential high dielectric constant replacement for SiO<sub>2</sub> in next generation metal-oxide-semiconductor devices, and I was curious to test my dielectrics

in contact with new electrode materials. Reactions become inherently more complex as the number of reactive species present increases, and it is difficult to predict the properties of different material combinations without physically testing them. Zhong had been studying the behavior of Ru and RuO<sub>2</sub> electrode materials on SiO<sub>2</sub> and was also curious to see how stacks of candidate gate electrode and high dielectric constant materials would behave. When he indicated that he was interested in testing his electrode materials on some high dielectric constant materials, I was eager for him to include my materials. We discussed the results of the experiments including differences in oxygen content and bonding in my thermally oxidized Y-silicate and the deposited materials, ZrO<sub>2</sub> and Al<sub>2</sub>O<sub>3</sub>, included in the study.

For the experiments, I prepared yttrium silicate dielectrics on n- and p-type patterned field oxide wafers under conditions known to produce films with 20Å and 30Å equivalent oxide thickness (EOT). Yttrium films were deposited by a plasma-assisted dc sputter process and oxidized *ex-situ* at 900°C in N<sub>2</sub>O ambient. This work describes results from the 30Å EOT films on p-type substrates. This work yielded crucial insights that helped develop a framework in which to understand electrode/dielectric reactions. Specifically, it highlighted important factors in controlling the formation of interface layers and defects that affect the electrical performance (EOT, flatband voltage, mobility, etc.) of devices containing the gate stack. We found that the electrode material itself exhibited good physical stability during thermal stress in all the stacks studied. Electrically, however, there were changes in EOT and flatband voltage for all the devices. The Y-silicate devices exhibited lower flatband voltage shift and a smaller increase in EOT after annealing than devices with either PVD ZrO<sub>2</sub> or CVD Al<sub>2</sub>O<sub>3</sub> dielectrics.

## **6 Promising Gate Stacks with Ru & RuO<sub>2</sub> Gate Electrodes and Y-silicate Dielectrics**

### **6.1 Introduction**

Aggressive scaling of MOSFET technology makes the evaluation of high-conductivity metal gate electrodes and alternative gate dielectrics important [1]. Gate dielectric materials with high dielectric constant, low leakage current, good thermal stability, and good interface characteristics comparable to Si-SiO<sub>2</sub> are needed as alternative dielectrics. High conductivity and excellent thermal stability properties are required for metal gate electrodes to decrease gate depletion effect and to improve interface properties between gate electrode and gate dielectric. Thin films of transition metal oxides such as ruthenium oxide, RuO<sub>2</sub> not only have large workfunctions (~5 eV), but also very low resistivity and excellent thermal/chemical stability [2,3,4].

Studies performed by our group have demonstrated that Ru and RuO<sub>2</sub> gate electrodes on SiO<sub>2</sub> offer good thermal stability [5]. Ru and RuO<sub>2</sub> on ZrO<sub>2</sub> and ZrSiO<sub>4</sub> dielectrics with good thermal stability up to 800°C were recently reported [6]. In this paper, we report the material, electrical and thermal stability properties of Ru and RuO<sub>2</sub> gate electrodes on Y-silicate dielectrics and compare them to ZrO<sub>2</sub> and Al<sub>2</sub>O<sub>3</sub>.

### **6.2 Experimental Details**

Ru and RuO<sub>2</sub> thin films were deposited using a RF magnetron sputtering system. The sputtering target was a 2-inch diameter of Ru (99.9% purity) metal. Reactive sputtering was performed in Ar (for Ru) or in a mixture of Ar and O<sub>2</sub> (for RuO<sub>2</sub>). Prior to sputtering, the

system was pumped to base pressure of  $\sim 8 \cdot 10^{-7}$  Torr. The target was pre-sputtered for 30min in Ar before film deposition. No intentional heating was applied to the substrate. The partial pressure of O<sub>2</sub> was 40% for RuO<sub>2</sub> and the sputtering power was 100W. A Sloan Dectak profilometer was used to measure the thickness of films and the thickness of all films was in the range of 70nm. The substrates used were (100) Si wafers with active areas defined by 3500Å field oxidation. The Y silicate dielectrics were prepared by post-deposition oxidation of sputtered Y and Al<sub>2</sub>O<sub>3</sub> dielectrics were synthesized by MOCVD. ZrO<sub>2</sub> were prepared by PVD. The gate electrodes were patterned using lift-off lithography. After gate formation, the samples were annealed at temperatures of 400°C, 600°C and 800°C in N<sub>2</sub> for 30min. Rapid thermal anneal up to 800°C for 30sec was also utilized. The crystal structure of the films was determined by X-ray diffraction (XRD) using Cu K $\alpha$  radiation. The bonding states of Ru and RuO<sub>2</sub> films were determined by X-ray photoelectron spectroscopy (XPS). Atomic force microscope (AFM) was used to detect the morphology of the gate electrodes films before and after anneal. Electrical resistivity was measured by 4-point probe method. Capacitance-voltage (CV) and current-voltage (IV) characteristics were obtained using HP4145 and HP4824B, respectively.

### **6.3 Results**

The resistivity values of Ru films were  $\sim 12\mu\Omega\text{-cm}$  after high temperature annealing. The resistivity of RuO<sub>2</sub> films for as-deposited, annealed at 400°C, 600°C and 800°C annealed in N<sub>2</sub> for 30min were  $500.3\mu\Omega\text{-cm}$ ,  $117.8\mu\Omega\text{-cm}$ ,  $81.6\mu\Omega\text{-cm}$  and  $65.0\mu\Omega\text{-cm}$ , respectively. The RuO<sub>2</sub> resistivity decreased as temperature increased owing to the growth of grain size

and expansion of grain boundaries [6]. Both Ru and RuO<sub>2</sub> resistivities are much lower than heavily doped poly-Si and the poly-depletion effects thus would be effectively eliminated.

XRD analysis showed that Ru and RuO<sub>2</sub> films before anneal were nanocrystalline and poly-crystalline, respectively. After 600°C or higher temperature anneal, the RuO<sub>2</sub> films were crystallized, as shown in Figure 6.1. Sputter-depth XPS analysis of 800°C annealed RuO<sub>2</sub> and Ru films indicated a 2eV position difference of Ru 3d peak between Ru and RuO<sub>2</sub> implying that even after a 800°C furnace anneal the Ru films were not oxidized (Figure 6.2). AFM images, shown in Figure 6.3, do not show indicate any presence of void formation after 800°C anneals. As shown, the RMS roughness of the films increased after high temperature annealing.

Figure 6.4(a) shows the C-V curves of capacitors with RuO<sub>2</sub> gate electrodes on Y-silicate dielectrics after 400°C, 600°C, and 800°C post-gate-deposition anneals in N<sub>2</sub> for 40 min. All capacitance-voltage curves were measured at a frequency of 1MHz on an area equal to 2.5x10<sup>-5</sup>cm<sup>2</sup>. The flat-band voltage (V<sub>FB</sub>) and equivalent theoretical value of silicon oxide thickness (EOT) for the capacitors were obtained by using NCSU CV program [7]. After 400°C annealing, the equivalent oxide thickness was 3.1nm and the flat-band voltage was 1.03V consistent with RuO<sub>2</sub> workfunction of 5.1eV, an appropriate value for PMOSFET gates. However, after 600°C annealing, the flat-band voltage changed to 1.33V with a minimal change in EOT. No frequency dependency of CV measurement was detected. The change in V<sub>FB</sub> of ~0.3eV is attributed to fixed charges in the dielectric created upon annealing as will be discussed later. Further annealing at 800°C resulted in equivalent oxide thickness to 3.9nm with no additional change in flatband voltage.

Figure 6.4(b) shows Ru gate electrodes on Y-silicate gate dielectric after 400°C, 600°C and 800°C anneal in N<sub>2</sub> followed by a subsequent forming gas at 400°C. Similar trends were observed with Ru gates, as were seen with RuO<sub>2</sub> gates. After the initial 400°C annealing, EOT is 3.1nm with V<sub>FB</sub> equal to 1.05V. A ~0.9nm increase in EOT was observed after 800°C anneal. The V<sub>FB</sub> increased steadily from 1.05V at 400°C anneal to 1.30V at 800°C annealing in N<sub>2</sub>. The ~0.9nm increase of EOT is attributed to the oxidation of Si-substrate when the samples were annealed under high temperature, as will be discussed. In an effort to reduce the V<sub>FB</sub> change, a subsequent forming gas annealing was done for capacitors with Ru gate at 400°C for 30min. This resulted in a substantial decrease of V<sub>FB</sub> to 1.2V with no additional change in EOT. The effectiveness of the forming gas anneal indicated that the V<sub>FB</sub> shift observed after 600°C and 800°C annealing in N<sub>2</sub> may be related to negative fixed charge (or interface charge) created in the gate dielectric. The analogous behavior of both RuO<sub>2</sub> and Ru gate electrodes on Y-silicate dielectrics indicate that both gates have very similar properties on these emerging high-K dielectrics.

In order to better understand the behavior of Ru and RuO<sub>2</sub> gates on Y-silicate films, we also studied the characteristics of Ru and RuO<sub>2</sub> gate electrodes on other high-K dielectrics, such as ZrO<sub>2</sub> and Al<sub>2</sub>O<sub>3</sub>. Capacitors with Ru and RuO<sub>2</sub> gate electrodes on SiO<sub>2</sub> were studied as monitors. The changes in EOT and V<sub>FB</sub> as a function of anneal temperature are summarized in Figures 6.5(a) and (b), respectively. For RuO<sub>2</sub> gate electrodes on ZrO<sub>2</sub> and Al<sub>2</sub>O<sub>3</sub> dielectrics, a ~1nm EOT increase was found after 400°C, 600°C and 800°C anneals in N<sub>2</sub>. A significant V<sub>FB</sub> shift of ~0.7V, compared to Y-silicate, was also found for capacitors with ZrO<sub>2</sub> and Al<sub>2</sub>O<sub>3</sub> dielectrics. We suggest that the significant EOT increase in these dielectrics after high temperature annealing is also the result of Si-substrate oxidation which

forms a  $\text{SiO}_x$  interfacial layer. Capacitors with Ru gate electrodes on  $\text{ZrO}_2$  also exhibited similar trends. However, the magnitude of EOT was slightly smaller as compared to  $\text{RuO}_2$ . A subsequent forming gas annealing resulted in a substantial decrease of  $V_{\text{FB}}$  to 1.25V with no further change in EOT. For Ru gate electrodes on  $\text{Al}_2\text{O}_3$  dielectric, the 0.8V  $V_{\text{FB}}$  shift after 800°C  $\text{N}_2$  anneal could also be reduced to 0.3V by subsequent forming gas anneal.

It is worthwhile to note here that the significant increase of EOT and large  $V_{\text{FB}}$  shift of capacitors with Ru and  $\text{RuO}_2$  gate electrodes on Hi-K dielectrics including Y-silicate and  $\text{ZrO}_2$  could be minimized when the samples were annealed by rapid thermal anneal method. For e.g., C-V curves of Ru on  $\text{ZrO}_2$  dielectric (not shown) after 800°C RTA anneal for 30sec showed no  $V_{\text{FB}}$  shift and underwent only a  $\sim 0.3$  nm increase in EOT. Similar results were found for Ru and  $\text{RuO}_2$  gate electrodes on Y-silicate and on  $\text{Al}_2\text{O}_3$ . The minimal change of EOT and  $V_{\text{FB}}$  after RTA indicates the good thermal stability of Ru and  $\text{RuO}_2$  films on Hi-K dielectrics and suggests that the charge creation process has low activation energy. The current-voltage measurements of all high-K samples indicated that the current density decreased owing to the dielectric thickness increase after high temperature annealing.

## **6.4 Discussion and Conclusion**

As discussed above, an increase in EOT of Y-silicate,  $\text{ZrO}_2$  and  $\text{Al}_2\text{O}_3$  dielectrics with Ru and  $\text{RuO}_2$  gates after annealing was observed. This was attributed to the interfacial growth between the dielectric and the Si substrate. When annealed at high temperatures the Si-substrate can be oxidized by quasi-atomic oxygen, which migrates from the dielectric toward the Si-dielectric interface. One possible source of this oxygen is the dielectric itself. E. E. Khawaja et al found the excess oxygen due to the oxygen embedded in the films during

deposition and absorbed water in zirconium oxide by RBS and XPS[10]. Similar results were reported for  $Y_2O_3$  and Y-silicate[11]. It has been recently shown that many of these high-k dielectric films are  $H_2O$  absorbents. The slightly larger decrease in capacitance with  $RuO_2$  gates suggests that some oxygen may be accumulating in the gate dielectric during the  $RuO_2$  sputtering process. However, the  $RuO_2$  gate is not believed to be a source of oxygen because the increase in capacitance saturates after  $800^\circ C$  anneal for all the dielectrics studied, indicating that this gate stack is a sealed system not allowing any additional oxygen to enter from the outside ambient or the gate itself. Moreover, TEM results of  $RuO_2$  gates have shown stable interfaces. This is also consistent with the excellent oxygen diffusion barrier properties of  $RuO_2$  and Ru. This implies the gate electrode stability when accounted for by monitoring changes in EOT and  $V_{FB}$  is critically dependent on the state of the dielectric. Therefore, the high-K dielectric needs to be optimized such that it contains low levels of excess oxygen prior to gate electrode deposition. The quantitative difference in  $ZrO_2$  and  $Al_2O_3$  compared to Y-silicate may originate from their deposition conditions and the water content of the films. The overall stability of Ru and  $RuO_2$  gate electrodes on the various dielectrics studied here is attributed to their thermodynamic stability. With the knowledge of the stable binary phases, it can be shown via thermodynamic calculations that enthalpy of formation for  $RuO_2$  is  $72.9\text{kcal/mole}$ , less negative than  $262.3\text{kcal/mole}$  of  $ZrO_2$ ,  $455.43\text{kcal/mole}$  of  $Y_2O_3$  and  $400\text{kcal/mole}$  of  $Al_2O_3$  [8], thereby indicating that the dielectrics will not be reduced by the gate electrodes. Furthermore, since Ru and  $RuO_2$  are excellent oxygen diffusion barriers [9] (i.e. poor oxygen sink) preventing oxygen obtaining from annealing ambience. Oxygen exposure of the Ru surface also leads to surface oxidation which then act as oxygen diffusion barrier.

After high temperature annealing, all capacitors with RuO<sub>2</sub> and Ru gates on ZrO<sub>2</sub>, Al<sub>2</sub>O<sub>3</sub> and Y-silicate displayed significant flatband voltage shifts, which was attributed to fixed charges within the dielectrics. However, these did not exhibit any frequency dependencies, which indicating that the V<sub>FB</sub> shift may be attributed to fixed charge created within the dielectrics. Although capacitor with Y-silicate dielectrics had just ~0.3V V<sub>FB</sub> shift, capacitors with ZrO<sub>2</sub> and Al<sub>2</sub>O<sub>3</sub> displayed larger V<sub>FB</sub> shifts. These fixed charges may be related to the oxygen vacancies resulted from oxygen transportation within the dielectrics during high temperature anneal. The significant flatband shift was partially reduced by subsequent forming gas anneal for capacitors with Ru gate electrode, which can survive a H-based anneal. Further work needs to be done to understand the source of the charges.

In a summary, we have demonstrated that Ru and RuO<sub>2</sub> gates on Y-silicate, ZrO<sub>2</sub> and Al<sub>2</sub>O<sub>3</sub> dielectrics provided reasonable thermal stability but were accompanied by a significant increase of EOT and a steady increase in V<sub>FB</sub>. The V<sub>FB</sub> shift was minimized by a forming gas anneal for Ru-gate capacitors. The source of the oxygen that results in an EOT increase is believed to be the dielectrics themselves. Apart from the EOT increases observed, the Ru and RuO<sub>2</sub> interface with the high-K dielectrics was found to be stable under high temperature annealing. This is attributed to their low enthalpy of oxide formation compared to Y<sub>2</sub>O<sub>3</sub>, ZrO<sub>2</sub> and Al<sub>2</sub>O<sub>3</sub> and excellent oxygen diffusion barrier properties, which prevents oxygen penetration through the dielectric and maintains its electrical performance.

## 6.5 References

- 1 J. R. Hauser and W. T. Lynch, SRC working paper (1997)
- 2 L. Krusin-Elbaum and M. Wittmer, J. Electrochem. Soc., Vol 135, 2610 (1988)
- 3 K. M. Classford and J. R. Chelickowsky, Phys. Review B, 47, 1732 (1993)
- 4 T. S. Kalkur and Y. C. Lu, Thin Solid Films, 205, 266 (1991)
- 5 HC. Zhong, G.P. Heuss and Veena Misra, Electr. Dev. Lett., 21: (12) 593 (2000)
- 6 Zhong HC, Heuss G, Misra V, et al, Appl Phys Lett, 78(8), 1134 (2001 )
- 7 J. R. Hauser and K. Ahmed, Characterization of ultrathin oxides using electrical C-V and I-V measurements,” National Institute of Standards and Technology, Gaithersburg (1995)
- 8 J. A. Dean, Lange’s Handbook of Chemistry, 13<sup>th</sup> ed, (McGraw-Hill, New York, 1972), P9-5
- 9 S. H. Oh, C. G. Park, C. Park, Thin Solid Films, 118 (2000)
- 10 E. E. Kawaja, F. Bouamrane, A. B. Hallak, J. Vac. Sci. Technol. A 11(3), 580 (1993)
- 11 R. N. Sharma, A. C. Rastogi, J. Appl. Phys., 76(7), 4215, 1994

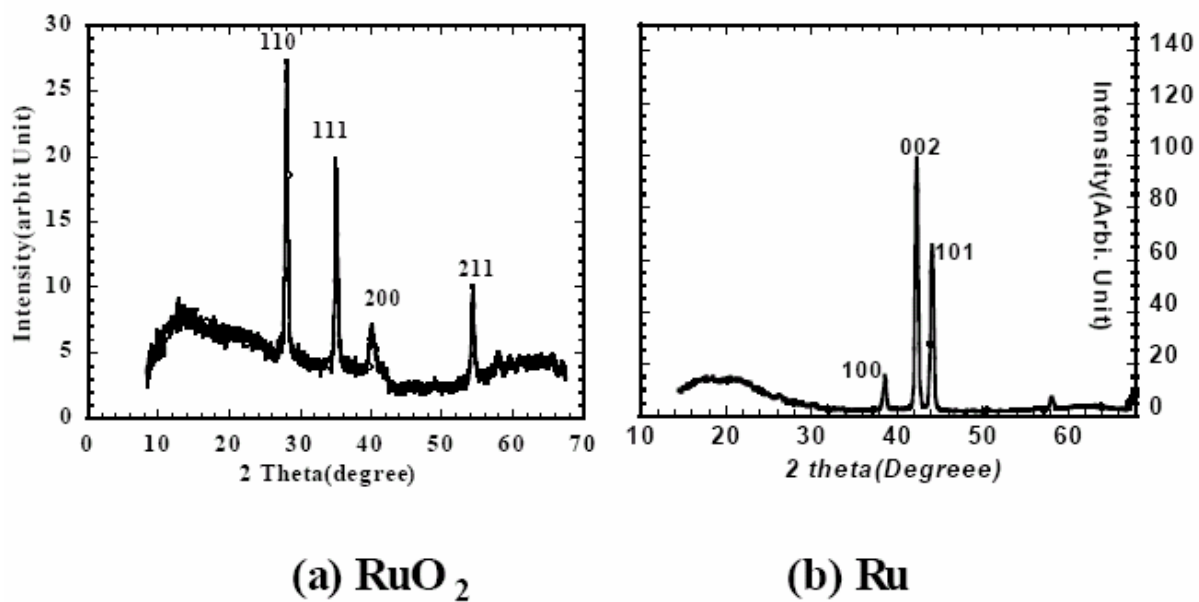


**Figure 6.1** XRD of RuO<sub>2</sub> on SiO<sub>2</sub> (a) and Ru on SiO<sub>2</sub> (b) after 800°C anneal in N<sub>2</sub>

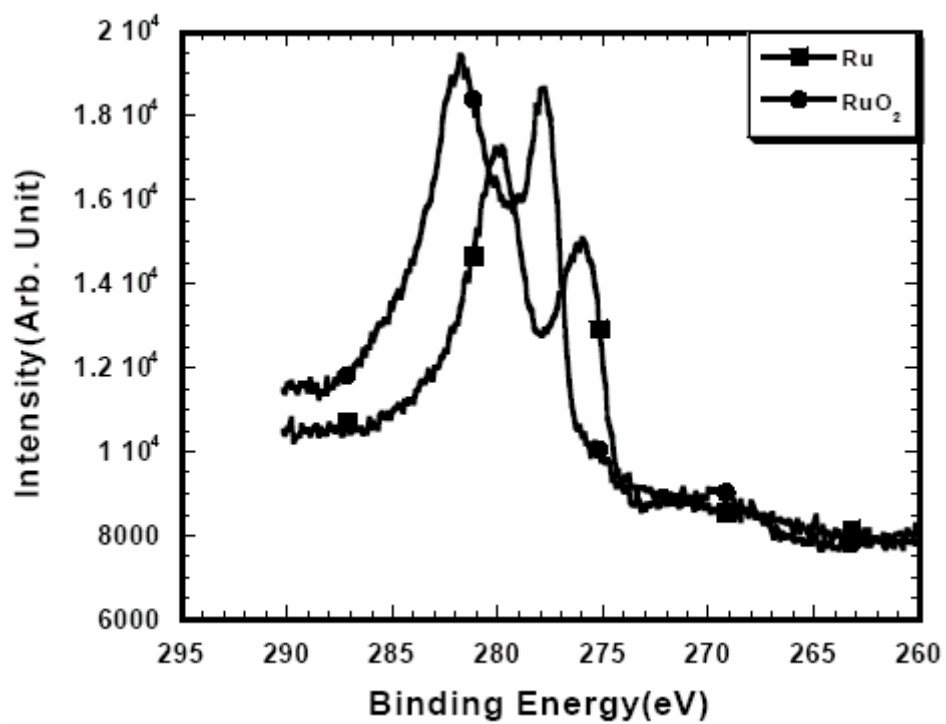


**Figure 6.2** XPS of Ru and RuO<sub>2</sub> films on ZrO<sub>2</sub> after the surfaces of Ru and RuO<sub>2</sub> films were sputtered

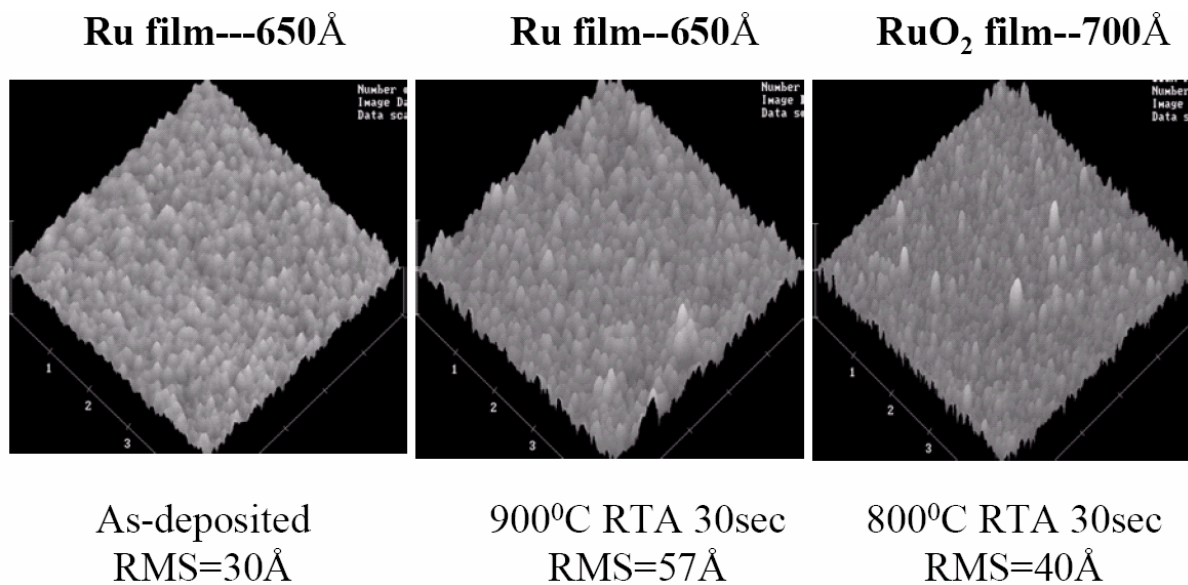


**Figure 6.3** Atomic force microscopy images of Ru and RuO<sub>2</sub> films before and after rapid thermal anneal in N<sub>2</sub>.

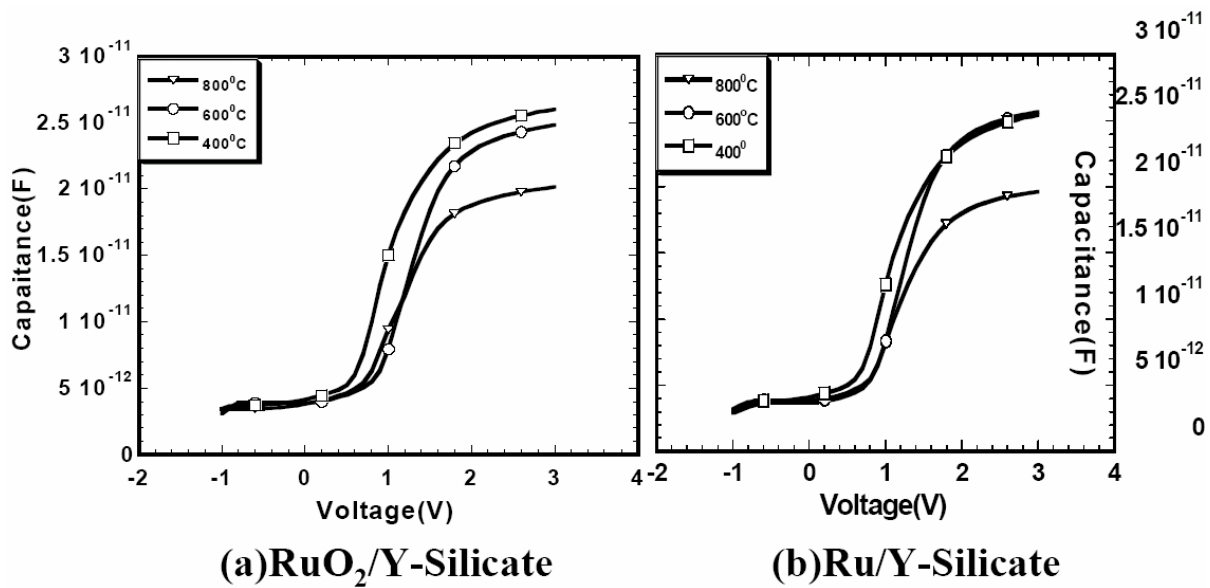


**Figure 6.4** C-V curves of RuO<sub>2</sub> and Ru gate electrodes on Y-Silicate after 400°C, 600°C and 800°C anneal in N<sub>2</sub>.

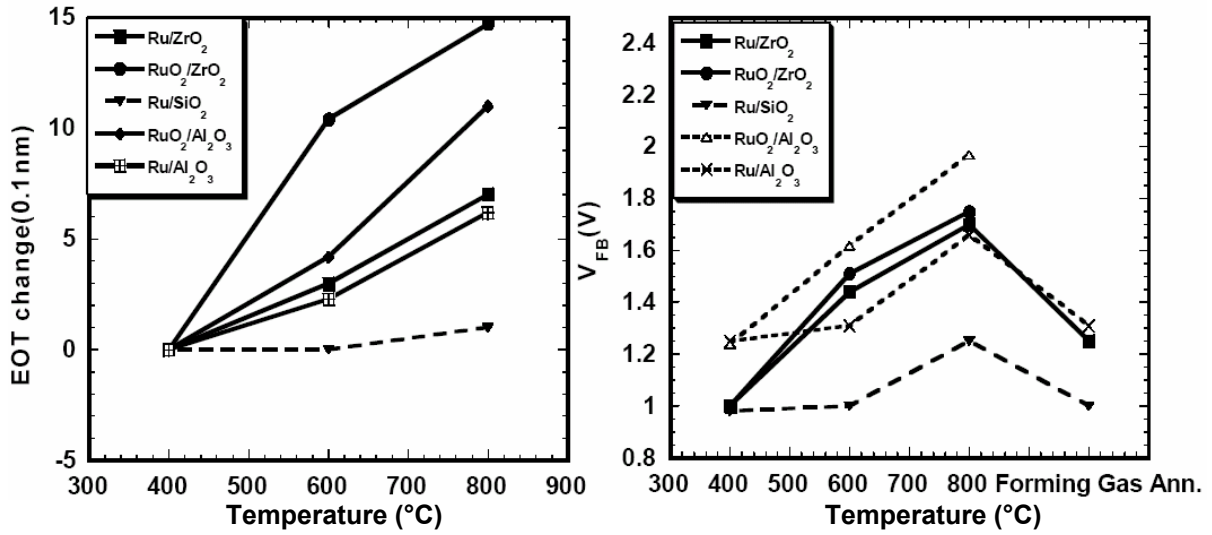


**Figure 6.5** (a) EOT change and (b)  $V_{FB}$  shift as a function of annealing temperature of Ru and  $RuO_2$  gate electrodes on  $SiO_2$ ,  $Al_2O_3$  and  $ZrO_2$  after 400°C, 600°C and 800°C anneal in  $N_2$  and subsequent forming gas anneal.

Chapter 7 is a reprint of a paper that appeared on pages 4419 – 4421 of  
Applied Physics Letters, Volume 80, Issue 23 in 2002

## **The Role of the OH Species in High-k/Polycrystalline Silicon Gate Electrode Interface Reactions**

Theodosia Gougousi, Michael J. Kelly and Gregory N. Parsons

Department of Chemical Engineering, North Carolina State University

### **Abstract**

In this article, reactions occurring at the interface between polycrystalline silicon (poly-Si) and  $\text{LaSiO}_x$  high-dielectric-constant (high-k) insulating layers are characterized using X-ray photoelectron spectroscopy. Dielectrics were formed by sputter deposition of metal on silicon, followed by oxidation at  $900^\circ\text{C}$ . Amorphous silicon was deposited on top by plasma-enhanced chemical vapor deposition (PECVD) from silane, followed by anneal at  $650\text{-}1050^\circ\text{C}$ . We show that if the dielectric layer is exposed to sufficient water vapor before polysilicon deposition, annealing at  $1050^\circ\text{C}$  for 10s is sufficient to completely oxidize  $\sim 25\text{\AA}$  of deposited silicon. Minimal reaction is observed without deliberate water exposure. This demonstrates the importance of the dielectric surface condition in determining reactivity of high-k/polysilicon interfaces.

## **Specific Contribution**

During these experiments, I was training the principal author in the techniques involved with preparing high-k materials using the plasma-assisted dc sputter tool and the tube furnace. We worked closely together to prepare the films and to plan the experiments used to evaluate interface reactions. She deposited the lanthanum silicate dielectrics, and I performed the rapid thermal annealing experiments and collected the x-ray photoelectron spectra. We discussed the XP and FTIR spectra and worked together to interpret the results in terms of possible mechanisms for high-k/polycrystalline silicon interactions.

## 7 The Role of the OH Species in High-k/Polycrystalline Silicon Gate Electrode Interface Reactions

Significant work is currently focused on high dielectric constant insulators as possible replacements to SiO<sub>2</sub> in Metal Oxide Semiconductor devices.<sup>1</sup> Several high-k candidate materials have been proposed. However, there are still serious obstacles such as fixed charge, poor carrier mobility, and instability when in contact with silicon.<sup>2,3</sup> Several factors influence the Si-dielectric interface reactivity, and significant effort has been devoted in understanding it.<sup>4,5,6,7</sup> However, there is very little documented work on the reactions occurring in the upper interface, between the dielectric and the gate material. In this article we offer some insight into the role H<sub>2</sub>O plays on the poly-Si/LaSiO<sub>x</sub> interface reactivity.

We prepared LaSiO<sub>x</sub> dielectrics by La metal sputtering on Si <100> substrates and ex-situ high temperature furnace annealing in the presence of an oxidizing agent (N<sub>2</sub>O) using the tools and procedures published previously.<sup>8</sup> Approximately 330Å of La was deposited, resulting in thick (>500Å) LaSiO<sub>x</sub> films. Prior to deposition, the substrates were cleaned in J.T. Baker Clean 100, rinsed in DI water, and dipped in buffered oxide etch (BOE). Films were characterized using X-ray photoelectron spectroscopy (XPS) and infrared absorption spectroscopy. The XP spectra were obtained using a Riber LAS3000 equipped with a single pass mirror MAC2 analyzer and a Mg Kα (hν=1253.6 eV) non-monochromatic X-ray source at a 90° take-off angle with 0.1eV step size. Charge compensation was performed by setting the adventitious C 1s peak to a binding energy of 285.0 eV. The Infrared (IR) spectra were obtained in transmission mode using a Magna-IR System 750 from ThermoNicolet.

XPS analysis indicated that under our process conditions La mixed with Si very efficiently to produce material with predominantly La-O-Si bonding (i.e. lanthanum

“silicate”). Additional experiments have shown that the hydroxyl content of the silicate films can be controlled by predeposition substrate cleaning or postdeposition atmospheric exposure. Figure 7.1 shows the IR absorbance spectra for two such samples. The so-called “dry” sample was prepared by deposition of 330Å of La and subsequent anneal at 900°C for 10 min, and kept in the dry atmosphere of a desiccator to prevent H<sub>2</sub>O absorption. Such films were fairly insensitive to H<sub>2</sub>O uptake and had not absorbed IR detectable amounts of H<sub>2</sub>O even after two weeks of atmospheric exposure. However, identically prepared samples that were deposited on insufficiently cleaned substrates exhibited a more hydrophilic nature. The so-called “wet” sample in Fig. 7.1 was deposited on a surface rinsed in poor quality deionized (DI) water and exposed to H<sub>2</sub>O vapor at room temperature for about 40h after preparation. Its absorption IR spectrum exhibited a broad peak around 3500cm<sup>-1</sup> associated with H<sub>2</sub>O/OH presence<sup>9</sup> in the bulk of the film.

Thin layers of amorphous silicon were deposited by PECVD at ~150°C using silane/helium mixtures. These were 25 and 35Å thick for the “wet” and “dry” samples respectively. Deposition of a-Si layers on c-Si and SiO<sub>2</sub> is known to progress through the nucleation of Si islands, which, as growth proceeds, increase in size and number and eventually coalesce to form a uniform layer. Under the conditions used in this experiment, Atomic Force Microscopy analysis indicated that 25Å of a-Si deposition is sufficient to achieve fully coalesced films on c-Si and SiO<sub>2</sub>.<sup>10</sup> Slightly larger root mean square (RMS) roughness was observed for Si deposited on the high-k than for Si on c-Si and SiO<sub>2</sub>, especially for the “wet” sample, which could be related to the underlying dielectric roughness or to incomplete coalescence of the silicon layer.

After deposition of the a-Si film, each “wet” and “dry” sample was divided into 3 parts, and each part was exposed to different thermal treatment. One was left as deposited, while the others were annealed at 650°C for 30s in Ar in a Rapid Thermal Anneal (RTA) instrument. One of the samples was further annealed at 1050°C for 10s. Subsequently, XPS was used to probe the polySi/LaSiO<sub>x</sub> interface for each sample.

Figure 7.2 (top) shows typical XP spectra for the 3 samples originating from the “dry” sample while Fig. 7.2 (bottom) shows the corresponding spectra for the “wet” sample. This energy range includes contributions from the Si 2p and La 4d electrons making peak deconvolution difficult. However, the Si<sup>0</sup> peak at 99.3 eV, originating from the amorphous Si layer,<sup>11</sup> is readily distinguished. Upon annealing the “dry” sample, the position of the Si<sup>0</sup> peak did not shift substantially, although its magnitude decreased somewhat consistent with a small amount of silicon oxidation. For the “wet” sample, anneal at 1050°C resulted in the disappearance of the Si<sup>0</sup> peak, consistent with nearly complete consumption of the polysilicon layer.

A close look at the XPS data for the LaSiO<sub>x</sub> films gives insight into possible mechanisms for the observed silicon oxidation. For the spectra in the top part of Figure 7.3, corresponding to the “dry” sample: (a) as deposited; (b) annealed at 650°C; and (c) annealed at 1050°C, the La 3d peaks shifted by about 0.5 eV to higher binding energy upon anneal, and are consistent with a mixed metal/silicon oxide (silicate) with fairly stable composition. The increase in the integrated intensity is consistent with an increase in the La concentration near the surface due to silicon or La diffusion. For the “wet” sample (Fig. 7.3, bottom) the La 3d spectrum shows a markedly different bonding environment for the as-deposited and annealed states. For the as deposited film, the peaks were shifted by almost 2.5 eV to higher

binding energy as compared to the “dry” sample, which was attributed to the presence of  $\text{La}(\text{OH})_x$ . Upon anneal, the spectra have features qualitatively similar to the annealed “dry” sample.

In the O 1s XP spectra (not shown), annealing of the “dry” sample resulted in no significant shifts in the peak position. However, annealing the “wet” sample at  $1050^\circ\text{C}$  resulted in significant shift ( $\sim 1.5$  eV to lower binding energy). It is important to note that for both samples the XPS data in Fig. 7.3 indicates that the dielectric did not phase separate into  $\text{La}_2\text{O}_3$  and  $\text{SiO}_2$  even when heated at  $1050^\circ\text{C}$  for 10s.

The IR and XPS data are consistent with the following possible explanation. Exposing  $\text{LaSiO}_x$  films to significant water vapor results in OH absorption into the film bulk. When silicon is deposited on the dielectric, the incorporated OH enables reactions to proceed at the interface. Annealing the “wet” sample at  $650^\circ\text{C}$  results in significant loss of H and OH species, producing a large number of unsatisfied bonds. Silicon atoms diffusing from the deposited silicon layer can then satisfy these bonds and be oxidized to form a mixed metal/silicon oxide. The reaction proceeds further upon anneal at  $1050^\circ\text{C}$ , consistent with the distinct increase in La-related peak intensities. If the concentration of hydroxyl groups is sufficiently large and the thickness of the silicon is sufficiently thin, the oxidation reaction may completely oxidize the silicon layer (consistent with the Si 2p data shown for the “wet” sample in Figure 7.2). In contrast, XPS data for the “dry” sample shows no substantial change in the bonding structure at the interface. The small decrease in silicon thickness could be due to a reaction proceeding at a much-reduced rate. We must conclude that the presence of the OH groups substantially enhances reactivity at the interface between polysilicon and La-silicates. We are currently investigating similar effects in other high-k materials.

The authors would like to thank Scott Burnside, Tammi Schmit and Justin Bennett for assistance with the XPS data, Rob Ashcraft and Dong Niu for assistance with the IR and RTA, and Kevin Bray for assistance with the surface roughness analysis. Financial support from SRC and NSF is gratefully acknowledged.

## References

- 1 S. I. Association, The International Technology Roadmap for Semiconductors, 1999 Edition, International SEMATECH Austin, TX, 1999.
- 2 G.D. Wilk, R.M. Wallace and J.M. Anthony, *J. Appl. Phys.* **89**(10), 5243 (2001) and references therein.
- 3 L. Manchanda, M.D. Morris, M.L. Green, R.B. van Dover, F. Clemens, T.W. Sorsch, P.J. Silverman, G. Wilk, B. Busch, S. Aravamundham, *Microelectron. Eng.* **59**, 351 (2001).
- 4 J. J. Chambers and G. N. Parsons, *Appl. Phys. Lett.* **77**(25), 2385 (2000).
- 5 H. Ono, T. Katsumata, *Appl. Phys. Lett.* **78**(13), 1832 (2001)
- 6 J. J. Chambers, B. W. Busch, W. H. Schulte, T. Gustafsson, E. Garfunkel, S. Wang, D. M. Maher, T. M. Klein, G. N. Parsons, *Appl. Surf. Sci.* **181**, 87 (2001)
- 7 P. D. Kirsch and J. G. Ekerdt, *J. Vac. Sci. Technol. A* **19**(1), 207 (2001).
- 8 J. J. Chambers and G. N. Parsons, *J. Appl. Phys.* **90**(2), 918 (2001)
- 9 A. Gupta and G. N. Parsons, *J. Vac. Sci. Technol. B* **18**(3), 1764 (2000).
- 10 K. R. Bray and G. N. Parsons, *Phys. Rev. B* **65**(3), 035311/1-035311/8 (2002).
- 11 J. F. Moulder, W. F. Stickle, P. E. Sobol, and K. D. Bomben, *Handbook of X-ray Photoelectron Spectroscopy* (Perkin-Elmer Corporation, Eden Prairie, MN, 1992).

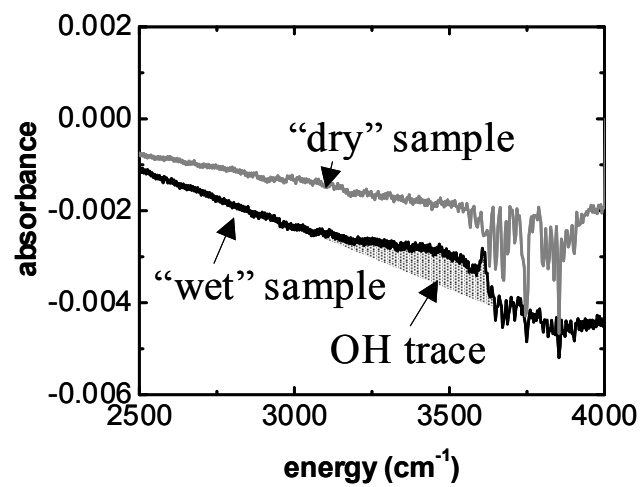


**Figure 7.1** IR absorbance spectra for the “wet” and “dry” samples. The OH peak is clearly distinguishable in the so-called “wet” sample spectrum.

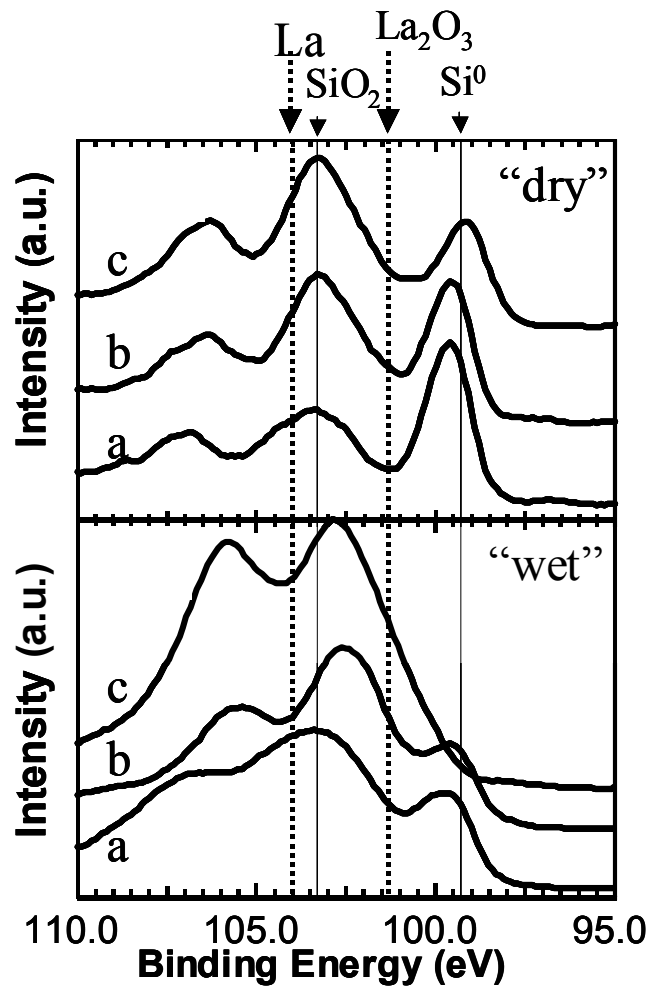


**Figure 7.2** Si 2p and La 4d XPS spectra for the “dry” and “wet” samples. Samples (a) are as deposited, (b) annealed at 650°C for 30s in Ar, and (c) annealed at 1050°C for 10s in Ar after deposition of the a-Si. For the “wet” sample the Si layer is completely consumed after anneal at 1050°C.

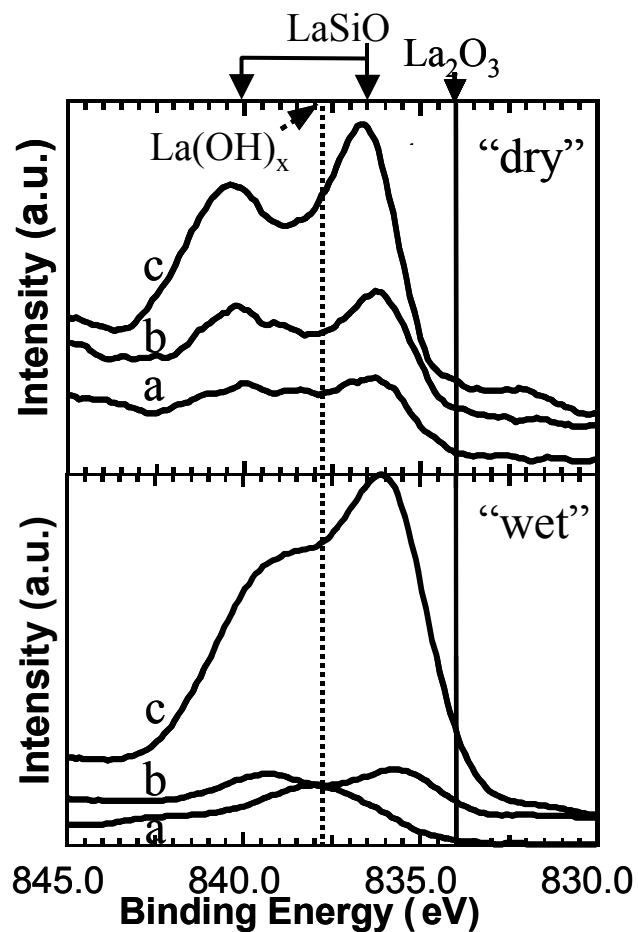


**Figure 7.3** La 3d XPS spectra for the “dry” and “wet” samples. Samples (a) are as deposited, (b) annealed at 650°C for 30s in Ar, and (c) annealed at 1050°C for 10s in Ar after deposition of the a-Si. For the as deposited “wet” sample, the La bonding environment is different from the other samples. This is attributed to the presence of OH. Upon anneal, the OH is desorbed/replaced by Si and the XPS spectra become comparable to those for the “dry” sample.

Chapter 8 is a paper that appeared on pages 5305 – 5314  
of Chemistry of Materials, Volume 17, Issue 21, in 2005

**In-Situ Infrared Spectroscopy and Density  
Functional Theory Modeling of Hafnium Alkylamine  
Adsorption on Si-OH and Si-H Surfaces**

M. Jason Kelly, Joseph H. Han,\* Charles B. Musgrave\* and Gregory N. Parsons

Department of Chemical and Biomolecular Engineering  
North Carolina State University, Raleigh North Carolina 27695

\*Department of Chemical Engineering,  
Stanford University, Stanford California 94305

## Abstract

In-situ attenuated total internal reflection infrared spectroscopy has been used to examine initial adsorption and reaction steps in atomic layer deposition of HfO<sub>2</sub> from tetrakis(diethylamino) hafnium (TDEAHf) on SiO<sub>2</sub> and hydrogen-terminated Si(100) surfaces. At low deposition temperatures (25- 250 °C), TDEAHf directly reacts with the Si-H surface, resulting in partial removal of Si-H bonds and formation of a four-membered Si-O-Hf-Si bonding structure that can rapidly oxidize. The hydrogen removal process is observed to continue through many cycles of TDEAHf/H<sub>2</sub>O exposure, signifying continued reactivity of the Hf precursor with the silicon surface. Density functional theory calculations have been performed for various reactions between tetrakis(dimethylamino) hafnium and Si-H surfaces, and several possible reaction pathways for hydrogen removal have been identified and analyzed. The calculations suggest that hydrogen removal proceeds by H abstraction by an amine ligand of the Hf precursor, and that the abstraction reaction is made more facile by the presence of OH on the otherwise H-terminated Si surface.

## 8 In-Situ Infrared Spectroscopy and Density Functional Theory Modeling of Hafnium Alkylamine Adsorption on Si-OH and Si-H Surfaces

### 8.1 Introduction

Techniques to experimentally observe and analyze fundamental reaction mechanisms during deposition of advanced dielectric materials on silicon surfaces are important to help direct reactions and achieve well-controlled bonding at dielectric/semiconductor interfaces.<sup>1</sup> In typical processes for deposition of high dielectric constant (high-k) insulators on silicon, an oxide or nitride interface layer is usually formed at the dielectric/semiconductor interface either intentionally before deposition (to control nucleation and interfacial reaction) or as a reaction byproduct during film deposition. This interfacial layer influences interface defect density, and reduces the gate capacitance, limiting reduction of the equivalent oxide thickness. Atomic layer deposition (ALD) is an attractive method for forming ultrathin gate stacks because, in principle, well-controlled sequential reactions in ALD allow the desired film composition and structure to be achieved.<sup>2,3</sup> Several groups have reported the effects of various surface pretreatments, including hydrogen termination, on atomic layer deposition of high- $\kappa$  dielectrics.<sup>4-7</sup> Hydrogen termination of the silicon surface significantly inhibits dielectric film growth during the initial ALD cycles<sup>4-6</sup> resulting in poorly controlled interface structures. In-situ infrared absorption has been used to study detailed reactions between trimethyl aluminum (TMA) and hydrogen-terminated silicon surfaces.<sup>8,9</sup> Results demonstrate a direct reaction between Si-H and TMA, resulting in Si-Al-(CH<sub>3</sub>)<sub>2</sub> surface

units. It is suggested that upon exposure to water vapor, these surface species promote subsurface silicon oxidation and formation of a silicon oxide interface layer. These results have been used to suggest Al-methyl groups as an alternate surface passivation approach for ALD of other dielectrics, including HfO<sub>2</sub>. Ab initio calculations<sup>10</sup> show that the reaction between TMA and the Si-H surface forms Si-Al-(CH<sub>3</sub>)<sub>2</sub> and CH<sub>4</sub> as products and is exothermic overall, with a reaction barrier of ~28 kcal/mol. TMA is a very reactive precursor, where, for example, it can react directly with siloxane bridges on SiO<sub>2</sub> surfaces with no Si-OH present.<sup>11</sup> Reactions between metal-containing precursors and silicon surfaces are of interest to enable control over dielectric/silicon interface structure, and here we investigate the case of hafnium alkylamine reactions with Si-OH and Si-H surfaces.

Metal-alkylamine precursors are of interest as precursors for ALD because they do not involve halogen atoms, and many are liquids at room temperature or have low melting points. Furthermore, alkylamines are generally more easily oxidized than metal alkoxides because metal-nitrogen bonds are usually weaker, and therefore more easily broken, than the metal-oxygen bonds in alkoxides. Similarly, alkylamines are generally more stable than metal-alkyls, providing a balance between reactivity and stability in processing.<sup>12</sup> This article presents a study of reaction mechanisms in insulator deposition by ALD on hydrogen-terminated and preoxidized silicon surfaces. Of particular interest are the mechanisms associated with atomic layer deposition of hafnium oxide from hafnium ethylamine precursors onto a hydrogen-terminated silicon (100) surface. The goal is to better understand the initial reaction sequences in HfO<sub>2</sub> deposition that can help enable the fabrication of well-controlled, atomically abrupt silicon/metal-oxide interfaces.

## 8.2 Experimental Methods

In this article, initial adsorption of tetrakis(diethylamino)hafnium on SiO<sub>2</sub> and hydrogen-terminated Si surfaces is characterized using in-situ attenuated total internal reflection Fourier transform infrared spectroscopy (ATR-FTIR). In this approach<sup>13</sup> infrared radiation is focused through KBr reactor windows onto the beveled edge of a high resistivity silicon wafer resulting in total internal reflection and propagation of the radiation along the wafer. Upon exiting the wafer, the photon flux is directed by a parabolic mirror to a HgCdTe IR detector cooled with liquid N<sub>2</sub>. The IR bench, beam path, and external detector are all enclosed and flushed with a continuous flow of purge gas (dry air with reduced CO<sub>2</sub> levels). Species adsorbed on the silicon surface will interact with and absorb the evanescent IR wave directed along the surface normal. Comparing the IR signal before and after surface adsorption steps allows the vibrational properties of the adsorbed species to be observed. A schematic of the reactor setup used for the experiment (base pressure  $\sim 2 \times 10^{-7}$  Torr) is shown in Figure 8.1. The chamber is equipped with a plasma generation source to study effects of surface plasma exposure. The liquid precursor flux is introduced from a heated vessel through an ultrahigh vacuum leak valve. Before beginning experiments, the precursor vessel is cooled and pumped through a bypass line to help remove volatile impurities. For the geometry used, the IR signal interacts with the front surface of the ATR crystal approximately 40 times as it progresses through the 40-mm wafer. Because of oxygen impurities and silicon multiphonon modes in the Si ATR crystal, the IR signal is absorbed at energies below  $\sim 1500\text{cm}^{-1}$ . The instrument therefore allows analysis between  $\sim 4000\text{cm}^{-1}$  and  $1500\text{cm}^{-1}$ , which is sufficient for a large number of vibrational modes of interest in metal-organic/Si reactions, including C-H ( $2800\text{-}3100\text{cm}^{-1}$ ), Si-H ( $2000\text{-}2200\text{cm}^{-1}$ ), N-H ( $3400\text{-}$

$3500\text{cm}^{-1}$ ), OH ( $3500\text{-}3900\text{cm}^{-1}$ ) and others. This approach is sensitive to in-plane and out-of-plane vibrations of the adsorbate species. Polarization was not used for the work reported here, and all spectra shown are referenced to a spectrum of the starting surface without any further correction or baseline subtraction unless specifically noted. Figure 8.2(a) shows a spectrum from an octadecyltrichlorosilane (OTS) self-assembled monolayer measured on an oxidized silicon ATR crystal in this system. Features associated with carbon-hydrogen stretches on methyl and methylene groups are observed. Figure 8.2(b) shows the total single-beam signal through the ATR crystal as a function of substrate temperature. The signal decreases somewhat between room temperature and  $175\text{ }^{\circ}\text{C}$ , but at higher temperatures, thermal free-carrier generation increases the IR scattering, and at  $300\text{ }^{\circ}\text{C}$ , the signal is attenuated by  $>50\%$ . The temperature range for experiments is limited to about  $300\text{ }^{\circ}\text{C}$ . At elevated temperature ( $200\text{-}250^{\circ}\text{C}$ ), the system was stable, and transmission signal intensity was very reproducible.

The starting surfaces of Si(100) ATR crystals were prepared in air by thermal or wet-chemical treatment before each exposure sequence and were loaded into the system within 10 min of preparation. Several pretreatment approaches were studied, including chemical surface oxidation to produce  $5\text{ \AA}$  hydroxyl-rich  $\text{SiO}_2$ <sup>4</sup> (following the common RCA oxidation process: aqueous  $\text{H}_2\text{O}_2/\text{NH}_4\text{OH}$  at  $45\text{ }^{\circ}\text{C}$ ), and silicon/hydrogen termination by thermal oxidation at  $900\text{ }^{\circ}\text{C}$  to produce  $\sim 30\text{ \AA}$  sacrificial oxide followed by surface etching in dilute HF acid solution. Thermal  $\text{SiO}_2$  surfaces were also prepared by oxidation of HF-last surfaces in air at  $900\text{ }^{\circ}\text{C}$  for 3 min. Tetrakis(diethylamino)hafnium [ $\text{Hf}(\text{N}(\text{C}_2\text{H}_5)_2)_4$ ] (TDEAHf) was used as the source for hafnium. The precursor is generally kept at room temperature and then is heated to  $65\text{ }^{\circ}\text{C}$  for the experiment.

The reaction sequence involved: (i) preparing the ATR wafer surface by external wet chemical treatment and placing the surface in a vacuum system to pump to the  $10^{-6}$  -  $10^{-7}$  Torr range; (ii) comparing the IR signal from the clean surface to a reference wafer to confirm surface cleanliness; (iii) heating the sample and allowing 30 min for the temperature to equilibrate; and (iv) introducing precursor to the reaction chamber and monitoring pressure and IR signal as a function of time. The total reactant exposure in Langmuirs was estimated for each spectrum collected, and a range of surface exposures between  $10^3$  and  $10^7$  Langmuirs ( $1 \text{ L} = 10^{-6} \text{ Torr-sec}$ ) was investigated. Typical exposure pressure was in the 1 - 10 mTorr range. Exposure flux and the signal to noise in the spectroscopy system are sufficient to enable reproducible data set acquisition at approximately 30-s intervals. For the spectra shown here, the chamber was evacuated before each measurement, and typically 512 or 1024 scans were collected at  $4 \text{ cm}^{-1}$  resolution, corresponding to a data collection time of ~10-20 min per spectrum. Substrate temperature was fixed between room temperature and ~250 °C, and IR spectra were collected at the substrate temperature. After precursor exposure, the reaction sequence concluded with: (v) evacuating the system and then repeating the exposure and measurement procedure using the water vapor reactant.

### **8.3 Theoretical Methods**

The theoretical analysis was based on quantum chemical calculations using the B3LYP hybrid density functional theory (DFT) method<sup>14, 15</sup> and a mixed Gaussian basis set. For computational efficiency, simulations were performed using the dimethyl precursor, which has similar reactivity and spectroscopic properties to the diethyl species, except that it precludes beta-hydride elimination and, for example, C-C stretching modes. Hf and Si atoms are described using the Los Alamos LANL2 effective core potential (ECP) and a valence

double- $\zeta$  basis set.<sup>16-18</sup> Previous calibration studies have shown that polarization functions on first row atoms are critical to obtaining accurate energies;<sup>19</sup> as such, the D95(d,p)<sup>20</sup> basis set was applied to all H, C, N, and O atoms including the OH\* and H\* surface species and Hf[N(CH<sub>3</sub>)<sub>2</sub>]<sub>4</sub> ligands. The \* denotes surface groups as opposed to the atoms used to terminate the subsurface atoms. We optimize the molecular geometries to locate stationary points and perform frequency calculations at these geometries to predict the vibrational signatures of each structure, to verify the nature of the stationary points, to calculate zero-point energy corrections, and to construct the associated partition functions from which thermochemical properties are calculated. For the frequency calculations, the hydrogen atoms that terminate the subsurface silicon atoms were given a mass of 1000.0 amu in order to decouple those vibrational modes from the ones generated by surface Si-H\* species. All calculations are performed using GAUSSIAN 98.<sup>21</sup> The default convergence criteria were applied, and the calculated frequencies that are presented have not been scaled.

## **8.4 Experimental Results**

### **8.4.1 Analysis of starting surfaces**

Figure 8.3 shows the infrared signal for the as-prepared chemical oxide and HF-last surfaces. Spectra are shown as acquired immediately after placing the substrates in the chamber, and after heating and vacuum exposure. The background spectra for these spectra were obtained from a thermally oxidized silicon wafer. For the chemical oxide, shown in Figure 8.3(a), broad features consistent with a high density of associated hydroxyl surface groups (3000-3800 cm<sup>-1</sup>) are observed, and the intensity of the OH modes decreases upon vacuum anneal for 3h at 200 °C. Some C-H modes are also observed, which are likely due to

organic adsorption during sample transfer in ambient. For the precursor adsorption studies described below at 200°C, a large fraction of surface hydroxyl groups will remain. For the HF-last surface, shown in Figure 8.3(b), Si-H stretching modes are observed, consistent with a typical rough and faceted hydrogen terminated Si(100) surface.<sup>22</sup> Some absorption due to hydroxyl groups may also be present. The surface hydrogen is stable upon a 90-min anneal at 40 °C, but the hydrogen desorbs upon annealing at 600 °C for 20 min.

#### 8.4.2 TDEAHf exposure on SiO<sub>2</sub>

Figure 8.4 shows infrared spectra collected as a function of TDEAHf exposure at room temperature on the thermally oxidized silicon surface. The bottom spectrum corresponds to a  $1.2 \times 10^4$  L TDEAHf exposure, and spectra for progressively increasing exposure are also shown. The top two spectra were collected after the surface was exposed to water vapor. All the spectra in Figure 8.4 show several characteristic features, including modes at ~2970, 2930, 2870, and 2830  $\text{cm}^{-1}$  and a shoulder near 2775  $\text{cm}^{-1}$ . The features between 2830 and 2970  $\text{cm}^{-1}$  are consistent with symmetric and asymmetric methyl (CH<sub>3</sub>) and methylene (CH<sub>2</sub>) stretches of a surface-bound Hf-diethylamine ligand. Features are also expected to arise from charge-induced frequency lowering of the primary C-H mode because of interaction with the neighboring N lone pair,<sup>23, 24</sup> giving rise to additional structure (i.e., Bohlmann band) in the C-H stretch spectrum. Several sharp modes from ~3600 to 3900  $\text{cm}^{-1}$  are related to vapor-phase water and CO<sub>2</sub> in the beam path, and data in this range is removed from the figures. A strong doublet at 2340/2360  $\text{cm}^{-1}$  is also observed because of CO<sub>2</sub> in the beam path. A broad mode near 3200  $\text{cm}^{-1}$  is assigned to N-H modes related to adsorption or reaction on the KBr reactor windows. Pumping on the chamber at  $<10^{-6}$  Torr for several hours resulted in selective loss of the 3200  $\text{cm}^{-1}$  mode. On the oxide surface, the intensity of the C-H modes is

observed to increase with exposure time and a plot of total absorbance versus exposure follows first-order Langmuir kinetics:  $(1 - \theta) = \exp[-(J \cdot t)/n_0 \zeta]$  where  $\theta$  is the surface coverage fraction,  $(J \cdot t)$  is the surface precursor exposure,  $n_0$  is the density of surface sites for adsorption, and  $\zeta$  is the chemisorption reaction probability. Comparison of the integrated absorbance in the C-H stretching regime of the OTS monolayer in Figure 8.2 with the C-H absorbance from the adsorbed precursor after  $7.7 \times 10^6$  L exposure in Figure 8.4 results in an absorbance ratio  $[\int(A_{\text{TDEAHf}}) d\omega / \int(A_{\text{OTS}}) d\omega]$  of  $\sim 0.43$ . Extracting quantitative comparisons of molecular surface coverage from the relative integrated mode strengths of these different molecules is difficult because of expected differences in mode strengths and uncertainty in the number and nature of ligands remaining on the adsorbed precursor, but the magnitude of the absorbance ratio is only slightly larger (by a factor of  $\sim 1.2$ ) than what would be expected for monolayer coverage for TDEAHf with two diethylamino ligands and a smaller molecular surface density for TDEAHf relative to OTS. The exposure of  $\sim 8 \times 10^6$  L observed for saturation is larger than expected for typical ALD processing, and the fit to Langmuirian kinetics results in a small chemisorption reaction probability ( $\sim 3 \times 10^{-7}$ ). A reaction probability near 0.5 has been observed<sup>25</sup> for titanium alkylamide (tetrakis dimethylamino titanium, TDMAT) exposure on SiO<sub>2</sub>, and a large difference in adsorption probability between TDMAT and TDEAHf is not necessarily expected. Rapid oxidation of adsorbed precursor could, for example, reduce the surface ligand concentration, or surface impurities that act to block adsorption could reduce surface reaction probability. Organic impurities on the starting surface are observed in the IR data in Figure 8.3, and the ratio of integrated absorbance of the C-H related impurities to that for the OTS layer in Figure 8.2 is  $\sim 0.1$ .

After exposing the chemisorbed precursor to  $2 \times 10^8$  L of  $\text{H}_2\text{O}$ , the C-H related modes are observed to decrease, but they are not completely removed. We also observe the appearance of a broad mode near  $3700 \text{ cm}^{-1}$ , consistent with precursor oxidation and formation of surface OH groups. With continuing exposure to  $\text{H}_2\text{O}$ , a mode is observed to appear near  $2220 \text{ cm}^{-1}$ , possibly because of surface carbon-nitrogen stretching modes.

### 8.4.3 TDEAHf exposure on hydrogen-terminated silicon

Hydrogen-terminated silicon (100) surfaces were also exposed to TDEAHf at room temperature and at  $250^\circ\text{C}$ , and results are shown in Figures 8.5 and 8.6. The data in Figure 8.5 shows IR absorbance after exposing the hydrogen-terminated surface to various doses of TDEAHf at room temperature. The resulting spectra exhibit features similar to those in Figure 8.4 for room-temperature exposure on the  $\text{SiO}_2$  surface, but the C-H mode intensity is smaller on Si-H after nearly similar precursor exposure conditions. A plot of integrated C-H absorbance versus precursor exposure follows the trend of a Langmuir isotherm, where the saturation integrated intensity is approximately 10 times smaller than that observed for adsorption on  $\text{SiO}_2$ . The spectra in Figure 8.5 are referenced to the Si-H starting surface, so the negative-going features between  $2085$  and  $2130 \text{ cm}^{-1}$  correspond to the removal of Si-H stretching vibrational modes from the surface during exposure. This decrease is ascribed to hydrogen abstraction from Si-H surface bonds during precursor exposure, and proposed mechanisms for this abstraction are described below. The negative-going features in the Si-H stretch region are consistent with removal from  $\text{SiH}_2$  and  $\text{SiH}_3$  surface units, and that a complementary positive-going mode near  $2060 \text{ cm}^{-1}$  is likely due to formation of monohydride bonds, possibly by abstraction of hydrogen from  $\text{SiH}_2$ . Comparing the integrated absorbance of the negative-going Si-H mode relative to the Si-H starting surface,

the Si-H loss after  $\sim 2.5 \times 10^6$  L of TDEAHf exposure at room temperature corresponds to  $\sim 10\%$  of the total Si-H originally on the surface. This magnitude of Si-H loss along with the observed submonolayer ( $\sim 10\%$ ) surface coverage of TDEAHf is consistent with a concerted mechanism involving precursor adsorption and Si-H removal. The larger size of the TDEAHf compared to Si-H may suggest loss of multiple Si-H bonds for each precursor molecule adsorbed. However, experimental accuracy makes it difficult to draw detailed quantitative conclusions. Exposing the Si-H surface to the precursor, the C-H mode intensity is observed to follow Langmuir adsorption kinetics, similar to precursor exposure on SiO<sub>2</sub>, but the saturation concentration is  $\sim 10\%$  of the intensity observed on SiO<sub>2</sub>. The slope of the Langmuirian fit also shows a small surface reaction probability ( $\sim 10^{-7}$ ). The smaller uptake of precursor on Si-H versus SiO<sub>2</sub> is consistent with the mechanism and theoretical calculations presented below where precursor adsorption on Si-H occurs primarily on surface sites that are oxidized by water or other oxygen sources present in the reactor system.

Figure 8.6 shows results of sequential exposure of the Si-H surface to TDEAHf and water over many cycles at a substrate temperature of 250 °C. The first cycle consisted of long exposures to TDEAHf ( $3 \times 10^7$  L) and water ( $6 \times 10^7$  L), followed by 200 shorter cycles of  $\sim 2 \times 10^4$  L TDEAHf and  $2 \times 10^5$  L water, respectively. The figure shows results after each half cycle (i.e., after TDEAHf or H<sub>2</sub>O exposure) for cycles 1 and 20, as well as after TDEAHf exposure cycle numbers 100 and 200. In this case, cycle 1 was long exposures ( $3 \times 10^7$  L TDEAHf and  $6 \times 10^7$  L H<sub>2</sub>O) and cycles 2–200 were shorter ( $\sim (1-2) \times 10^4$  L TDEAHf and H<sub>2</sub>O). After the initial  $3 \times 10^7$  L TDEAHf exposure at 250 °C, the integrated absorbance of the negative-going Si-H mode is approximately the same as that shown in Figure 8.5 for  $3 \times 10^6$  L exposure at room temperature. The results in Figures 8.5 and 8.6

consistently show removal of Si-H modes during TDEAHf exposure to be not strongly dependent on substrate temperature. However, the Si-H starting surface is expected to be different at different temperatures, making quantitative comparisons of temperature dependence difficult to interpret. It is interesting to note in Figure 8.6 that as the Si-H surface is exposed to repeated TDEAHf/H<sub>2</sub>O cycles, the intensity of the negative-going Si-H mode continues to increase indicating that hydrogen continues to be removed even after more than 100 TDEAHf/H<sub>2</sub>O cycles. Therefore, H removal is not strongly related to exposure for a single cycle, but it continues to increase upon repeated TDEAHf and H<sub>2</sub>O exposures. A precursor adsorption and hydrogen abstraction scheme consistent with these results is discussed below. Figure 8.7 shows X-ray photoelectron spectroscopy data of Si-H and SiO<sub>2</sub> surfaces after exposure to 10 cycles of TDEAHf and H<sub>2</sub>O at 250 °C. The XPS measurements were performed with a Riber LAS3000 (MAC2 analyzer, Mg K $\alpha$   $h\nu=1253.6$  eV, nonmonochromatic X-ray source) at 75° takeoff-angle with 0.1 eV step size, and the adventitious C 1s peak was set to a binding energy of 285.0 eV. The data confirms the presence of Hf and O on both surfaces, with somewhat less Hf present on the initially hydrogen-terminated surface. The peak positions are consistent with mixed Si-O and Hf-O bonds in the near surface region.

The structures of the Si-H IR vibrational modes for the initial surface and after various exposure doses at 25 and 250 °C are shown in detail in Figure 8.8. The spectrum of the initial surface shows a broad Si-H mode, consistent with surface roughness and a variety of Si-H, SiH<sub>2</sub>, and SiH<sub>3</sub> surface species.<sup>22</sup> After a single long exposure of the Si-H surface to TDEAHf at 25 or 250 °C, the Si-H mode shows a decrease between 2070 and 2150 cm<sup>-1</sup>, consistent with loss of H from SiH<sub>3</sub> and SiH<sub>2</sub> bonding sites. After the initial precursor

exposure dose at 25 and 250°C, both spectra show a positive-going feature at 2060 cm<sup>-1</sup> which indicates a change in the local environment for the Si-H vibration. This could result from conversion of the higher hydrides to monohydride (Si-H) units on the surface through hydrogen abstraction, or it may result from a change in one or more of the back-bonds made by the local silicon atom, where charge donation to the silicon can result in a shift of the Si-H frequency to lower wavenumbers. The conversion of higher hydrides to Si-H is consistent with a preference for abstraction of H from SiH<sub>2</sub> and SiH<sub>3</sub> units over monohydride modes on the growth surface. After many cycles at 250 °C (top spectrum in Figure 8.8), the mode shows a net decrease at 2060 cm<sup>-1</sup>, indicating the loss of these converted (or otherwise frequency shifted) Si-H bonds.

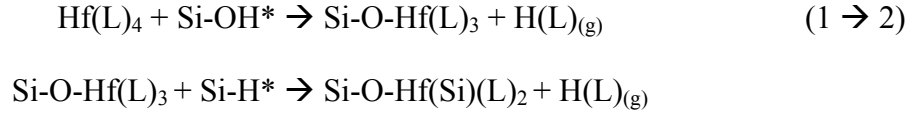
## **8.5 Theoretical Results**

The theoretical analysis of hafnium alkylamine adsorption and reaction on SiO<sub>2</sub> and Si-H\* surfaces is made complex by the fact that the hydrogen-terminated Si(100) surface explored experimentally has significant atomic-scale surface roughness and faceting, resulting in a wide range of surface hydride modes. Modeling of this rough extended surface using quantum chemical methods is not readily feasible. To theoretically explore the nature of the reaction between hafnium alkylamines and the SiO<sub>2</sub> and Si-H\* surfaces, we have used the 2 x 1 reconstructed Si(100) surface with tetrakis(dimethylamino) hafnium (TDMAHf) as a model system and have obtained reaction potential energy surfaces (PES) and representative vibrational spectra. In this case, the vibrational spectra obtained from theoretical analysis are expected to indicate and identify modes of interest, but they are not expected to reproduce or fully describe all the spectral features obtained experimentally. We consider the case of pure TDMAHf reacting with a fully hydrogenated Si-H\* (100) surface,

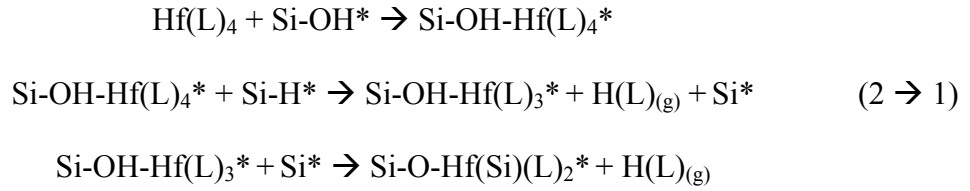
where hydrogen abstraction occurs by direct reaction of the Si-H with the Hf precursor, forming a reactive Si radical surface site. Our calculations predict a barrier of 16.8 kcal/mol for this abstraction reaction. While this process is not expected to be excluded, we postulate that an abstraction reaction will likely be more facile with some oxygen present, either in the form of isolated OH\* groups on the surface, or possibly as OH on the precursor itself, where the precursor has reacted with residual water vapor in the gas phase.<sup>26</sup> It is not unreasonable to expect some oxygen, most likely in the form of water, to be present in the reaction chamber during processing. Furthermore, it is likely that HF-last Si(100) will involve some surface OH groups because H<sub>2</sub>O is present in most HF sources, including anhydrous mixtures, and H<sub>2</sub>O is a product of HF and SiO<sub>2</sub>. We therefore consider the case of hydrogen abstraction from Si-H sites on the dimerized Si(100) surface where the Si-H are initially on a dimer site with an isolated Si-OH unit.

To model the reaction pathway for the first ALD half-reaction (i.e., TDMAHf reaction with a hydrogen-terminated Si surface with isolated Si-OH sites), we consider two possible reactions involving OH groups: (1) the TDEAHf reacts with the isolated Si-OH\* group through a hydrogen transfer to achieve a stable configuration; and (2) the TDEAHf reacts at the isolated OH\* site and abstracts a hydrogen atom from an adjacent Si-H\* site, resulting in Si-H bond removal. These reaction steps could occur sequentially, producing the final product state that is independent of the reaction sequence. We therefore explore theoretically two pathways: pathway 1 → 2, where hydrogen is first transferred from the OH\* to TDEAHf, followed by abstraction of neighboring hydrogen from Si-H\* by the surface –O–Hf(L)<sub>3</sub>\* product, and alternately, pathway 2 → 1, where physisorption of TDMAHf on the Si-OH site occurs first, leading to H abstraction from adjacent Si-H\*, followed by hydrogen

transfer to the surface  $\text{-Hf(L)}_3^*$  from the surface  $\text{Si-OH}^*$  group. The reaction pathway (1  $\rightarrow$  2) is written schematically as



and pathway (2  $\rightarrow$  1) can be written as



where (L) refers to the precursor dimethylamine ligand. Both pathways result in a four-membered Si-O-Hf-Si bonding structure that is expected to oxidize rapidly because of the high electron affinity of the Hf. We will show that on basis of the energetics of the reaction, the reaction pathway where reaction 1 precedes reaction 2 (i.e., pathway 1  $\rightarrow$  2) will likely dominate.

We consider the case of TDMAHf reacting first with a surface hydroxyl group. The PES for this reaction pathway (pathway 1  $\rightarrow$  2) for TDMAHf reacting with an  $\text{OH}^*$  site on H-terminated Si(100)-2 x 1 (modeled by  $\text{Si}_9\text{H}_{13}\text{-OH}$ ) is shown as the lower trace in Figure 8.9. In this case, TDMAHf first physisorbs at the  $\text{Si-OH}^*$  site through a hydrogen-bonded state that is 6.4 kcal/mol lower in energy than the gas-phase reactant (labeled Ads in Figure 8.9). The adsorbed precursor then reacts by transferring the H of the surface  $\text{Si-OH}^*$  through a transition state that is 1.2 kcal/mol above the H-bonded state. This leads to a product state that is 29.7 kcal/mol below the entrance channel, where  $\text{Hf}[\text{N}(\text{CH}_3)_2]_3^*$  is bonded to the

surface through a Si-O-Hf bridge, along with a dimethylamine (Ads Prod). Initially, the dimethylamine is bound to Hf through a dative bond, but it can readily desorb with an additional 2.4 kcal/mol (Des Prod). From this intermediate product (27.4 kcal/mol below the entrance channel), the surface Si-O-Hf[N(CH<sub>3</sub>)<sub>2</sub>]<sub>3</sub>\* can then abstract the neighboring Si-H\* through a barrier that is 4.8 kcal/mol below the original entrance channel. This results in a dimethylamine that is dative bonded to the Hf atom (12.8 kcal/mol below the entrance channel) (Ads Prod). When the dimethylamine desorbs, the final product with two dimethylamine ligands on the Hf atom is formed, along with a Si-O-Hf bond, and a direct Si-Hf bond (Des Prod). This final state is 2.0 kcal/mol above the original entrance channel. The energy for the desorption of the second dimethylamine is significantly larger than for the first, suggesting that residual dimethylamine may remain on the surface, necessitating a longer purge time or oxidant exposure time in the ALD process. The surface Si-Hf bond is expected to readily undergo oxidation during water exposure in the second ALD half-reaction. The overall calculated energy change of ~2 kcal/mol for this first half-reaction is small, even at room temperature.

An alternative reaction pathway (pathway 2 → 1) can initiate by reaction with a neighboring surface Si-H bond, and the PES for this route is shown as the upper line in Figure 8.9. In this reaction scheme, the gas-phase precursor amine ligand abstracts a H atom from a neighboring Si-H\* site without going through an initial physisorbed state, resulting in production of Si-OH-Hf[N(CH<sub>3</sub>)<sub>2</sub>]<sub>3</sub>\* where the Hf(L)<sub>3</sub> is dative bonded to the surface OH group. Again, hydrogen abstraction from the Si-H site by the N of the ligand leads to dimethylamine dative bonded to the Hf. Desorption of the dative-bonded dimethylamine byproduct leaves the dative bond between Hf and OH group intact and results in a Hf-Si

bond involving the Si from which the H was abstracted. This abstraction route proceeds over a transition-state barrier of 8.2 kcal/mol relative to the gas-phase reactant, with the resulting Si-OH-Hf[N(CH<sub>3</sub>)<sub>2</sub>]<sub>3</sub>\* and adsorbed dimethylamine intermediate 2.2 kcal/mol above the energy of the reactants. Desorption of dimethylamine from this intermediate requires an additional 3.5 kcal/mol. Next, the H from the surface Si-OH\* group could transfer to an alkylamine ligand via the four-centered ligand exchange reaction resulting in the elimination of a second dimethylamine ligand from the surface, forming the final product state. This product state is the same as for the pathway 1 → 2, where the Hf is linked to the surface through both a Si-O-Hf bridge and a Si-Hf bond.

The hydrogen transfer from the Si-OH\* in pathway 2 → 1 requires a significant distortion in the electronic and geometric configuration of the surface species, and the transition state (not calculated) between the endothermic intermediate state (Si-OH\*) and the final product state (Si-O-Hf-Si) becomes even less accessible at experimental temperatures. We conclude, therefore, that the surface reaction route which proceeds from 2 → 1 is not likely. For the direct abstraction route, the transition state is 16.8 kcal/mol above the entrance channel, whereas, for the reaction pathway 1 → 2, the fully stabilized intermediate states are all endothermic relative to the starting state. This means that if the reactants are not thermally accommodated, residual energy can be available to help drive the reaction, effectively increasing the rate of reaction through pathway 1 → 2 as compared to the direct abstraction route. We conclude, therefore, that the reaction scheme that proceeds from 1 → 2 is the likely mechanism for Si-H\* removal from hydrogen-terminated silicon surface during alkylamine precursor exposure.

Figure 8.10 shows the calculated vibrational spectra for the species involved in the calculated H transfer mechanism from the surface OH group. The first spectrum (bottom spectrum in the figure) shows the Si-H and O-H stretching modes of the initial surface at 2207 and 3880  $\text{cm}^{-1}$ , respectively. After reaction with TDMAH via H transfer from the OH group, the OH modes disappear while the Si-H stretch remains and other modes of the adsorbed precursor appear. An NH mode is calculated at 3512  $\text{cm}^{-1}$  from the dimethylamine byproduct that is dative bonded to  $\text{Hf}[\text{N}(\text{CH}_3)_2]_3^*$ . Upon exposure of the  $\text{Hf}[\text{N}(\text{CH}_3)_2]_3^*$  site to water, additional OH stretching modes appear as the amino ligand vibrational modes are removed.

Figure 8.11 shows the calculated vibrational spectra for the species involved in the calculated Si-H abstraction process. After reaction with TDMAH via H abstraction, the Si-H mode disappears while the other modes of the adsorbed precursor appear. The calculated results show an NH mode at 2916  $\text{cm}^{-1}$ , which is significantly red-shifted from its typical range. This mode is only present when the dimethylamine byproduct is dative bonded to the surface. Upon exposure of the  $\text{Hf}[\text{N}(\text{CH}_3)_2]_3^*$  site to water, additional OH stretching modes appear as the amino ligand vibrational modes are removed.

## **8.6 Discussion and Conclusions**

The experimental and theoretical results shown here give insight into the mechanisms and processes in hafnium alkylamine precursor adsorption and reaction on silicon oxide and hydrogen-terminated Si(100) surfaces. The data in Figure 8.4 is consistent with monolayer precursor adsorption on silicon oxide at low substrate temperatures, with incomplete removal of C-H containing ligands upon exposure to water vapor. Similar experiments for TDEAHf exposure on oxide surfaces at temperatures between 150 and 250°C show less C-H

absorbance, with a small reduction upon exposure to water vapor. Because of the high sensitivity of the TDEAHf to water vapor, some reaction between the precursor and ambient or physically absorbed water could proceed before the IR analysis. Also, changes in OH related features are difficult to interpret in the experimental system used, in part because of the broad width of the absorption band expected for associated surface OH, and because the surface OH density is sensitive to temperature and vacuum conditions for both the reference starting surface and the subsequent analyzed film. Precursor uptake on SiO<sub>2</sub> is also expected to be less than on HfO<sub>2</sub> surfaces because of differences in the nature and stability of reactive intermediates in these reactions.

It is important to note a significant distinction between physisorption of hafnium alkylamines on Si-OH surfaces (i.e., growth initiation on silicon oxide) versus on Hf-OH surfaces (i.e., growth continuation on hafnium oxide). For TDMAHf on the Si-OH surface, the dative-bonded complex initially formed between the precursor and surface Si-OH\* site is bound by ~6 kcal/mol, whereas the same precursor dative-bonded to Hf-OH\* sites is much more stable (~20 kcal/mol). This is because the precursor metal center has four Hf-N sigma bonds and four Hf-N d<sub>π</sub>-p<sub>π</sub> bonds which results in a fully occupied d-shell. This full shell does not allow formation of dative bonds between Hf and the lone pairs of the surface Si-OH\* sites and so the precursor forms an adduct that is hydrogen bonded to the surface OH. However, on Hf-OH\*, an amine ligand in the precursor can more readily break its d<sub>π</sub>-p<sub>π</sub> bond with the precursor metal because it can form a dative bond to a surface metal atom which acts as the Lewis acid, allowing the precursor metal atom to also act as a Lewis acid and dative bond to the oxygen of the surface OH. In the reactions considered above, after the N atom of the amine ligand removes H from either Si-H\* or Si-OH\*, the Hf center then accepts

electron density from the O atom of the surface OH site to form a stable Hf-O bond. Because the hydrogen-bonded precursor on SiOH\* is significantly less stable than the dative-bonded precursor to Hf-OH\*, this reaction does not involve intermediates that are as strongly trapped as on HfO<sub>2</sub>. Furthermore, the barrier to ligand exchange with the Si-OH site is insignificant. Consequently, we expect that most reactions at isolated Si-OH\* sites will proceed initially through hydrogen transfer from Si-OH\*. This is entirely exothermic relative to the entrance channel. However, the difference between Si-OH and Hf-OH in the initial precursor adsorption energy indicates that the chemisorption reaction probability at isolated Si-OH\* sites will be lower than that at Hf-OH\* sites.

Considering reactions on the Si-H terminated surface, the data in Figures 8.6-8 indicate that precursor adsorption involves a hydrogen removal step, and that the hydrogen removal continues over many precursor/water exposure cycles. Several different mechanisms could allow for hydrogen abstraction. For example, in the case of trimethyl aluminum exposure on Si-H surfaces, H abstraction is believed to proceed by direct formation of methane and dimethylaluminum bound to Si in an Al-Si linkage.<sup>9</sup> An analogous process for the hafnium alkylamine would result in formation of diethylamine and a Hf-Si bond, where three diethylamine ligands remained on the surface-bound hafnium. This “direct” abstraction from Si-H\* is not favorable because of the relatively large barrier of 16.8 kcal/mol for this pathway. Another possibility is the pathway described above, where the precursor adsorbs on reactive surface OH sites, followed by H abstraction from neighboring Si-H\* sites by surface-bound alkylamine ligands. On the Si-H starting surface, the OH density will normally be very low making the overall reactive sticking coefficient of the alkylamine also very low. This is consistent with the smaller intensity of surface C-H modes observed on the

Si-H surface as compared to the Si-OH surface. After undergoing the H transfer processes described above, the remaining alkylamine ligands are available to remove H atoms from neighboring Si-H\* surface sites. However, the removal of Si-H\* is limited to those sites within reach of the N atom of the alkylamine adsorbed at what was initially an Si-OH\* site. We believe, therefore, that the observed continuation in hydrogen removal occurs through the following mechanism. After the first half-reaction at the Si-OH\* sites on the H-terminated silicon surface, the product surface is exposed to H<sub>2</sub>O which readily reacts with the Hf-Si sites to create new Si-OH sites adjacent to existing Si-H sites. These new Si-OH/Si-H site pairs are then available to undergo the reaction set described above, so that precursors from subsequent growth cycles continue to remove H from the surface at positions further removed from the initial OH nucleation site. This scheme, on the basis of our predicted reaction mechanisms, is consistent with the data in Figure 8.6 that shows that subsequent exposure of the surface to water and precursor cycles results in continuous loss of Si-H from the growth surface.

The detailed reaction processes in ALD of HfO<sub>2</sub> on Si-H terminated surfaces is important for high-dielectric constant gate insulators in advanced transistor devices, where well defined reaction steps will be required to achieve submonolayer control of the Si/HfO<sub>2</sub> interface bonding structure. The results suggest that the hydrogen abstraction mechanism results in very reactive silicon radical and/or Si-Hf sites at the dielectric/insulator interface. These sites subsequently oxidize during processing forming interfacial silicon oxide and possibly mixed HfSiO<sub>x</sub> bonds. Alternate growth schemes or precursor structures may eventually be preferred that control or limit hydrogen abstraction to achieve better control of this critical interface during dielectric processing.

This work was supported by NSF grant # 0072784 and SRC/SEMATECH Front End Processing Center.

## 8.7 References

- 1 Murto, R. W.; Gardner, M. I.; Brown, G. A.; Zeitzoff, P. M.; Huff, H. R. *Solid State Technology* **2003**, 43-48.
- 2 Ritala, M.; Leskela, M. In *Handbook of Thin Film Materials*, Nalwa, H. S., Ed. Academic Press: San Diego, 2001; Vol. 1, Chapter 2.
- 3 Hausmann, D.; Kim, E.; Becker, J.; Gordon, R. G. *Chemistry of Materials* **2002**, *14*, 4350-4358.
- 4 Green, M. L.; Ho, M. Y.; Busch, B.; Wilk, G. D.; Sorsch, T.; Conard, T.; Brijs, B.; Vandervorst, W.; Raisanen, P. I.; Muller, D.; Bude, M.; Grazul, J. *Journal of Applied Physics* **2002**, *92*, 7168-7174.
- 5 Triyoso, D. H.; Hegde, R. I.; Grant, J.; Fejes, P.; Liu, R.; Roan, D.; Ramon, M.; Werho, D.; Rai, R.; La, L. B.; Baker, J.; Garza, C.; Guenther, T.; White, B. E.; Tobin, P. J. *Journal of Vacuum Science & Technology B* **2004**, *22*, 2121-2127.
- 6 Puurunen, R. L.; Vandervorst, W.; Besling, W. F. A.; Richard, O.; Bender, H.; Conard, T.; Zhao, C.; Delabie, A.; Caymax, M.; De Gendt, S.; Heyns, M.; Viitanen, M. M.; de Ridder, M.; Brongersma, H. H.; Tamminga, Y.; Dao, T.; de Win, T.; Verheijen, M.; Kaiser, M.; Tuominen, M. *Journal of Applied Physics* **2004**, *96*, 4878-4889.
- 7 Duenas, S.; Castan, H.; Garcia, H.; Barbolla, J.; Kukli, K.; Ritala, M.; Leskela, M. *Thin Solid Films* **2004**, *474*, 222-229.
- 8 Frank, M. M.; Chabal, Y. J.; Wilk, G. D. *Applied Physics Letters* **2003**, *82*, 4758-4760.

- 9 Frank, M. M.; Chabal, Y. J.; Green, M. L.; Delabie, A.; Brijs, B.; Wilk, G. D.; Ho, M. Y.; da Rosa, E. B. O.; Baumvol, I. J. R.; Stedile, F. C. *Applied Physics Letters* **2003**, *83*, 740-742.
- 10 Halls, M. D.; Raghavachari, K.; Frank, M. M.; Chabal, Y. J. *Physical Review B* **2003**, *68*.
- 11 Puurunen, R. L.; Root, A.; Sarv, P.; Haukka, S.; Iiskola, E. I.; Lindblad, M.; Krause, A. O. I. *Applied Surface Science* **2000**, *165*, 193–202.
- 12 Cardin, D. J.; Lappert, M. F.; Raston, C. L. *Chemistry of Organo-Zirconium and -Hafnium Compounds*. Ellis Horwood Limited: West Sussex, U.K., 1986.
- 13 Chabal, Y. J. *Surface Science Reports* **1988**, *8*, 211-357.
- 14 Becke, A. D. *Journal of Chemical Physics* **1993**, *98*, 1372-1377.
- 15 Becke, A. D. *Journal of Chemical Physics* **1993**, *98*, 5648-5652.
- 16 Hay, P. J.; Wadt, W. R. *Journal of Chemical Physics* **1985**, *82*, 270-283.
- 17 Wadt, W. R.; Hay, P. J. *Journal Of Chemical Physics* **1985**, *82*, 284-298.
- 18 Hay, P. J.; Wadt, W. R. *Journal of Chemical Physics* **1985**, *82*, 299-310.
- 19 Han, J. H.; Gao, G.; Widjaja, Y.; Garfunkel, E.; Musgrave, C. B. *Surface Science* **2003**, *550*, 199-212.
- 20 Dunning Jr., T. H.; Hay, P. J. In *Modern Theoretical Chemistry*, Schaefer III, H. F., Ed. Plenum: New York, 1976; 1-28.

- 21 Frisch, M. J.; Trucks, G. W.; Schlegel, H. B.; Scuseria, G. E.; Robb, M. A.; Cheeseman, J. R.; Zakrzewski, V. G.; Montgomery, J. A.; Stratmann, R. E.; Burant, J. C.; Dapprich, S.; Millam, J. M.; Daniels, A. D.; Kudin, K. N.; Strain, M. C.; Farkas, O.; Tomasi, J.; Barone, V.; Cossi, M.; Cammi, R.; Mennucci, B.; Pomelli, C.; Adamo, C.; Clifford, S.; Ochterski, J.; Petersson, G. A.; Ayala, P. Y.; Cui, Q.; Morokuma, K.; Rega, N.; Salvador, P.; Dannenberg, J. J.; Malick, D. K.; Rabuck, A. D.; Raghavachari, K.; Foresman, J. B.; Cioslowski, J.; Ortiz, J. V.; Baboul, A. G.; Stefanov, B. B.; Liu, G.; Liashenko, A.; Piskorz, P.; Komaromi, I.; Gomperts, R.; Martin, R. L.; Fox, D. J.; Keith, T.; Al-Laham, M. A.; Peng, C. Y.; Nanayakkara, A.; Challacombe, M.; Gill, P. M. W.; Johnson, B.; Chen, W.; Wong, M. W.; Andres, J. L.; Gonzalez, C.; Head-Gordon, M.; Replogle, E. S.; Pople, J. A. *Gaussian 98*, Revision A.11.2; Gaussian, Inc.: Pittsburgh, PA, 2001.
- 22 Chabal, Y. J.; Higashi, G. S.; Raghavachari, K.; Burrows, V. A. *Journal of Vacuum Science & Technology A - Vacuum Surfaces and Films* **1989**, *7*, 2104-2109.
- 23 Mui, C.; Wang, G. T.; Bent, S. F.; Musgrave, C. B. *Journal of Chemical Physics* **2001**, *114*, 10170-10180.
- 24 McKean, D. C.; Ellis, I. A. *Journal of Molecular Structure* **1975**, *29*, 81.
- 25 Killampalli, A. S.; Ma, P. F.; Engstrom, J. R. *Journal of the American Chemical Society* **2005**, *127*, 6300-6310.
- 26 Fenno, R. D.; Halls, M. D.; Raghavachari, K. *Journal of Physical Chemistry B* **2005**, *109*, 4969 - 4976.

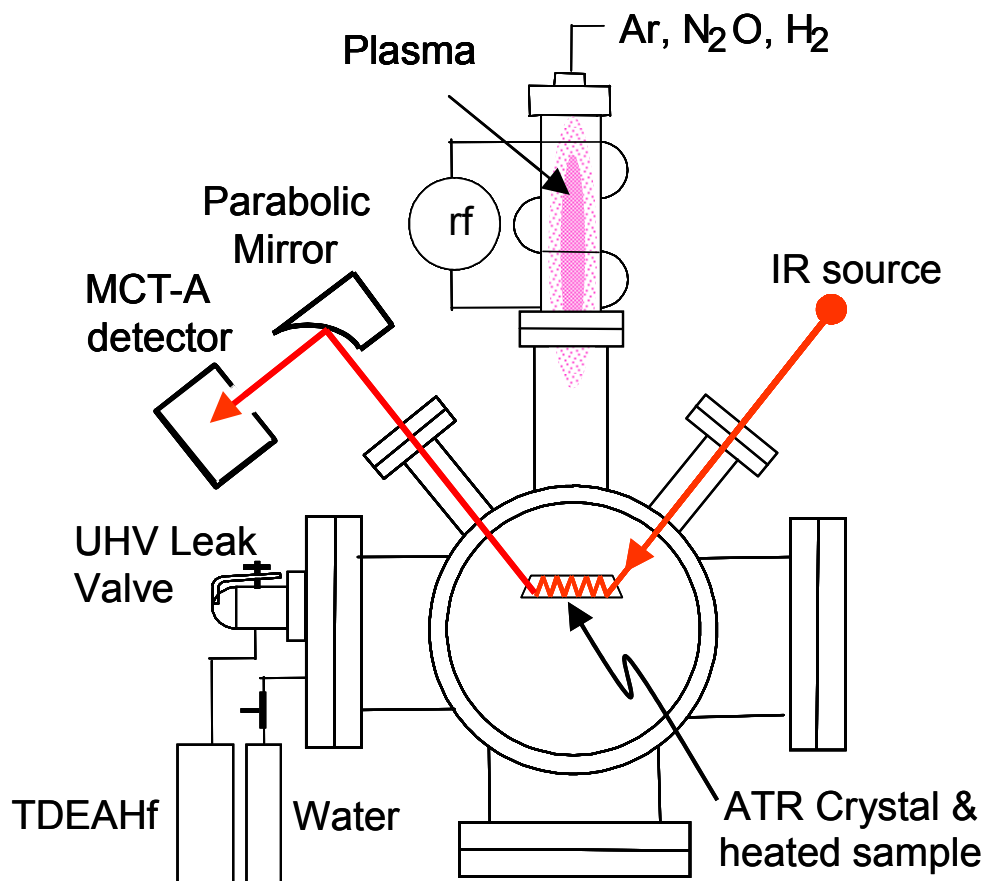


**Figure 8.1** Schematic of the attenuated total internal reflection FTIR system and reactor geometry used for in-situ spectroscopy.

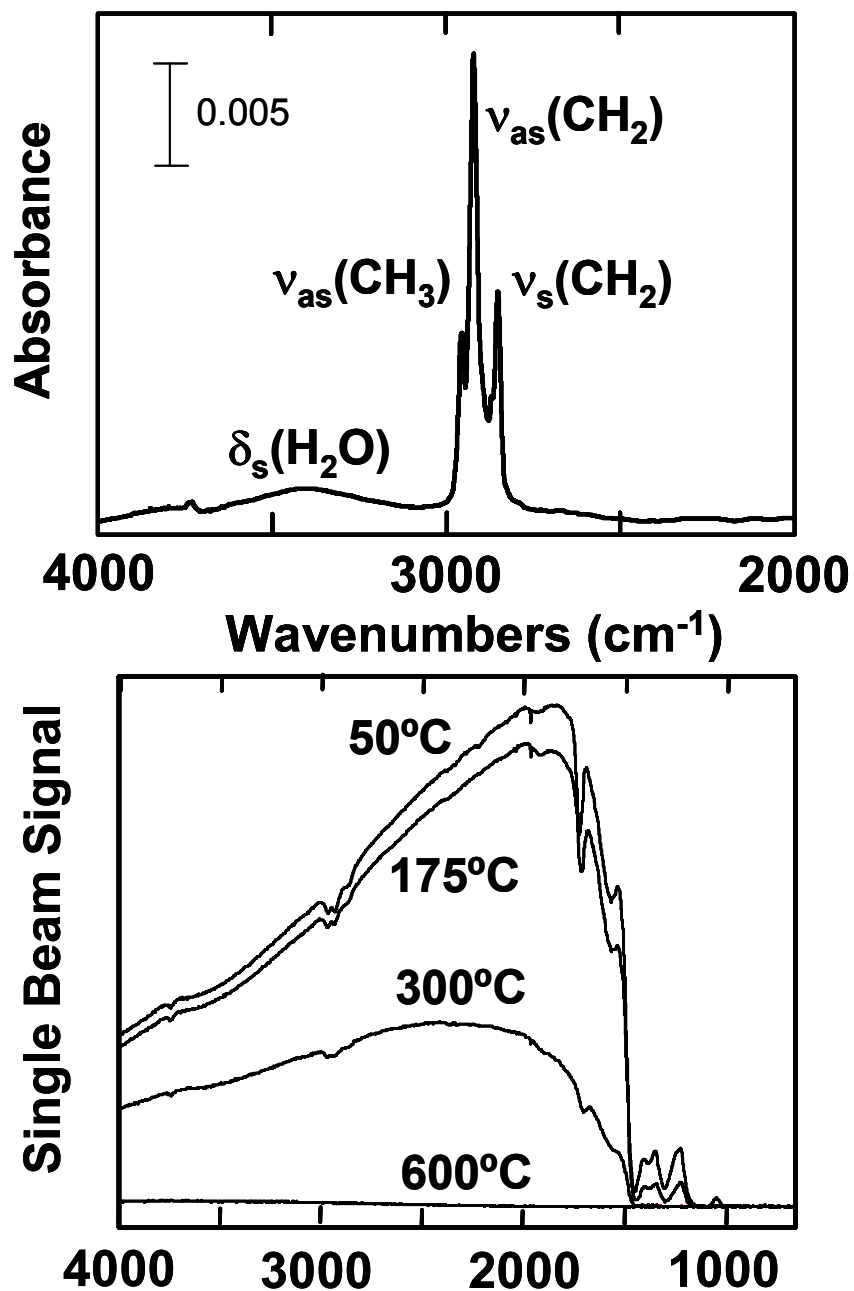


**Figure 8.2** (a) Attenuated total internal reflectance infrared absorbance spectrum for a reference octadecyl trichlorosilane monolayer on thin thermal SiO<sub>2</sub>. The thermal oxide was used as the reference spectrum. (b) Single beam spectra showing effect of temperature on IR transmission through an ATR silicon substrate with thermal oxide.

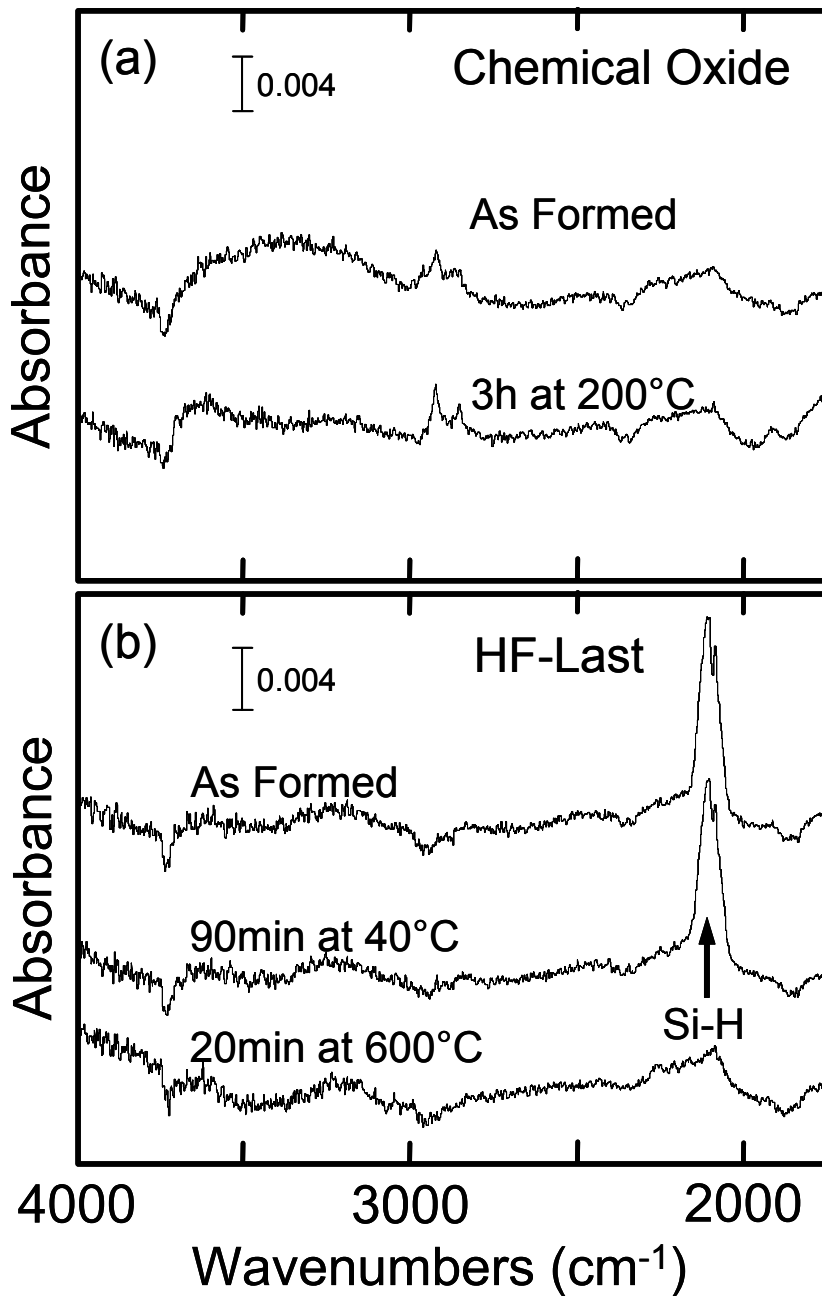


**Figure 8.3** Infrared signal for (a) chemical oxide and (b) HF-last Si(100) surfaces. The spectra are referenced to a thermally oxidized silicon crystal and are baseline corrected to minimize shifts resulting from optical mismatch between the sample and background crystals. The negative-going feature at  $3740\text{ cm}^{-1}$  is from variations in  $\text{H}_2\text{O}$  in the beam path within the spectrometer.

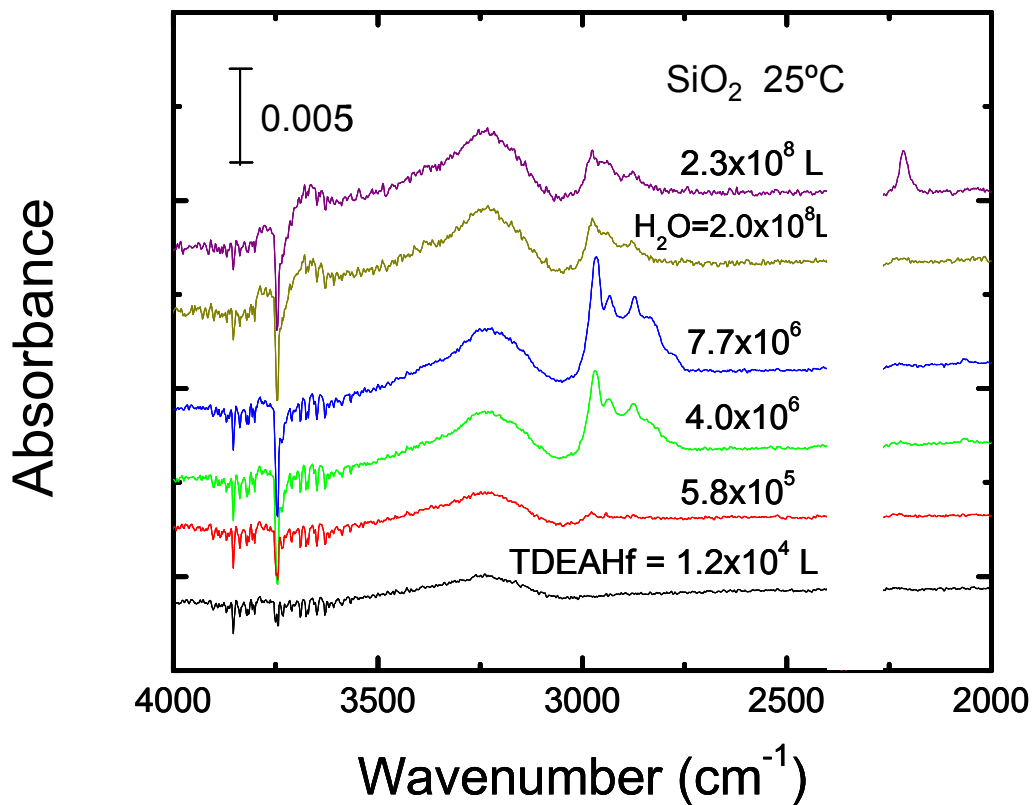


**Figure 8.4** ATR-FTIR absorbance after various exposures of the SiO<sub>2</sub> surface to TDEAHf at room temperature. Measurements were performed after evacuation of the precursor from the chamber, and typical scan conditions were 1024 scans at 4 cm<sup>-1</sup> resolution. The CH mode intensity is observed to increase with exposure, and subsequent exposure to H<sub>2</sub>O results in a decrease in CH modes, consistent with ligand oxidation. Spectra are referenced to the SiO<sub>2</sub> starting surface.

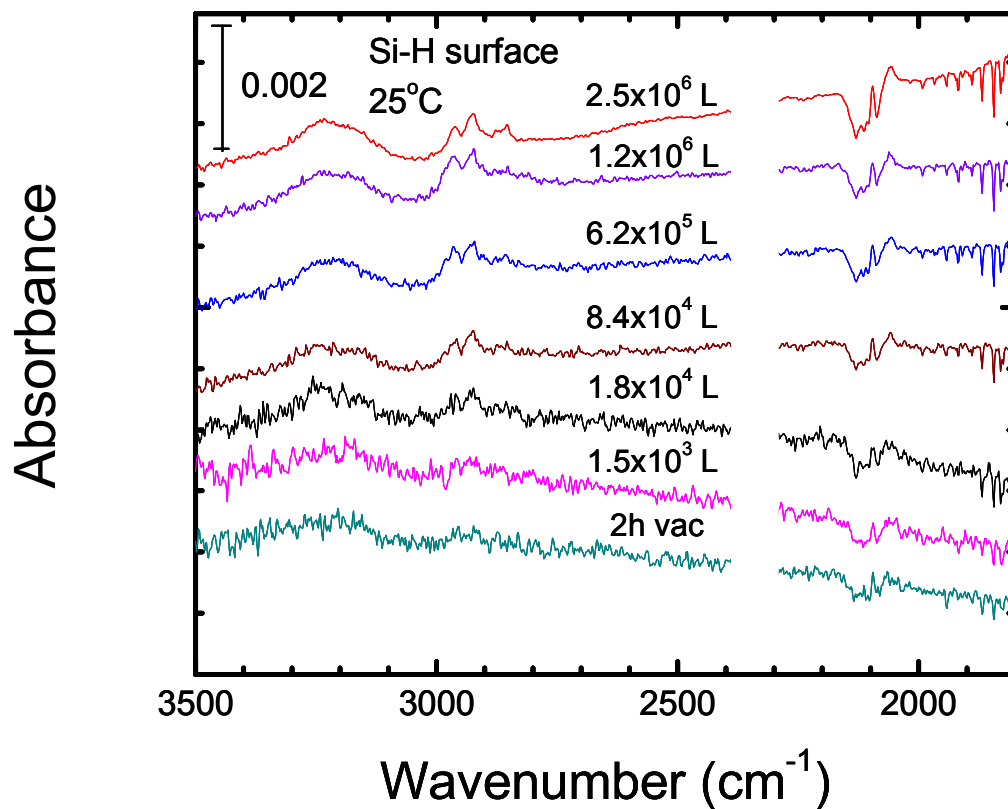


**Figure 8.5** ATR-FTIR absorbance after exposing the hydrogen-terminated surface to various doses of TDEAHf at room temperature. The C-H mode intensity for precursor on Si-H is reduced significantly compared to that on the SiO<sub>2</sub> surface. Reduction in Si-H is observed, consistent with hydrogen abstraction during TDEAHf precursor exposure. All spectra are referenced to the Si-H starting surface.

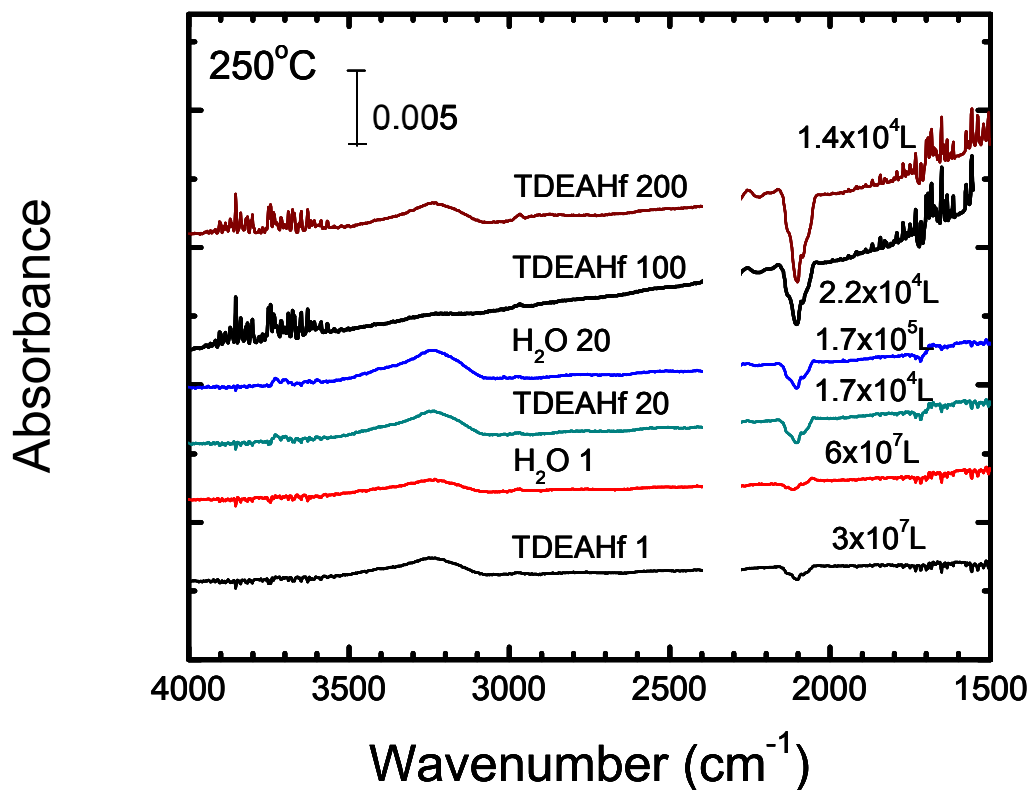


**Figure 8.6** ATR-FTIR spectra after sequential exposure of the Si-H surface to TDEAHf and water over many cycles at a substrate temperature of 250 °C. The first cycle consisted of long exposures to TDEAHf ( $3 \times 10^7$  L) and water ( $6 \times 10^7$  L), followed by 200 shorter cycles of  $\sim 2 \times 10^4$  L TDEAHf and  $2 \times 10^5$  L water, respectively. For cycles 1 and 20, results are shown from after each half-cycle, whereas for cycles 100 and 200, results only after the TDEAHf exposure step are shown. Spectra are referenced to the Si-H surface.

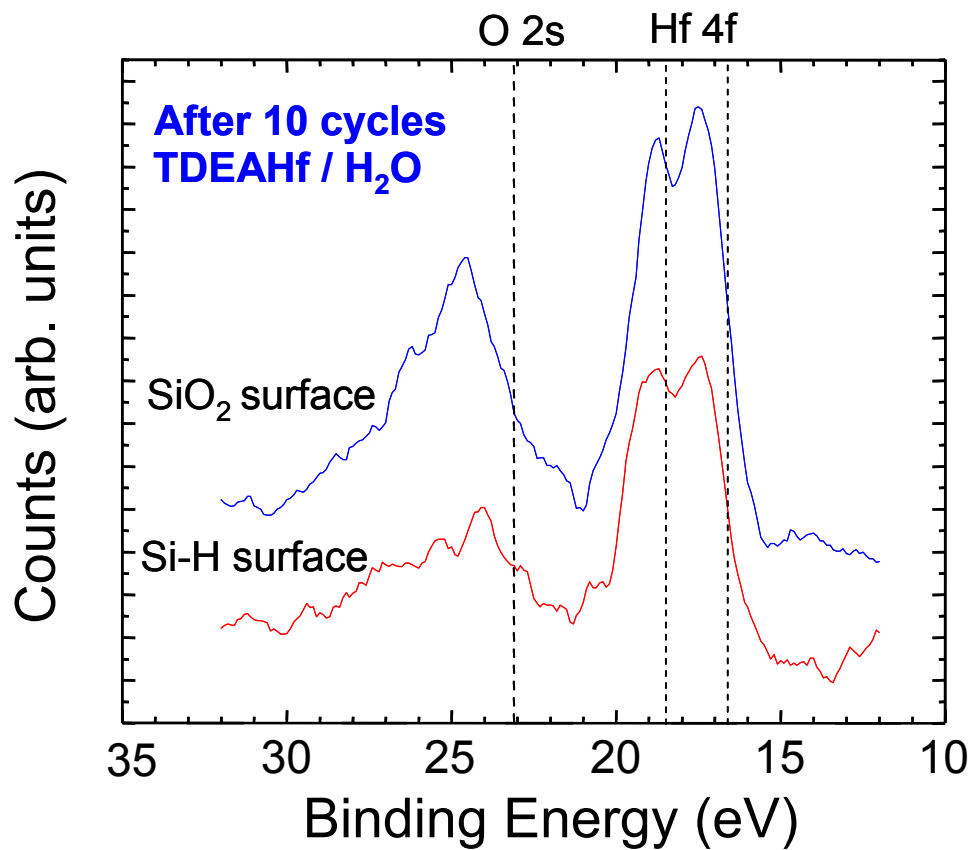


**Figure 8.7** X-ray photoelectron spectra of Si-H and SiO<sub>2</sub> surfaces after exposure to 10 cycles of TDEAHf and H<sub>2</sub>O at 250 °C. The data confirms the presence of Hf and O on both surfaces, with somewhat less Hf present on the initially hydrogen terminated surface. The peak positions are consistent with mixed Si-O and Hf-O bonds in the near surface region.

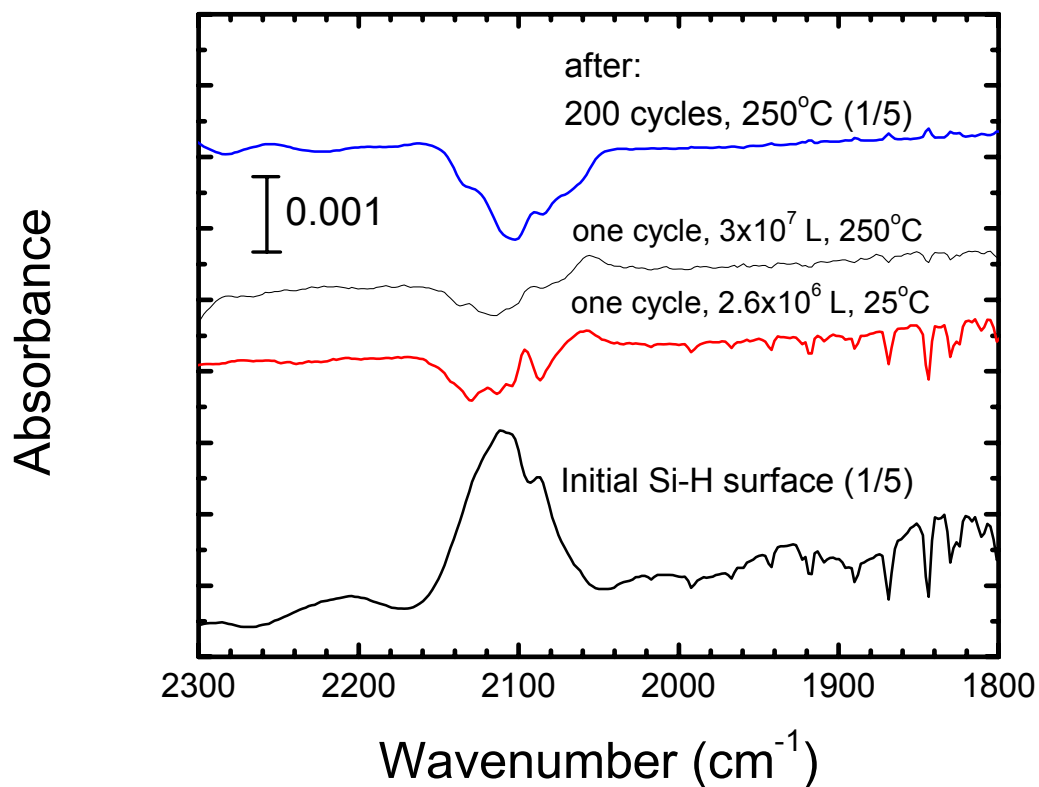


**Figure 8.8** Si-H IR vibrational modes for the initial surface and after various precursor exposure doses at 25 and 250 °C. The spectra for the initial surface and the surface after 200 cycles are reduced in scale by 5X relative to the scale bar. The initial Si-H surface is referenced to a SiO<sub>2</sub> surface, and subsequent spectra are referenced to the initial Si-H spectrum shown. The positive-going shoulder on the low wavenumber side of the Si-H modes suggests a possible shift from higher hydride to monohydride bonding. Longer exposure (top spectrum) indicates eventual removal of these monohydride features.

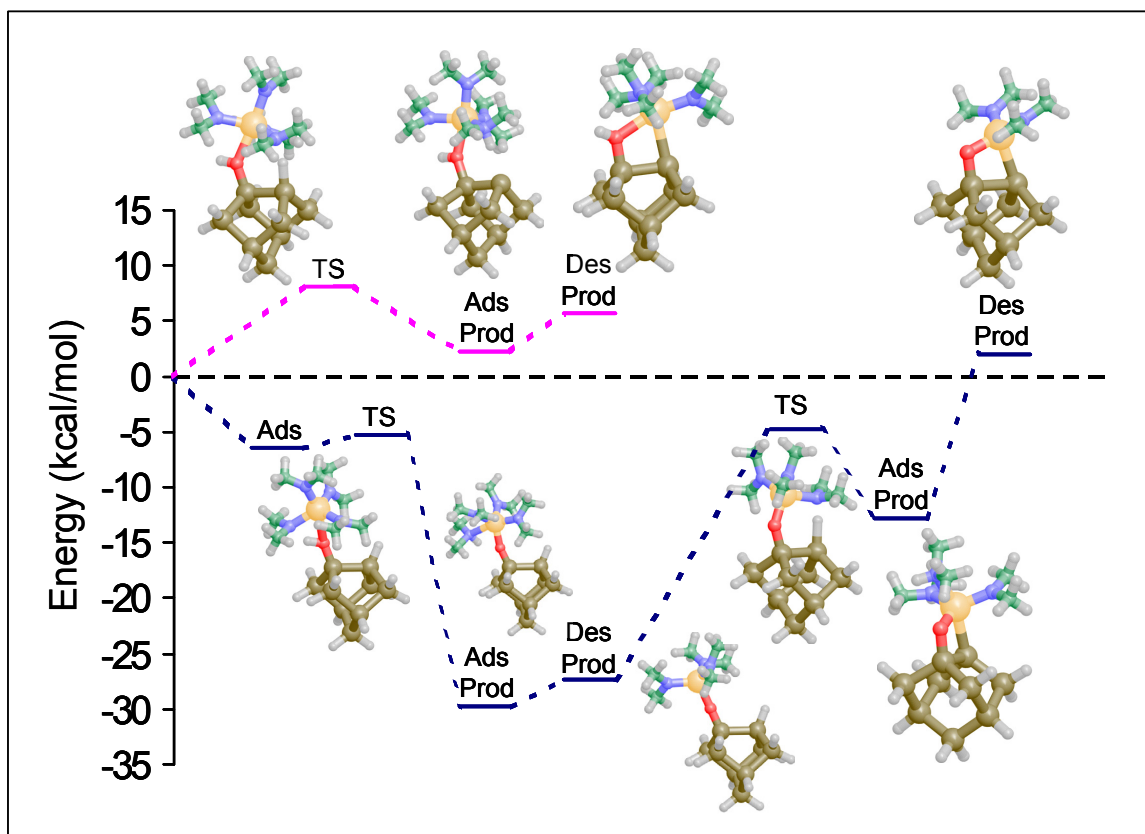


**Figure 8.9** Potential energy surface for TDMAHf reacting with the silicon hydride surface adjacent to a Si-OH surface bond site. Two reaction pathways are depicted. The bottom pathway corresponds to reaction sequence (1  $\rightarrow$  2) whereas the top pathway corresponds to sequence (2  $\rightarrow$  1).

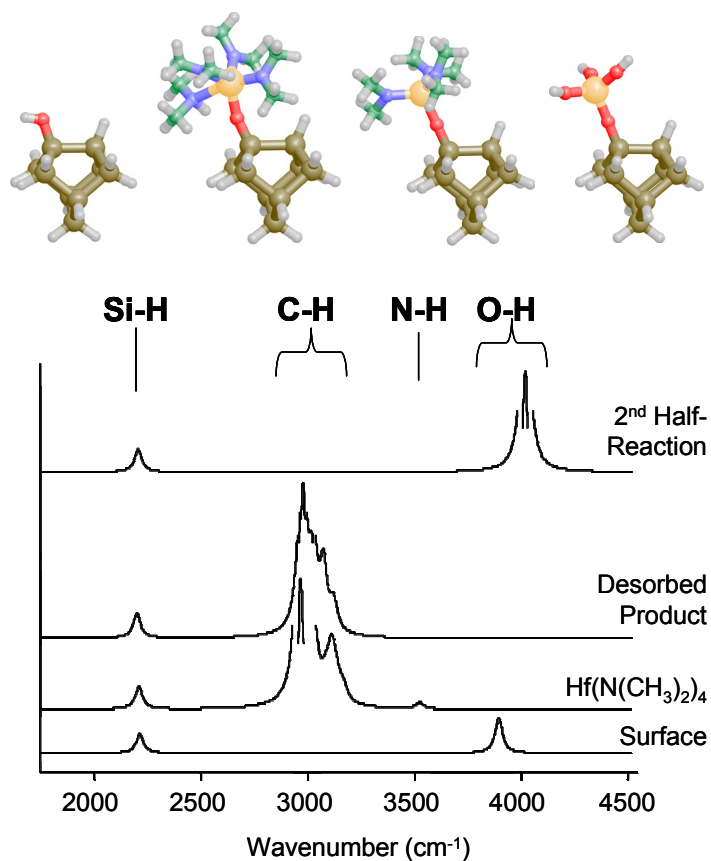


**Figure 8.10** Calculated vibrational spectra for the species present in the H transfer process from the surface OH group. The reaction sequence shown at top (left to right) correspond to the calculated spectra (bottom to top). The first spectrum (at bottom) shows the Si-H and O-H stretching modes of the initial surface at 2207 and 3880  $\text{cm}^{-1}$ , respectively. After reaction with TDMAHf via H transfer from the OH group, the OH modes disappear while the Si-H stretch remains and other modes of the adsorbed precursor appear including the N-H stretch of the adsorbed product at 3512  $\text{cm}^{-1}$ . The mode is not expected to be present after the product desorbs.

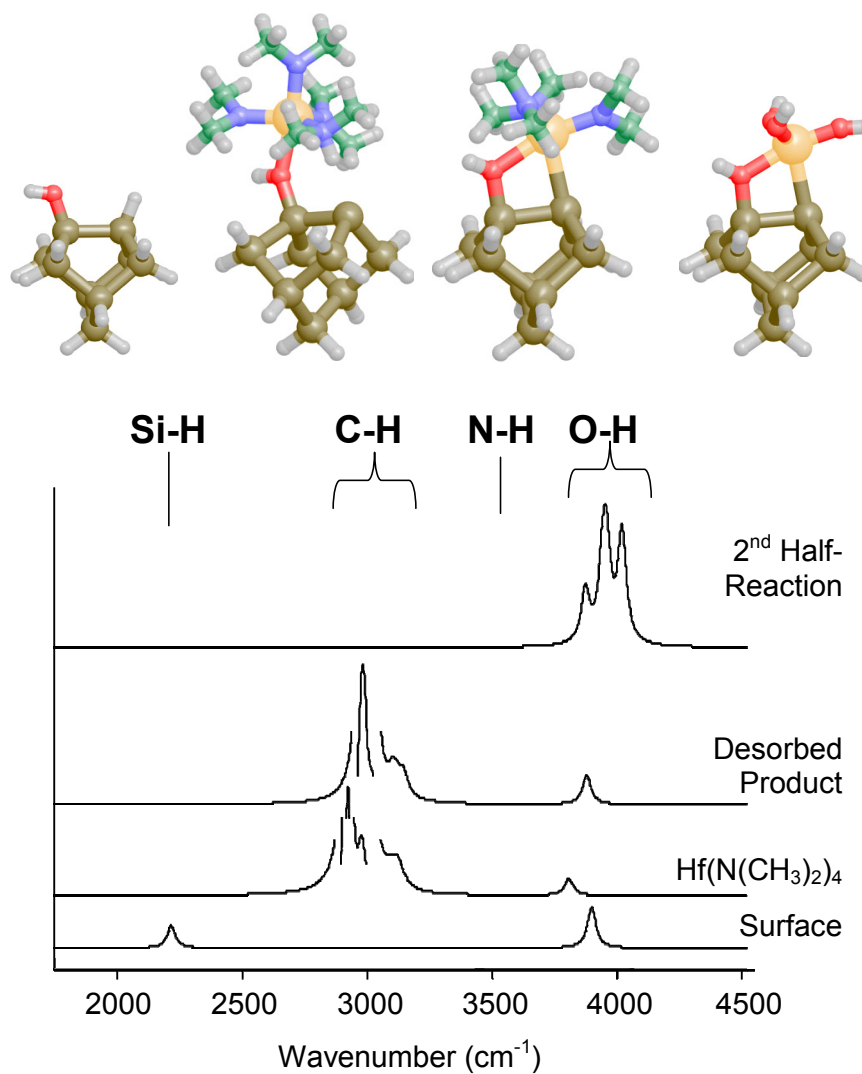


**Figure 8.11** Calculated vibrational spectra for surface species in the Si-H abstraction process. The reaction sequence shown at top (left to right) corresponds to the calculated spectra (bottom to top). The first spectrum (at bottom) shows the Si-H and O-H stretching modes of the initial surface at 2207 and 3880  $\text{cm}^{-1}$ , respectively. After reaction with TDMAH via H abstraction, the Si-H mode disappears while the other modes of the adsorbed precursor appear. For the adsorbed product, the N-H stretch has been shifted to 2916  $\text{cm}^{-1}$  because of interactions with the bare surface Si atom. This peak is not observed after the product desorbs.

## 9 Appendix 1: Technical Details (ATR-FTIR Apparatus)

This section describes the design and use of the optical apparatus used for *in-situ* FTIR measurements in more detail than may be of interest to a general reader. It is included for the benefit of future researchers who wish to build on this work. *In-situ* spectroscopy is a technically demanding experiment. A small change in a data acquisition setting or the positioning of an optical element may not change whether data is obtained, but it may indeed change whether the data has any meaning. An understanding of the relationships between the various system elements and the quality of the data derived is critical if one is to quickly make corrections when things go wrong. The author of this work has had some limited success and many, many failures. There is always a danger when a student graduates that his or her knowledge will be lost to the research group. Most of the information in this section has not been passed down into the group. By including this section, I hope to help future researchers get off to a running start and avoid making many of the mistakes I made.

### 9.1 Measurement Parameters Chosen Based on the SNR

When the system was first brought on-line, a self-assembled monolayer film was used to determine optimum measurement parameters for my instrument. The protocol followed for these measurements was to change the parameter, collect a spectrum and then use Omnic to measure the integrated area of the CH feature and the noise of the spectrum. The Signal to Noise Ratio (SNR) was calculated as the ratio of the CH feature area to the noise (peak to peak). Some of the spectra collected are shown in Figure 9.1. The integrated area of the CH features was measured in the range of  $3030 - 2770\text{cm}^{-1}$ , and the noise was measured in the range of  $2750 - 2400\text{cm}^{-1}$  where there are no spectral features. Parameters varied during this

experiment were the aperture size, the mirror scanning velocity, the spectral resolution, and the number of measurements. The parameter values for each spectrum are also displayed in Figure 9.1. The measurement parameters varied affect the SNR in different ways, and interested readers will find ample descriptions of the technical details elsewhere.<sup>1</sup> The purpose of this procedure was to experimentally determine reliable settings at which to obtain high quality data.

Table 9.1 shows that signal to noise ratios can be derived reliably by this procedure. Four spectra were collected at identical settings (aperture = 69, scanning velocity = 1.8988cm/s, and 256 scans), and the calculated SNR values ranged from 2655 to 2736. Of course, there is human error associated with this measurement, and the conclusion here is that two SNR values within 100 or so should be considered identical.

Table 9.2 shows the effect of varying the scanning mirror velocity in the interferometer. Three spectra were recorded with an aperture setting of 0 (iris diameter = 0.75mm) and 16 co-added scans each. Spectra were recorded with mirror velocities of 0.9494, 1.8988, and 3.1647cm/s. The SNR of the two scans with the slower mirror velocities were both about 1050 while the scan with the fastest mirror velocity was only about 600. A mirror velocity of 1.8988 was chosen and used as the default mirror setting for the rest of the ATR experiments. In general, HgCdTe detectors usually benefit from faster scanning velocities, but mechanical vibrations will offset this benefit at some point (defined by the instrument). Scans with several velocities between 1.8988 and 3.1647 were collected. The noise level was almost the same at the next velocity above 1.8988 (2.5317cm/s) and increased reproducibly at the next velocity higher (3.1647cm/s). A velocity of 1.8988 was

chosen because it seemed to give a good SNR and a noise value that was the same from measurement to measurement.

Very large apertures allow more light into the experiment, but also lower the resolution of the measurement. Close examination of the IR spectra collected shows that peak widths are higher for apertures of 32 and above than for an aperture of 6. Table 9.3 shows the variation of the SNR as the aperture is increased. The SNR increases rapidly between settings of 0 and 6, and the best SNR value in the table was for an aperture of 32. In separate measurements, noise values were compared for many more aperture values (data not shown). We observed that the noise values increase rapidly when going from 0 to 6 but quickly level off above 6 and vary slowly until 32 where they begin to rise more quickly. Lower apertures allow for higher resolution measurements and better resolved spectral features. The aperture setting chosen,  $APT = 9$ , was on the low end of the slowly varying, plateau region. Dual-beam spectra collected later exhibited an oscillating baseline for high resolution measurements. A resolution of 4 was the highest resolution we could use without seeing the interference.

Settings of  $\nu = 1.8988$ ,  $aperture = 9$ , and  $resolution = 4$  were used for all the ATR measurements. We opened the aperture completely ( $aperture = 100$ ) for Reflection Absorption Infrared Spectroscopy measurements. The number of scans was decided on a case by case basis. Measurements with as few as 32 scans and as many as 1024 scans were used.

## **9.2 Alignment Procedure**

There are two types of alignment. The first is the overall system alignment which is performed when the bench is first put into place. Once this alignment is complete, many variables are locked to simplify sample to sample alignment – the second alignment type.

There is a He-Ne laser coincident in the infrared beam that the spectrometer itself uses to maintain constant interferometer mirror velocity. This laser is very useful for the initial alignment, because the laser spot is centered in the infrared beam and is visible on a white card placed in the beam path if one works in a darkened room. Once the system is aligned well enough that infrared light is detectable, the Omnic software is used to monitor the interferogram and make further adjustments to maximize the signal strength. In the discussion below, the term “signal strength” refers to the height of the interferogram centerburst. This height is the maximum voltage output from the detector as the interferometer scans and is directly proportional to the amount of infrared radiation striking the detector.

This document contains results of internal reflection (i.e., ATR-FTIR) measurements. However, single-bounce, external reflection measurements were also performed. Although these Reflection Absorption Infra-Red Spectroscopy (RAIRS) experiments did not result in publishable data, procedures were developed that allowed internal and external IR measurements to be performed relatively quickly on the same sample. Aligning the system for external reflectance before aligning for total internal reflectance simplifies many aspects of the process, and a complete procedure (including external reflection) is presented below.

## 9.2.1 Overall system alignment

- 1) The deposition chamber itself should be as level as possible because the measurement plane must coincide with the plane defined by the infrared flanges and the sample.
- 2) Install the KBr lenses. The flanges are marked with an arrow to show which side to orient upwards. Always install them the same way every time.
- 3) With the bench configured for an external experiment and the instrument scanning, use a white card to verify that the infrared beam exits the spectrometer in the center of the external experiment port. The infrared beam is redirected outside the bench using the Passport Mirror which is on a worm drive in the bench. Adjust the screws on the back of the Passport Mirror until the laser spot is centered in the port.
- 4) Install the black tube in the spectrometer's external port that forms the purged beam path between the bench and the deposition chamber. Use a white card to verify that the beam is centered in the black tube. Adjust the black tube and the o-rings forming the seal between the bench and tube to center the red spot in the tube. One can verify that this is correct by checking that the infrared signal strength (after alignment is complete) is the same with the bench open and closed.
- 5) Set the deposition chamber manipulator to the settings used for single-bounce external reflection measurements ( $x=9.25$ ,  $y=5.0$ , and  $z\sim 1.0$ ). Once the system is aligned for external reflection, it can be aligned for internal reflection by moving the chuck forward (i.e., adjusting  $x$  to lower values) such that the bevels of the IRE intercept the beam path on both sides. The face of the chuck (where the platen, the

sample holder, and sample will be mounted) should face exactly back towards the plasma tube. Currently, this corresponds to  $\theta=268.5$ .

- 6) Position the bench such that the infrared beam is normal to the IR port. With the instrument scanning move the bench until a) the red spot is centered on the KBr lens and b) the red spot is centered on the platen horizontally.
- 7) Install a mirror onto the platen. A slightly cloudy evaporated or sputtered film works well for this purpose because it is possible to see the spot on the mirror if the film is microcrystalline enough to give specular reflection. Use a white card to determine where the beam intercepts the chamber wall after bouncing off the mirror. Reposition the bench until the red spot is aligned horizontally with the detector-side IR port while maintaining the centeredness of the beam at the bench-side lens and the sample holder. At this point, it is unlikely that the beam will intercept the chamber wall at the height of the detector-side IR port.
- 8) Adjust the height and pitch of the IR table until the beam emerges from the center of the detector-side IR port. Iterate steps 6-8 as necessary. Upon completion of this step, the optical plane matches the measurement plane, and the bench is in its final position.
- 9) The next task is to locate and lock the correct  $x$ -position for the parabolic mirror. Install the parabolic reflector and the MCT detector on the optical rail in the purged enclosure. Set both elements to  $y=6.50$ . Note that for elements located in the purged enclosure,  $x$  refers to positions along the optical rail. The  $y$ -direction is normal to the  $x$ -direction, and ranges from 0.00 to 13.00mm. A position of  $y=6.50$  is

centered on the optical rail while positions of  $y < 6.50$  are closer to the chamber and positions of  $y > 6.50$  are further from the chamber.

- 10) Position the parabolic mirror such that the laser strikes its center. Use a white card as necessary.
- 11) Position the detector far from the parabolic mirror, and adjust the radial position ( $\theta$ ) of the parabolic element until the beam strikes the center of the detection element.
- 12) Slide the detector along the optical rail and watch the laser spot. When the mirror is at the correct  $\theta$  and  $x$ -position the beam will travel parallel to the optical rail and will stay centered on the detection element for all detector positions. Adjust the parabolic mirror's  $\theta$  and  $x$ -position until the beam is traveling parallel. The parabolic element is a right-angle reflector, so when the beam stays centered on the detection element it should indicate that the beam is striking the mirror at  $90^\circ$ . However, it is necessary to verify that the image after the parabolic element is somewhat circular. There are  $\theta$  and  $x$ -position combinations that provide parallel beam travel but distort the beam quite a bit. There is always some distortion when using off-axis reflectors, but this distortion becomes worse when the beam is not incident on the exact center of the optic.
- 13) Lock the parabolic mirror position. This position is correct for both external and internal reflection measurements. At this point in the alignment, the overall beam path through the system is determined. For external reflection, the sample will be positioned as in step 5. For internal reflection, the crystal will be positioned so that the incident and exiting beams intersect with this beam path at the crystal's bevels.

- 14) Fill the MCT-A detector with liquid N<sub>2</sub>. In Omnic, use the Experiment Setup window to look at the centerburst of the interferogram. The height of the centerburst is directly proportional to the amount of infrared radiation striking the detector. Adjust the detector *x*- and *y*-position to maximize the centerburst height. When this is achieved, mark all the settings for future reference. The overall system alignment is complete.

### **9.2.2 Sample to sample alignment – External Reflection**

- 1) Return the detector settings to those marked in step 14 above.
- 2) Mount the sample.
- 3) Using the laser spot, adjust the *y*- and *z*-position of the sample such that the beam is centered on the sample. A freshly prepared silicon substrate will be too smooth to scatter the beam, so no spot will be visible where the laser strikes it. In this case, simply note the *z*-positions at the top and bottom of the sample and the *y*-positions at each side and locate the sample at the average coordinates.
- 4) Maximize the height of the interferogram centerburst by varying the *x*-position of the sample.
- 5) Verify that the beam is incident on the center of the sample to avoid any signal contribution from reflections off the platen. Avoid small samples for the same reason. One may open the aperture to allow more light into the experiment, but consider the image sizes shown in Table 9.9 and verify that the spot size is smaller than the sample.

- 6) It was not usually necessary to vary the detector position in the experiments presented in this work. If desired, the detector  $x$ - and  $y$ -positions may be varied iteratively to maximize the signal strength.
- 7) Notes:
  - Locked variables include the bench position, the rotation of the sample, and all of the parabolic mirror settings.
  - Variables that may be adjusted include the  $x$ -,  $y$ -, and  $z$ -position of the sample and the  $x$ - and  $y$ -position of the detector. In addition, it sometimes helps to adjust the position of the sample on the platen since the platen is not perfectly smooth.

### 9.2.3 Sample to sample alignment – Internal Reflection

- 1) Return the detector settings to those marked in Step 14 of Section 9.2.1 above.
- 2) Mount the silicon IRE using the scribe marks on the platen as a guide. Place two freshly cleaned substrate rectangles ( $\sim 1\text{mm} \times 20\text{mm}$ ) under the IRE to raise it off the platen and prevent contribution to the signal from species adsorbed on the platen. These substrate rectangles should be cleaved from silicon wafer with thermally grown  $\text{SiO}_2$  on its face to limit the loss of IR light into the silicon spacers. (Note that the indices of refraction for Si and  $\text{SiO}_2$  are 1.46 and 3.42, respectively.) Ideally, the  $\text{SiO}_2$  film would be thicker than the maximum penetration depth ( $5500\text{\AA}$  at  $1500\text{ cm}^{-1}$  for this material combination). In practice, spacers cleaved from silicon wafer bearing a  $1000\text{\AA}$  thick  $\text{SiO}_2$  film perform well.

- 3) Position the sample near an  $x$ -position of 2.20. Adjust the sample  $x$ - and  $y$ -position until some infrared signal is detected. It may be helpful to initially position the sample such that the laser spot is incident on the center of the bevel.
- 4) Compare the single-beam spectrum to Figure 9.2 below to verify that the system is aligned for a total internal reflection measurement. The signal should drop off abruptly below the silicon lattice absorption band near  $1500\text{cm}^{-1}$ .
- 5) Maximize the height of the interferogram centerburst by varying the  $x$ -,  $y$ -, and  $z$ -position of the sample.
- 6) Maximize the height of the interferogram centerburst by varying the  $x$ - and  $y$ -position of the detector.
- 7) Iterate steps 5 & 6 until the maximum signal strength is obtained while occasionally checking for the lattice absorption band in the single-beam spectrum.
- 8) Notes:
  - Locked variables include the bench position, the rotation of the sample, and all of the parabolic mirror settings.
  - Variables that may be adjusted include the  $x$ -,  $y$ -, and  $z$ -position of the sample and the  $x$ - and  $y$ -position of the detector.
  - It often helps to adjust the position of the sample on the platen since the platen is not perfectly smooth. Once a good position is found, it should be noted. It simplifies alignment greatly if the sample is positioned in exactly the same spot on the platen every time.

- Occasionally, a crystal exhibits large differences (4x – 10x) in signal strength when rotated 180° about an axis normal to the face of the platen. Be aware of this effect, and, if all else fails, try flipping the IRE.
- If possible, reuse the same IRE for each experiment. Although nominally the same size, the crystals vary slightly making it necessary to adjust the detector position each time a new crystal is installed. However, detector adjustments are unnecessary when the same crystal is cleaned and reused and is carefully positioned in the same spot on the platen. In this way, alignment can often be accomplished within 10 to 20 minutes.

### ***9.3 Pressure Dependence of Measurement***

When one is probing species that are present on a surface in concentrations of percents of a monolayer, very low gas pressures can give rise to absorptions as strong as or stronger than the adsorbed species. The following calculation estimates the number of gas molecules present in the beam path traversed on the way to and from the IRE in order to demonstrate at what pressures the gas-phase absorption becomes significant.

## Estimating Number of Gas-Phase Molecules in the Beam Path

**Formulas**  $PV=nRT$   
Molar Density =  $n/V = P/RT$   
Molecular Density = (Molar Density)\* $N_A = N_A(P/RT)$   
Number Molecules in a volume,  $V = N = (\text{Molecular Density}) * V$

**UNITS & CONSTANTS** P [=] torr R = 62.36 L-torr/mol-K  
V [=] L  $N_A = 6.022 * 10^{23}$  molecules/mol  
T [=] K

### What is the volume encompassed by the beam travelling to and from IRE?

-Calculating Volume as a cone that has a base of 1.37" and is 5.875" tall (bevel to KBr plate).  
-Volume of a cone w/ a circular base =  $(1/3)\pi * r^2 * h$  where r is radius of base and h is height perpendicular to the base.

r (mm)	17.399
h (mm)	149.225
Volume In (mm <sup>3</sup> )	47306.28
Volume In (L)	0.047306
Volume In & Out (L)	0.094613

### How many gas-phase molecules are in this beam volume at a given T & P?

Using the formula above and assuming we are near room temperature.

T (K)	V (L)
300	0.094613

P (mtorr)	P (torr)	$\rho_{\text{molar}}$	$\rho_{\text{molecular}}$	$N_{\text{Gas-Phase}}$
0.01	1.0E-05	5.3E-10	3.2E+14	3.0E+13
0.10	1.0E-04	5.3E-09	3.2E+15	3.0E+14
1.00	1.0E-03	5.3E-08	3.2E+16	3.0E+15
10.00	1.0E-02	5.3E-07	3.2E+17	3.0E+16

### How do these numbers compare to the number of molecules I could measure on my IREs?

Max  $N_{\text{IRE}}$  is if one molecule adsorbed on every surface site.

Density of atoms on a Si(100) surface is  $\sim 10^{15} \text{ cm}^{-2}$ .

IRE has an area of  $480 \text{ mm}^2$  on each side of the 40x12mm crystal.

Total IRE area is  $960 \text{ mm}^2$  or  $9.60 \text{ cm}^2$ .

**$N_{\text{IRE}} = 9.6 \times 10^{15}$  molecules**

Notice that the estimate for the number of molecules adsorbed on the IRE ( $N_{\text{IRE}}$ ) is an upper limit because fewer than one molecule will adsorb on each surface site. Therefore, the pressures at which measurements contain equivalent numbers of gas- and surface-phase species is a lower estimate. At a pressure of 0.1mtorr, at least 3% of measured signal is coming from the gas-phase, and at 1.0mtorr, at least 30% of the signal comes from gas-phase

molecules. At a pressure of approximately 3mtorr, the contribution from gas-phase species is at least as strong as that from surface-bound species. The practical implication of these estimates is that one should expect to observe gas-phase features in any spectrum collected at pressures near to or in the mtorr range. It may be possible to account for this feature of the measurement equipment by calibrating the IR signal for a given pressure. However, it is simpler to make measurements after evacuating the chamber whenever possible.

Another solution is to deliver the organometallic compounds in such a way that the species are directed directly toward the surface with a small tube. With this geometry, one can dose the surface with the compound while pumping the system, and the local concentration above the IRE is higher than in the beam path. This method of reactant delivery (an “effusive doser”) has been used for many surface reaction studies and is especially favored for very sticky or reactive species that might interact with the system walls or windows.<sup>2-6</sup> With this arrangement, knowing the actual exposure of the surface to the compound is a challenge, but one can explore higher surface fluxes at lower overall system pressures. Infrared spectra could be collected during exposure without interference from gas-phase species. We initially built such an “effusive doser” for the system and were unable to detect any adsorption using it. Future researchers may wish to revisit this design.

#### ***9.4 Magna 750 Optical Specifications***

This section contains a list of information on the Magna 750 FTIR obtained from Thermo-Nicolet technical support.<sup>7</sup> It is reproduced here because it is not available in the standard manuals supplied with the instrument and will be useful to future researchers. This section assumes measurements are performed in the bench and the detector is located in the detector compartment.

#### **9.4.1 Infrared source**

Consider the source a 0.16inch square with a 0.032inch slit halfway up the middle. For image sizes consider the source 0.16inches square or 0.21inches (5.3mm) across its widest part. The IR source runs between 1398 and 1523K.

#### **9.4.2 White light source**

The white light source is a filament about 0.12inches in diameter and about 0.375inches long. For a symmetric shape consider the image as 0.12inches (3mm) in diameter. This source normally runs between 2600 and 2800K.

#### **9.4.3 Source ellipse mirror**

This element is a 30° elliptical reflector, has focal lengths of 6.00 and 3.42inches, and is 2.0inches in diameter (P/N 160-709803). This element focuses the image of the source onto the iris aperture. The image of the IR source (5.3mm) is magnified by  $6.00/3.42$  or 1.75. Thus, the image of the source on the iris is  $5.3\text{mm} \times 1.75 = 9.3\text{mm}$ . Note that 9.3mm corresponds to an aperture setting of  $\text{APT}=115$ . Aperture sizes greater than 115 do not give much more signal, and the energy is coming from the heated material next to the source (insulation in the source assembly).

#### **9.4.4 Source collimation mirror**

The beam goes through the iris to a 6.00inch focal length, 90degree, 2.5inch diameter parabolic mirror (P/N 160-709903). This mirror collimates the beam into the interferometer (with some beam divergence due to the iris size).

#### **9.4.5 Sample compartment mirror**

This mirror is a 6.00inch focal length, 90°, 2.5inch diameter parabolic mirror (P/N 160-709903). Because this mirror is the same as the source collimation mirror, the image size in the sample compartment is the same as the iris size (with some distortion due to off-axis parabolics).

#### **9.4.6 Detector mirror**

This element is an 80° elliptical reflector, has focal lengths of 1.66 and 8.97inches, and is 2.25inches in diameter (P/N 160-710006). This mirror takes the beam image in the sample compartment and focuses it onto the detector. The image in the sample compartment is reduced by a factor of 5.4 ( $8.97/1.66 = 5.4$ ).

#### **9.4.7 Iris**

The variable iris is controlled by the Omnic software.<sup>8</sup> Iris diameters produced at various aperture (APT) settings are shown in Table 9.4. Light from the infrared source is focused on the iris, and the iris is imaged by a 6.00inch FL parabolic mirror. Image diameters produced at the in-bench detector are listed. The beam divergence varies with the aperture setting, and italicized beam divergence values in Table 9.4 are approximated by the method below.

#### **9.4.8 Beam divergence**

The beam divergence can be approximated by using the angle generated by the iris size to a point 6.00inches away (the distance between the iris and the center of the 6inch focal length parabolic mirror). Note that the beam divergence is slightly greater on the short

focal length side of the mirror and slightly smaller on the longer focal length side of the mirror.

#### **9.4.9 Interferometer**

Rapid scanning, DSP-driven Vectra interferometer capable of better than  $0.1\text{ cm}^{-1}$  resolution. The mirrors in the interferometer are 1.50inches in diameter. Thus, the beam coming out of the interferometer has a diameter of 1.50inches.

### **9.5 ATR-FTIR Optical System – Percent Throughput**

This section consists of various details and calculations that govern the performance of the ATR-FTIR tool. Some of the parts that make up the apparatus along with part numbers and suppliers are listed in Table 9.5.

#### **9.5.1 Factors that affect throughput**

As mentioned in Section 2.4: Practical Design and Measurement Considerations, the optical throughput is a critical factor in determining the signal to noise ratio of the final data. Several factors influence the throughput including the total distance the light must travel, the diameter of any apertures it must pass through, losses due to interaction with optical elements, and how tightly the IR beam is focused at the bevel of the IRE. The effects each of these factors has are detailed in this section. The overall throughput of IR light that reaches the detector in the current configuration is estimated to be  $\sim 1\%$ . However, the KBr lenses used to focus the IR radiation on the IRE bevel are cracked and are not the correct focal length. We estimate that by replacing these lenses with uncracked ones of the correct focal length, the overall throughput can be raised to  $\sim 4\%$ .

### **9.5.2 Beam travel losses**

The beam diameter grows as the beam travels. The angle at which it diverges depends on the physical size of the source image (i.e., the iris) as mentioned in Section 9.4.8 above. Table 9.4 displays the general trend that larger apertures produce more divergent beams. Table 9.6 shows the dimensions of the beam at various locations as it progresses towards the IR Port on the system chamber. The initial beam diameter is fixed at the diameter of the interferometer at 1.5inches for all aperture settings. The beam travels 13inches from the interferometer to the External Beam Port located on the side of the Magna 750 bench. The External Beam Port has an inner diameter of 2inches, so any portion of the beam larger in diameter than 2inches is lost. The beam then travels an additional 18inches to the IR Port on the deposition chamber where the KBr window flange forms an aperture of 1.37inches. All but the center 1.37inches of the beams are attenuated at the IR Port. The general trend displayed in Table 9.6 is that lower aperture settings produce higher overall percent throughputs. However, that trend must be interpreted in light of the fact that more IR radiation is available initially for higher aperture settings. As described in Section 9.1, an aperture setting of 9 was used for our ATR measurement. When the aperture is set to 9, 100% of the beam passes through the Magna 750's External Beam Port, and 26% of the initial beam passes into the chamber where it can be used for the experiment.

### **9.5.3 Reflection losses**

FTIR beam losses also occur as the beam interacts with optical element. Reflection at a mirror is not 100% efficient. Typically, between 90 and 95% of the beam is reflected for aluminum mirrors, and mirrors evaporatively plated with gold reflect 95 to 99%. Light incident on the KBr lenses and windows is partially transmitted and partially reflected as

described in Section 2.4. If reflection losses are only due to differences in the refractive index of air and KBr, then only ~5% of the light will be lost. However, any surface imperfections, haziness due to atmospheric water adsorption, or deposition on the inside of the windows will further increase the losses. Table 9.7 shows how reflective losses from each of the optical elements in the beam path affect the overall throughput. Minimum (Pessimistic), maximum (Optimistic), and average (Realistic) percent transmission values are included so as to give an estimate for the expected range. Note that the KBr lenses are expected to vary from 80 to 95% transmissive while the KBr windows are only expected to range from 90 to 95%. We are estimating 10% additional loss at each lens to compensate for the large cracks that run through each lens. The main result of Table 9.7 is that about 63% of the beam would remain at the detector if only reflective losses occurred. Comparing this to the 26% that remained after accounting for losses during beam travel shows that reflective losses are not limiting performance as much as beam travel. When reflection losses are combined with beam travel losses (for an aperture setting of 9), the total percent transmission drops to about 16% as shown in Table 9.8.

#### **9.5.4 Beam losses at IRE (quality of focus)**

The last element that must be considered when estimating the Percent Throughput is the Internal Reflection Element itself. The focus of the IR beam on the bevel of the trapezoidal IRE determines the maximum amount of IR light that can pass through the IRE. For the purposes of this section, we will assume that all the light that enters the IRE exits. This is not strictly true as there is multi-phonon absorption by the silicon lattice, but including it in the calculation is senseless because it cannot be adjusted to improve performance. How focused the beam is at the IRE bevel is determined by the optics used to

image it there. This aspect of focus was treated in Section 2.4. It was mentioned that an aperture setting of 9 along with a 5 1/4 inch lens would produce an image measuring 2.625mm in diameter and result in ~34% of the radiation being coupled into the IRE.

However, another effect must be considered. Because the lenses cracked during installation, we redesigned the IR Port flanges to accommodate separate windows and lenses. In the original design, the lenses doubled as windows, and in the current configuration the lenses are 1 3/8 inches further from the chamber than expected. Also, the sample could not be positioned as far forward as initially expected so that the difference between the designed focal length and the actual IR Port to IRE Bevel distance is 1 7/8 inches. The focal length of the currently installed KBr lenses is 5 1/4 inches while the IR Port to IRE bevel distance is 7 1/8 inches. Because of this 1 7/8 inch mismatch, the IR beam comes to a focal point and reaches its minimum diameter (i.e., its image size) 1 7/8 inches away from the IRE bevel. The beam then diverges for 1 7/8 inches before striking the bevel. Table 9.9 shows the effects this mismatch has on the image diameter produced at the IRE bevel. Instead of being focused to a spot that is 2.625mm in diameter, the infrared light measures 14.1mm in diameter when it reaches the bevel of the IRE. Dividing the ratio of the lighted area (the whole bevel,  $12 \times 0.707 \text{mm}^2$ ) by the image area ( $\pi (14.12^2)/4$ ), we find that only ~5.4% of the IR light enters the IRE instead of the 34% we would obtain if the IRE were located at the focal point of the 5 1/4 inch lens. This affects the throughput drastically. As shown in Table 9.10, when losses due to focusing the beam at the IRE are added into the overall throughput calculations, the overall Percent Throughput drops to ~1%.

### 9.5.5 Improving overall throughput

In summary, we estimate that 37%, 74%, and 95% of the beam are lost due to reflectance losses, beam travel losses, and losses due to quality of focus at the IRE, respectively. The overall throughput is most sensitive to changes in the quality of focus at the IRE, then to changes in the beam travel, and then to changes in reflectivity of the optical elements. Therefore, it seems that improving the optical elements in the system (gold coating the mirrors inside the spectrometer, for example) would yield only modest improvements in the overall throughput. Reducing the beam travel beyond its current value would be very difficult since the Magna 750 Bench is currently butted up various parts of the deposition system.

However, since the greatest loss occurs at the IRE due to problems with the system lenses, the overall throughput may be improved most easily by replacing the lenses. Installing lenses that are uncracked will reduce the reflection losses due to scattering at the grain boundaries. The greatest improvement comes as a result of correct focus of the IR light on the IRE bevel. As shown in Table 9.9, using a lens with a focal length of 7 1/8 inches and positioning the IRE at the focal point will produce an image measuring 3.56mm in diameter on the IRE bevel. Taking the ratio of the lighted area ( $3.56 \times 0.707 \text{mm}^2$ ) by the image area ( $\pi (3.56^2)/4$ ), we find that 25.3% of the IR radiation is coupled into the IRE. Table 9.11 shows the dramatic difference these changes bring about. The estimated Overall Percent Throughput increases 5-fold from 0.8% to 4.4%. I expect that a change of this magnitude would bring about a huge improvement in the final data both in terms of the minimum concentration of surface species one can measure and in the signal to noise ratio.

## **9.6 Recommendations for Future Improvements**

### **9.6.1 Bench positioning**

This infrared apparatus is fairly robust but could be improved. One main shortcoming is that the bench is positioned completely by hand. The initial alignment is quite delicate and also quite difficult since one must make miniscule adjustments by pushing a heavy instrument (i.e., the Magna 750 FTIR bench) around on a table top. No techniques exist for making small, reproducible adjustments in position. One could mount the bench on the table using linear bearings and a worm drive to make bench positioning more reproducible. The bench has tapped holes in its frame that are perfectly suited to a worm drive, and making linear bearings is fairly simple.

### **9.6.2 Lens specifications and fabrication**

The system needs new lenses and lens mounts that will allow the lenses to be removed and polished periodically. The lenses currently in use (Spectral Systems Inc. LNS-945-7342) are cracked. In addition, the focal length of these lenses is 5.25inches. Because of system changes made after receiving the lenses, the optimum focal length for those lenses is now 7.125inches. Lens mounts can be purchased from Oriel that will secure the lenses without cracking them. The lenses can be made in house by a literature procedure.<sup>9</sup> After a small initial investment (~\$200 for a lens polishing kit) each lens can be produced in a couple of hours at a cost of only ~\$50 each since the lenses would be ground from the same 38mm X 6mm thick KBr discs used as the system windows. The lenses currently in use cost \$550 each and required 2 months for the vendor to prepare. We were able to obtain usable IR spectra despite the severe defocus of the IR beam at the IRE bevel caused by using 5.25inch

FL lenses instead of 7.125inch FL lenses. However, using lenses of the correct focal length would provide a 5-fold increase in the amount of infrared radiation coupled into the IRE and would improve the SNR considerably as discussed in Section 9.5.5 above. Having the ability to prepare lenses in-house would yield significant cost- and time-savings for the group.

### **9.6.3 Temperature control**

The heater currently installed on the system uses radiant heating. The thermocouple is installed on the chuck, a large piece of stainless steel with a high thermal mass. During calibration, a second thermocouple is installed temporarily on the face of the platen to determine the steady-state sample temperature at a given temperature set point. Obviously, the chuck is less susceptible to temperature swings than the sample which has a much smaller thermal mass, and the sample temperature overshoots and oscillates before settling at the steady state temperature. Temperature swings in the sample were reduced by following a procedure of always retuning the temperature controller (the controller has an autotune algorithm) and manually limiting the maximum heater current after changing the temperature set point. Although temperature swings are reduced by this procedure, they cannot be eliminated as long as the thermocouple is located remotely from the sample. Two types of solutions exist for this problem. One can change the way the temperature is sensed or the way the sample is heated. The easiest improvement to make is to improve the temperature measurement. The thermocouple could be mounted on a piece of molybdenum that shares the same line of sight with the platen (which is molybdenum). It could also be mounted on a monitor sample near the crystal or attached to a piece of highly conductive metal in thermal contact with the platen. Careful tuning of the feedback controller would limit slight temperature oscillations. Another approach would be to redesign the heater such that the

crystal was mounted directly on a sample stage with very uniform heating and a thermal mass much larger than that of the sample. This design is different from the current one because only the outer edges of the platen touch the stainless steel chuck, and the back of the molybdenum platen is exposed directly to the quartz heater. Deshmukh and Aydil used a copper stage with oil heating to provide stable heating at temperatures between 45 and 300°C.<sup>10</sup> Another reported solution is to redesign the chuck so that the samples are mounted directly on top of a molybdenum “can” (a hollow cylinder open at one end) and mount the thermocouple on top of the can. Because the sample is in direct thermal equilibrium with the temperature controlled surface, accurate temperature control and good stability can be achieved while heating the cylinder either radiatively or resistively with cartridge heaters.<sup>11</sup>

#### **9.6.4 Infrared polarizer**

A few notes on equipment are appropriate and will serve as a starting point for future adaptations. A polarizer would be very helpful in identifying peaks as one could distinguish between in-plane and out-of-plane vibrations. Installing a polarizer in the beam path of the current system involves very little change to the system. As soon as it is feasible, the group should invest in one.

#### **9.6.5 Microscope detector**

While it may not be immediately practical to purchase another detector, the group may need a different detector in the future to investigate, for example, features that absorb at lower wavelengths than the current detector can measure. At that time, a detector designed for use in infrared microscopy should be considered. We used a standard MCT-A detector (Thermo-Nicolet, P/N 840-130000) for the *in-situ* FTIR measurements described in Chapter

8. The active area of the detection element in this detector is square and measures 1mm x 1mm. Thermo-Nicolet produces a similar MCT-A detector for their infrared microscopes that has a 0.25mm x 0.25mm square detection element. For modern infrared detectors, the smallest signal that can be detected is usually limited by the background radiation that reaches the detection element from blackbody emission of room temperature objects. The amount of blackbody radiation that reaches the detection element depends on the field-of-view of the detection element and the size of the element itself. All other factors being equal, a detector with a smaller detection element sees much less of this background radiation and can detect a lower photon flux per unit area of detection element. Switching from a standard detector to one designed for microspectroscopy can reduce the noise from background radiation by as much as 10 times.<sup>12</sup> Having access to a microscope MCT detector would have lowered the photon detection threshold greatly, reduced the noise, and increased the SNR of the measurements reported here, and it would improve future work in similar ways.

#### **9.6.6 Modifications for transmission and reflectance measurements**

When the system was designed, we hoped to be able to augment the ATR measurements with transmission and/or grazing angle reflectance measurements. An optical table is attached to the frame behind the deposition chamber and beside the Thermo-Nicolet bench to allow easy positioning of optical elements to direct the infrared radiation through the rear flange, and the detector-side optics table is engineered in such a way that it can be mounted in different positions on the system frame to detect light exiting at either the IR port or at another port on the front of the system. Two gold-plated reflectors (4inch planar mirrors, Janos P/N A8010P402) were purchased along with the parabolic reflector and may be rod-mounted on the rear optics table to direct the IR beam into and out of the chamber as

necessary. Although modifying the system optics for transmission and/or grazing angle reflectance measurements is conceptually simple, a few notes are in order. Many gas lines and other ports currently enter the system through the rear of the chamber and must be relocated. A short nipple having 8inch conflat flanges on two sides and 2 ¾ inch conflat flanges located about its circumference is stored with the rest of the system hardware. Installing it directly below the main system chamber and above the butterfly valve would allow ample access for the displaced fittings. While single-bounce reflectance measurements only require passing the light through the chamber with the sample in the proper orientation, transmission measurements require further modifications. Sample mounting and heating are challenges for measuring transmission. The sample mounting must be reengineered to allow passage of light straight through the sample without interference from the chuck and heater. Resistive heating through the sample may be the best option for this experiment.

### **9.6.7 IRE characteristics and fabrication**

The internal reflection elements used in this work were purchased from Spectral Systems Incorporated at a cost of \$100 each (when purchased in lots of 10). Prices quoted from other suppliers were higher. The IREs were mechanically polished and were initially quite rough (~15Å rms by atomic force microscopy). Because of the low quality of these crystals, IREs should be purchased from another supplier in the future. (Harrick Scientific is a reputable source.)

Another option offering lower costs and higher quality is to prepare the crystals in-house, and we assembled a procedure for doing so. Because of time and funding constraints we were never able to implement this procedure. Some trial and error will be required to optimize the process conditions, but this information should be a great help to future

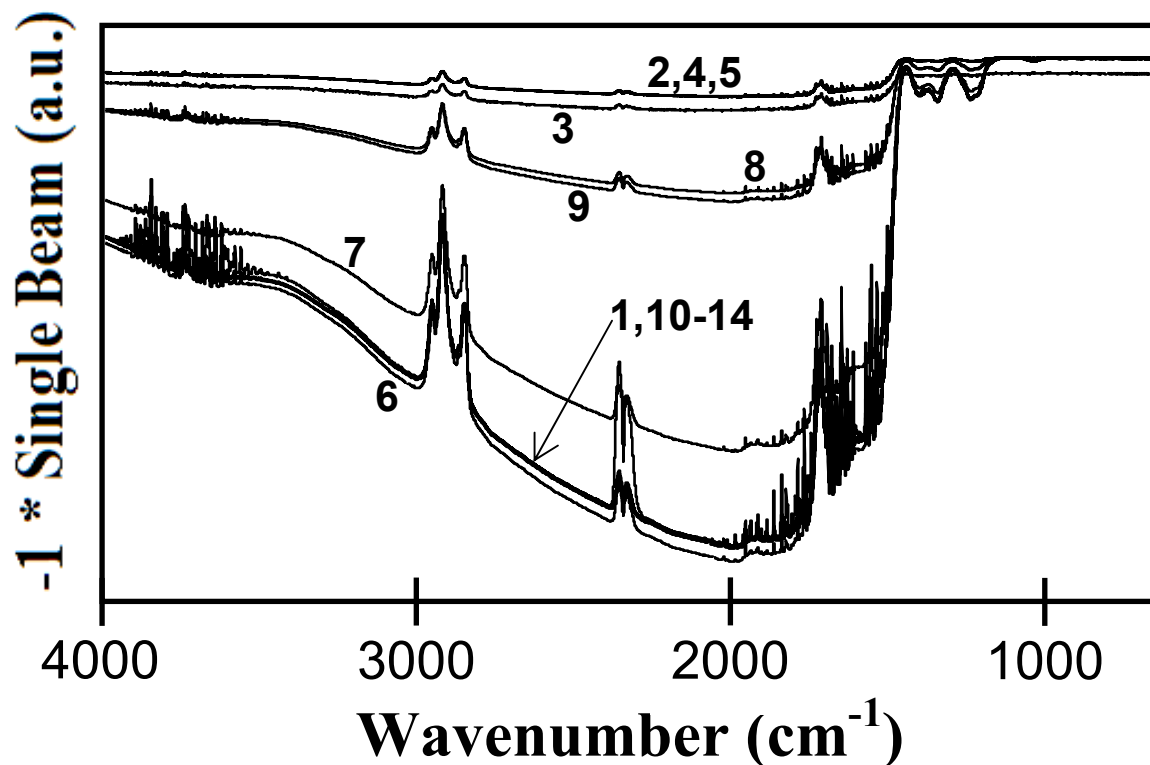
researchers. Bender et al. report preparing Si(100) IREs of very high quality via anisotropic etching of silicon nitride masked Si(100) wafers with an aqueous KOH solution at 80°C.<sup>13</sup> After etching, the IRE bevels are formed by the Si (111) planes and are at 54.74°. A general process flow is shown as Figure 9.3, and Figure 9.4 shows a suggested mask pattern (dark-field) for etching 36mm long IREs from 4inch, optical-grade, high-resistivity silicon wafers. The primary wafer flat on 4inch Si(100) wafers is parallel to the <110> direction in the silicon crystal, and anisotropic etching will leave (111) planes that run parallel and perpendicular to the <110> direction, so aligning to the wafer flat is both helpful and convenient. Given the large dimensions of the features on this mask, a reasonable first mask can be made by printing the mask on a transparency and taping the transparency to a glass plate. The rectangular pieces of silicon produced will have bevels on all four sides, and IREs of the desired size may be produced by cleaving the “long IREs” produced. Anisotropic etching of silicon using KOH and other alkaline reagents is well-known, and many references are available for optimizing the process conditions and etchant composition.<sup>14-19</sup> The quality of future *in-situ* measurements would be greatly improved if adsorption was limited to the Si (100) surface.

## 9.7 References

- 1 Griffiths, P. R.; de Haseth, J. A. *Fourier Transform Infrared Spectroscopy (Vol. 83 in Chemical Analysis: A Series of Monographs on Analytical Chemistry and Its Applications)*. John Wiley & Sons, Inc: 1986.
- 2 Bent, B. E.; Nuzzo, R. G.; Dubois, L. H. *Journal of the American Chemical Society* **1989**, *111*, 1634 - 1644.

- 3 Donnelly, V. M.; Gross, M. E. *Journal of Vacuum Science & Technology A - Vacuum Surfaces and Films* **1993**, *11*, 66 - 77.
- 4 Gross, M. E.; Fleming, C. G.; Cheung, K. P.; Heimbrook, L. A. *Journal of Applied Physics* **1991**, *69*, 2589 - 2592.
- 5 McCaulley, J. A.; Shul, R. J.; Donnelly, V. M. *Journal of Vacuum Science & Technology A - Vacuum Surfaces and Films* **1991**, *9*, 2872 - 2886.
- 6 Squire, D. W.; Dulcey, C. S.; Lin, M. C. *Journal of Vacuum Science & Technology B* **1985**, *3*, 1513 - 1519.
- 7 Oas, S. Manufacturing Engineer - Customer Specials, Thermo-Nicolet Corporation, Personal Communication, February 27, 2002
- 8 *Omnic E.S.P. v5.2*, Thermo Electron Corporation: Madison, Wisconsin, Copyright 2000.
- 9 Treffman, L. M.; Morrison, P. W., Jr. *Review of Scientific Instruments* **1996**, *67*, 1454 - 1457.
- 10 Deshmukh, S. C.; Aydil, E. S. *Journal of Vacuum Science & Technology A - Vacuum Surfaces and Films* **1995**, *13*, 2355 - 2366.
- 11 Yates, J. T., Jr *Experimental Innovations in Surface Science: A Guide to Practical Laboratory Methods and Instruments*. Springer-Verlag: New York, 1998.
- 12 Carr, G. L.; Scott, J.; Williams, G. P. *Detectors for Infrared Science (Infrared Working Group Report)*; DetectorSync, Workshop on Detectors for Synchrotron Research Washington, DC, October 30-31, 2000.
- 13 Bender, H.; Verhaverbeke, S.; Heyns, M. M. *Journal of the Electrochemical Society* **1994**, *141*, 3128 - 3136.

- 14 Bassous, E. *IEEE Transactions on Electron Devices* **1978**, *ED-25*, 1178 - 1185.
- 15 Bean, K. E. *IEEE Transactions on Electron Devices* **1978**, *ED-25*, 1185 - 1193.
- 16 Kohler, M. *Etching in Microsystem Technology*. Wiley-VCH: Weinheim, 1999.
- 17 Kovacs, G. T. A. *Micromachined Transducers Sourcebook*. McGraw-Hill: Boston, 1998.
- 18 Seidel, H.; Csepregi, L.; Heuberger, A.; Baumgärtel, H. *Journal of the Electrochemical Society* **1990**, *137*, 3612 - 3626.
- 19 Price, J. B. In *Semiconductor Silicon*, Huff, H. R.; Burgess, R. R., Eds. The Electrochemical Society: Princeton, 1973; 339 - 353.



Spectrum	Aperture	Velocity (cm/s)	Res (cm <sup>-1</sup> )	Number of Scans	Integrated Area [CH]	Noise (peak to peak)	Noise (rms)	SNR
1	69	1.8988	2	512	-215.163	0.0795016	0.0243807	2706
2	0	0.9494	2	16	-16.751	0.0162926	0.0026793	1028
3	0	3.1647	2	16	-16.416	0.0269594	0.0055373	609
4	0	0.9494	2	256	-16.656	0.0079525	0.0017480	2094
5	0	1.8988	4	16	-16.633	0.0149917	0.0032416	1109
6	100	1.8988	4	16	-223.538	0.0886374	0.0264667	2522
7	32	1.8988	4	16	-167.663	0.0602527	0.0172812	2783
8	6	0.9494	2	256	-57.467	0.0200154	0.0058178	2871
9	6	1.8988	4	16	-60.509	0.0279036	0.0065059	2169
10	69	1.8988	4	16	-213.376	0.0826373	0.0245654	2582
11	69	1.8988	4	256	-210.563	0.0792999	0.0249781	2655
12	69	1.8988	4	256	-212.016	0.0793953	0.0244970	2670
13	69	1.8988	4	256	-212.638	0.0781751	0.0243005	2720
14	69	1.8988	4	256	-213.143	0.0778966	0.0245185	2736

**Figure 9.1** Single beam spectra of a self-assembled OTS monolayer film collected using the settings shown and the SNR values that result for each spectrum. Although the y-axis units are arbitrary, all spectra are plotted on a common scale. All spectra have been multiplied by a factor of -1 so peak areas can be measured using the Omnic software.

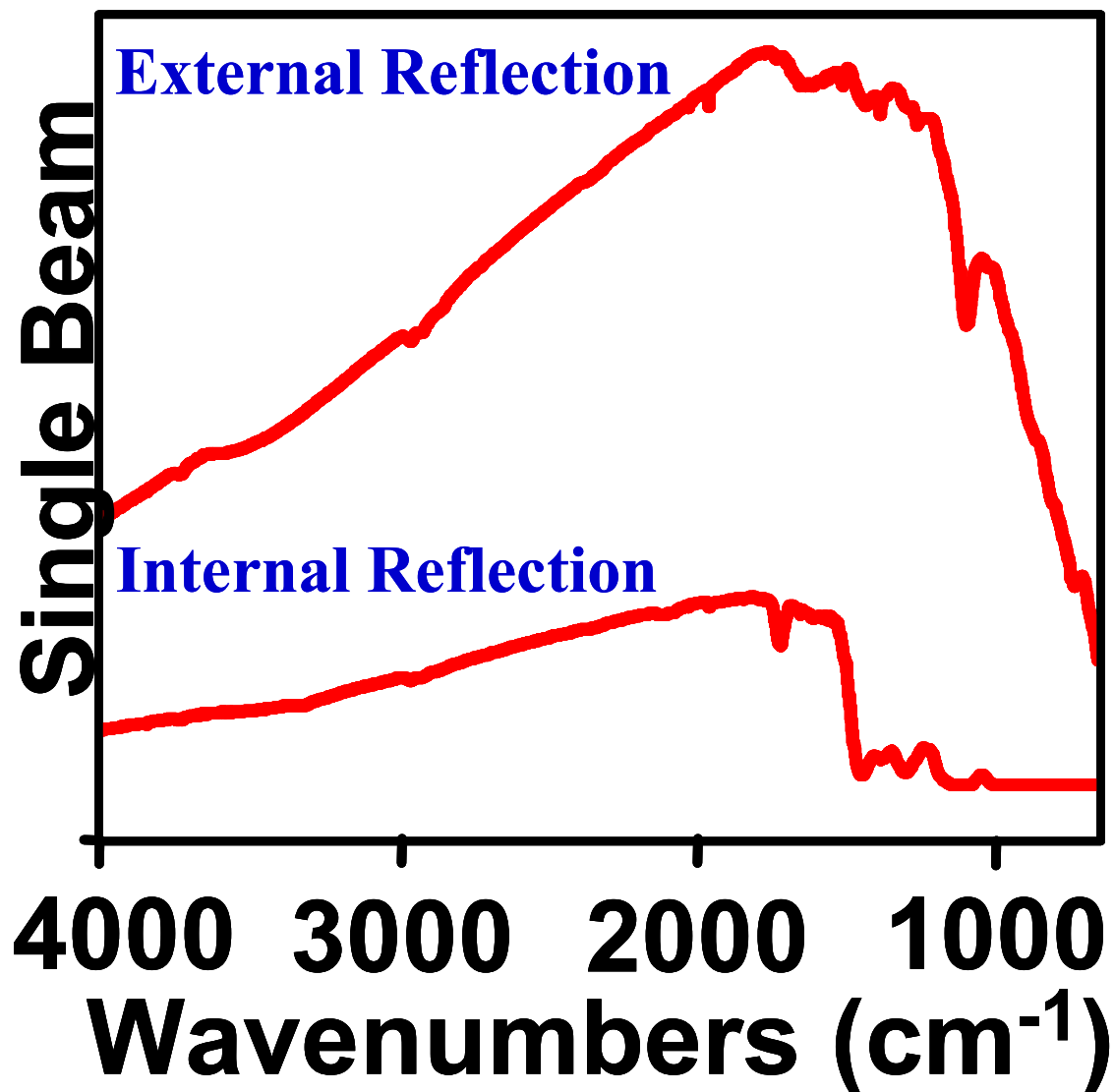
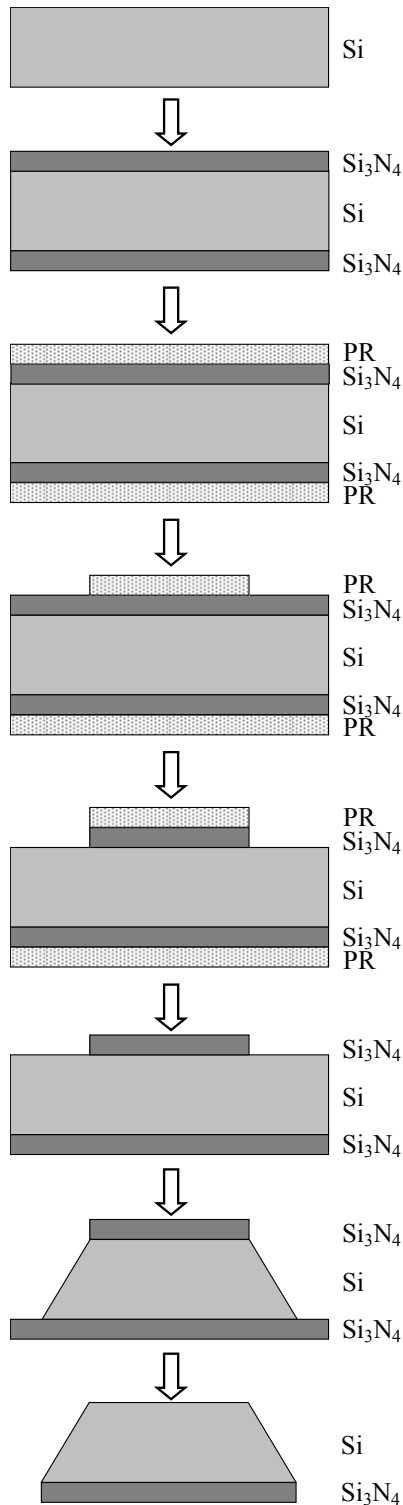


**Figure 9.2** Representative FTIR single-beam spectra for our instrument when aligned for single-bounce external reflection and attenuated total internal reflection (ATR). The silicon lattice absorption band is visible below 1500cm<sup>-1</sup> when aligned for ATR.



**Step #1:** Start with 4inch Si(100) wafers. Clean them in JT Baker solution (5min). Grow a sacrificial oxide and etch with dilute HF solution (10s past dewet).

**Step #2:** Deposit  $>1000\text{\AA}$  LPCVD  $\text{Si}_3\text{N}_4$  on both sides of the wafer. Use a recipe that gives a dense nitride.

**Step #3:** Spin positive photoresist (PR) on both sides of the wafer.

**Step #4:** Pattern, develop, and digest the photoresist.

**Step #5:** Etch the  $\text{Si}_3\text{N}_4$  leaving the tops and bottoms of IREs protected. Either a wet, hot  $\text{H}_3\text{PO}_4$ -based etch or a dry, reactive ion etch (RIE) process may be used.

**Step #6:** Strip the photoresist to eliminate organic contamination from the IRE etch bath.

**Step #7:** Etch the patterned, Si wafers in hot KOH solution to form the bevels.

**Step #8:** Dry etch (RIE) the  $\text{Si}_3\text{N}_4$  to remove the nitride from the top of the IREs and free the IREs from each other.

**Figure 9.3** A suggested process flow for preparing Si IREs chemically.

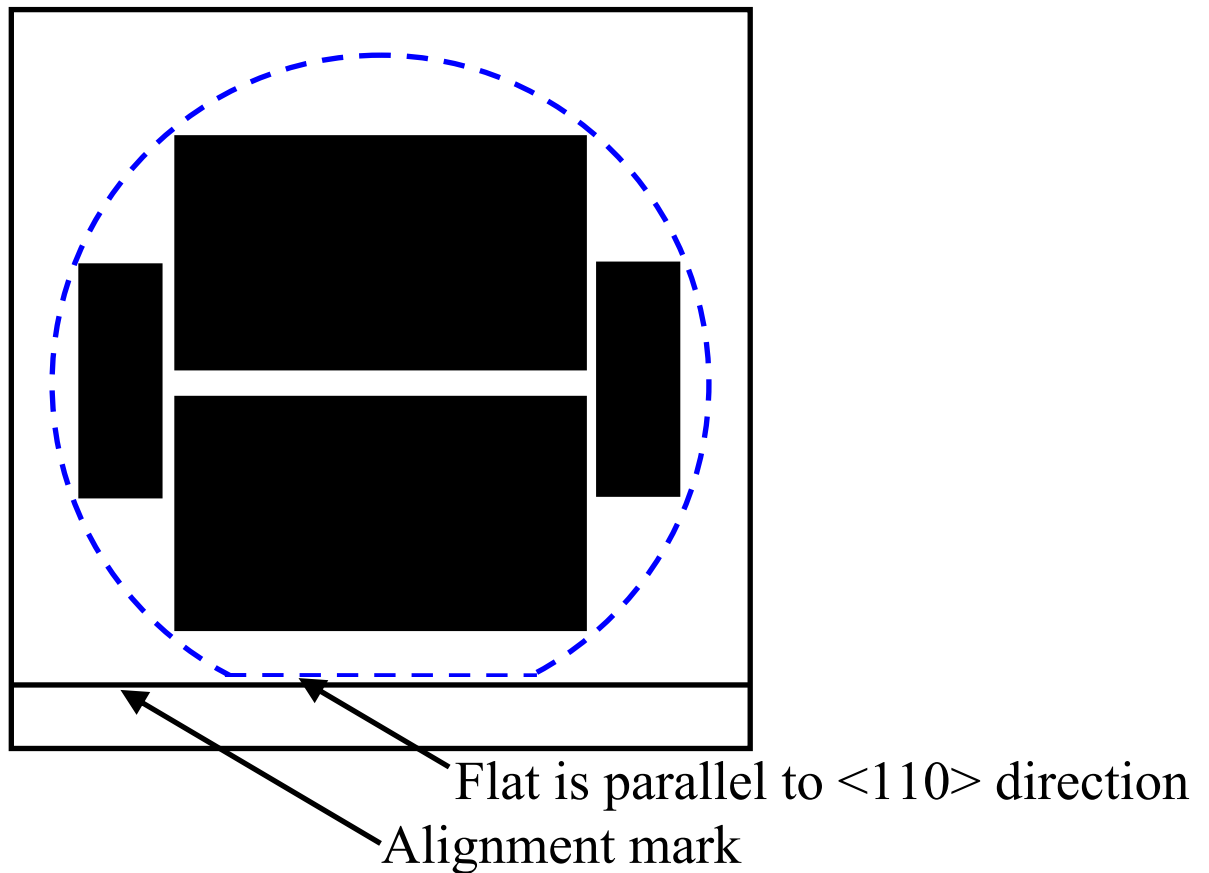


**Figure 9.4** Possible dark field mask used with positive photoresist for preparing Si(100) IREs chemically. Masked areas will remain after etching. The silicon wafer will be etched completely away in unmasked areas leaving the (111) plane at all remaining edges. All four sides of the rectangles will be beveled at  $54.74^\circ$ . IREs of the desired size will be cleaved from the long IREs produced. The hashed line shows the position of a 4inch wafer under the mask.

**Table 9.1** Four spectra were collected at identical settings to judge the repeatability with which one can derive the SNR by the procedure used here. It appears that SNR values within 100 of one another are statistically the same.

<b>Spectrum</b>	<b>Aperture</b>	<b>Velocity (cm/s)</b>	<b>Number of Scans</b>	<b>Integrated Area [CH]</b>	<b>Noise (peak to peak)</b>	<b>SNR</b>
11	69	1.8988	256	-210.563	0.0792999	2655
12	69	1.8988	256	-212.016	0.0793953	2670
13	69	1.8988	256	-212.638	0.0781751	2720
14	69	1.8988	256	-213.143	0.0778966	2736

**Table 9.2** Three measurements performed with identical aperture and number of co-added scans to show the effect of scanning mirror velocity.

<b>Spectrum</b>	<b>Aperture</b>	<b>Velocity (cm/s)</b>	<b>Number of Scans</b>	<b>Integrated Area [CH]</b>	<b>Noise (peak to peak)</b>	<b>SNR</b>
2	0	0.9494	16	-16.751	0.0162926	1028
5	0	1.8988	16	-16.633	0.0149917	1109
3	0	3.1647	16	-16.416	0.0269594	609

**Table 9.3** The effect of varying the source aperture was tested by collecting spectra with several different aperture settings.

<b>Spectrum</b>	<b>Aperture</b>	<b>Velocity (cm/s)</b>	<b>Number of Scans</b>	<b>Integrated Area [CH]</b>	<b>Noise (peak to peak)</b>	<b>SNR</b>
6	100	1.8988	16	-223.538	0.0886374	2522
10	69	1.8988	16	-213.376	0.0826373	2582
7	32	1.8988	16	-167.663	0.0602527	2783
9	6	1.8988	16	-60.509	0.0279036	2169
5	0	1.8988	16	-16.633	0.0149917	1109

**Table 9.4** The aperture (APT) setting controls the iris size through which the infrared source is imaged. This table shows the variation of the image produced at the detector located in the bench. The bolded row shows the aperture setting typically used for ATR measurements in this work. Estimated beam divergence values are italicized.

<b>Iris Setting (APT=?)</b>	<b>Iris Diameter (mm)</b>	<b>Beam Divergence</b>	<b>Image Size at Bench Detector (mm)</b>
150	10.7	<i>3.9°</i>	1.98
115	9.30	<i>3.4°</i>	1.72
100	8.75	<i>3.2°</i>	1.61
75	7.52	<i>2.8°</i>	1.38
50	6.27	<i>2.3°</i>	1.15
32	5.08	<i>1.9°</i>	0.94
25	4.50	<i>1.7°</i>	0.85
<b>9</b>	<b>3.00</b>	<b><i>1.1°</i></b>	<b>0.55</b>
6	2.50	<i>0.94°</i>	0.46
4	2.00	<i>0.74°</i>	0.37
1	1.30	<i>0.50°</i>	0.24
0	0.75	<i>0.28°</i>	0.14

**Table 9.5** List of various parts that comprise the ATR-FTIR apparatus.

<i>Part</i>	<i>Supplier</i>	<i>P/N</i>	<i>Description</i>
FTIR Instrument	Thermo-Nicolet	Magna 750	FTIR bench with Vectra interferometer capable of better than 0.1cm <sup>-1</sup> resolution.
MCT-A Detector	Thermo-Nicolet	840-130000	High D* detector, 11,700 - 600cm <sup>-1</sup> useful range, 1mm x 1mm detection element
Lenses	Spectral Systems Inc.	LNS-945-7342	KBr lens, 1.6" diam. x 0.500" center thickness, 5.25±0.25" FL, 80/50 scratch dig
Parabolic Mirror	Janos Technology	A8037P305	Protected gold coated turned aluminum, 3" FL, 3" diameter, 90° parabolic reflector
Adapter Plate	Janos Technology	2154-0005	Adapter plate for 3" diameter off-axis parabolic
Window Mounts	Burlington Machine Shop, NCSU	N/A	Modified Kurt Lesker P/N F0275X150N. Added window retaining ring, o-rings on both faces, and VCR port for differentially pumping space between o-rings.
IREs	Spectral Systems Inc.		Trapezoidal, mechanically-polished Si(100) crystals (40x12x0.5mm)
Purged Beam Path	Home Depot	Assorted	Assorted pieces schedule 40 PVC tube painted black
Optical Positioning	Oriel	Assorted	Optical rail, multiple micrometers, and lens mounts.

**Table 9.6** The infrared beam diverges as it travels through the FTIR spectrometer to the External Beam Port and then on to the deposition chamber IR Port. The white sections show the percent beam throughput that results from traveling one of those distances individually, and the shaded section at right shows the overall percent beam throughput over the whole pathlength. The beam passes through two apertures (the External Beam Port on the Magna 750 FTIR spectrometer and the IR Port on the deposition chamber) along the way, and any portion of the beam that is larger than the aperture is lost. All distances listed in the table are in inches.

Throughput Calculations - Losses due to DIVERGENCE OF BEAM DURING TRANSPORT												
Inside Magna 750 Bench			From Interferometer to Bench's External Beam Port				From External Beam Port to Chamber IR Port				Overall % Throughput from Interferometer to Chamber IR Port	
Aperture Setting	Divergence (degrees)	$D_{\text{beam}}$ at Interferometer	Beam Travel	$D_{\text{beam}}$ at Ext Beam Port	$D_{\text{physical}}$ Ext Beam Port	% Beam Throughput	Beam Travel	$D_{\text{beam}}$ at IR Port	$D_{\text{physical}}$ IR Port	% Beam Throughput		
150	3.9	1.5	13	3.27	2	37.4%	18	4.45	1.37	9.5%	4%	
115	3.4	1.5	13	3.04	2	43.1%	18	4.14	1.37	11.0%	5%	
100	3.2	1.5	13	2.95	2	45.9%	18	4.01	1.37	11.7%	5%	
75	2.8	1.5	13	2.77	2	52.1%	18	3.76	1.37	13.3%	7%	
50	2.3	1.5	13	2.54	2	61.8%	18	3.45	1.37	15.8%	10%	
32	1.9	1.5	13	2.36	2	71.7%	18	3.19	1.37	18.4%	13%	
25	1.7	1.5	13	2.27	2	77.5%	18	3.07	1.37	19.9%	15%	
<b>9</b>	<b>1.1</b>	<b>1.5</b>	<b>13</b>	<b>2.00</b>	<b>2</b>	<b>100%</b>	<b>18</b>	<b>2.69</b>	<b>1.37</b>	<b>25.9%</b>	<b>26%</b>	
6	0.94	1.5	13	1.93	2	100%	18	2.52	1.37	29.6%	30%	
4	0.74	1.5	13	1.84	2	100%	18	2.30	1.37	35.5%	35%	
1	0.5	1.5	13	1.73	2	100%	18	2.04	1.37	45.1%	45%	
0	0.28	1.5	13	1.63	2	100%	18	1.80	1.37	57.7%	58%	

**Table 9.7** This table shows the Percent Transmission that would results if IR beam losses only occurred due to imperfect reflection at mirrors and imperfect transmission at lenses and windows.

**Throughput Calculations - Losses due to REFLECTION only**

Optical Element (Details)	Percent Transmission <sub>Element</sub>			Percent Transmission <sub>Cumulative</sub>		
	<i>Pessimistic</i>	<i>Optimistic</i>	<i>Realistic</i>	<i>Pessimistic</i>	<i>Optimistic</i>	<i>Realistic</i>
Initial Energy (at Beam Splitter/Interferometer)				100	100	100
Passport Mirror (Aluminum)	0.90	0.95	0.93	90.0	95.0	93.0
Lens (KBr, source side, cracked)	0.80	0.95	0.90	72.0	90.7	83.7
Window (KBr, source side)	0.90	0.95	0.93	64.8	86.6	77.8
Window (KBr, detector side)	0.90	0.95	0.93	58.3	82.7	72.4
Lens (KBr, detector side, cracked)	0.80	0.95	0.90	46.7	79.0	65.2
Parabolic Reflector (Gold coated)	0.95	0.99	0.97	44.3	78.2	63.2
<b>Percent Initial Energy Remaining at Detector:</b>				<b>44%</b>	<b>78%</b>	<b>63%</b>

**Table 9.8** Combining reflection losses with the beam transport losses expected for our apparatus (aperture setting = 9) shows that ~16% of the beam is available for interaction with the IRE.

**Throughput Calculations - Losses due to REFLECTION and BEAM TRANSPORT**

Optical Element (Details)	Percent Transmission <sub>Element</sub>			Percent Transmission <sub>Cumulative</sub>		
	<i>Pessimistic</i>	<i>Optimistic</i>	<i>Realistic</i>	<i>Pessimistic</i>	<i>Optimistic</i>	<i>Realistic</i>
Initial Energy (at Beam Splitter/Interferometer)				100	100	100
Passport Mirror (Aluminum)	0.90	0.95	0.93	90.0	95.0	93.0
Beam Transmission (IR Port)	0.26	0.26	0.26	23.3	24.6	24.1
Lens (KBr, source side, cracked)	0.80	0.95	0.88	18.7	23.5	21.2
Window (KBr, source side)	0.90	0.95	0.93	16.8	22.5	19.7
Window (KBr, detector side)	0.90	0.95	0.93	15.1	21.4	18.4
Lens (KBr, detector side, cracked)	0.80	0.95	0.88	12.1	20.5	16.2
Parabolic Reflector (Gold coated)	0.95	0.99	0.97	11.5	20.3	15.7
<b>Percent Initial Energy Remaining at Detector:</b>				<b>11%</b>	<b>20%</b>	<b>16%</b>

**Table 9.9** The size to which the IR beam can be focused in the deposition chamber varies with the size of the initial Iris/Aperture Setting. The IRE is not located at the design focal length of the current lens (5 1/4"). Instead it is located 1 7/8 inches further away at 7 1/8 inches. Because of this severe mismatch, a large loss of the IR radiation is lost unnecessarily and can be reclaimed by using a lens of the correct focal length. An Aperture Setting of 9 was used in this work, and the bolded values below are of specific interest.

<i>Iris Setting (APT=?)</i>	<i>Iris Diameter (mm)</i>	<i>Image Diameter (mm) at Focal Point</i>		<i>Image Diameter (mm) at IRE Bevel</i>	
		<i>Current Lens (FL = 5 1/4")</i>	<i>Correct Lens (FL = 7 1/8")</i>	<i>Current Lens (FL = 5 1/4")</i>	<i>Correct Lens (FL = 7 1/8")</i>
150	10.70	9.36	12.7	18.4	12.7
115	9.30	8.14	11.0	17.7	11.0
100	8.75	7.66	10.4	17.3	10.4
75	7.52	6.58	8.93	16.7	8.93
50	6.27	5.49	7.45	16.0	7.45
32	5.08	4.45	6.03	15.3	6.03
25	4.50	3.94	5.34	15.0	5.34
<b>9</b>	<b>3.00</b>	<b>2.63</b>	<b>3.56</b>	<b>14.1</b>	<b>3.56</b>
6	2.50	2.19	2.97	13.8	2.97
4	2.00	1.75	2.38	13.6	2.38
1	1.30	1.14	1.54	13.2	1.54
0	0.75	0.66	0.89	12.8	0.89

**Table 9.10** This table takes into account all the relevant beam losses. The beam intensity at the detector is expected to only be ~1% the strength of the initial beam with the current optical apparatus.

<b>Throughput Calculations - Losses due to REFLECTION, BEAM TRANSPORT, and FOCUS AT IRE</b>						
<b>Optical Element (Details)</b>	<b>Percent Transmission<sub>Element</sub></b>			<b>Percent Transmission<sub>Cumulative</sub></b>		
	<i>Pessimistic</i>	<i>Optimistic</i>	<i>Realistic</i>	<i>Pessimistic</i>	<i>Optimistic</i>	<i>Realistic</i>
Initial Energy (at Beam Splitter/Interferometer)				100	100	100
Passport Mirror (Aluminum)	0.90	0.95	0.93	90.0	95.0	93.0
Beam Transmission (IR Port)	0.26	0.26	0.26	23.3	24.6	24.1
Lens (KBr, source side, cracked)	0.80	0.95	0.88	18.7	23.5	21.2
Window (KBr, source side)	0.90	0.95	0.93	16.8	22.5	19.7
IRE (Si(100), trapezoidal, 45°, 40x12x0.5mm <sup>3</sup> )	0.05	0.05	0.05	0.9	1.2	1.1
Window (KBr, detector side)	0.90	0.95	0.93	0.8	1.2	1.0
Lens (KBr, detector side, cracked)	0.80	0.95	0.88	0.7	1.1	0.9
Parabolic Reflector (Gold coated)	0.95	0.99	0.97	0.6	1.1	0.8
<b>Percent Initial Energy Remaining at Detector:</b>				<b>0.6%</b>	<b>1.1%</b>	<b>0.8%</b>

**Table 9.11** This table shows the effect of replacing the current lenses with uncracked lenses having a focal length of 7 1/8 inches. The overall percent throughput increases 5-fold as compared to the results shown in Table 9.10

**New Lenses (Uncracked, Correct Focal Length)**

**Throughput Calculations - Losses due to REFLECTION, BEAM TRANSPORT, and FOCUS AT IRE**

Optical Element (Details)	Percent Transmission <sub>Element</sub>			Percent Transmission <sub>Cumulative</sub>		
	<i>Pessimistic</i>	<i>Optimistic</i>	<i>Realistic</i>	<i>Pessimistic</i>	<i>Optimistic</i>	<i>Realistic</i>
Initial Energy (at Beam Splitter/Interferometer)				100	100	100
Passport Mirror (Aluminum)	0.90	0.95	0.93	90.0	95.0	93.0
Beam Transmission (IR Port)	0.26	0.26	0.26	23.3	24.6	24.1
Lens (KBr, source side, cracked)	0.90	0.95	0.93	21.0	23.5	22.4
Window (KBr, source side)	0.90	0.95	0.93	18.9	22.5	20.9
IRE (Si(100), trapezoidal, 45°, 40x12x0.5mm <sup>3</sup> )	0.25	0.25	0.25	4.8	5.7	5.3
Window (KBr, detector side)	0.90	0.95	0.93	4.3	5.4	4.9
Lens (KBr, detector side, cracked)	0.90	0.95	0.93	3.9	5.2	4.6
Parabolic Reflector (Gold coated)	0.95	0.99	0.97	3.7	5.1	4.4
<b>Percent Initial Energy Remaining at Detector:</b>				<b>3.7%</b>	<b>5.1%</b>	<b>4.4%</b>

## 10 Appendix 2: Quotable (and Unquotable) Quotes

At any given time and during any given endeavor, “*there exists an infinitesimally small, but finite, probability*” that someone will say exactly the right thing. (Why yes, Dr. Parsons! I was already quoting you right there, you physicist you... Although I do find that phrase slightly more appropriately used in a research document than over lunch at East Village...)

Perhaps it’s the “right thing” because it amuses us, or maybe it sums up in a trim way something we’ve felt but never quite found the words to express. For various reasons, I enjoy each of the quotes I’ve collected below. I hope you enjoy them, too. –MJK

### 10.1 Notable quotes from friends and acquaintances

- 1) **Jim Chambers** (11-9-2004) at the SRC/SEMATECH FEP Transition Center Review  
*Hey man. Good to see you. Get the hell out of here!*  
Of course, Jim was referring to the length of time I’ve been at NC State, and, as usual, his delivery was perfect. He noticed me sitting there, walked up quickly with a big, happy-to-see-you grin on his face, and shook my hand vigorously as he exclaimed “Hey man. Good to see you.” Then after pausing for a single heart beat, he leaned in while still grasping my hand and with a look of complete and intense sincerity on his face commanded me to “Get the hell out of here!” Then, without hesitation, he turned on his heel and walked away. Brief. In your face. Irreverent, but well-considered. Pure Jim.
- 2) **Gerry Lucovsky** (11-4-2002) at the SRC/SEMATECH FEP Center Review  
*You don’t put bananas in the refrigerator, and you don’t put silicon nitride on silicon.*
- 3) **Chris Palmstrom** to Brian Schultz.  
*Sleep? I pay you to work. I don’t pay you to sleep!*  
Chris, Brian’s advisor at the University of Minnesota, captures the essence of the advisor-advisee relationship.
- 4) **Greg Parsons** (10-3-2000) referring to reactions in high-k materials.  
*There’s some weird sh\*t that goes on with this stuff.*  
We were discussing my latest zirconium silicate experiments... In all fairness, I think he was trying to make me feel better, but he was staring straight at my data as he said it.
- 5) **Theodosia Gougousi** (11-1-2002) referring to infrared data manipulation.  
*I’m done with that sh\*t, man.*  
Ironically, she said this just before finding out that she was not, in fact, done. She spent the next three months working with the IR data.
- 6) **Greg Parsons** (8-10-2004) talking about my *in-situ* ATR-FTIR experiments.  
*I think the experiment we tried here is an incredible b\*tch.*  
You know what, Dr. Parsons? You’re right.

## 10.2 Interesting quotes from famous thinkers

1) **Goethe**

*Live each day as if your life had just begun.*

This sentiment says so much more than the modern version, “*Live each day as if it were your last,*” which I find a bit macabre.

2) **Goethe**

*It is not doing the thing we like, but liking the thing we have to do that makes life happy.*

3) **John Lubbock**

*Rest is not idleness, and to lie sometimes on the grass under the trees on a summer's day, listening to the murmur of water, or watching the clouds float across the blue sky is by no means a waste of time.*

4) **Mark Twain**

*There are lies, damn lies, and statistics.*

5) **J.M. Prausnitz et al.** in the 2<sup>nd</sup> edition of their excellent thermodynamics text remind us of two famous sayings.

*Patriotism is the last refuge of a scoundrel. – Samuel Johnson*

*An ounce of prevention is worth a pound of cure. – Benjamin Franklin*

Then, they present their own “research appropriate” versions.

*Statistics is the last refuge of a poor experimentalist.*

*A gram of good data is worth more than a ton of consistency tests.*

6) **Albert Einstein**

*If I were not a physicist, I would probably be a musician.*

*I often think in music. I live my daydreams in music.*

*I see my life in terms of music. I get the most joy in life out of music.*

7) **John Erskine**

*Music is the only language in which you cannot say a mean or sarcastic thing.*

8) **Albert Szent-Györgyi** in his 1974 essay on research grants

*Scientific research is, in many ways, related to art. If one wants good music to be produced, one looks for a good musician and not for a project.*

- 9) **Mark Twain**  
*Forgiveness is the fragrance the violet sheds on the heel that has crushed it.*
- 10) **Thomas Edison**  
*As a cure for worrying, work is better than whiskey.*
- 11) **Albert Einstein**  
*I think and think, for months, for years;  
ninety-nine times the conclusion is false.  
The hundredth time I am right.*
- 12) **Albert Szent-Györgyi**  
*Research is to see what everybody else has seen  
and to think what nobody else has thought.*
- 13) **G.K. Chesterson**  
*It isn't that they can't see the solution.  
It is that they can't see the problem.*
- 14) **Albert Einstein**  
*Imagination is more important than knowledge... knowledge is limited, but  
imagination encircles the world. To see with one's own eyes, to feel and judge  
without succumbing to the suggestive power of the fashion of the day, to be able  
to express what one has seen and felt in a trim sentence or even in a cunningly  
wrought word... is that not glorious?*
- 15) **Leonardo da Vinci**  
*Simplicity is the ultimate sophistication.*
- 16) **Robert Noyce** (Co-founder of Intel, 1967)  
*Don't be encumbered by history.  
Go off and do something wonderful.*
- 17) **Calvin Coolidge**  
*Nothing in this world can take the place of persistence.  
Talent will not; nothing is more common than unsuccessful people with talent.  
Genius will not; unrewarded genius is almost a proverb.  
Education will not; the world is full of educated derelicts.  
Persistence and determination alone are omnipotent.  
The slogan "press on" has solved and always will solve the problems of the human  
race.*
- 18) **Albert Einstein**  
*I want to know God's thoughts. The rest are details.*